

**Precision measurement of and search for dark matter
in the transverse momentum spectra of Z bosons**

by

Dylan George Hsu

B.S., Syracuse University (2014)

Submitted to the Department of Physics

in partial fulfillment of the requirements for the degree of

Doctor of Philosophy

at the

MASSACHUSETTS INSTITUTE OF TECHNOLOGY

September 2019

© Massachusetts Institute of Technology 2019. All rights reserved.

Author
.....

Department of Physics
July 26, 2019

Certified by
.....

Christoph Paus
Professor of Physics
Thesis Supervisor

Accepted by
.....

Nergis Mavalvala
Associate Department Head of Physics

Precision measurement of and search for dark matter in the transverse momentum spectra of Z bosons

by

Dylan George Hsu

Submitted to the Department of Physics
on July 26, 2019, in partial fulfillment of the
requirements for the degree of
Doctor of Philosophy

Abstract

A measurement of the differential Z boson production cross section in proton-proton collisions is presented. It furnishes a precision test of the Standard Model, and constrains the parton distribution functions of the proton. Moreover, it is a building block for future measurements of the mass of the W^\pm boson. A study of the efficiency of lepton identification algorithms is performed which drives the precision of the measurement at lower values of transverse momentum.

In tandem, a search for new physics in events with a Z boson produced in association with large missing transverse momentum is presented. The results of this search are interpreted in the context of several dark matter models: generic spin-0 or spin-1 mediators, invisible decays of a Higgs-like boson, unparticles, and large extra spatial dimensions. A multivariate analysis was developed to enhance the sensitivity of the invisible Higgs interpretation. The theoretical uncertainty on the irreducible background from electroweak diboson processes is constrained by emulating the missing energy using pure control samples in the fully leptonic final states.

The data were collected with the Compact Muon Solenoid detector at the Large Hadron Collider and correspond to an integrated luminosity of 35.9 fb^{-1} . No significant deviations from the Standard Model are found.

Thesis Supervisor: Christoph Paus

Title: Professor of Physics

Acknowledgments

Firstly, I wish to thank my family for their support and love. I am not sure I would have made it to writing this without Mallory, who is a ray of sunshine in my life.

I am indebted to my advisor Christoph Paus for a steady guiding hand, carrying practical wisdom and a great wellspring of life experience. I was truly inspired by my officemates at CERN, Zeynep Demiragli and Guillermo Gómez-Ceballos, with their limitless work ethic and positive attitude. I thank the others in the MIT group for their camaraderie and advice. I am grateful to have been able to look up to the previous generation of graduate students, including Axel Schmidt, Aram Apyan, and John Hardin. I cannot forget to thank the Syracuse University High Energy Physics group for inspiring me to pursue further studies in physics, in particular Ray Mountain and Marina Artuso.

I am glad to have had some spice in my life during my time in Geneva, thanks to Sebastian Pétitat, Thomas Florin, Élise Courbet, Matthieu Llodra, Jessica Brouzes, Evaristo Pérez, and others. I also had the good fortune to share a small apartment and speak a little Polish with Wojciech Jarosz and Krzysztof Sielewicz.

Lastly, I would like to thank Markus Klute for, among many things, organizing great summer barbecues.

Contents

1	Introduction	11
1.1	Differential measurements of gauge bosons	12
1.2	Dark matter searches	13
2	Fundamental physics	15
2.1	History	15
2.2	Standard Model	16
2.2.1	Electromagnetic force	16
2.2.2	Electroweak unification	17
2.2.3	Spontaneous symmetry breaking	18
2.2.4	The Higgs boson	21
2.2.5	Strong nuclear force	22
2.3	Proton parton distribution functions	25
2.4	New physics	26
2.4.1	Simplified models	26
2.4.2	Invisible Higgs bosons	28
2.4.3	Extra dimensions	28
2.4.4	Unparticles	28
3	Experimental apparatus	31
3.1	The Large Hadron Collider	31
3.2	The CMS Detector	32
3.2.1	Trackers	34
3.2.2	Electromagnetic calorimeter	36
3.2.3	Hadron calorimeters	38
3.2.4	Muon system	40
3.2.5	Trigger system	46
3.2.6	Offline world	47
4	Physics objects	49
4.1	Electrons	49
4.1.1	Electron reconstruction	49
4.1.2	Electron identification variables	49
4.1.3	Electron identification working points	51
4.2	Muons	51

4.2.1	Muon reconstruction	51
4.2.2	Muon identification variables	52
4.2.3	Muon identification working points	53
4.3	Jets	54
4.3.1	Jet reconstruction	54
4.3.2	Jet identification	55
4.3.3	b-tagging	55
4.4	Photons	56
4.5	Particle-flow reconstruction	56
4.6	Missing transverse energy	57
5	Data samples	59
5.1	Experimental data	59
5.1.1	Silicon strip hit efficiency loss	59
5.2	Simulated samples	60
5.2.1	Standard Model processes	60
5.2.2	Dark matter hypotheses	63
5.3	Triggers	63
5.4	Corrections to the simulated samples	65
5.4.1	Pileup reweighting	65
5.4.2	Trigger efficiencies	66
5.4.3	Lepton selection efficiencies	66
5.4.4	Lepton momentum scale and resolution	66
5.4.5	Higher order corrections	67
6	Efficiency of lepton trigger, reconstruction, and identification	69
6.1	Event selections for the tag-and-probe method	69
6.1.1	Probe multiplicity calculation	70
6.2	Control samples for the lepton efficiencies	70
6.2.1	Lepton pion selection	70
6.2.2	Electron muon selection	71
6.3	Fitting techniques	71
6.4	Assessment of systematic uncertainty	73
6.4.1	Background shape modeling	73
6.4.2	Signal resolution modeling	81
6.4.3	Signal final state radiation modeling	85
6.4.4	Choice of generator	94
6.4.5	Bias from choice of tag selection	95
6.4.6	Total impact of systematic uncertainties	99
7	Measurements of differential Z boson production cross sections	101
7.1	Event selection	102
7.2	Background estimation	102
7.3	Systematic uncertainties	109
7.3.1	Sources of systematic uncertainties	109

7.3.2	Correlations	112
7.3.3	Total systematic uncertainty	112
7.4	Results	112
7.4.1	Inclusive fiducial cross section measurements	112
7.4.2	Differential cross section measurements	119
8	Diboson studies	133
8.1	Theoretical uncertainties in diboson calculations	134
8.1.1	Electroweak corrections	134
8.1.2	QCD corrections	137
8.1.3	Cross terms	137
8.2	Visible ZZ process	139
8.3	Visible WZ process	143
9	Search for dark matter produced in association with a boosted Z boson	147
9.1	Event selection	147
9.1.1	Preselection	147
9.1.2	Signal selection	151
9.2	Background estimation	155
9.2.1	Diboson processes	155
9.2.2	Nonresonant backgrounds	155
9.2.3	Drell-Yan background estimation	159
9.3	Systematic uncertainties	160
9.3.1	Luminosity	161
9.3.2	Trigger, lepton reconstruction and identification efficiencies	161
9.3.3	Lepton momentum and electron energy scale	162
9.3.4	Jet energy scale (JES) and resolution (JER)	162
9.3.5	B-tagging efficiency	162
9.3.6	Pileup	163
9.3.7	Theoretical uncertainties	163
9.3.8	MC statistical uncertainty	164
9.3.9	Summary	164
9.4	Maximum likelihood fit	167
9.4.1	The ZZ/WZ ratio	167
9.5	Multivariate analysis	168
9.5.1	Classifier variables and training	168
9.5.2	Analysis selection	169
9.5.3	Improvement in sensitivity	172
9.6	Search results	172
9.6.1	Invisible Higgs interpretation	176
9.6.2	Simplified Model dark matter interpretation	179
9.6.3	Unparticle interpretation	185
9.6.4	ADD Interpretation	187
9.6.5	Simplified Likelihood	190

10 Conclusion and Outlook	193
A Lepton identification efficiencies and scale factors	195
A.1 Central values	195
A.2 Alternative methods	205
B Dark matter multivariate analysis	215
B.1 Boosted decision trees	215
B.1.1 Gradient boosting	215
B.2 Choice of input variables	216
B.3 Mapping the experimental uncertainties	217
C QCD NNLO/NLO k-factors for $\text{qq} \rightarrow \text{ZZ}$	227
D Interpolation of Simplified Model dark matter limits	231
D.1 Calculating the weights	231
D.2 Choosing a reference	232
D.3 Closure testing	232
E Cross sections for ADD model	239

Chapter 1

Introduction

At the energy scales of everyday life in the 21st century, the preponderance of the human experience is described by the electromagnetic and gravitational forces. As it fights gravitational attraction walking on the ground of the Earth, the human body is held together by chemical bonds having energy of several electron volts (eV), and it observes its environment by absorbing photons of comparable energies. The saga of the evolution of the Universe far surpasses these energy scales. According to the theory of the Big Bang, it began approximately 13.8 billion years ago. The energy of the fundamental interactions occurring in the first few seconds after the Big Bang was much higher.

The Standard Model of particle physics is a unified theory of three of the four fundamental forces of nature. It describes the strong and weak nuclear forces alongside the electromagnetic force. These interactions occur among elementary particles, and the forces amongst them are carried by gauge bosons. The Standard Model is not yet a Grand Unified Theory, which would describe a single, unified force at the time of the Big Bang. Besides unification, there are several unanswered questions. What is the internal structure of the proton, one of the building blocks of all chemical elements? Is there additional undetected dark matter in our Universe? Are there more undiscovered fundamental particles? Are there more than four spacetime dimensions?

Compared to the electromagnetic force, the weak nuclear force is stronger, but only at very short ranges ($< 10^{-18}$ m). It is mediated by the extremely massive W^\pm and Z bosons. By the mass-energy equivalence principle, they weigh around 80 and 91 GeV (giga-electron volts), respectively. Compared to the weak force, the strong nuclear force is even more powerful and short-ranged. It is mediated by the massless gluon. It overcomes the electrostatic repulsion of nucleons to hold together nuclei at distances measured in femtometers.

To study the strong and weak nuclear forces, it is necessary to observe the products of interactions on the energy scales of hundreds of GeV or even TeV (tera-electron volts). In order to produce a large multitude of these interactions, machines such as the Large Hadron Collider (LHC) are built. The purpose of the LHC is to collide protons having energies of several TeV. These supercolliders are financial undertakings amounting to billions of US dollars. Today, their construction and operation are directed by international organizations such as CERN (European Center for Nuclear

Research). Meanwhile, to observe those interactions, detector systems such as the CMS Detector are built to capture and measure most of the interaction products. These function as very fast cameras which provide a detailed picture of what particles came out of a particular proton-proton collision event.

To date, this work contains the most precise measurement of the production of Z bosons via proton collisions at center-of-mass energy 13 TeV. Also presented is a search for the production of invisible particles at the LHC, which could point to dark matter, extra spacetime dimensions, or some other new phenomenon. Both results make use of the experimentally clean signature where a Z boson decays leptonically into an electron-positron or muon-antimuon pair¹.

1.1 Differential measurements of gauge bosons

The production of charged lepton pairs via the Drell–Yan (DY) process is essential for the physics program of the CERN LHC. The large cross section and clean experimental signature provide important precision tests of the standard model (SM), as well as constraints on the parton distribution functions (PDFs) of the proton. In addition, the study of the DY process allows for stringent constraints on physics beyond the standard model (BSM). Furthermore, dilepton events are valuable for calibrating the detector and monitoring the stability of the luminosity.

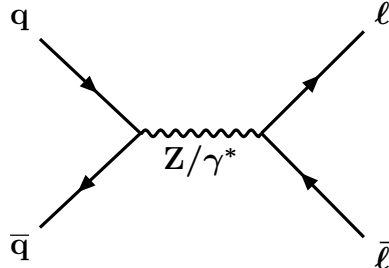


Figure 1-1: The Drell-Yan process.

The intermediate vector bosons W^\pm and Z/γ^* (referred to as Z boson) can have non-zero momentum transverse to the beam direction (p_T). This is due to the intrinsic p_T of the initial-state partons inside the proton as well as the initial-state radiation of gluons and quarks. Measurements of the p_T distributions of the W^\pm and Z bosons probe various aspects of the strong interaction. In addition, accurate theoretical prediction of the p_T distribution is a key ingredient for a precise measurement of the W^\pm boson mass at the LHC.

The measurement of the W^\pm boson mass relies on a fit to the experimental data, with the target distribution being either the p_T of the visible charged lepton daughter or the transverse mass of the system of this lepton and the missing energy. Both

¹Strictly speaking, the term “lepton” refers to electrons, muons, taus, and neutrinos. In experimental high-energy physics, it is frequently used to refer to the first two generations of charged leptons: electrons and muons.

of these methods depend on the modeling of the W^\pm boson p_T distribution, which suffers from uncertainties in the QCD renormalization and factorization scale and the proton parton distribution functions. To mitigate this, it is possible to extrapolate from a measured Z boson p_T distribution, using the *ratio* of theoretical predictions for W^\pm and Z boson p_T distributions:

$$\frac{d\sigma(W)}{dp_T} = \left[\frac{d\sigma(W)/dp_T}{d\sigma(Z)/dp_T} \right]_{\text{theory}} \times \left[\frac{d\sigma(Z)}{dp_T} \right]_{\text{measured}} \quad (1.1)$$

This strategy was previously employed for the W^\pm boson mass measurements using the Tevatron [1, 2] and LHC Run-I data at 7 TeV [3]. One benefit is that some uncertainties in the “theory” term partially cancel. The price is that the Z differential p_T spectrum must be measured experimentally. Therefore, it is essential to do this using the LHC Run-II data at center-of-mass energy 13 TeV, on the path toward a future W^\pm boson mass measurement using those data.

Theoretical predictions of both the DY production total cross section and differential distributions are available up to next-to-next-to-leading order (NNLO) accuracy in perturbative quantum chromodynamics (QCD) [4, 5]. The complete NNLO calculations of vector boson production in association with a jet in hadronic collisions have recently become available at $\mathcal{O}(\alpha_S^3)$ accuracy in the strong coupling constant [6, 7, 8]. These calculations significantly reduce the factorization and renormalization scale uncertainties which in turn reduce theoretical uncertainties in the prediction of the p_T distribution in the high- p_T region to the order of one percent. Electroweak (EW) corrections are non-negligible at high- p_T [9, 10].

The fixed order calculations are unreliable at low- p_T region due to soft and collinear gluon radiation, resulting in the appearance of large logarithmic corrections. Resummation of the logarithmically divergent terms up to next-to-next-to-leading logarithmic (NNLL) accuracy has been matched with the fixed order predictions. This matching is done by subtracting resummed terms of the same order as the fixed order calculations to avoid double-counting. It allows accurate predictions for the entire range of p_T [11, 12]. Fixed order perturbative calculations can also be combined with parton shower models to obtain fully-exclusive predictions [13, 14, 15, 16] with no fiducial requirements.

The Z boson p_T and rapidity distributions have been previously measured, using e^+e^- and $\mu^+\mu^-$ pairs, by the ATLAS, CMS, and LHCb Collaborations for proton-proton (pp) collisions at 7, 8, and 13 TeV at the LHC [17, 18, 19, 20, 21, 22, 23, 24, 25, 26, 27, 28, 29, 30], and by the CDF and D0 Collaborations at the Tevatron for proton-antiproton ($p\bar{p}$) collisions at $\sqrt{s} = 1.96$ TeV [31, 32, 33, 34, 35].

1.2 Dark matter searches

One of the most significant puzzles in modern physics is the nature of dark matter. In the culmination of over a century of observations, the “ Λ_{CDM} ” standard model of cosmology has established that, in the total cosmic energy budget, known matter

only accounts for about 5%, dark matter corresponds to 27%, and the rest is dark energy [36]. Although several astrophysical observations indicate that dark matter exists and interacts gravitationally with known matter, there is no evidence yet for nongravitational interactions between dark matter and Standard Model particles. While the nature of dark matter remains a mystery, there are a number of models that predict a particle physics origin.

A promising possibility is that dark matter may take the form of weakly interacting massive particles. If these particles exist, they can possibly be produced directly from, annihilate into, or scatter off Standard Model particles. Recent dark matter searches have exploited various methods including direct [37] and indirect [38] detection. If dark matter can be observed in direct detection experiments, it must have substantial couplings to quarks and/or gluons, and could also be produced at the LHC [39, 40, 41, 42, 43, 44].

In this work we search for such a mechanism producing a Z boson recoiling against a pair of dark matter particles. This final state is well-suited to probe such beyond-the-Standard Model scenarios, as it has relatively small and precisely known Standard Model backgrounds. Previous searches of this nature have been performed using the LHC Run-I datasets at center-of-mass energies 7 and 8 TeV. Some make use of the same Z boson signature [45, 46, 47], while others rely on final states with hadrons, photons, or a single energetic lepton [48, 49, 50, 51, 52, 53, 54, 55, 56, 57, 58, 59, 60].

Chapter 2

Fundamental physics

First, I will give a brief history of how the elementary particles were discovered. Then I will describe their subsummation in the Standard Model.

2.1 History

The year in which particle physics was conceived is a fungible number, but a strong case could be made for 1897, when Sir Joseph John Thomson discovered the electron [61]. The following decades brought Ernest Rutherford's atomic nuclei in 1911 [62], Niels Bohr's atomic model in 1913 [63], and then James Chadwick's neutron in 1932 [64].

After the electron, the next elementary particle discovered was the photon. The evidence was provided by: Max Planck's study of quantized blackbody radiation in 1900 [65]; Albert Einstein's controversial explanation of the photoelectric effect in 1905 [66]; and Arthur Holly Compton's scattering experiment in 1923 [67].

In 1935, Yukawa Hideki proposed a light, yet massive meson to mediate the nucleon interaction [68]. By 1937, multiple efforts searching for Yukawa's meson in the cosmic rays, instead found an impostor. This was the next elementary particle, the muon (μ^-): a second-generation charged lepton [69] [70].

The so-called Yukawa meson really did exist, although it was not discovered until 1947 at the University of Bristol [71]. Today we call it the charged pion (π^\pm), and it is a composite subatomic particle, not an elementary one. But in hindsight, this was our initial foray into the strong nuclear force, since we continue to describe the force between proximate nucleons via the exchange of one or more such light, virtual mesons.

After the discovery of the neutron, Enrico Fermi and Wolfgang Pauli's work in the early 1930s led to the prediction of the neutrino, another elementary particle [72]. It was not discovered until 1956 by Clyde Cowan and Frederick Reines using inverse beta decay [73]. This was our first conception of the weak nuclear force. The second and third generation neutrinos came later. Lederman, Schwartz, and Steinberger observed the second-generation muon neutrino (ν_μ) in 1962 [74].

The third-generation charged lepton, the tau (τ), was discovered at the Stanford

Linear Accelerator Center in 1975 [75]. The DONUT experiment observed its partner, the tau neutrino (ν_τ), in 2000 [76].

The constituents of mesons and atomic matter were found to be the quarks. Most of the quarks can be bound together for a time by gluons. Quarks, or aces, were originally conceived of by Murray Gell-Mann [77] and George Zweig [78]. Briefly, the order of their observation is as follows: the up, down, and strange quarks in 1968 [79] [80]; the charm quark 1974 [81] [82]; the bottom quark in 1977 [83]; the gluon in 1978; [84] and the top quark in 1995 [85] [86].

The unified electroweak theory was validated when the W^\pm and Z bosons were discovered in 1983 by the UA1 and UA2 experiments [87] [88] [89] [90]. Finally, the last missing component of the Standard Model, the Higgs boson, was discovered in 2012 by the CMS and ATLAS collaborations [91] [92].

The Standard Model of particle physics was built up over a century of arduous and incremental observations. Thus, the remainder of this work is written standing on the shoulders of giants.

2.2 Standard Model

Here, I will present the individual interactions and their unification in the theory. Beyond the scope of this work are discussions of gravitation, general relativity, and previous outdated theories. The internal symmetries of the Standard Model are represented by the unitary product group $SU(3) \times SU(2) \times U(1)$.

The Lagrangian density of the Standard Model is

$$\mathcal{L}_{\text{SM}} = \mathcal{L}_{\text{EW}} + \mathcal{L}_{\text{QCD}} \quad (2.1)$$

The components are described below.

2.2.1 Electromagnetic force

The quantum field theory for electromagnetism is quantum electrodynamics or QED for short, with internal symmetry represented by the group $U(1)$. QED was the first quantum field theory to incorporate special relativity. It describes the interactions between charged particles, the force being carried by the photon. The Lagrangian density for a fermion field interacting with the electromagnetic field is

$$\mathcal{L}_{\text{QED}} = \bar{\psi} (i\gamma^\mu D_\mu - m) \psi - \frac{1}{4} F_{\mu\nu} F^{\mu\nu} \quad (2.2)$$

- The indices μ, ν represent spacetime.
- e is the coupling constant, also known as the elementary charge of the electron.
- γ^μ are the Dirac matrices which act on Dirac spinors to produce four-vectors.
- ψ is a Dirac bi-spinor representing the field for a charged spin-1/2 particle and antiparticle e.g. an electron and positron at spacetime point x .

- m is the mass of that particle.
- $\bar{\psi}$ is the Dirac adjoint of ψ , defined as $\psi^\dagger \gamma^0$.
- D_μ is the gauge covariant derivative $\partial_\mu + ieA_\mu + ieB_\mu$.
- A_μ is the electromagnetic four-potential from the particle itself.
- B_μ is the external EM four-potential.
- $F_{\mu\nu}$ is the electromagnetic field tensor $\partial_\mu A_\nu - \partial_\nu A_\mu$.

In QED there is only the fermion-fermion-photon vertex. This quantum field theory offered uncanny accuracy for observables such as the energy levels of the hydrogen atom and the anomalous magnetic moment of the electron. It has been subsumed into the electroweak theory, which will be described next.

2.2.2 Electroweak unification

The weak interaction describes the interactions between fermions. The conserved quantum number is the weak isospin (T^3). The classic example is beta decay, where a down quark ($T^3 = -1/2$) changes into an up quark ($T^3 = +1/2$), producing an additional electron and electron antineutrino (both $T^3 = -1/2$). In such a process, the weak isospin, electron number, and charge are all conserved. A historical discussion of the weak interaction alone is omitted.

The electromagnetic and weak nuclear forces are unified in the theory of electroweak (EW) interactions, wrought by Sheldon Glashow, Steven Weinberg, and Abdus Salam (GWS). Above unification energy circa 250 GeV, or temperature 10^{15} Kelvins, these forces are merged into a combined force. EW is a Yang-Mills theory based on the gauge group $SU(2) \times U(1)$. The $SU(2)$ group represents the three gauge bosons of weak isospin, A_1 , A_2 , and A_3 . The $U(1)$ group represents the gauge boson B of weak hypercharge. All of these gauge bosons are massless. The coupling constants are g for $SU(2)$ and g' for $U(1)$.

The left-handed fermion fields transform as doublets under $SU(2)$. The lepton doublets are $L_i = \begin{pmatrix} \nu_i \\ \ell_i^- \end{pmatrix}$ where ν_i are the three neutrinos and ℓ_i^- are the three charged leptons. The quark doublets are $Q_i = \begin{pmatrix} u_i \\ V_{ij} d_j \end{pmatrix}$, where u_i are the three up-type quarks, d_j are the three down-type quarks, and V_{ij} is the Cabibbo-Kobayashi-Maskawa (CKM) matrix describing the weak mixing among the quark generations.

The Lagrangian density for the pure, unadulterated electroweak interaction is

$$\begin{aligned}
\mathcal{L}_{\text{EW}} &= \mathcal{L}_{\text{Gauge}} + \mathcal{L}_{\text{Fermion}} + \mathcal{L}_\phi + \mathcal{L}_{\text{Yukawa}} \text{ where} \\
\mathcal{L}_{\text{Gauge}} &= -\frac{1}{4} A_a^{\mu\nu} A_{\mu\nu}^a - \frac{1}{4} B^{\mu\nu} B_{\mu\nu} \\
\mathcal{L}_{\text{Fermion}} &= \sum_{f \in \{Q, u, d, L, i\}} \bar{f}_i i \gamma_\mu D^\mu f_i \\
\mathcal{L}_\phi &= |D_\mu \phi|^2 - \lambda \left(|\phi|^2 - \frac{1}{2} v^2 \right)^2 \\
\mathcal{L}_{\text{Yukawa}} &= \sum_f -G_f (\bar{f}_{\text{L.H.}} \phi f_{\text{R.H.}} + \bar{f}_{\text{R.H.}} \phi^\dagger f_{\text{L.H.}})
\end{aligned} \tag{2.3}$$

Breaking it down piece by piece,

- $\mathcal{L}_{\text{Gauge}}$ is the interaction among the gauge fields, described by the field strength tensors $A_{1,2,3}^{\mu\nu}$ and $B^{\mu\nu}$ for the weak isospin and weak hypercharge gauge fields.
- $\mathcal{L}_{\text{Fermion}}$ is the interaction of the gauge bosons and the fermions. The symbol f represents the left-handed doublet quark fields, the right-handed singlet up-type quark fields, the right-handed singlet down-type quark fields, the left-handed doublet lepton fields, and the right-handed singlet lepton fields.
- D_μ is the electroweak gauge covariant derivative, defined as $\partial_\mu - i \frac{g}{2} \hat{T}^j A_\mu^j - i \frac{g'}{2} Y B_\mu$ where $\hat{T}^{j=1,2,3}$ are the weak isospin operators and \hat{Y} is the weak hypercharge operator.
- \mathcal{L}_ϕ is the scalar field's interaction with itself and the gauge bosons.
- $\mathcal{L}_{\text{Yukawa}}$ is the Yukawa interaction of the scalar field with the fermions f , where $f_{\text{L.H.}}, f_{\text{R.H.}}$ are the left-handed and right-handed fermion fields.

2.2.3 Spontaneous symmetry breaking

Motivated by the necessity to generate the masses, a complex scalar doublet field is added for this purpose:

$$\phi \equiv \begin{pmatrix} \phi^+ \\ \phi^0 \end{pmatrix}, \text{ where } \phi^+, \phi^0 \text{ are complex numbers} \tag{2.4}$$

This ϕ field lives in a potential given by

$$V(\phi) = \mu^2 \phi^\dagger \phi + \lambda (\phi^\dagger \phi)^2 \tag{2.5}$$

The constant λ must be positive in order for the potential V to have a minimum. For negative values of μ^2 , V could be visualized as a sombrero or similar hat with a rounded brim; see Figure 2-1. Since the lowest point is somewhere in the brim, the ϕ doublet develops a vacuum expectation value $v/\sqrt{2}$. This breaks the $SU(2)$ symmetry, but a new $U(1)$ symmetry is maintained. The value of v is experimentally

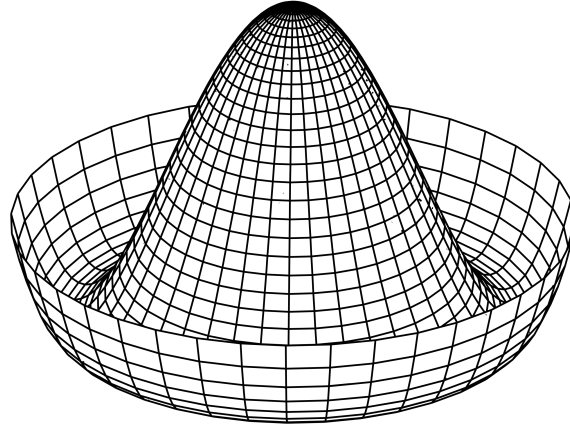


Figure 2-1: Visualization of $V(\phi)$ as the so-called ‘Mexican hat’ potential.

found to be around 246 GeV, providing a basis for the earlier statement about the unification energy.

Undertaking a unitary gauge transformation in $SU(2)$, ϕ^+ vanishes and ϕ^0 remains as a physical scalar field. Expanding this scalar field around the minimum of the potential in Equation 2.5, $\phi^0 \rightarrow \frac{v+H(x)}{\sqrt{2}}$, where $H(x)$ is a scalar at spacetime position x with expected value 0.

Symmetry breaking alters the terms \mathcal{L}_ϕ and $\mathcal{L}_{\text{Yukawa}}$ in Equation 2.3, leaving the others unchanged. In a Lagrangian density, the kinetic and potential terms for such a scalar field ϕ are

$$\mathcal{L}_\phi = (D_\mu \phi)^\dagger (D^\mu \phi) - V(\phi) \quad (2.6)$$

Let us expand Equation 2.6 for the ϕ -field using the previously defined D_μ :

$$\begin{aligned} \mathcal{L}_\phi &= \frac{1}{2} (\partial^\mu H) (\partial_\mu H) - \lambda \left[v^2 H^2 + v H^3 + \frac{1}{4} H^4 \right] \\ &\quad + \frac{1}{8} \left| g \hat{T}^1 A_\mu^1 + g \hat{T}^2 A_\mu^2 + g \hat{T}^3 A_\mu^3 + g' Y B_\mu \right|^2 (v + H)^2 \end{aligned} \quad (2.7)$$

Noting that $(\hat{T}^1 \pm i \hat{T}^2)/2 \equiv \hat{T}^\pm$ are the raising and lowering operators for the third component of weak isospin in the $SU(2)$ symmetry, and the charge operator $\hat{Q} = \hat{T}^3 - \hat{Y}$, the last term in \mathcal{L}_ϕ simplifies:

$$\mathcal{L}_\phi = \dots + \frac{1}{8} \left[g^2 (A_\mu^1)^2 + g^2 (A_\mu^2)^2 + (g A_\mu^3 + g' B_\mu)^2 \right] (v + H)^2 \quad (2.8)$$

If we define a weak angle $\theta_W = \arctan \frac{g'}{g}$, we view $g A_\mu^3 + g' B_\mu$ as the A^3 and B bosons being rotated into two other bosons. These will be the massive Z boson and the massless γ boson, also known as the photon [93]. Meanwhile, we can view the A^1 and

A^2 bosons combining to give the charged W^\pm bosons:

$$W^\pm = \frac{A^1 \mp i A^2}{\sqrt{2}} \quad (2.9)$$

For completeness, let us rewrite the electroweak gauge covariant derivative in terms of the physical bosons. The Z boson is represented by the gauge field Z_μ and the photon is represented by the gauge field A_μ without a superscript.

$$D_\mu^{\text{EW}} = \partial_\mu - \frac{ig}{\sqrt{2}}(W_\mu^+ \hat{T}^+ + W_\mu^- \hat{T}^-) - \frac{ig}{\cos \theta_W} Z_\mu (\hat{T}^3 - \sin^2 \theta_W \hat{Q}) - ie A_\mu \hat{Q} \quad (2.10)$$

We can now rewrite \mathcal{L}_ϕ from before, in terms of the physical W^\pm and Z bosons:

$$\begin{aligned} \mathcal{L}_\phi = & \frac{1}{2}(\partial^\mu H)(\partial_\mu H) - \lambda \left[v^2 H^2 + v H^3 + \frac{1}{4} H^4 \right] \\ & + \left[\frac{g^2}{4} W_\mu^+ W^{-\mu} + \frac{g^2}{8 \cos^2 \theta_W} Z_\mu Z^\mu \right] (v + H)^2 \end{aligned} \quad (2.11)$$

From this expression, we can extract expressions for the W^\pm and Z bosons' masses at leading-order:

$$m_W = \frac{vg}{2}, \quad m_Z = \frac{vg}{2 \cos \theta_W} \quad (2.12)$$

Lastly, let us reframe Equation 2.3 in terms of the physical gauge bosons. The antisymmetric photon, Z, and W^\pm field strength tensors $A_{\mu\nu}$, $Z_{\mu\nu}$, $W_{\mu\nu}^\pm$ are provided as

$$\begin{aligned} A_{\mu\nu} &= \partial_\mu A_\nu - \partial_\nu A_\mu \\ Z_{\mu\nu} &= \partial_\mu Z_\nu - \partial_\nu Z_\mu \\ (\vec{W}_{\mu\nu}^+)_a &= \partial_\mu (\vec{W}_\nu^+)_a - \partial_\nu (\vec{W}_\mu^+)_a - ig \varepsilon_{abc} (\vec{W}_\mu^+)_b (\vec{W}_\nu^+)_c \\ \vec{W}_{\mu\nu}^- &= (\vec{W}_{\mu\nu}^+)^{\dagger} \end{aligned} \quad (2.13)$$

where the vector notation indicates components in three-dimensional weak isospin space. Einstein summation convention is used and ε is the antisymmetric Levi-Civita symbol.

Finally, we can write down the full EW Lagrangian density after symmetry breaking. As before, $\mathcal{L}_{\text{EW}} = \mathcal{L}_{\text{Gauge}} + \mathcal{L}_{\text{Fermion}} + \mathcal{L}_\phi + \mathcal{L}_{\text{Yukawa}}$. The $\mathcal{L}_{\text{Gauge}}$ term contains the gauge field tensor dynamic terms, the triple-gauge couplings, and the quartic-gauge

couplings:

$$\begin{aligned}
\mathcal{L}_{\text{Gauge}} = & -\frac{1}{4} \left[A^{\mu\nu} A_{\mu\nu} + 2W_{\mu\nu}^+ W^{-\mu\nu} + Z_{\mu\nu} Z^{\mu\nu} \right] \\
& - ig \left[(W_{\mu\nu}^+ W^{-\mu} - W^{+\mu} W_{\mu\nu}^-) (A^\nu \sin \theta_W - Z^\nu \cos \theta_W) \right. \\
& \quad \left. + W_\nu^- W_\mu^+ (A^{\mu\nu} \sin \theta_W - Z^{\mu\nu} \cos \theta_W) \right] \\
& + \frac{g^2}{4} \left[-(2W_\mu^+ W^{-\mu} + (A_\mu \sin \theta_W - Z_\mu \cos \theta_W)^2)^2 \right. \\
& \quad \left. + (W_\mu^+ W_\nu^- + W_\nu^+ W_\mu^- + (A_\mu \sin \theta_W - Z_\mu \cos \theta_W)(A_\nu \sin \theta_W - Z_\nu \cos \theta_W))^2 \right]
\end{aligned} \tag{2.14}$$

The allowed gauge self-coupling vertices are pictured in Figures 2-2 and 2-3.

The $\mathcal{L}_{\text{Fermion}}$ term contains the interaction between the gauge bosons and the fermions, in the neutral current and the charged current:

$$\begin{aligned}
\mathcal{L}_{\text{Fermion}} = & \left[\frac{g}{\cos \theta_W} (J_\mu^3 - \sin^2 \theta_W J_\mu^{\text{EM}}) Z^\mu + e J_\mu^{\text{EM}} A^\mu \right] \\
& - \frac{g}{\sqrt{2}} \left[(\bar{u}_i \gamma^\mu \frac{1-\gamma^5}{2} V_{ij} d_j + \bar{\nu}_i \gamma^\mu \frac{1-\gamma^5}{2} e_i) W_\mu^+ + \text{h.c.} \right]
\end{aligned} \tag{2.15}$$

The electromagnetic current is defined as $J_\mu^{\text{EM}} \equiv \sum_f q_f \bar{f} \gamma_\mu f$, with the bilinear covariant γ_μ representing the vector spin-1 coupling. The weak neutral current is defined as $J_\mu^3 \equiv \sum_f T_f^3 \bar{f} \gamma_\mu \frac{1-\gamma^5}{2} f$, with the bilinear covariant representing the infamous “vector minus axial” spin-1 coupling. The matrix V_{ij} is the CKM matrix.

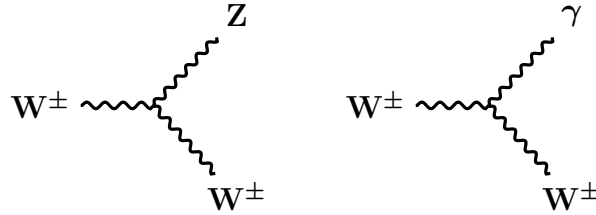


Figure 2-2: Triple gauge boson vertices in the electroweak theory.

2.2.4 The Higgs boson

Let us look at the second term of Equation 2.11. The portion $-\lambda v^2 H^2$ suggests to us we can identify the quantum of the H -field as a physical boson with mass $m_H = \sqrt{2v^2\lambda}$. We will call this quantum the Higgs boson, and the field, the Higgs field.

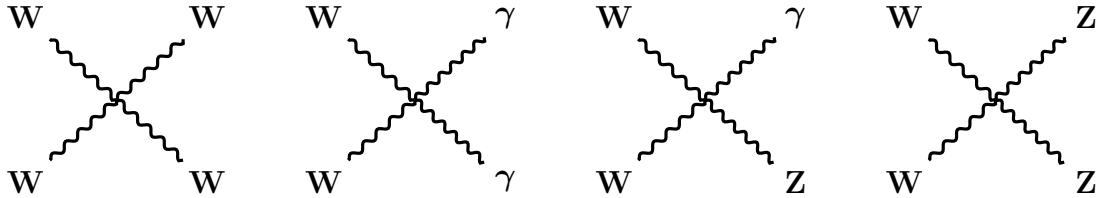


Figure 2-3: Non-Abelian quartic gauge couplings in the electroweak theory.

The \mathcal{L}_ϕ term from the electroweak Lagrangian density can be expanded to find the Higgs couplings to itself and the other gauge bosons, in particular to the Z boson which is relevant to this work:

$$\begin{aligned} \mathcal{L}_\phi = & \left[\frac{1}{2}(\partial^\mu H)(\partial_\mu H) - \frac{1}{2}m_H^2 H^2 \right] - \left[\frac{gm_H^2}{4m_W} H^3 + \frac{g^2 m_H^2}{32m_W^2} H^4 \right] \\ & + \left[\left(W_\mu^+ W^{-\mu} + \frac{1}{2\cos^2 \theta_W} Z_\mu Z^\mu \right) \left(gm_W H + \frac{g^2}{4} H^2 \right) \right] \end{aligned} \quad (2.16)$$

Meanwhile, the $\mathcal{L}_{\text{Yukawa}}$ term from the Lagrangian density becomes

$$\mathcal{L}_{\text{Yukawa}} = - \sum_f \frac{gm_f}{2m_W} \bar{f} f H \quad (2.17)$$

It provides for the Higgs boson to interact with and decay into fermions, more likely for massive fermions. The fermion mass m_f truly arises from the coupling to the Higgs field, and not vice versa.

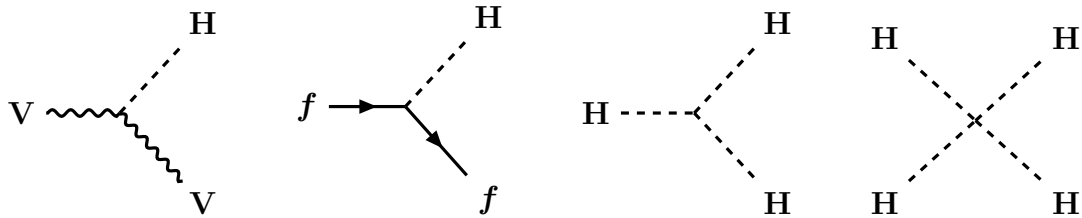


Figure 2-4: Higgs boson couplings. V is a W^\pm or Z boson. f are fermions.

2.2.5 Strong nuclear force

The strong nuclear force arises from the theory of the interactions of the quarks and the gluon, called quantum chromodynamics (QCD). It is a non-Abelian gauge theory whose internal symmetry is represented by the group SU(3).

Quarks and gluons carry color charge, of which there are three kinds: red, green, and blue. Negative color charge, carried by the antiquarks and the gluons, is usually represented by the prefix *anti-*, e.g. anti-red. In transmitting the strong force as its carrier, the gluon carries a positive color charge and a negative color charge. A

gluon could carry red and anti-blue color charge, for example. There are eight such possible combinations, each of which is a different kind of gluon. These eight gluons correspond to the eight generators of the SU(3) group.

Quarks are fermions, having intrinsic spin of 1/2. There are six quarks. Each quark has a bare mass and an electric charge. In bound states such as the proton, the quarks appear to weigh more. This constituent quark mass is heavier because of the field of virtual quarks and gluons around the bare quarks.

Quark	Symbol	Charge	Isospin	Bare mass [MeV c ⁻²]	Constituent mass [MeV c ⁻²]
Up	u	+2/3	+1/2	$2.3 \pm 0.7 \pm 0.5$	336
Down	d	-1/3	-1/2	$4.8 \pm 0.5 \pm 0.3$	340
Charm	c	+2/3	0	1275 ± 25	1550
Strange	s	-2/3	0	95 ± 5	486
Top	t	+2/3	0	$173,210 \pm 510 \pm 710$	4730
Bottom	b	-1/3	0	4180 ± 30	177,000

Table 2.1: The quarks. When significant, bare masses quote statistical followed by systematic uncertainty.

The Dirac Lagrangian density which defines the interactions between quarks and gluons is

$$\mathcal{L}_{\text{QCD}} = \sum_{\psi} \bar{\psi}_i (i\gamma^{\mu}(\partial_{\mu}\delta_{ij} - ig_s G_{\mu}^a T_{ij}^a) - m_{\psi}\delta_{ij}) \psi_j - \frac{1}{4}G_{\mu\nu}^a G_a^{\mu\nu} \quad (2.18)$$

- The index a represents the eight gluons.
- The index i represents the three colors.
- The indices μ, ν represent spacetime.
- g_s is the strong coupling constant, sometimes expressed as $\sqrt{4\pi\alpha_s}$ which varies as a function of energy scale (see Figure 2-5).
- ψ_i is a Dirac bi-spinor representing the field for a quark and its antiquark at spacetime point x . $\bar{\psi}_i$ is the adjoint as in section 2.2.1.
- G_{μ}^a is the SU(3) gauge field.
- T_{ij}^a are the eight generators of the SU(3) group, also known as Gell-Mann matrices.
- Lastly, the symbol $G_{\mu\nu}^a$ is the gluon field strength tensor...

The gluon field strength tensor comes from the gluon fields, $\mathcal{A}_{\mu}^a(x)$, as such:

$$G_{\mu\nu}^a = \partial_{\mu}\mathcal{A}_{\nu}^a - \partial_{\nu}\mathcal{A}_{\mu}^a + g f^{abc} \mathcal{A}_{\mu}^b \mathcal{A}_{\nu}^c \quad (2.19)$$

This quantum field theory permits the quark-quark-gluon vertex, the three-gluon vertex, and the four-gluon vertex.

For experimental physics at the LHC, QCD is important even for studying electroweak processes. Since we collide protons, the internal dynamics of the proton are

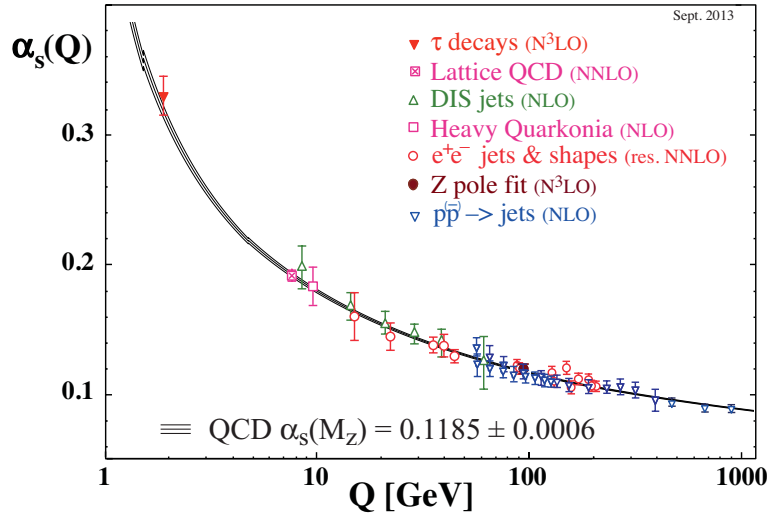


Figure 2-5: The so-called “running” of α_S as the energy scale [94].

an essential ingredient of Monte Carlo simulations. The momentum fractions carried by the quarks and gluons are determined empirically as what are called the proton parton distribution functions. Internal gluon loop corrections and the possibility of emitting extra gluons before or after the hard process can enhance the total cross section significantly for physics processes. QCD activity resulting in charged hadrons may interfere with the ability to identify charged leptons in physics events of interest.

2.3 Proton parton distribution functions

The quarks and gluons inside a proton are collectively called partons. The parton distribution functions (PDFs) $f_i(x, Q^2)$ give the probability of finding inside the proton a quark or gluon with momentum fraction x , in a hard process with momentum transfer Q . According to the central feature of QCD, known as asymptotic freedom, the partonic interactions become asymptotically weak at short distances. QCD can quantitatively predict the dependence of the PDFs on the energy scale, Q^2 , by way of the QCD evolution equations developed by Dokshitzer, Gribov, Lipatov, Altarelli, and Parisi (DGLAP). These equations are valid in the regime where the strong coupling constant is small ($\alpha_S(Q^2) \ll 1$) so perturbative calculations are effective. The DGLAP equations can make a statement about the Q^2 dependence, but the x dependence is still unknown. By the QCD factorization theorems, the PDFs can be related to the observable cross section of a hard process by writing the cross section as a parton interaction convoluted with the PDFs [95]. The parton interaction can be calculated using perturbative quantum field theory techniques. The PDF shapes as a function of x are not calculated theoretically and are instead determined empirically by experimental data.

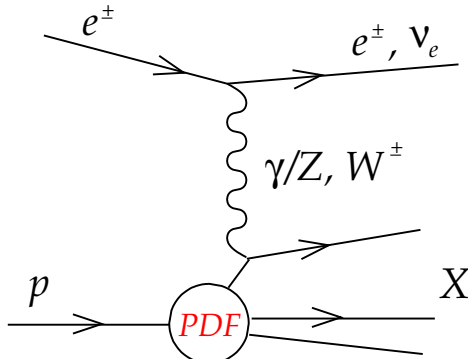


Figure 2-6: Probing the PDFs with deep inelastic scattering. From [96].

The HERA experiment provided important data for the PDF determination by performing deep inelastic scattering of electrons or positrons with protons, at center of mass energies of a few hundred GeV. Two different scattering processes can occur, called the neutral current and charged current; see Figure 2-6. In the charged current interaction, the cross sections of electron and positron on proton are sensitive to different quark PDFs.

In $p\bar{p}$ and pp collisions at the Tevatron and LHC, we can learn more about the proton PDFs through Standard Model precision measurements. In particular, the Z boson differential cross section studied in this work contributes to the global fit of the quark distributions. Meanwhile, ultraperipheral lead-lead heavy ion collisions are also an unconventional source of high energy photon probes which help us study the gluon distribution down to very small values of x (see [97]). Overall, the PDFs are an important quantity for simulating the Standard Model background in a search for

new physics. An example of the PDF set provided by the NNPDF collaboration at $Q = 50$ GeV is shown in Figure 2-7.

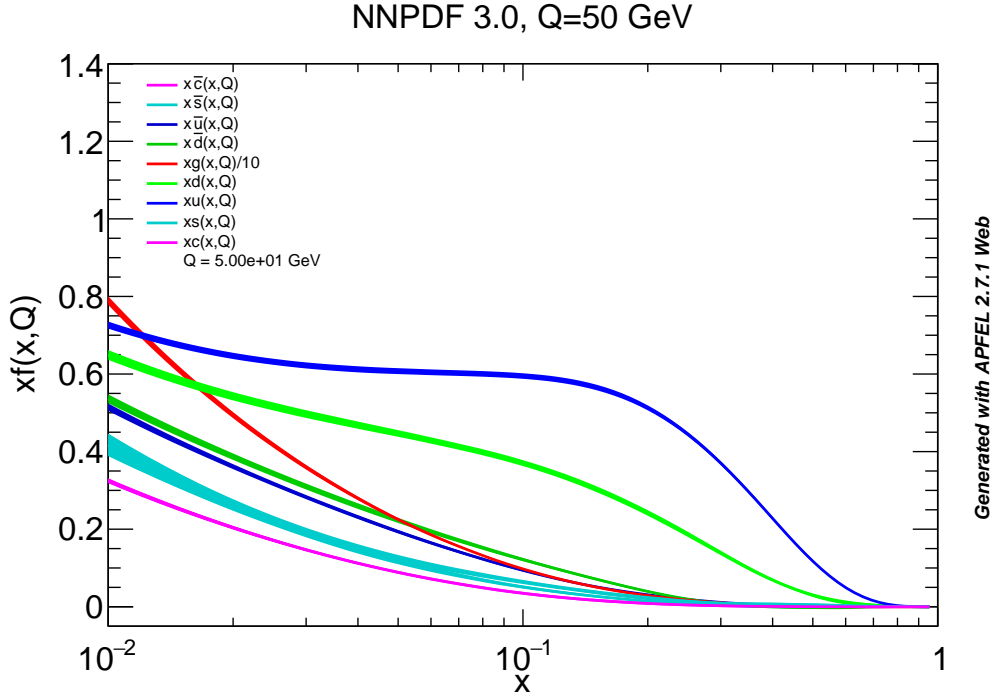


Figure 2-7: NNPDF 3.0 set at momentum transfer 50 GeV. Presented in [98].

2.4 New physics

The study presented here considers one possible mechanism for producing weakly interacting massive particles at the LHC [99]. In this scenario, a Z boson, produced in pp collisions, recoils against a pair of DM particles, $\chi\bar{\chi}$. The Z boson subsequently decays into two charged leptons (electrons or muons), recoiling against E_T^{miss} due to the undetected DM particles. We assume the final state dark matter particle χ is a Dirac fermion.

2.4.1 Simplified models

Four simplified models of DM production via an s -channel mediator exchange are considered. In these models, the mediator has a spin of 1 (0) and vector or axial-vector (scalar or pseudoscalar) couplings to quarks and DM particles. The free parameters of each model are the masses m_{med} and m_{DM} of the mediator and DM particle, respectively, as well as the coupling constant g_q (g_{DM}) between the mediator and the quarks (DM particles). The vector coupling model is described with the following Lagrangian:

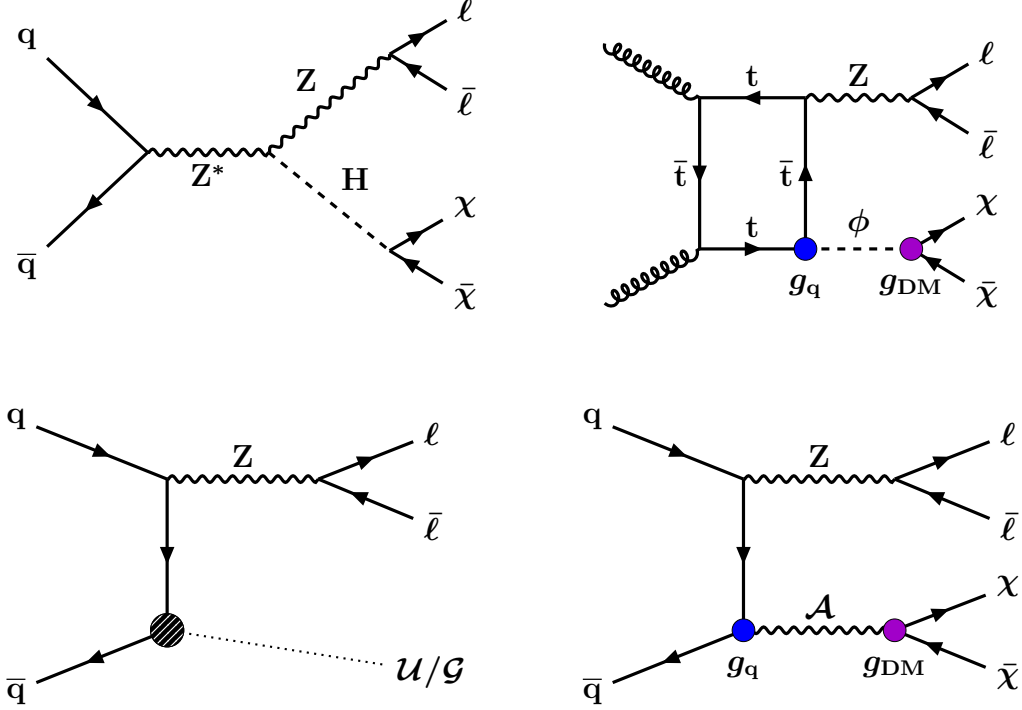


Figure 2-8: Some diagrams beyond the Standard Model in which are produced two charged leptons and missing energy. Clockwise from upper left: associated production of an invisible Higgs boson; gluon-induced production of a Z boson and a massive spin-0 dark matter mediator via top-quark loop; production of a Z boson and a massive spin-1 dark matter mediator; production of a Z boson in association with gravitons (ADD model) or unparticles.

$$\mathcal{L}_{\text{vector}} = g_{\text{DM}} Z'_\mu \bar{\chi} \gamma^\mu \chi + g_q \sum_q Z'_\mu \bar{q} \gamma^\mu q$$

where the spin-1 mediator is denoted as Z' and the SM quark fields are referred to as q and \bar{q} . The Lagrangian for an axial-vector coupling is obtained by making the replacement $\gamma^\mu \rightarrow \gamma^5 \gamma^\mu$. In the case of a spin-0 mediator ϕ , the couplings between mediator and quarks are assumed to be Yukawa-like, with g_q acting as a multiplicative modifier for the SM Yukawa coupling $y_q = \sqrt{2}m_q/v$ (where $v = 246$ GeV is the SM Higgs field vacuum expectation value), leading to the Lagrangian:

$$\mathcal{L}_{\text{scalar}} = g_{\text{DM}} \phi \bar{\chi} \chi + g_q \frac{\phi}{\sqrt{2}} \sum_q y_q \bar{q} q$$

The Lagrangian with pseudoscalar couplings is obtained by inserting a factor of $i\gamma^5$ into each of the two terms (i.e., $\bar{\chi}\chi \rightarrow i\bar{\chi}\gamma^5\chi$ and $\bar{q}q \rightarrow i\bar{q}\gamma^5q$). Example diagrams of DM production via spin-0 and spin-1 mediators are shown in Fig. 2-8 (upper right and lower right, respectively).

2.4.2 Invisible Higgs bosons

A primary focus of the LHC physics program after the discovery of the Higgs boson [100, 101] by the ATLAS and CMS Collaborations is the study of the properties of this new particle. The observation of a sizable branching fraction of the Higgs boson to invisible states [102, 103, 104] would be a strong sign of BSM physics. Supersymmetric (SUSY) models embodying R-parity conservation contain a stable neutral lightest SUSY particle (LSP), e.g., the lightest neutralino [105], leading to the possibility of decays of the Higgs boson into pairs of LSPs. Certain models with extra spatial dimensions predict graviscalars that could mix with the Higgs boson [106]. As a consequence, the Higgs boson could oscillate to a graviscalar and disappear from the SM brane. The signature would be equivalent to an invisible decay of the Higgs boson. There could also be contributions from Higgs boson decays into graviscalars [107]. Other “Higgs portal” models [108, 109, 110] construct a generic connection between SM and DM particles via a Higgs boson mediator. This work considers decays into invisible particles of an SM-like Higgs boson produced in association with a Z boson, as shown in Fig. 2-8 (upper left).

2.4.3 Extra dimensions

A popular BSM paradigm considered here is the Arkani-Hamed–Dimopoulos–Dvali (ADD) model with large extra spatial dimensions [111, 112, 113], which is motivated by the hierarchy problem, i.e., the disparity between the electroweak unification scale ($M_{\text{EW}} \sim 1 \text{ TeV}$) and the Planck scale ($M_{\text{Pl}} \sim 10^{16} \text{ TeV}$). The Planck scale is the energy scale at which quantum effects of gravity become dominant and the Standard Model becomes unified with gravitation. In the ADD model, the apparent Planck scale in four space-time dimensions is given by $M_{\text{Pl}}^2 \approx M_{\text{D}}^{n+2} R^n$, where M_{D} is the true Planck scale of the full $n+4$ dimensional space-time and R is the compactification radius of the extra dimensions. The meaning of compactification is that the extra dimensions are finite or periodic in length. In the limit of sufficiently high length scales or low energy scales, no fields depend on this extra dimension, so it reduces to a standard 4-dimensional space-time. Assuming M_{D} is of the same order as M_{EW} , the observed large value of M_{Pl} points to an R of order 1 mm to 1 fm for 2 to 7 extra dimensions. The consequence of the large compactification scale is that the mass spectrum of the Kaluza–Klein graviton states becomes nearly continuous, resulting in a broad Z boson transverse momentum (p_{T}) spectrum. Therefore, this model predicts graviton (G) production via the process $q\bar{q} \rightarrow Z + G$. The graviton escapes detection, leading to the signature of a Z boson and missing energy (Fig. 2-8, lower right).

2.4.4 Unparticles

The final BSM model considered in this work is the phenomenologically interesting concept of unparticles, which appear in the low-energy limit of conformal field theories. In the Standard Model, only massless particles exhibit scale invariance.

Undertaking a scale transformation, all dimensional quantities are multiplied by a rescaling factor raised to the mass dimension. Thus, the massless particle's mass is unaffected. Unparticles arise from massive BSM fields which scale with fractional dimensions [114, 115, 116]. In other words, the field's quantities are multiplied by fractional powers of the rescaling parameter, allowing for scale invariance.

In the high-energy regime, a scale invariant Banks–Zaks field with a nontrivial infrared fixed point is introduced [117]. The interaction between the SM and Banks–Zaks sectors is mediated by particles of large mass scale M_U , below which the interaction is suppressed and can be treated via an effective field theory (EFT). The low-energy regime will include unparticles. In this work, the emission of spin-0 unparticles from SM quarks is considered. Because of the weakness of the unparticle interactions with the SM fields, the unparticle evades detection. The EFT Lagrangian used to interpret the results is defined as follows:

$$\mathcal{L}_U = \frac{\lambda}{\Lambda_U^{d_U-1}} \mathcal{O}_U \bar{q} q,$$

where λ represents the coupling between the SM and unparticle fields, Λ_U is the cutoff scale of the EFT, and d_U is the characteristic scaling dimension of the theory. The unparticle operator is denoted as \mathcal{O}_U . A representative Feynman diagram of the interaction is shown in Fig. 2-8 (lower right).

Chapter 3

Experimental apparatus

The data studied in this work were collected at the Compact Muon Solenoid (CMS) Experiment. The CMS Detector is a multi-purpose apparatus which records the particle collisions of the Large Hadron Collider. It is installed about 100 meters underground close to the French village of Cessy, between Lake Geneva and the Jura mountains.

3.1 The Large Hadron Collider

The LHC is a two-ring superconducting hadron accelerator [118]. It is designed to collide counter-rotating proton beams with a center-of-mass energy of 14 TeV and instantaneous luminosity of $10^{34} \text{ cm}^{-2}\text{s}^{-1}$. In 2016, protons were collided at center-of-mass energy of 13 TeV. The LHC has also collided lead ions with an energy of 2.8 TeV per nucleon and xenon ions with 2.72 TeV per nucleon.

First, hydrogen atoms are stripped of their protons with a large electric field. They are accelerated to 450 GeV in the CERN LHC injector chain [119]. The chain is as follows: Linac2 (50 MeV), Proton Synchotron Booster (1.4 GeV), Proton Synchotron (25 GeV), Super Proton Synchotron (450 GeV). After the SPS, the protons are injected into the LHC's two separate rings in discrete proton bunches. At the designed spacing of 25 nanoseconds between bunches, there are about 2800 proton bunches per beam.

The LHC achieves the final beam energy with 1232 dipole magnets, each 15 m in length with peak dipole field of 8.3 T. The beam is focused using 492 quadrupole magnets of length 5-7 m. These magnets are twin bore niobium-titanium superconducting electromagnets which operate at 1.9° K. The pipes for the counter-rotating beams are magnetically coupled and the magnets share the same cryostat. Due to the necessity of very efficient heat transfer for prolonged periods, superfluid helium is used as a coolant.

The physics processes studied at the LHC are rare compared to the total proton-proton collision cross section. A high beam intensity is needed to deliver them at a

sufficient rate. For a Gaussian beam distribution, the machine luminosity is

$$L = \frac{N_b^2 n_b f_{\text{rev}} \gamma_r F}{4\pi \varepsilon_n \beta^*} \quad (3.1)$$

where

- N_b is the number of protons per bunch $\approx 10^{11}$.
- n_b is the number of bunches per beam ≈ 2800 .
- f_{rev} is the revolution frequency .
- γ_r is the Lorentz factor.
- F is the reduction factor due to the geometric crossing angle.
- ε_n is the transverse beam emittance normalized to the beam energy, describing the spread in position and momentum space.
- β^* is the beta function at the interaction point, which alongside ε_n determines the beam envelope.

The LHC has 4 interaction points. The two general purpose, high luminosity experiments are ATLAS and CMS. The LHCb experiment has only forward coverage and specializes in heavy flavor physics and spectroscopy. The ALICE experiment studies heavy ion collisions.

In 2016, the LHC delivered around 36 inverse femtobarns worth of data which was recorded by CMS.

3.2 The CMS Detector

CMS was designed with the following requirements in mind (in no particular order):

- Good muon identification and momentum resolution over a wide range of momenta and angles, good dimuon mass resolution (1% at 100 GeV), and the ability to determine unambiguously the charge of muons with $p < 1$ TeV
- Good charged-particle momentum resolution and reconstruction efficiency in the inner tracker. Efficient triggering and offline tagging of τ 's and b-jets, requiring pixel detectors close to the interaction region
- Good electromagnetic energy resolution, good diphoton and dielectron mass resolution (1% at 100 GeV), wide geometric coverage, π^0 meson rejection, and efficient photon and lepton isolation at high luminosities
- Good missing transverse energy and dijet mass resolution, requiring hadron calorimeters with a large hermetic geometric coverage and with fine lateral segmentation

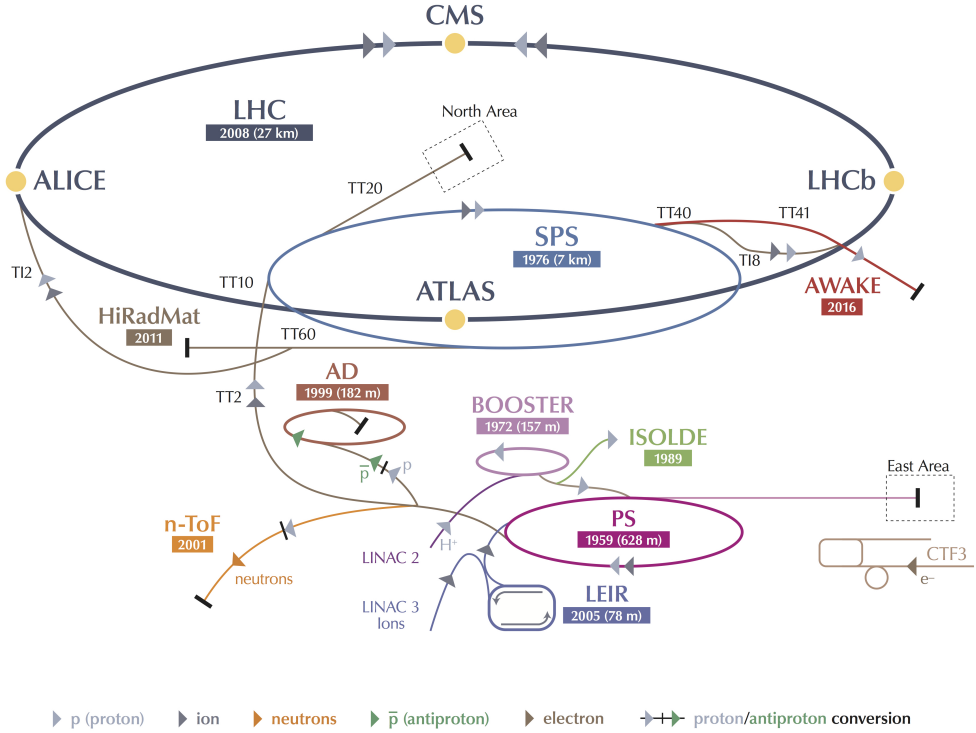


Figure 3-1: Schematic of the CERN accelerator complex.

The central feature of the CMS apparatus is a superconducting solenoid of 6 m internal diameter, providing a magnetic field of 3.8 T. Within the solenoid volume are a silicon pixel and strip tracker, a lead tungstate crystal electromagnetic calorimeter (ECAL), and a brass and scintillator hadron calorimeter (HCAL), each composed of a barrel and two endcap sections. Forward calorimeters extend the pseudorapidity coverage provided by the barrel and endcap detectors. Muons are detected in gas-ionization chambers embedded in the steel flux-return yoke outside the solenoid.

Events of interest are selected using a two-tiered trigger system [120]. The first level, composed of custom hardware processors, uses information from the calorimeters and muon detectors to select events at a rate of around 100 kHz within a time interval of less than 4 μ s. The second level, known as the high-level trigger, consists of a farm of processors running a version of the full event reconstruction software optimized for fast processing, and reduces the event rate to around 1 kHz before data storage.

Coordinate system

To describe location, CMS uses a standard right-handed Cartesian coordinate system where the x direction points to the center of the LHC ring, the y direction points to the sky, and the z direction points in the counterclockwise beam direction at the interaction point. This is used for locating interaction vertices and tracks' impact

parameters with respect to those vertices. However, this work will also frequently use a set of modified spherical coordinates (r, ϕ, η) which are conventional in particle physics. Here, r is the radial coordinate, ϕ is the azimuthal angle, and η is the *pseudorapidity*, given by

$$\eta \equiv -\ln \tan \frac{\theta}{2} \implies \theta \equiv 2 \arctan(e^{-\eta}) \quad (3.2)$$

where θ is the polar angle. In these coordinates, the transverse momentum p_T of a particle is related to its total momentum $|\vec{p}|$ and the hyperbolic secant of pseudorapidity as

$$p_T = |\vec{p}| \operatorname{sech} \eta \quad (3.3)$$

A variable used to denote the angular separation between two objects in the detector is ΔR , which is defined as

$$\Delta R = \sqrt{(\phi_1 - \phi_2)^2 + (\eta_1 - \eta_2)^2} \quad (3.4)$$

3.2.1 Trackers

The inner tracking system of CMS is designed to provide a precise and efficient measurement of the trajectories of charged particles emerging from the LHC collisions,

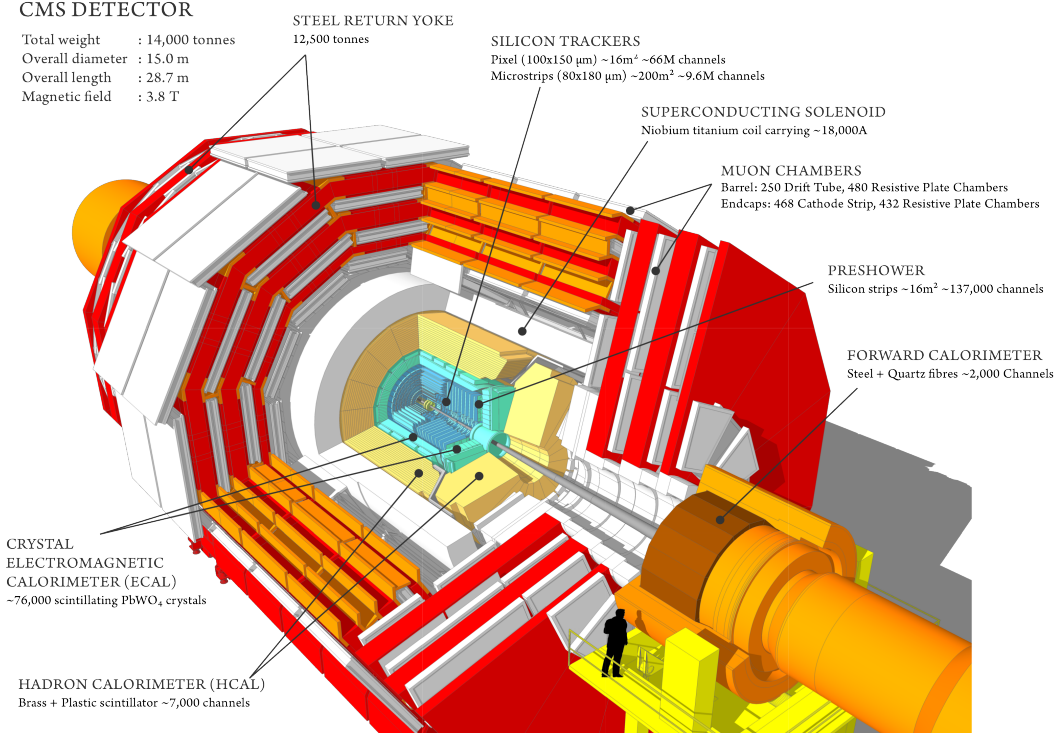


Figure 3-2: Schematic of the CMS Detector.

as well as a precise reconstruction of secondary vertices. It surrounds the interaction point and has a length of 5.8 m and a diameter of 2.5 m. The CMS solenoid provides a homogeneous magnetic field of 4 T over the full volume of the tracker.

At the LHC design luminosity of $1034 \text{ cm}^{-2} \text{ s}^{-1}$, there are on average about 1000 particles from more than 20 overlapping proton-proton interactions traversing the tracker for each bunch crossing, i.e. every 25 ns. Therefore, a detector technology featuring high granularity and fast response is required, such that the trajectories can be identified reliably and attributed to the correct bunch crossing. However, these features imply a high power density of the on-detector electronics which in turn requires efficient cooling. This is in direct conflict with the aim of keeping to the minimum the amount of material in order to limit multiple scattering, bremsstrahlung, photon conversion, and nuclear interactions. Thus, the design was optimized to balance these competing needs.

The intense particle flux will also cause severe radiation damage to the tracking system. The main challenge in the design of the tracking system was to develop detector components able to operate in this harsh environment for an expected lifetime of 10 years. These requirements on granularity, speed and radiation hardness lead to a tracker design entirely based on silicon detector technology. The CMS tracker is composed of a pixel detector with three barrel layers at radii between 4.4 cm and 10.2 cm and a silicon strip tracker with 10 barrel detection layers extending outwards to a radius of 1.1 m. Each system is completed by endcaps which consist of 2 disks in the pixel detector and 3 plus 9 disks in the strip tracker on each side of the barrel, extending the acceptance of the tracker up to a pseudorapidity of $|\eta| < 2.5$. With about 200 m^2 of active silicon area the CMS tracker is the largest silicon tracker ever built.

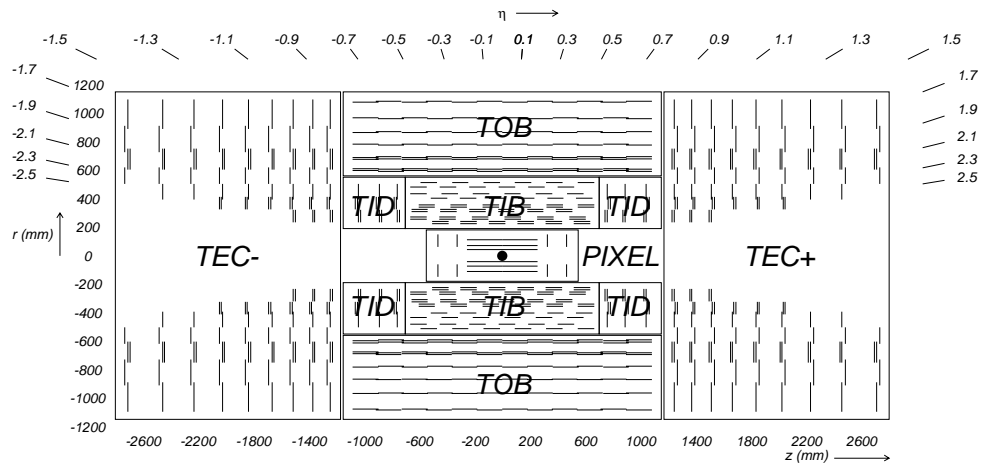


Figure 3-3: Layout of the CMS tracker. From [121].

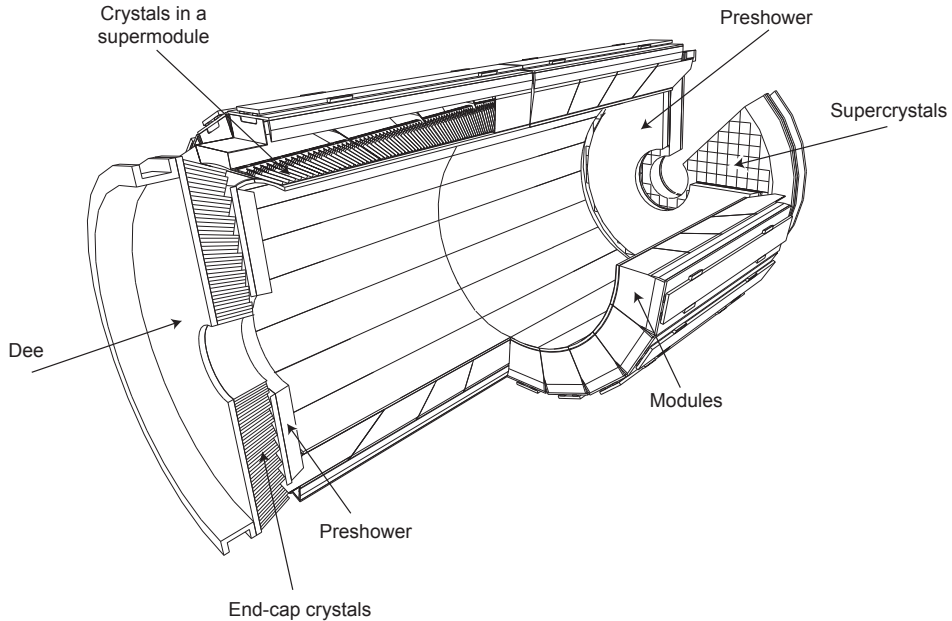


Figure 3-4: Layout of the CMS electromagnetic calorimeter showing the arrangement of crystal modules, supermodules and endcaps, with the preshower in front. From [121].

3.2.2 Electromagnetic calorimeter

The electromagnetic calorimeter of CMS (ECAL) is a hermetic homogeneous calorimeter made of 61,200 lead tungstate (PbWO_4) crystals mounted in the central barrel part, and 7,324 crystals in each of the two endcaps. A preshower detector is placed in front of the endcap crystals. Avalanche photodiodes (APDs) are used as photodetectors in the barrel and vacuum phototriodes (VPTs) in the endcaps. The use of high density crystals has allowed the design of a calorimeter which is fast, has fine granularity and is radiation resistant, all important characteristics in the LHC environment. One of the driving criteria in the design was the capability to detect the decay to two photons of the postulated Higgs boson. This capability is enhanced by the good energy resolution provided by a homogeneous crystal calorimeter.

The number of scintillation photons and the electronic amplification thereof both are decreasing with temperature. So the ECAL must be kept at a stable temperature of $18 \pm 0.05^\circ \text{ C}$. Water cooling and aluminum tubing are used to meet this need.

ECAL barrel

The ECAL barrel (EB) covers the pseudorapidity range $|\eta| < 1.479$. The granularity is 360 in ϕ and 170 in η , giving 61,200 crystals in all. The crystals have a tapered shape. They are mounted in a quasi-projective geometry to avoid cracks aligned with particle trajectories. In other words, their central axes are not exactly parallel to a path from the interaction point, in either the ϕ or η projections. The crystal cross-

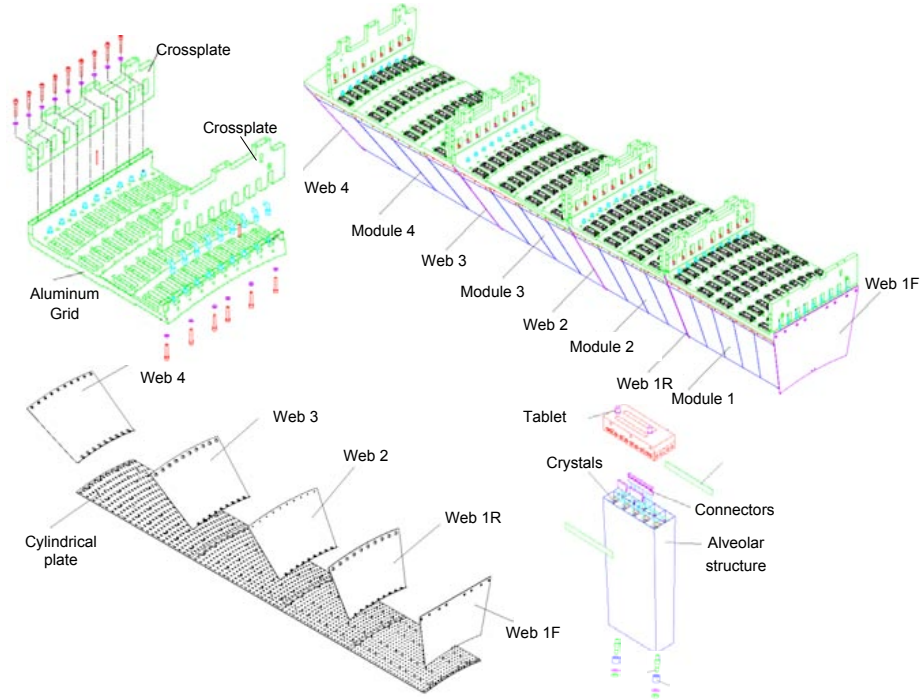


Figure 3-5: Layout of the ECAL barrel. From [121].

section corresponds to approximately 0.0174×0.0174 in $\eta \times \phi$ or $22 \times 22 \text{ mm}^2$ at the front face of the crystal—and $26 \times 26 \text{ mm}^2$ at the rear face. The crystals' radial length is 230 mm, corresponding to 25.8 radiation lengths.

In the barrel, the scintillation photons are collected by Hamamatsu type S8148 reverse structure avalanche photodiodes. Their active area is $5 \times 5 \text{ mm}^2$. Two are mounted on each crystal.

ECAL endcaps

The ECAL endcaps (EE) cover the rapidity range $1.479 < \eta < 2.5$. The distance from the interaction point and the endcaps is 315.4 cm with the 4 T magnetic field on. Most of each endcap consists of identically shaped crystals grouped in mechanical units of 5×5 crystals, called supercrystals. As with the EB crystals, the central axes of the EE supercrystals are not exactly parallel to a path from the interaction point. The front face of these crystals has an area of $28.62 \times 28.62 \text{ mm}^2$. The rear face has an area of $30 \times 30 \text{ mm}^2$. The crystals' length is 220 mm or 24.7 radiation lengths.

In the endcaps, the scintillation photons are collected by type PMT188 vacuum phototriodes from National Research Institute Electron in St. Petersburg. Their active area is 280 mm^2 . One is mounted on each crystal.

It is relevant to make a note here that the physical cracks between the EB and EEs exist at $1.4442 < |\eta| < 1.566$. This has a negative effect on the electron identification

efficiency, to be described in great detail later. This motivates the non-intuitive kinematic binnings in η which are used later in Chapter 6 and Appendix A.

3.2.3 Hadron calorimeters

The hadron calorimeters (HCALs) exist to measure the energy of hadrons and hadronic jets. Most hadrons pass through the ECAL due to its limited stopping power and then deposit the rest of their energy in the HCAL. Muons, and the few energetic hadrons which punch through the HCAL, traverse past it and reach the muon system. From the visible particle energies recorded in the ECAL, HCAL, and muon systems, it is possible to construct the quantity of missing transverse energy in order to infer the production of neutrinos or exotic particles. Figure 3-6 shows the longitudinal view of the CMS Detector. The dashed lines are at fixed η values. The hadron calorimeter barrel and endcaps sit behind the tracker and the electromagnetic calorimeter as seen from the interaction point. The hadron calorimeter barrel is radially restricted between the outer extent of the electromagnetic calorimeter ($R = 1.77$ m) and the inner extent of the magnet coil ($R = 2.95$ m). This constrains the total amount of material which can be put in to absorb the hadronic shower. Therefore, an outer hadron calorimeter or tail catcher is placed outside the solenoid complementing the barrel calorimeter. Beyond $|\eta| = 3$, the forward hadron calorimeters placed at 11.2 m from the interaction point extend the pseudorapidity coverage down to $|\eta| = 5.2$ using a Cherenkov-based, radiation-hard technology. The HCAL subsystems are described briefly below, with more detailed information on the geometry and readout being available in [122].

HCAL barrel

The HCAL barrel (HB) is a sampling calorimeter and covers the pseudorapidity range $|\eta| < 1.3$. It consists of 36 identical azimuthal wedges which form two half-barrels. The wedges are constructed out of flat brass absorber plates which are parallel to the beam axis. Each wedge is segmented into four azimuthal angle (ϕ) sectors. The innermost and outermost plates are made of stainless steel for structural strength.

The absorber consists of a front steel plate 40 mm thick, followed by eight 50.5 mm thick brass plates, six 56.5 mm thick brass plates, and a 75 mm thick steel back plate. The last layer is thicker to correct for late developing showers which could leak out the back. The total absorber thickness at 90° is 5.82 interaction lengths (λ_I). The HB effective thickness increases with polar angle (θ) as $1/\sin \theta$, resulting in 10.6 λ_I at $|\eta| = 1.3$.

The HB baseline active material is 3.7 mm thick Kuraray SCSN81 plastic scintillator, chosen for its long-term stability and moderate radiation hardness. The first layer of scintillator is located in front of the steel support plate, and is made of 9 mm thick Bicron BC408. Its purpose is to sample hadronic showers developing in the inert material between the ECAL barrel and the HCAL barrel. The plastic scintillator is divided into 16 η sectors, resulting in a segmentation of $(\Delta\eta, \Delta\phi) = (0.087, 0.087)$.

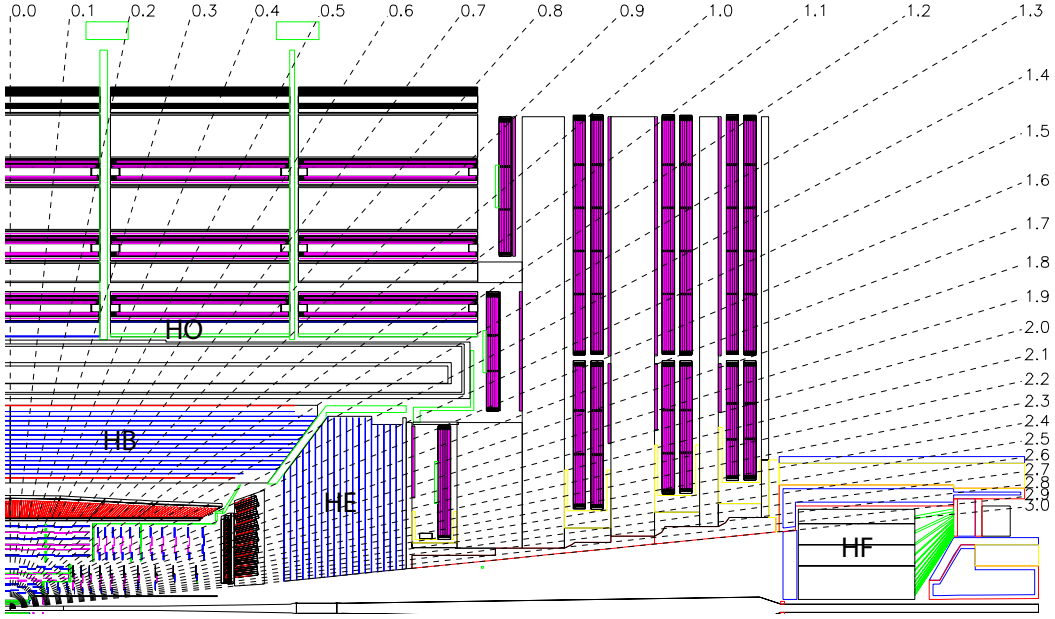


Figure 3-6: Longitudinal slice of the CMS Detector showing the locations of the hadron barrel (HB), endcap (HE), outer (HO) and forward (HF) calorimeters.

HCAL endcaps

The hadron calorimeter endcaps (HE) cover the rapidity range $1.3 < |\eta| < 3$. It is designed for high radiation tolerance, in order to survive 10 MRad after 10 years of operation. The total length of the endcap calorimeter, after the ECAL and HCAL endcaps, is about 10 interaction lengths.

The absorber is made of C26000 cartridge brass. The material was chosen because it is non-magnetic, has a short interaction length and was available at a relatively low cost. The absorber is assembled in a staggered geometry which minimizes the cracks between HB and HE and contains no projective dead material.

The scintillators are of trapezoidal shape and there are 18 layers of them in total. The first layer are made of 9 mm thick Bicron BC408. All the rest are made of 3.7 mm thick SCSN81. The scillation light is read out via wavelength shifting fibers. The granularity of the calorimeters is $(\Delta\eta, \Delta\phi) = (0.087, 0.087)$ for $|\eta| < 1.6$ and $(\Delta\eta, \Delta\phi) = (0.170, 0.170)$ for $|\eta| \geq 1.6$.

HCAL outer

The combined stopping power of the ECAL and HCAL barrels does not provide adequate stopping power in the central region $|\eta| < 1.3$. This is problematic for the missing energy resolution. To further measure and contain these showers, the hadron calorimeter is extended outside the solenoid with a tail catcher called the HO. Only 40 mm of space in the radial direction is available, 24 mm of which is used for aluminum

honeycomb support structures.

The scintillator plates of the HO are made of 10 mm thick Bicron BC408. There are 5 rings in η , each of those rings having 12 identical ϕ sectors, and each of those sectors having 6 azimuthal slices. The sizes and positions of the tiles in HO are supposed to roughly map the layers of HB to make towers of granularity $(\Delta\eta, \Delta\phi) = (0.087, 0.087)$.

The magnetic solenoid coil is used as an additional absorber equal to $1.4/\sin\theta$ interaction lengths. Outside the vacuum tank, the magnetic field is returned through an iron yoke roughly 20 mm thick, with 5 rings corresponding to the scintillator plates. The central ring has scintillators both inside and outside of the iron yoke ring. The others have scintillators only outside their yoke rings. All told, the total depth of the calorimeter system is extended to a minimum of $11.8\lambda_I$ except at the barrel-endcap boundary region at around $|\eta| = 1.4$.

HCAL forward

The forward calorimeter, or HF, exists in an extremely hostile environment. At $|\eta| = 5$ we expect to have delivered 10 MGy after 10 years of operation. The active material is fused-silica core, polymer hard-cladded quartz fibers, which have sufficient radiation hardness. These fibers measure $600 \pm 10\mu\text{m}$ in diameter for the fused-silica core, $630^{+5}_{-10}\mu\text{m}$ with the polymer hard-cladding, and $800 \pm 30\mu\text{m}$ with the protective acrylate buffer.

The geometry consists of a steel absorber structure composed of 5 mm thick grooved plates. Fibers are inserted in these grooves. The detector is functionally subdivided into two longitudinal segments. Half of the fibers run over the full depth of the absorber ($165\text{ cm} \approx 10\lambda_I$) while the other half starts at a depth of 22 cm from the front of the detector. These two sets of fibers are read out separately. This arrangement makes it possible to distinguish showers generated by electrons and photons, which deposit the majority of their energy in the first 22 cm, from those generated by hadrons, which produce nearly equal signals in both calorimeter segments on average. The absorber has grooves which make a square grid separated by $5.0 \pm 0.1\text{ mm}$ center-to-center, with long and short fibers alternating in the grooves.

This calorimeter is mostly sensitive to the electromagnetic component of hadronic showers. Only light that hits the core-cladding interface at an angle larger than the critical angle (71°) contributes to the calorimeter signal in the form of Cherenkov light. After the quoted 10 MGy dose has accumulated over the HF lifetime, the optical transmission of the fibers is reduced just by a factor of 2.

3.2.4 Muon system

The CMS muon system is capable of reconstructing the momentum and charge of muons over the entire kinematic range of the LHC. Due to the shape of the CMS solenoid magnet, the muon system has a barrel section and 2 endcap sections. Three types of gaseous particle detectors are used. Since the total area of the muon detection planes is around $25,000\text{ m}^2$, the detectors were chosen to be inexpensive but reliable.

In the barrel region, rectangular drift tubes (DT) are used, since there is little neutron-induced muon background, the magnetic field is uniform, and the real muon rate is relatively low. In the endcap regions, there is a high muon rate, high muon background, and a very nonuniform magnetic field, so cathode strip chambers (CSC) are used there. The third subsystem is the resistive plate chambers (RPC). Their spatial resolution is relatively poor. But their fast response and good time resolution are useful for the trigger. They also help resolve ambiguity in the standalone muon reconstruction, which only uses information from the muon system.

The DTs and CSCs are each capable of triggering on muon p_T independently of the other detector subsystems. The p_T resolution of this triggering muon object is 15% in the barrel and 25% in the endcap. For muon p_T up to 200 GeV, the DTs and CSCs together can give a standalone momentum resolution of 9%. Approaching muon momenta of 1 TeV, the standalone momentum resolution is 5%. The muon resolution is improved when combined with the tracker information.

Lastly, an alignment system measures the relative positions of the muon detectors amidst the inner tracker to optimize the momentum resolution of muons.

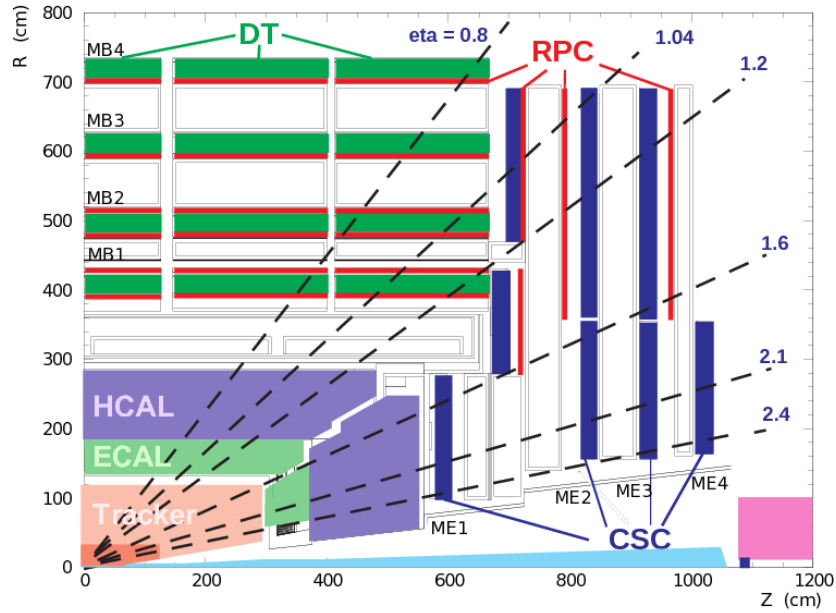


Figure 3-7: Quarter-view of the CMS Detector showing the muon system components. From [121].

Drift tubes

The DTs cover the pseudorapidity region $|\eta| < 1.2$. There are 4 stations forming concentric cylinders around the beam line. The 3 inner cylinders have 60 drift chambers each and the outer cylinder has 70. There are about 172,000 sensitive wires of about 2.4m in length. The maximum drift path length is 21 mm. In a gaseous admixture of

85% Ar and 15% CO₂ the maximum drift time is 380 ns. For the LHC design luminosity, this produces a negligible occupancy and permits the use of single-hit electronics. Meanwhile, the cell size is sufficiently large to keep the number of electronic channels low and affordable.

Each DT chamber is made of 2 or 3 superlayers (SL). Each SL is made of layers of rectangular drift cells staggered by half a cell. The wires in the 2 outer SLs are parallel to the beam line and provide a track measurement in the magnetic bending plane. The wires in the inner SL are orthogonal to the beam line and measure the z position. This innermost SL is not present in the fourth DT station. Thus, a muon first encounters a ϕ -measuring SL, passes through a honeycomb spacer plate, then crosses the z -measuring SL and the second ϕ -measuring SL. Due to discontinuities in the design, a muon could end up crossing only two stations instead of the maximum four.

One superlayer has time resolution on the order of nanoseconds. The time measurement is delayed by the drift-time, determined by the design parameters of the drift tubes. Using the SL information, pattern recognition circuits deliver the position and angle of the track segment's center of gravity with precision of 1.5 mm and 20 mrad, respectively.

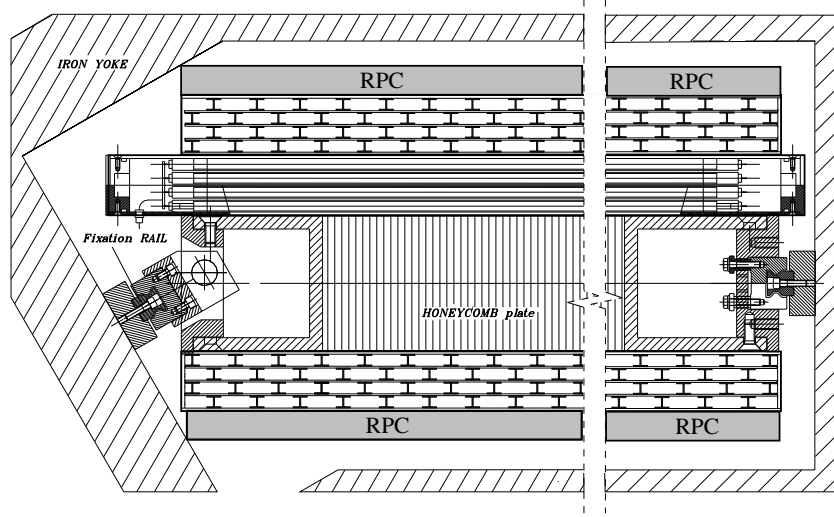


Figure 3-8: Chambers of the CMS DT system including the honeycomb support. From [121].

Cathode strip chambers

The CSCs cover the pseudorapidity region $0.9 < |\eta| < 2.4$. There are 4 stations of CSCs in each endcap. The chambers are perpendicular to the beamline and interspersed between the magnetic flux return plates. The cathode strips point radially outward from the beamline and provide a precision measurement in the $r - \phi$ bending plane.

The CSCs are multiwire proportional chambers comprised of 6 anode wire planes interleaved among 7 cathode panels. Wires run azimuthally and define a track's radial

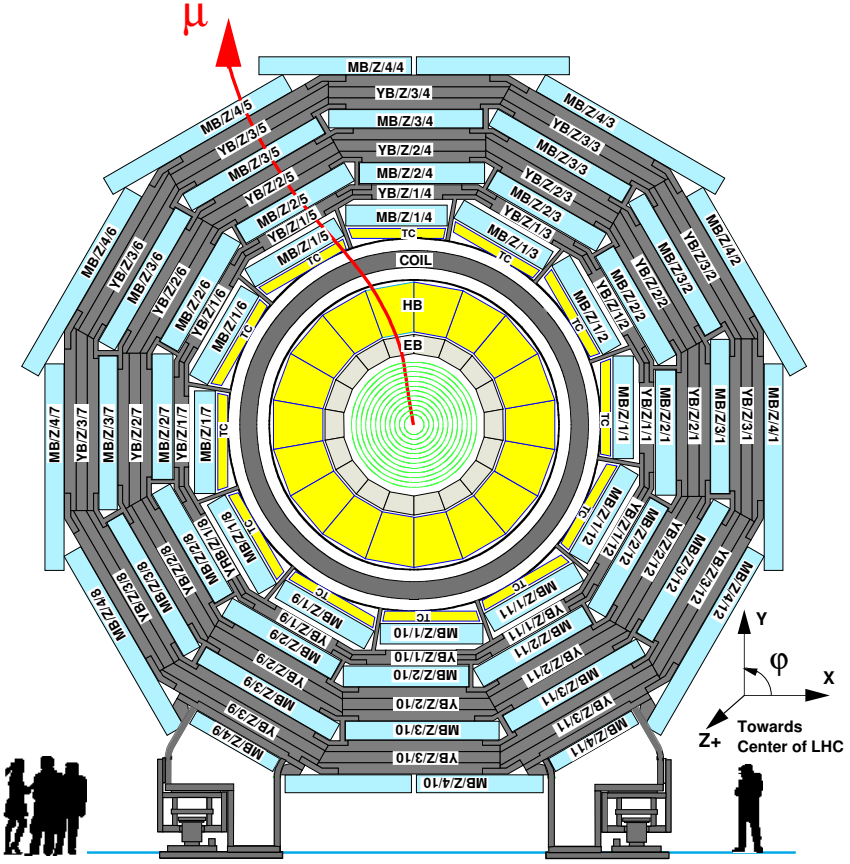


Figure 3-9: Layout of the CMS barrel muon DT chambers in one of the 5 wheels. From [121].

coordinate. Strips are milled on cathode panels and run lengthwise at constant $\Delta\phi$ width. The muon coordinate along the wires is obtained by interpolating between charges induced on strips. The largest chambers, ME2/2 and ME3/2, are about $3.4 \times 1.5 \text{ m}^2$ in size. The overall area covered by the sensitive planes of all chambers is about $5,000 \text{ m}^2$, the gas volume is over 50 m^3 , and there are about 2 million wires. There are about 9000 high-voltage channels in the system, about 220,000 cathode strip read-out channels with 12-bit signal digitization, and about 180 000 anode wire read-out channels.

An avalanche on a wire induces charge on a cathode plane. The charge shape can be approximately parameterized by the Gatti function; see Equation 15 in Ref. [123]. Given the CSC geometry, most of the induced charge is shared among three or four strips. A strip signal waveform is sampled and digitized every 50 ns. The overall pulse duration is about 300 ns. The charge cluster is fit to obtain the spatial coordinate, time, and cluster charge. Using this method, the spatial resolution for a 6-plane chamber is $80 \mu\text{m}$.

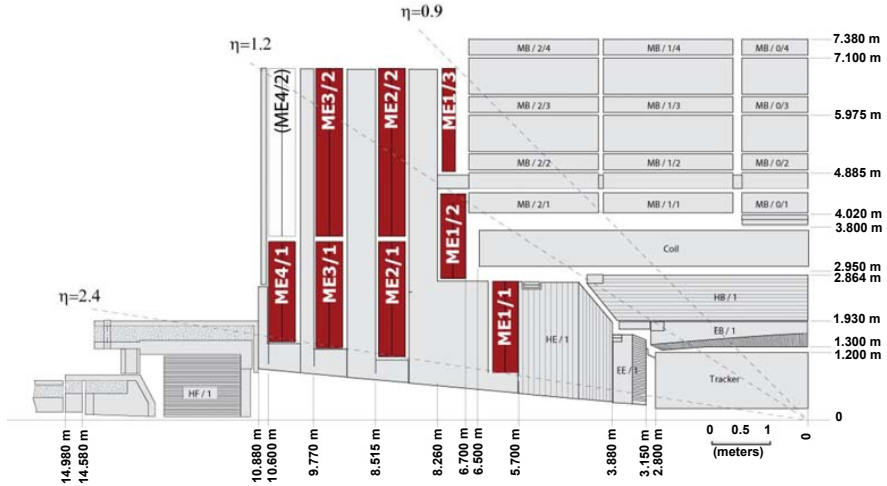


Figure 3-10: Quarter-view of the CMS Detector. Cathode strip chambers of the Endcap Muon system are highlighted. From [121].

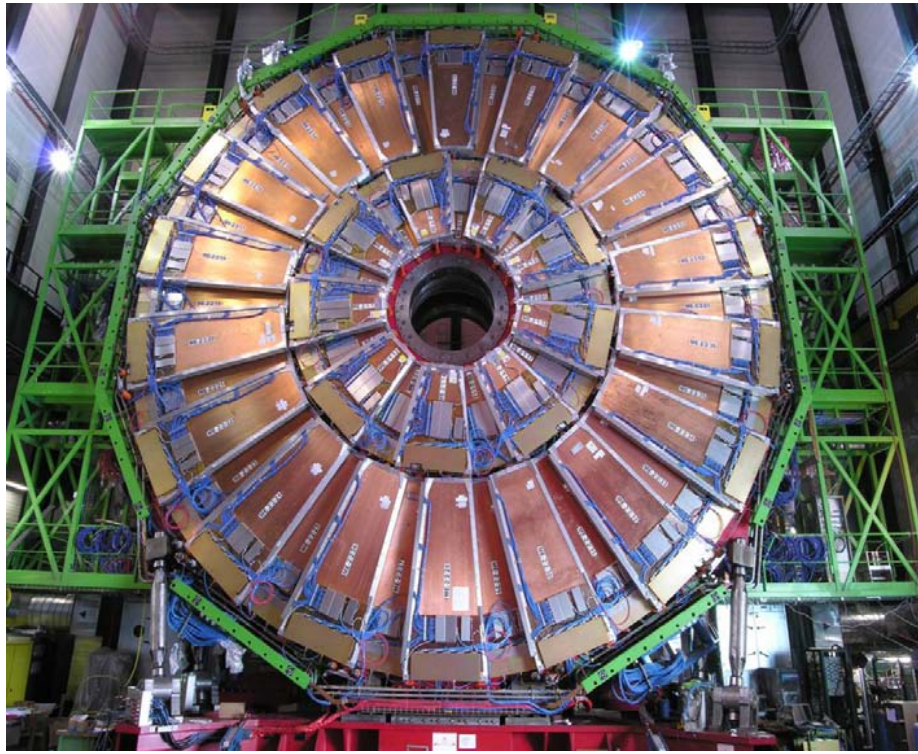


Figure 3-11: The ME2 station of CSCs. The outer ring consists of 36 ME2/2 chambers, each spanning 10° in ϕ , and the inner ring of eighteen E2/1 chambers. The chambers overlap to provide contiguous coverage in ϕ . From [121].

Resistive plate chambers

The RPCs are gaseous parallel-plate detectors with adequate spatial resolution and scintillator-level time resolution. They are much faster than the 25 ns proton bunch crossing period at the LHC. Using the RPC information, there is no ambiguity in the association of muon tracks and bunch crossings.

The CMS RPC basic double-gap module consists of two gaps operated in avalanche mode with common pickup readout strips between them. The total induced signal is the sum of the two single-gap signals. Thus, the single-gaps can operate at a lower voltage gap, with better effective efficiency than a single gap.

In the barrel iron return yoke, the RPC chambers form 6 coaxial sensitive cylinders that are approximated with concentric dodecagon arrays arranged into 4 stations. See Figure 3-12.

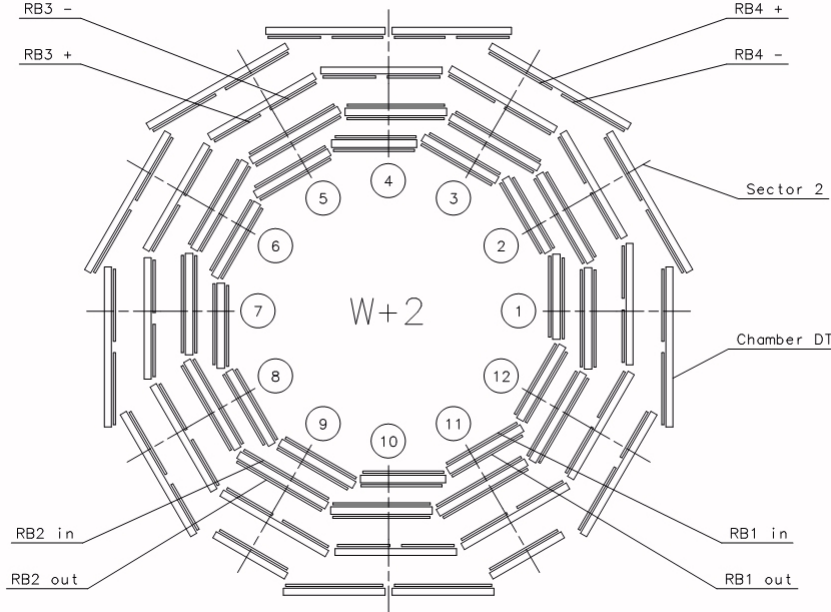


Figure 3-12: Schematic layout of one of the 5 RPC barrel wheels. Each wheel is divided into 12 sectors. From [121].

3.2.5 Trigger system

Triggering algorithms decide which data are recorded in the experiment. They are implemented in two stages via a combination of hardware and software.

Level-1 trigger

The trigger decision process begins with the Level-1 Trigger (L1T) [120] [124]. The hardware implementation of the Level-1 Trigger is in the form of application-specific integrated circuits (ASICs), field-programmable gate arrays (FPGAs), programmable logic devices (PLDs), and random access memory used for memory look-up tables (LUTs). The FPGAs and LUTs may be reprogrammed, allowing for the algorithms to be revised. The Level-1 Trigger is subject to a large data flow carried on optical fibers, copper cables, and backplanes within hardware crates. The data is transmitted in parallel at frequencies which are integer multiples of 40 MHz.

Data from calorimeters and the muon system are used by the L1T to perform the first level of online event selection using custom electronic systems. The algorithms process data in pipeline fashion, using pattern recognition and fast summing techniques, without introducing dead-time. Pipeline memories of depth equal to the trigger latency store the data on the detector until the L1T decision arrives. The algorithms use input data of reduced granularity and resolution. The calorimeters transmit energy sums along with data that carry information to characterize the energy deposition (electron/photon, tau, narrow jet, muon). The muon system hits are summarized in terms of track stubs. The L1T output quantities are muon, electron, photon, tau and jet candidates, along with jet counts and global transverse and missing transverse energy sums.

Data events passing the Level-1 Trigger are then transmitted to the so-called “high-level trigger,” described next.

High-Level Trigger

Data events accepted by the Level-1 Trigger are next processed by the High-Level Trigger (HLT). Unlike the L1T’s readout boards, the HLT is implemented on a commercial Linux computing cluster called the File-based Filter Farm (F^3). There are three types of computing units in the F^3 :

- The Readout Units take the information from the readout boards and assemble event fragments from a given detector partition.
- The Builder Units take the event fragments and assemble full events. The full events are buffered here during the next step.
- The Filter Units apply the final event selection of the HLT algorithms.

The HLT algorithms running on the FUs operate on full-granularity event data from all subdetector systems. They accept between 1-10% of events accepted by the L1T. The algorithms make use of the CMS offline reconstruction framework called CMSSW.

3.2.6 Offline world

Events accepted by the HLT are merged into larger agglomerate files which are stored locally in a Lustre parallel distributed file system. Then, they are transferred from the “online” CMS experimental site to the “offline” CERN Tier-0 computing center at the main CERN campus in Meyrin for prompt processing and archival storage. This transfer system is a multithreaded software, optimized to handle rates of several gigabytes per second during data taking. Finally, data are distributed worldwide from Tier-0 to the global CMS computing grid for physics studies.

Chapter 4

Physics objects

4.1 Electrons

4.1.1 Electron reconstruction

Electrons in the CMS Detector are reconstructed through association of a track from the silicon detector with a cluster of energy in the ECAL. Electron tracks are formed from initial seeds likely to correspond to initial electron trajectories, which are then used to build tracks by collecting hits in the silicon tracker using the combinatorial Kalman filter procedure. Next, a track fitting procedure is undertaken using a Gaussian Sum Filter (GSF), in which the energy loss in each tracker layer is approximated by a mixture of Gaussian distributions. Meanwhile, the electron energy has been collected in several crystals of the ECAL. These depositions undergo two steps of clustering. The first step finds clusters from crystal arrays of 5×1 in $\eta \times \phi$ for the ECAL barrel, and 5×5 crystals for the ECAL endcaps. The second step forms a supercluster (SC) comprising the energy of constituent clusters. The supercluster position and energy, along with the GSF track, reconstruct the electron in the detector.[125] The reconstruction procedure is also informed by the Particle-Flow algorithm, described later in Section 4.5.

The final reconstructed electron momentum is found using a multivariate regression tuned on simulation to give better energy resolution. A residual energy scale correction is applied to the reconstructed electrons based on time, electron η , and shower shape variables such that the Z mass peak resolution is enhanced. In addition, a smearing is applied to simulation such that the energy resolution in data and simulation match.

4.1.2 Electron identification variables

The shower shape of the hits in the ECAL provides discriminating variables for identifying electrons. One such variable is $\sigma_{inj\eta}$. To understand $\sigma_{inj\eta}$, we first discuss its predecessor, $\sigma_{\eta\eta}$, which is a weighted second moment of the energies deposited in the 5×5 crystals centered on the ECAL supercluster seed crystal. Here, η_i is the

pseudorapidity coordinate of the i^{th} ECAL crystal. The formula for $\sigma_{\eta\eta}$ is:

$$\sigma_{\eta\eta} = \sqrt{\frac{\sum_i^{5\times 5} w_i (\eta_i - \bar{\eta}_{5\times 5})^2}{\sum_i^{5\times 5} w_i}} \quad \text{with} \quad w_i = 4.2 + \ln \frac{E_i}{E_{5\times 5}} \quad (4.1)$$

This variable does not perform well near cracks in the ECAL, where there is a gap in *eta*. A 5×5 supercluster containing this gap will arbitrarily have a higher value of $\sigma_{\eta\eta}$. For this reason, a simple correction is made where we consider instead the crystal index instead of absolute η , and multiply it by the average crystal η size of 0.0175. Counting the i^{th} crystal ordering in the η direction, $N(i)$, we derive the variable $\sigma_{i\eta i\eta}$ (using the same weights w_i):

$$\sigma_{i\eta i\eta} = \sqrt{\frac{\sum_i^{5\times 5} w_i (0.0175 N(i) + \eta_{\text{Seed}} - \bar{\eta}_{5\times 5})^2}{\sum_i^{5\times 5} w_i}} \quad (4.2)$$

Other ECAL-related variables are: H/E_{SC} , the ratio of HCAL to ECAL energy deposition associated with a supercluster seed; and $|1/E_{\text{SC}} - 1/p|$, which is technically computed as $|(1 - E_{\text{SC}}/p_{\text{Track}})/E_{\text{ECAL}}|$. Compared to charged hadron fakes, the true electron will deposit all or most of its energy in the ECAL.

Another class of useful variables are related to matching attributes of the ECAL supercluster and the tracker track. $\Delta\eta(\text{SC}, \text{trk})$ is the difference in η between the supercluster and the track at the track's point-of-closest-approach to the supercluster, extrapolated from the innermost track state. $\Delta\phi(\text{SC}, \text{trk})$ is the analogous quantity in ϕ -coordinate.

The reconstructed electron candidate's impact parameter is important for suppressing pileup. Thus, we apply cuts on the transverse impact parameter $d_0(\text{vtx})$ and the longitudinal impact parameter $d_z(\text{vtx})$ with respect to the best primary vertex.

The term “missing hits” refers to how many hits we would expect to see in the inner tracker due to this particle which were missed. A conversion veto is applied which also accounts for missing hits, along with the minimum distance between conversion tracks and the difference in $\cot\theta$ between the partner tracks.

Lastly, we apply a combined isolation requirement, I_{rel}^e , relative to the electron transverse momentum and corrected for effective area. This bounds the amount of hadronic activity and other EM activity arriving near the electron. The computation of the isolation relies on information from the Particle Flow algorithm, described further below in Section 4.5. The isolation of the lepton candidates is computed from the flux of particle candidates found within a cone of $\Delta R = 0.4$ built around the lepton direction [126]. The flux of particles is computed independently for the charged hadrons, neutral hadrons and photon candidates. The contribution from neutral hadron candidates is corrected for the influence of pileup by using the *effective area* approach. The average energy density per area due to pileup (ρ) is multiplied with an effective area (A_{eff}) and subtracted from the isolation sum. A_{eff} is chosen in such a way that the isolation is independent of the number of pileup interactions.

The relative electron isolation sum is defined as:

$$I_{\text{rel}}^e = \frac{1}{p_T} [I_{\text{ch}} + \max(I_{\text{nh}} + I_g - A_{\text{eff}} \cdot \rho, 0)] \quad (4.3)$$

4.1.3 Electron identification working points

After the electron reconstruction procedure, there are still fake electrons from other objects such as charged pions which can be mistaken for electrons. The purpose of electron identification is to improve the purity of electrons used in a physics analysis while maintaining a high efficiency. Different use cases require differing amounts of stringency. An extreme example would be a resonant final state with four electrons. Due to the combinatorics, and the rarity of three-electron final state processes, it will be very difficult to have a false positive. In such a case it is best to maximize the identification efficiency. On the other extreme end, consider the final state with only a single electron, as seen in W^\pm boson production. There, due to the huge fake rate, it is best to maximize the purity at the cost of efficiency by using tighter identification criteria. The different working points for electron identification are standardized in the CMS experiment. Those relevant to this work are described below.

For the purpose of vetoing events with more than two leptons, the electrons are required to fulfill the so-called “*Veto*” working point. It consists of a series of requirements on the supercluster shape, impact parameter, and geometric distance between the electron track and the supercluster. The ratio of energy deposits in HCAL and ECAL is also used in the definition of the “*Veto*” ID. In this case, no veto for reconstructed photon conversions in the vicinity of the electron is applied.

Only electrons passing the “*Medium*” ID are considered for the Z candidate. The “*Medium*” ID imposes tighter cuts than the “*Veto*” ID and suppresses potential electrons from photon conversions. Electrons used to build the Z candidate must have a $p_T > 20$ GeV and be reconstructed in the tracker acceptance, i.e. $|\eta| < 2.5$. In addition to the ID requirements, there must be no tracker or global muon with at least 10 tracker hits reconstructed inside a cone of $\Delta R = 0.1$ built around the momentum of the electron candidate.

Lastly, the “*Tight*” ID is used to identify Tags for the tag-and-probe method used to determine the electron identification efficiencies, seen in Chapter 6.

Table 4.1 summarizes the identification criteria used for electrons.

4.2 Muons

4.2.1 Muon reconstruction

Muon tracks are reconstructed in the CMS Detector in both the silicon tracker and the muon spectrometer, resulting respectively in tracker tracks and standalone-muon tracks. Subsequently, these tracks inform two reconstruction approaches:

Requirement	Barrel $ \eta < 1.479$			Endcap $1.479 < \eta < 2.5$		
	“Veto”	“Medium”	“Tight”	“Veto”	“Medium”	“Tight”
$\sigma_{in in}$	< 0.0115	< 0.00998	< 0.00998	< 0.037	< 0.0298	< 0.0292
$\Delta\eta(SC, trk)$	< 0.00749	< 0.00311	< 0.00308	< 0.00895	< 0.00609	< 0.00605
$\Delta\phi(SC, trk)$	< 0.228	< 0.103	< 0.0816	< 0.213	< 0.045	< 0.0394
H/E_{SC}	< 0.356	< 0.253	< 0.0414	< 0.211	< 0.0878	< 0.0641
I_{rel}^e	< 0.175	< 0.0695	< 0.0588	< 0.159	< 0.0821	< 0.0571
$ 1/E_{SC} - 1/p $	< 0.299	< 0.134	< 0.129	< 0.15	< 0.14	< 0.13
$d_0(vtx)$ (cm)	< 0.05	< 0.05	< 0.05	< 0.1	< 0.1	< 0.1
$d_z(vtx)$ (cm)	< 0.1	< 0.1	< 0.1	< 0.2	< 0.2	< 0.2
Missing hits	≤ 3	≤ 1	≤ 1	≤ 3	≤ 1	≤ 1
pass conversion veto	✓	✓	✓	✓	✓	✓

Table 4.1: Electron ID requirements.

1. *Global Muon reconstruction (outside-in)*: starting from a standalone muon in the muon system, a matching tracker track is found and a *global-muon track* is fitted combining hits from the tracker track and standalone-muon track. At large transverse momenta ($p_T \gtrsim 200$ GeV/c), the global-muon fit can improve the momentum resolution compared to the tracker-only fit.
2. *Tracker Muon reconstruction (inside-out)*: in this approach, all tracker tracks with $p_T > 0.5$ GeV/c and $p > 2.5$ GeV/c are considered as possible muon candidates and are extrapolated to the muon system, taking into account the expected energy loss and the uncertainty due to multiple scattering. If at least one muon segment (i.e. a short track stub made of DT or CSC hits) matches the extrapolated track, the corresponding tracker track qualifies as a *tracker-muon track*. The extrapolated track and the segment are considered to be matched if the distance between them in local x is less than 3 cm or if the value of the pull for local x is less than 4. At low momentum (roughly $p < 5$ GeV/c) this approach is more efficient than the global muon reconstruction, since it requires only a single muon segment in the muon system, whereas global muon reconstruction is designed to have high efficiency for muons penetrating through more than one muon station.

The majority of muons from collisions (with sufficient momentum) are reconstructed either as a Global Muon or a Tracker Muon, or very often as both. A third, rare case is where both approaches fail and only a *standalone-muon track* is found [127]. Standalone muons suffer from low purity and poor momentum resolution, so they are not used in this work.

4.2.2 Muon identification variables

There are several sources of real or fake reconstructed muons in CMS:

1. Primary Interaction
2. Decay-in-Flight (Kaon, Pion)

3. Cosmic Muon

4. Hadronic Punch-Through

For the purposes of this work, we are interested in identifying real muons from a hard primary interaction, and rejecting the nonprompt or fake reconstructed muons. The chance that a kaon or pion is reconstructed as a muon increases along with its transverse momentum. It goes from less than one percent at low momentum, to ten percent at high momentum. Cosmic muons come from the atmosphere, not the interaction point, and are in general easy to deal with using vertexing. Hadronic punch-through results from imperfect absorption of hadronic cascades in the hadron calorimeter, which reach the muon stations.

Track-related quality cuts are effective against these backgrounds. We place requirements on the fraction of valid tracker hits, the number of valid pixel hits, and the number of tracker layers with measurement. For Global-reconstructed muons, we also compute the normalized global track χ^2 and compare the position match of the tracker and the standalone muon reconstruction algorithms.

Decays in flight introduce a kink in the muon candidate track. We use a kink-finding algorithm to reject such candidates, operating as follows. At each tracker layer, the extrapolated states from the two halves of the tracker tracks are compared to get a χ^2 . The maximum χ^2 across all layers is used as the per-track discriminator. This is effective even at low p_T , allowing rejection of 10-20% of such background while maintaining greater than 98% efficiency for real muons.

The segment compatibility is another useful discrimination quantity for the muons. It is computed by evaluating which crossed stations have matching muon statements, and the expected uncertainty of the extrapolated position due to multiple scattering.

Analogous to the electrons, for muons we also compute the transverse and longitudinal impact parameters, and a corrected relative isolation quantity, I_{rel}^μ . For the muon isolation, in the same manner as for electrons, a cone of $\Delta R = 0.4$ is built to compute the flux of particle flow candidates, the “delta-beta” correction is applied to correct for pileup contamination. This correction is achieved by subtracting half the sum of the p_T of the charged particles in the cone of interest but with particles not originating from the primary vertex. The muon isolation is therefore defined as:

$$I_{\text{rel}}^\mu = \frac{1}{p_T} [I_{\text{ch}} + \max(I_{\text{nh}} + I_g - 0.5 \cdot I_{\text{chPU}}, 0)] \quad (4.4)$$

The factor 0.5 corresponds to an approximate average of neutral to charged particles and has been measured in jets in [126].

4.2.3 Muon identification working points

Similar to the electron identification working points described above, a variety of muon identification working points are designed for different use cases. The Medium muon algorithm allows for both global and tracker muons, with different requirements

for each. It is used in this work for the reconstruction of Z boson candidates decaying to muons. The Tight muon algorithm only allows for global muons. It is used to identify Tags for measuring muon identification efficiency in the tag-and-probe method of Chapter 6. The specific cut values for the Medium and Tight algorithms are quoted in Table 4.2.

Requirement	<i>Medium (global)</i>	<i>Medium (tracker)</i>	<i>Tight</i>
Reconstruction	Global muon	Tracker muon	Global muon
Fraction of valid tracker hits	> 0.49	> 0.49	-
Segment compatibility	> 0.303	> 0.451	-
Track kink	< 20	-	-
Normalized global track χ^2	< 3	-	< 10
Tracker-standalone position match	< 12	-	-
$d_0(\text{vtx})$ (cm)	-	-	< 0.2
$d_z(\text{vtx})$ (cm)	-	-	< 0.5
Number of valid pixel hits	-	-	≥ 1
Tracker layers with measurement	-	-	≥ 5
I_{rel}^μ	< 0.15	< 0.15	< 0.15

Table 4.2: Muon ID requirements.

4.3 Jets

Due to the nature of QCD, it is impossible to observe a free quark or gluon in the final state. Suppose two color charged objects are created in a collision and begin to move apart. The QCD interaction between them is transmitted via gluons. Since gluons themselves carry color charge, the force between the particles does not fall off as their separation increases. The gluon field maintaining this force over the ever-increasing distance is contained in a narrow flux tube. As the distance continues to increase, it becomes energetically favorable to produce a new quark-antiquark pair instead of further lengthening the flux tube. Through this so-called “color confinement” process, many quarks and antiquarks are formed. In turn, it is energetically preferred for them to assemble into color-neutral configurations of multiple quarks. This is known as hadronization. The result of this is that, in a hard process producing a high momentum quark, the observable experimental signature of that quark is a collimated spray of hadrons. That spray is called a (hadronic) jet.

Much work has been done on the reconstruction and classification of jets. This is briefly described below. However, the focus of this work is not in the predominantly hadronic final states.

4.3.1 Jet reconstruction

Jets are reconstructed from all the particle candidates using the anti- k_t clustering algorithm [128] with a distance parameter of 0.4, as implemented in the FASTJET package [129, 130]. The reconstruction may be seeded using all reconstructed particle candidates after having removed the charged hadron candidates which are not associated

to the primary vertex of the event (charge hadron subtracted AK4PFchs). The energy of the reconstructed jets is corrected in 3 steps: L1FastJet (for pileup/underlying event subtraction), L2 (for relative corrections), and L3 (for absolute scale corrections). For data, an extra residual correction is included in the absolute scale correction, derived by the JetMET working group within the CMS collaboration.

An extra correction is applied for the simulated jets in order to reproduce the measured jet energy resolution. For each jet the transverse momentum is smeared using the transverse momentum of the generator level matched jet and the measured Data/MC resolution ratio. The correction transformation is given by:

$$p_T \rightarrow \max [0, p_T^{\text{gen}} + c \cdot (p_T - p_T^{\text{gen}})] \quad (4.5)$$

in which $c = \sigma_{\text{data}}/\sigma_{\text{MC}}$ are the data-to-MC resolution scale factors.

4.3.2 Jet identification

We consider for analysis all jets with $p_T > 20$ GeV and $|\eta| < 5$ passing a set of loose identification requirements given in Table 4.3. Jets that are within $\Delta R < 0.4$ of one of the identified leptons are disregarded, this is referred to as jet cleaning. The number of jets is used as a selection variable. Here, we define it as how many of these nominal jets have $p_T > 30$ GeV and $|\eta| < 2.4$.

Quantity	Requirement
Neutral Hadron Fraction	< 0.99
Neutral EM Fraction	< 0.99
Number of Constituents	> 1
Charged Hadron Fraction	> 0
Charged Multiplicity	> 0
Charged EM Fraction	< 0.99

Table 4.3: Loose jet identification criteria for jets having $|\eta| < 2.4$.

4.3.3 b-tagging

Jets originating from b -quark fragmentation (b -jets) are identified by “ b -tagging.” B -tagging is useful for enhancing physics signatures with one or more boosted b -quarks in the final state. Such signatures include flavor changing decays of the top quark, and resonant Higgs or Z boson decays into $b\bar{b}$. In this work, the b -tagging technique employed is based on the “combined secondary vertex” CSVv2 algorithm [131]. The algorithm provides high efficiency for b -jets, with a low probability of light-flavor jet misidentification. The B-Tagging and Vertexing Group within the CMS Experiment is responsible for calibrating the algorithm working points. Loose, medium, and tight working points of the CSVv2 algorithm were calibrated to provide misidentification

probabilities of 10%, 1%, and 0.1%, respectively. For the studies presented here, b-tagging serves the purpose of rejecting combinatorial background processes involving top quark production. The medium and tight CSVv2 working points are used, corresponding to values of 0.8484 and 0.9535.

4.4 Photons

Photon candidates are reconstructed from energy deposits in the ECAL using algorithms that constrain the clusters to the size and shape expected from a photon [132]. The identification of the candidates is based on shower-shape and isolation variables, and depends on whether the energy deposit was in the ECAL barrel or endcaps. For isolated photons, scalar sums of the p_T of PF candidates within a cone of $\Delta R < 0.3$ around the photon candidate are required to be below the bounds defined. Only the PF candidates that do not overlap with the EM shower of the candidate photon are included in the isolation sums. The photon candidates used in this analysis are required to have a minimum p_T of 15 GeV and to be within $|\eta| < 2.5$ passing the loose identification criteria given in Table 4.4.

Quantity	ECAL barrel req.	ECAL endcap req.
Full 5x5 $\sigma_{i\eta i\eta}$	< 0.0103	< 0.0301
H/E	< 0.0597	< 0.0481
charged hadron isolation	< 1.295	< 1.011
neutral hadron isolation	$< 10.92 + (0.0148 \text{ GeV}^{-1})p_T + (1.7 \times 10^{-5} \text{ GeV}^{-2})p_T^2$	$< 5.931 + (0.0163 \text{ GeV}^{-1})p_T + (1.4 \times 10^{-5} \text{ GeV}^{-2})p_T^2$
photon isolation	$< 3.630 + (0.0047 \text{ GeV}^{-1})p_T$	$< 6.641 + (0.0034 \text{ GeV}^{-1})p_T$
Conversion safe electron veto	Yes	Yes

Table 4.4: Loose photon identification criteria.

4.5 Particle-flow reconstruction

The particle-flow (PF) event reconstruction algorithm [133] is used. It is designed to leverage information from all CMS Detector components to reconstruct and identify individual particles, namely: electrons, muons, photons, and charged and neutral hadrons. This collection of individual particles is used for reconstructing jets, determining the missing transverse energy, reconstructing tau leptons from their decay products, identifying b-jets, and more.

The CMS Detector is well suited for this reconstruction algorithm. The strong magnetic field and large silicon tracker allow us to reconstruct charged particle tracks with high efficiency and low fake rate at transverse momenta as low as 150 MeV, at pseudorapidities as large as $|\eta| = 2.6$. The reconstructed vertex of origin with the largest value of summed track p_T^2 is taken to be the primary proton-proton interaction vertex.

Electrons are reconstructed by a combination of a track and of several energy deposits in the ECAL, from the electron itself and from possible bremsstrahlung photons radiated by the electron in the tracker material on its way to the ECAL. Muons are reconstructed and identified inside and outside of jets with very large efficiency and purity from a combination of the tracker and muon chamber information. Photons are reconstructed with an excellent energy resolution by the hermetic electromagnetic calorimeter at pseudorapidities as large as $|\eta| = 3.0$. Together with the magnetic field, the ECAL granularity allows photons to be separated from charged-particle energy deposits by way of shower shape discrimination. It is functional even in jets with transverse momenta of several hundred GeV.

Charged and neutral hadrons deposit their energy in the HCAL. The granularity of the HCAL is 25 times coarser than that of the ECAL. This does not allow charged and neutral hadrons to be spatially separated in jets with transverse momentum above 100 GeV. But the combined ECAL-HCAL system has hadron energy resolution of around 10% at 100 GeV. This allows neutral hadrons to be detected as an energy excess on top of the energy deposited by the charged hadrons pointing to the same calorimeter cells. Charged hadrons are reconstructed with the superior angular and energy resolution of the tracker. Particles with pseudorapidities in the range $3 < |\eta| < 5$ are more coarsely measured with the HF forward calorimeter.

The presence of neutrinos and other weakly-interacting particles can be detected by formulating the missing transverse energy, described below.

4.6 Missing transverse energy

The missing transverse momentum vector, \vec{p}_T^{miss} , is defined as the projection of the negative vector sum of the momenta of all reconstructed PF candidates in an event onto the plane perpendicular to the beams. Its magnitude is referred to as E_T^{miss} . Since all visible objects contribute to this quantity, the mismeasurement or failed reconstruction of any object adversely affects its accuracy. Several event-level filters are applied to discard events with anomalous E_T^{miss} arising from specific well-understood issues with the detector components or event reconstruction [134]. Jet energy corrections are propagated to the missing transverse momentum by adjusting the momentum vector of the PF candidate constituents of each reconstructed jet. Any particle which is produced outside the acceptance of the relevant detector subsystems will also be counted towards missing energy, limiting the resolution.

Chapter 5

Data samples

5.1 Experimental data

This analysis uses a sample of pp collisions collected in 2016 with the CMS experiment at the LHC at $\sqrt{s} = 13$ TeV. Five primary datasets are used to ensure a very high trigger efficiency: MuEG, DoubleMuon, DoubleElectron, SingleMuon, and SingleElectron. Only the luminosity sections are used in which all detector subsystems reported accurately. The so-called “good run list” is furnished by the data certification working group.

The total integrated luminosity with the associated uncertainty is $35.9 \pm 0.9 \text{ fb}^{-1}$.

5.1.1 Silicon strip hit efficiency loss

During 2015, a reduced silicon strip hit efficiency and a reduced tracking efficiency were observed. It was found to be correlated with the increase of the LHC instantaneous luminosity. This is due to the effect of highly ionizing particles (HIPs) which were studied in test beams before the tracker construction. A HIP saturates the readout chips, or APVs, of several of the strips from the hit cluster. The baseline is shifted toward negative values. The chips are fully blinded in the next few bunch crossings, and remain partially blind for some time after, until they fully recover.

In total, as the instantaneous luminosity continued to increase, we observed a lower cluster charge, lower signal-to-noise ratio, lower hit efficiency, shorter tracks, and lower track efficiency. The tracker modules most affected were wider and of higher occupancy. Any particles identified using tracks were affected by the so-called “HIP effect.” In particular, the electrons and muons are reconstructed from tracks and they are a crucial part of this work.

The data taken in 2016 suffered from the HIP effect until a task force was convened to mitigate the decline in tracking performance. The solution was found in the electronics parameters of the silicon strip readout chips. In particular, the preamplifier feedback voltage bias (VFP) affects the duration of the signal at the output of the preamplifier. Reducing the VFP from 0.3 Volts to 0 Volts was found to mitigate the HIP effect.

These 2016 data were subdivided into Run Eras labeled alphabetically. The Run Eras used in this work are B through H.

The HIP mitigation fix was deployed close to the demarcation of Run Eras F and G, in the data run numbered 278803. Run Era F comprised runs numbered (277772, 278808) and Run Era G comprised runs numbered (278820, 280385). Due to the era-dependent nature of the HIP effect, which had a significant effect on the lepton identification, separate empirical corrections for leptons were derived. They are discussed later in Chapter 6. For brevity, the corrections intended to represent the data before the fix are denoted as “B-F” or “BCDEF”, despite the fact that the mitigation did not occur precisely at the Run Era changeover. Similarly, the corrections representing the data after the fix are denoted as “G-H” or “GH”.

5.2 Simulated samples

Several Monte Carlo (MC) event generators are used to simulate the signal and background processes. For all processes, the detector response is simulated using a detailed description of the CMS Detector, based on the GEANT4 package [135], and event reconstruction is performed with the same algorithms as used for data. The simulated samples include additional interactions per bunch crossing (pileup). The simulated events are weighted so that the pileup distribution matches the data, with an average pileup of about 25 interactions per bunch crossing.

5.2.1 Standard Model processes

Resonant Z boson background processes (WZ, ZZ, tribosons, etc.) are estimated using Monte Carlo (MC) samples. Nonresonant background processes ($t\bar{t}$, tW, WW, $Z/\gamma^* \rightarrow \tau^+\tau^-$, etc.) are estimated using $e\mu$ data events.

The WZ and ZZ processes, via $q\bar{q}$ annihilation, are generated at next-to-leading-order (NLO) with POWHEG2.0 [136, 14, 137, 138]. The $gg \rightarrow ZZ$ process is simulated with MCFM [139]. The $Z\gamma$, $t\bar{t}Z$, WWZ, WZZ, and ZZZ processes are generated with MADGRAPH5_AMC@NLO [140]. The signal samples are simulated using MADGRAPH5_AMC@NLO at next-to-leading-order (NLO), MADGRAPH5 at leading-order (LO), and POWHEG at NLO. The default MC generator is MADGRAPH5_AMC@NLO. The PYTHIA8 [141, 142] package is used for parton showering, hadronization, and the underlying event simulation, with tune CUETP8M1. The NNPDF 3.0 [98] set is used as the default set of parton distribution functions (PDFs). Simulated datasets from the RunIISummer16MiniAODv2 campaign are used.

The processed dataset names and cross sections for the Standard Model processes considered in the analysis are shown in Table 5.1. The table is categorized in the following way: Resonant Diboson, Triboson, Nonresonant, and Drell-Yan. In general, the cross sections are calculated using a small sample of generated events. A notable exception is the $t\bar{t} \rightarrow 2\ell 2\nu 2b$ process, where the state-of-the-art NNLO calculation is used [143]. The factors coming after the first cross section number represent either higher order corrections or branching ratios and combinatorics. For example, the

factor of 1.109 applied to the WZ process is the aforementioned electroweak NLO correction factor. The factor of 2.3 applied to the gluon-induced ZZ processes is a QCD NLO correction factor. The extra factors on the $t\bar{t} \rightarrow 2\ell 2\nu 2b$ process represent the leptonic decay ratio of the W^\pm boson (0.1086) and the $3 \times 3 = 9$ possible lepton flavor combinations.

Process	Simulated sample name	Cross section [pb]
$WZ \rightarrow 3\ell\nu$	WZTo3LNu_TuneCUETP8M1_13TeV-powheg-pythia8	4.42965×1.109
$WZ \rightarrow 2\ell 2q$	WZTo2L2Q_13TeV_amcatnloFXFX_madspin_pythia8	5.595×1.109
$ZZ \rightarrow 4\ell$	ZZTo4L_13TeV_powheg_pythia8	1.256
$gg \rightarrow ZZ \rightarrow 4\mu$	GluGluToContinToZZTo4mu_13TeV_MCFM701_pythia8	0.001586×2.3
$gg \rightarrow ZZ \rightarrow 4e$	GluGluToContinToZZTo4e_13TeV_MCFM701_pythia8	0.001586×2.3
$gg \rightarrow ZZ \rightarrow 4\tau$	GluGluToContinToZZTo4tau_13TeV_MCFM701_pythia8	0.001586×2.3
$gg \rightarrow ZZ \rightarrow 2\mu 2e$	GluGluToContinToZZTo2mu2e_13TeV_MCFM701_pythia8	0.001586×2.3
$gg \rightarrow ZZ \rightarrow 2\mu 2\tau$	GluGluToContinToZZTo2mu2tau_13TeV_MCFM701_pythia8	0.001586×2.3
$gg \rightarrow ZZ \rightarrow 2e 2\tau$	GluGluToContinToZZTo2e2tau_13TeV_MCFM701_pythia8	0.001586×2.3
$gg \rightarrow ZZ \rightarrow 2e 2\mu$	GluGluToContinToZZTo2e2mu_13TeV_MCFM701_pythia8	0.001586×2.3
$gg \rightarrow ZZ \rightarrow 2\mu 2\nu$	GluGluToContinToZZTo2mu2nu_13TeV_MCFM701_pythia8	0.001586×2.3
$ZZ \rightarrow 2\ell 2\nu$	ZZTo2L2Nu_13TeV_powheg_pythia8	0.564
$ZZ \rightarrow 2\ell 2q$	ZZTo2L2Q_13TeV_amcatnloFXFX_madspin_pythia8	3.220
$Z + \gamma$	ZGTo2LG_13TeV_amcatnloFXFX_pythia8	117.864
WWZ	WWZ_TuneCUETP8M1_13TeV_amcatnlo_pythia8	0.05565
WWZ	WWZ_TuneCUETP8M1_13TeV_amcatnlo_pythia8	0.16510
ZZZ	ZZZ_TuneCUETP8M1_13TeV_amcatnlo_pythia8	0.01398
$Z \rightarrow \tau\tau \rightarrow e\mu$	DYJetsToTauTau_ForceMuEleDecay_M-50_TuneCUETP8M1_13TeV-amcatnloFXFX-pythia8	$1921.8 * (0.1741 + 0.1783)^2$
$qq \rightarrow WW \rightarrow 2\ell 2\nu$	WWTo2L2Nu_13TeV-powheg	$(118.7-3.974) \times 0.1086 \times 0.1086 \times 9$
$gg \rightarrow WW \rightarrow 2\ell 2\nu$	GluGluWWTo2L2Nu_MCFM_13TeV	$(3.974 \times 0.1086 \times 0.1086 \times 9 \times 1.4$
$t\bar{t}Z(\ell\ell + \nu\nu)$	TTZToLLNuNu_M-10_TuneCUETP8M1_13TeV-amcatnlo-pythia8	0.2529
$t\bar{t}Z(q\bar{q})$	TTZToLLNuNu_M-10_TuneCUETP8M1_13TeV-amcatnlo-pythia8	0.5297
$t\bar{t}W(\ell\nu)$	TTWJetsToLNu_TuneCUETP8M1_13TeV-amcatnloFXFX-madspin-pythia8	0.2043
$t\bar{t}W(q\bar{q})$	TTWJetsToQQ_TuneCUETP8M1_13TeV-amcatnloFXFX-madspin-pythia8	0.4062
$t\bar{t} \rightarrow 2\ell 2\nu 2b$	TTTo2L2Nu_13TeV-powheg	$831.76 \times 0.1086 \times 0.1086 \times 9$
tW	ST_tW_top_5f_inclusiveDecays_13TeV-powheg-pythia8	35.6
$\bar{t}W$	ST_tW_antitop_5f_inclusiveDecays_13TeV-powheg-pythia8	35.6
$t\bar{t}Z(\ell\ell + \nu\nu)$	DYJetsToLL_M-50_TuneCUETP8M1_13TeV-amcatnloFXFX-pythia8	2008×3
$t\bar{t}Z(q\bar{q})$	DYJetsToLL_M-10to50_TuneCUETP8M1_13TeV-amcatnloFXFX-pythia8	2008×3
$t\bar{t}W(\ell\nu)$	DYJetsToLL_M-50_TuneCUETP8M1_13TeV-madgraphMLM	2008×3
$t\bar{t}W(q\bar{q})$	ZToLL_NNPDF30_13TeV-powheg_M_50_120	1975×2
$Z/\gamma^* \rightarrow \ell^+\ell^-$	DYJetsToLL_Pt-50To100_TuneCUETP8M1_13TeV-amcatnloFXFX-pythia8	375
	DYJetsToLL_Pt-100To250_TuneCUETP8M1_13TeV-amcatnloFXFX-pythia8	86.5
	DYJetsToLL_Pt-250To400_TuneCUETP8M1_13TeV-amcatnloFXFX-pythia8	3.32
	DYJetsToLL_Pt-400To650_TuneCUETP8M1_13TeV-amcatnloFXFX-pythia8	0.449
	DYJetsToLL_Pt-650ToInf_TuneCUETP8M1_13TeV-amcatnloFXFX-pythia8	0.0422

Table 5.1: Processed dataset names and cross sections for the Standard Model processes considered in the analysis.

5.2.2 Dark matter hypotheses

Samples of simulated DM particle events in the simplified model are generated using MADGRAPH5_AMC@NLO 2.2.2 [140] at leading order (LO) and matched to PYTHIA 8.205 [144] using tune CUETP8M1 for parton showering and hadronization [145, 146]. The factorization and renormalization scales are set to the geometric mean of $\sqrt{p_T^2 + m^2}$ for all final-state particles [140, 99], where p_T and m are the transverse momentum and mass of each particle.

For the simplified model of DM production, couplings are chosen according to the recommendations in Ref. [147]. The coupling g_χ is set to one. For g_q , values of 1.0 and 0.25 are considered. The width of the mediator is assumed to be determined exclusively by the contributions from the couplings to quarks and the DM particle χ . Under this assumption, the width ranges 1–5% (30–50%) of the mediator mass for $g_q = 0.25$ ($g_q = 1.00$). The signal simulation samples with $g_q = 1.0$ are processed using the detector simulation described below. Signal predictions for $g_q = 0.25$ are obtained by applying event weights based on the E_T^{miss} distribution at the generator level to the fully simulated samples with $g_q = 1.0$. This procedure takes into account the nontrivial dependence of the mediator width on the coupling choice [147]. The exact dependence of the width on the model parameters is reported in [147].

Events for the ADD extra-dimension scenario are generated at LO using an effective field theory (EFT) implementation in PYTHIA 8 [148, 149]. Event samples are produced for $M_D = 1, 2$ and 3 TeV, each with $n = 2, 3, 4, 5, 6, 7$. The signal is truncated for $\hat{s} > M_D^2$ in order to ensure the validity of the EFT.

The events for the unparticle model are generated at leading-order with PYTHIA 8 [148, 149] assuming a cutoff scale $\Lambda_U = 15$ TeV, using tune CUETP8M1 for parton showering and hadronization. We evaluate other values of Λ_U by rescaling the cross sections as needed. The parameter Λ_U acts solely as a scaling factor for the cross section and does not influence the kinematic distributions of unparticle production [149].

The ZH production modes via $q\bar{q}$ annihilation and gluon-gluon fusion are modeled the same way as for the WZ and ZZ processes.

A comparison of kinematic spectra for various signal models is shown in Figs. 5-1 and 5-2.

5.3 Triggers

The triggers used in this work are the so-called “single and double lepton triggers.” In general, they are designed to pick out events with one or two electrons or muons, with momentum of 20 GeV or more. The overall trigger efficiency is larger than 99% and consistent with 1 after all other selection requirements are applied.

Electron triggers start from Level-1 ECAL primitive objects, also known as the Level-1 e/γ seeds [120]. In the ECAL barrel, five strips of five crystals (along the azimuthal direction) are combined into trigger towers forming a 5×5 array of crystals. The transverse energies detected by the crystals in a single trigger tower are summed into a trigger primitive by the front-end electronics and sent to off-detector trigger

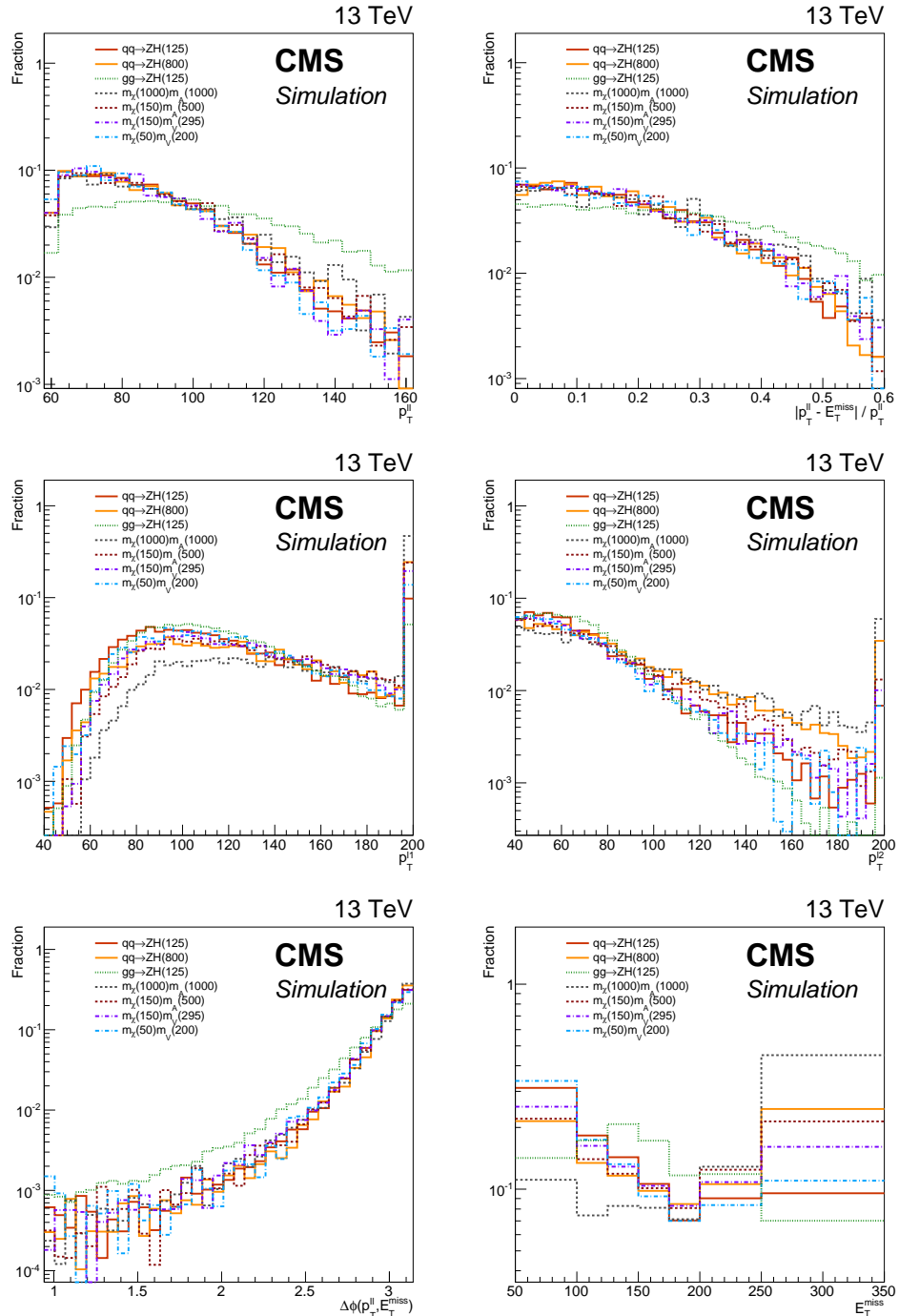


Figure 5-1: Comparison of kinematic distributions for a variety of the signal hypotheses. The full distributions are normalized to 1. Top left: dilepton p_T (in GeV) in $Z \rightarrow \ell^+\ell^-$ events with $p_T^{\ell\ell} > 60$ GeV and $E_T^{\text{miss}} > 40$ GeV. Top right: $|E_T^{\text{miss}} - p_T^{\ell\ell}| / p_T^{\ell\ell}$ in $Z \rightarrow \ell^+\ell^-$ events with $p_T^{\ell\ell} > 60$ GeV and $E_T^{\text{miss}} > 40$ GeV. Center left: leading lepton p_T (in GeV) at final selection level. Center right: subleading lepton p_T (in GeV) at final selection level. Bottom left: $\Delta\phi_{\ell\ell-E_T^{\text{miss}}}$ at final selection level. Bottom right: the final E_T^{miss} shape used for the shape analysis.

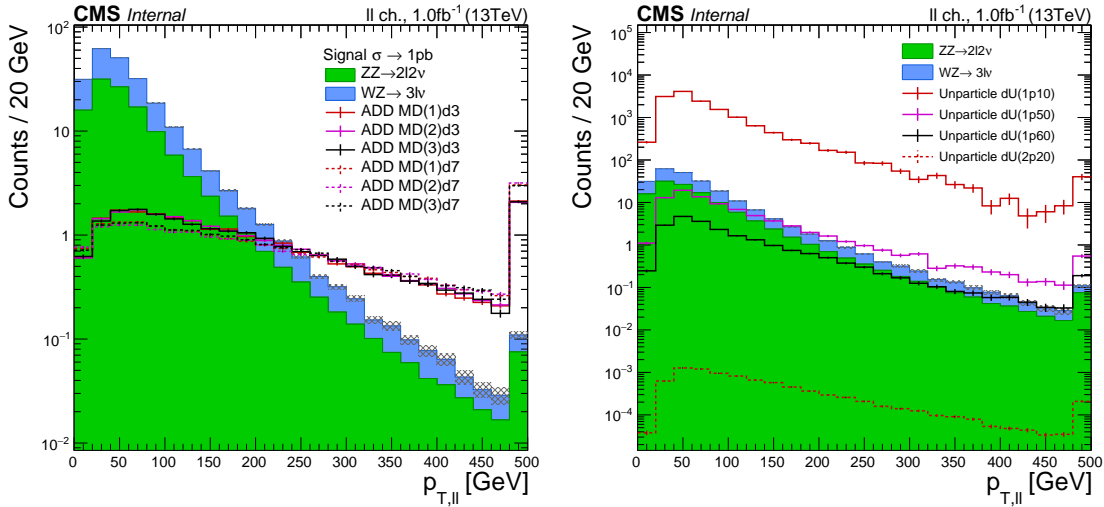


Figure 5-2: Comparison of reconstructed dilepton transverse momentum ($p_{\text{T}}^{\ell\ell}$) distributions for ADD (left) and unparticle (right) models. For the ADD models, cross sections are normalized to 1pb.

concentrator cards via optical fibers. In the ECAL endcaps, each front-end board computes 5 partial sums of 5 crystals called pseudo-strips, then sends them to the trigger concentrator card which completes the primitive calculation. Then, events selected with the Level-1 seed are subject to additional requirements in the High-Level Trigger including calorimetric isolation requirements.

The Level-1 muon trigger system is informed by all three muon detector subsystems (DTs, CSCs, and RPCs) described in Section 3.2.4. Local track segments are formed within the DTs and CSCs. Detector hits on the RPCs are used directly for recognition of muon trigger primitive candidates. The global muon trigger synchronizes and reconciles these pieces of information from the regional muon primitives to assign momenta, track quality, et cetera to the muon candidates. Similar to electron primitives, muon primitives passing the L1T also must pass additional requirements such as isolation in the HLT.

5.4 Corrections to the simulated samples

5.4.1 Pileup reweighting

Besides the main hard process in a proton collision, secondary interactions from the other protons in the bunches are also relevant. These are called pileup interactions. The particles produced from pileup interactions are observed in the detector. Accurate tracking allows us to associate their final products with distinct interaction vertices. This is particularly important for jets and missing energy, since additional jets can be observed in a physics event originating from a pileup interaction.

Pileup concerns the simulated samples in the following way. The pileup distribution is the distribution of the number of pileup interactions in physics events. The simulated samples are generated with a pileup distribution close to what is expected

in the experimental data. Meanwhile, the actual pileup distribution in the collected data sample is measured [150]. To match the expected number of pileup interactions in simulation with data, the number of reconstructed vertices is reweighted to match the distribution in data. This carries an inherent uncertainty due to the estimation of the minimum bias cross section. A cross section of 69 millibarns with an uncertainty of 5% is used.

The lepton efficiency studies shown in Chapter 6 split the data sample in two, at the point where the HIP effect discussed in Section 5.1.1 was mitigated. For these studies, the pileup profile of the relevant simulated samples was reweighted to the pileup profiles of the two subsets of the data samples, which were substantially different.

5.4.2 Trigger efficiencies

The efficiency of each of the single and double lepton triggers is determined by measuring the fraction of events which pass the trigger in an unbiased control sample. Such an unbiased sample is obtained by using missing transverse energy triggers, as has been previously done in Ref. [151]. Provided sufficient statistics, the trigger efficiency is parameterized as a function of the transverse momentum and pseudorapidity of the lepton or leptons.

The so-called “trigger soup” of all of these triggers put together has an efficiency consistent with 1. The ratio of trigger efficiency in data versus simulation is also consistent with 1. For sake of brevity, the exact numbers are omitted. Any systematic uncertainty from the determination of the trigger efficiency is negligible in all of the studies presented in this work.

5.4.3 Lepton selection efficiencies

One of the crucial elements in the analysis is the determination of the lepton efficiency scale factors. Algorithms for selecting good leptons can have different efficiencies in data and simulation. The ratio of the selection efficiencies in data and simulation constitutes the scale factor. The scale factors are computed in many bins of electron and muon kinematics to account for relevant dependent effects. Then, the simulated event weights are multiplied once by the appropriate scale factor for every lepton identified in that event. A detailed discussion of the methodology to determine these efficiencies is given in Chapter 6.

5.4.4 Lepton momentum scale and resolution

The lepton momentum scale and resolution are affected by detector misalignment and miscalibration. The calibration procedure includes corrections to both data and simulation. In data momentum corrections are applied differentially in p_T , η , and charge in order to match the value of known resonances. These corrections are derived using a multivariate regression technique. For more details see Ref. [152]. In simulation,

additional stochastic smearing is applied to match the observed resolution of the Z boson resonance peak.

For muons, these corrections are known as the Rochester corrections. The additional effect of uncertainty in the magnetic field is considered. The methodology and validation is provided in Ref. [153].

5.4.5 Higher order corrections

The diboson MC samples, including the invisible Higgs signal, are initially generated at electroweak leading-order.

The ZZ and WZ processes are corrected to next-to-leading order in electroweak, and next-to-next-to-leading order in QCD. For further details, see Chapter 8.

For the invisible Higgs boson signal, we apply a differential NLO electroweak correction as a function of the transverse momentum of the Z boson. This correction only concerns the Drell-Yan-like ZH production via $q\bar{q}$ annihilation as pictured in the upper left of Figure 2-8. The small contributions to the overall ZH cross section from the gluon-induced, photon-induced, and top-loop production are not corrected in this way.

Chapter 6

Efficiency of lepton trigger, reconstruction, and identification

After reconstructing leptons in CMS using the information from the detector subsystems, further offline requirements are applied for the purpose of high quality and low background lepton identification. The choice of these requirements depends on the analysis, and several well-defined working points are optimized and released by the relevant Physics Object Groups. The figure of merit for lepton identification is the efficiency, and the various working points are usually described qualitatively in terms of “tightness,” with a tighter selection corresponding to lower efficiency and higher purity. In this note we refer to the whole slew of offline requirements applied to reconstructed leptons under the umbrella term of identification, including quantities such as relative isolation.

Previously, at lower center-of-mass energies, resonant leptonic decays of the J/ψ meson were used to measure lepton identification efficiency. In Run II at the LHC, we make use of the large cross section of the Z boson resonance and observe its leptonic decays to extract the lepton efficiencies for a wide range of lepton energies and rapidity; while the J/ψ meson is also still used for efficiency studies at lower transverse momentum. This chapter describes how the efficiency is measured in data and simulation by studying dilepton events where the dilepton mass is close to the Z boson resonance peak at 91.1876 GeV. The ensuing discussion presents results for the “Medium 2016” cut-based identification algorithm.

6.1 Event selections for the tag-and-probe method

The so-called “tag-and-probe” selection consists of a high purity $Z/\gamma^* \rightarrow \ell^+\ell^-$ selection with a well-identified tag lepton and an opposite sign probe. The tag electron (muon) must pass the tight identification, have transverse momentum greater than 30 (25) GeV, have $|\eta| < 2.5$ (2.4), and be matched to a lepton trigger object. The probe electron must have transverse momentum greater than 10 GeV and $|\eta| < 2.5$. For the probe muons, we consider a collection of general tracks. These tracks must have transverse momentum greater than 10 GeV, $|\eta| < 2.4$, and a vertex whose lon-

gitudinal position is within 4 cm of that of the tag. This affords us a loose collection of probe candidate electrons or muons without biasing the measurement.

The selection also includes a truth-matching procedure when applied to simulated Drell-Yan samples, so that all simulated reconstructed dileptons come from leptonic Z decays. This is necessary because fake electrons and muons can be produced and reconstructed in the simulation. The reconstructed leptons must each have a small angular separation $\Delta R = \sqrt{\Delta\phi^2 + \Delta\eta^2}$ less than 0.3 with a final-state lepton of the same flavor at generator level. For muons, the generator-level and reconstructed transverse momenta must also be compatible within 10%.

6.1.1 Probe multiplicity calculation

In order to increase the signal purity of the muon selection, we perform a probe multiplicity calculation to remove combinatorial background. The track collection as described above is considered, albeit with a lowered transverse momentum cut of 3 GeV. Then, the number of opposite sign tag-track pairs having system mass above 60 GeV is counted for each tag; this gives the probe multiplicity. Any muon tags having probe multiplicity greater than 1 are not considered in the ensuing tag and probe analysis.

6.2 Control samples for the lepton efficiencies

Two independent data samples are chosen to faithfully represent the background distributions for the tag-and-probe fitting methods. They are defined below.

6.2.1 Lepton pion selection

The mass spectrum of the combinatorial background in the Z selection can be modeled well by selecting essentially random pairs of tag leptons and charged hadrons whose system mass falls within the relevant window. We select a tag electron (muon) exactly the same as before, along with a PF charged hadron having $p_T > 10$ GeV and $|\eta| < 2.5$ which must originate from the primary event vertex.

The charged hadrons selected in such a way are predominantly but not exclusively pions. The CMS Detector does not have charged hadron particle ID capabilities beyond $\frac{dE}{dx}$, which is ineffective for such boosted particles. Thus, we have little way of knowing if they are really pions instead of kaons, protons, or something even more charming. We refer to them using π^\pm as shorthand.

To obtain a data sample orthogonal to the Z selection, and to suppress contamination by Z events, we remove events from the $\ell^\pm\pi^\pm$ selection with the following cuts:

- Reject events containing a tag electron (muon) and another reconstructed electron (muon)

- Reject π^\pm probes with separation ΔR less than 0.3 with any reconstructed electron or muon
- Require the same charge assignment for the tag lepton and the pion probe

Furthermore, due to low event yields in this selection at higher probe energies for the electron case, we use an η -inclusive form of this selection to build the shapes that are used in each bin of probe η for probes with $p_T > 50$ GeV.

The $\ell^\pm\pi^\pm$ selection is effective at modeling the background combinatorics, largely arising from QCD and the W+jets process. However, it fails to accurately model the lower energy contribution from the non-resonant background processes e.g. $t\bar{t} \rightarrow 2\ell 2\nu 2b$ and $Z/\gamma^* \rightarrow \tau^+\tau^-$.

6.2.2 Electron muon selection

The Z(ee) background can also be modeled by selecting a muon tag along with an electron probe. In this case, we choose tags from the muons passing tight identification, with kinematic cuts the same as the electron tags, but the probes are chosen as in the Z(ee) selection. The opposite sign charge requirement is dropped. As with the $\ell^\pm\pi^\pm$ selection, we also use an η -inclusive selection for the $e\mu$ -derived shape at probe $p_T > 50$ GeV. The shape obtained this way is effective for lower energy electrons, but does not accurately model the electron tag kinematics nor the lepton fake rate at higher energies.

Thus, the most effective data-driven background shape for the Z(ee) selection was determined to be a linear combination of the $\ell^\pm\pi^\pm$ and $e\mu$ selections, with the relative contribution a floating parameter. This allows the efficiency extraction procedure to empirically determine what would otherwise be a complicated expression of the lepton fake rates, the lepton efficiencies, the cross-sections of contributing background processes, and other factors.

Figure 6-1 shows how the true background shape is approximated using this linear combination of the two data-driven shapes.

6.3 Fitting techniques

The data efficiency is determined by performing a combined signal plus background fit to each of the passing and failing categories, in each of the bins of kinematic phase space. The efficiency extraction fit provides the number of signal Z events in the passing and failing categories by measuring the relative contribution of signal and background. The nominal values for the signal and background yields in data are fit using a signal hypothesis of truth-matched Drell-Yan Monte Carlo templates (as described in Section 6.1), convoluted with a Gaussian resolution function which allows for widening and shifting of the simulated peak position. The background hypothesis is a fixed shape derived from data, as described in Section 6.2. In the dielectron fits, the relative contribution of $e^\pm\pi^\pm$ versus $e\mu$ data is a free parameter in the fit.

The binning choice for the probe leptons is the following:

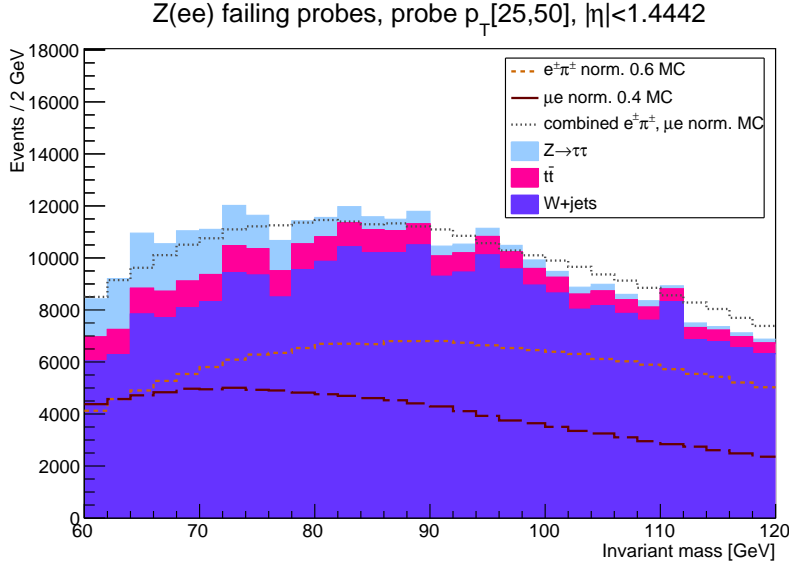


Figure 6-1: Simulation of the true background shape, compared with the shapes of the $\ell^\pm\pi^\pm$ selection, the $e\mu$ selection, and a linear combination of the two. The background is normalized to the integrated luminosity of the 2016 dataset.

- Probe electron p_T : {10, 15, 20, 25, 30, 35, 40, 42, 44, 46, 48, 50, 55, 60, 70, 100} GeV;
- Probe electron η : {-2.5, -2.4, -2.3, -2.2, -2.1, -2.0, -1.8, -1.566, -1.4442, -1.2, -1, -0.8, -0.6, -0.4, -0.2, 0, 0.2, 0.4, 0.6, 0.8, 1, 1.2, 1.4442, 1.566, 1.8, 2.0, 2.1, 2.2, 2.3, 2.4, 2.5};
- Probe muon p_T : {10, 15, 20, 25, 30, 35, 40, 45, 50, 55, 60, 120} GeV;
- Probe muon η : {-2.4, -2.1, -1.6, -1.2, -0.9, -0.3, -0.2, 0.2, 0.3, 0.9, 1.2, 1.6, 2.1, 2.4};

Representing the phase space bin and the pass/fail category with the index i , the number of signal events N_{sig}^i (and associated statistical uncertainty) in this bin is calculated as the total number of data events N_{total}^i (Poisson distributed), minus the estimated background yield N_{bkg}^i (with statistical uncertainty from the negative likelihood minimization procedure). Then, in each phase space bin, the efficiency is determined as

$$\varepsilon = \frac{N_{Signal}^{\text{pass}}}{N_{Signal}^{\text{pass}} + N_{Signal}^{\text{fail}}} \quad (6.1)$$

and the statistical uncertainties are propagated conservatively assuming no correlation between the passing and failing signal yields.

Examples of the nominal efficiency extraction fits for dimuons are shown in Figures 6-2 and 6-3. Similar examples for dielectrons are shown in Figures 6-4 and 6-5. In order to assess the goodness-of-fit, we compute a modified χ^2 test which accounts

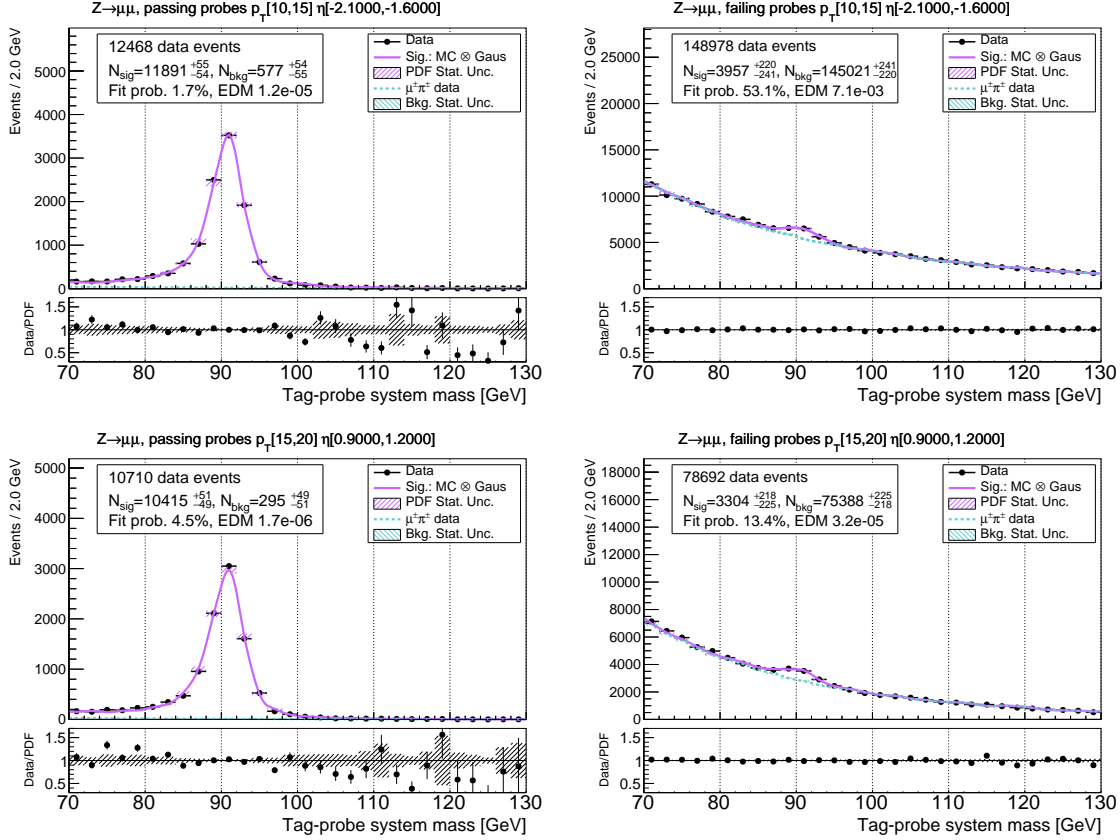


Figure 6-2: Efficiency extraction fits for the Medium muon working point using the data-driven background shape, at low muon transverse momentum.

for statistical uncertainties in the data as well as the MC signal template, as shown in the plots.

The MC efficiency is determined by counting the normalized yields of the passing and failing templates described above.

6.4 Assessment of systematic uncertainty

In this section, we quantify the systematic uncertainty arising from five distinct sources related to our ignorance of the true signal and background shapes, the generator-related uncertainty, and possible selection bias. In each case, the absolute difference between two alternative methods, δ , is taken as the systematic uncertainty $\pm\delta$ on the nominal value.

6.4.1 Background shape modeling

To quantify the uncertainty in deriving the background shape from the data-driven method, we use an analytic function as an alternative background shape. The function chosen is a linear combination of: a decaying exponential to model low-energy fakes,

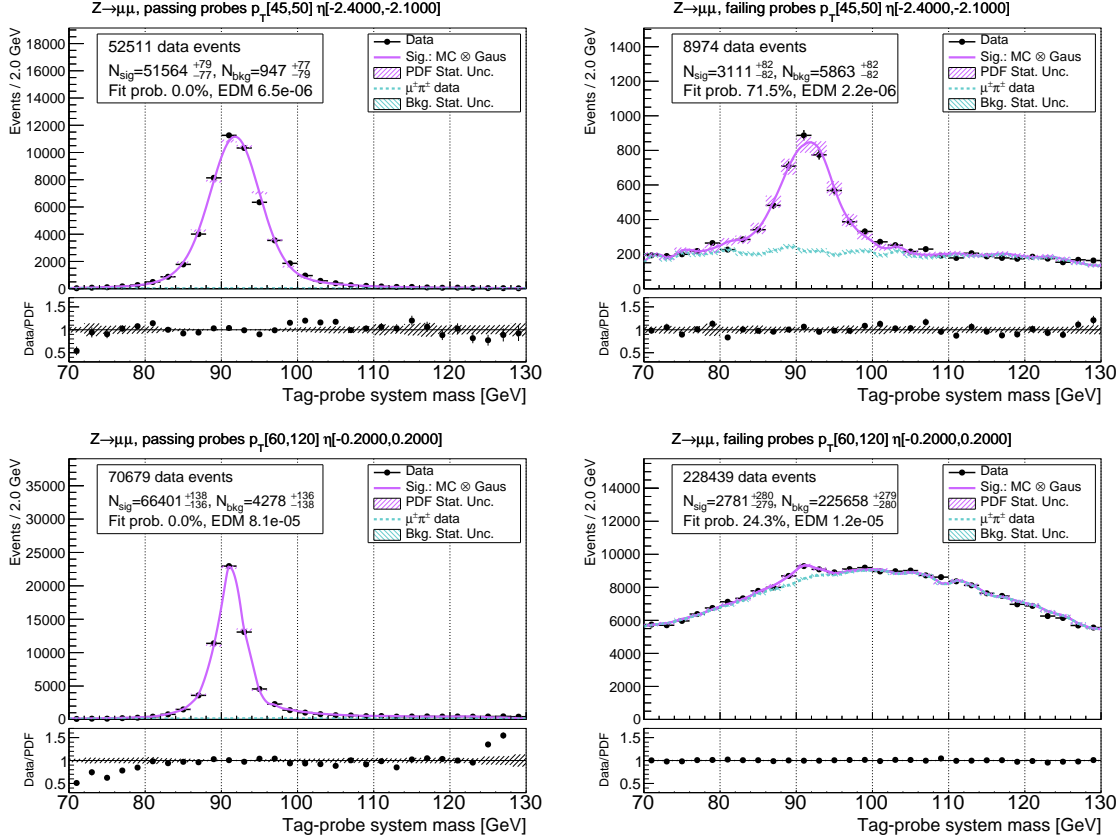


Figure 6-3: Efficiency extraction fits for the Medium muon working point using the data-driven background shape, at higher values of muon transverse momentum.

and a wide Gaussian with exponential tails to represent the peaking structure sculpted by applying energy cuts to a falling combinatorial background mass distribution. Previously, an error function multiplied with a decaying exponential was used, but this function has problems related to fit convergence due to poor parameterization.

Examples of fits for 2016 run eras B to F with the analytic background are shown for dimuons in Figures 6-6 and 6-7, and for dielectrons in Figures 6-8 and 6-9. These may be compared with the fits using the data-driven background shape in section 6.3. The difference in the Data/MC scale factors derived using the two methods is taken as a systematic; see Figures A-11 and A-12.

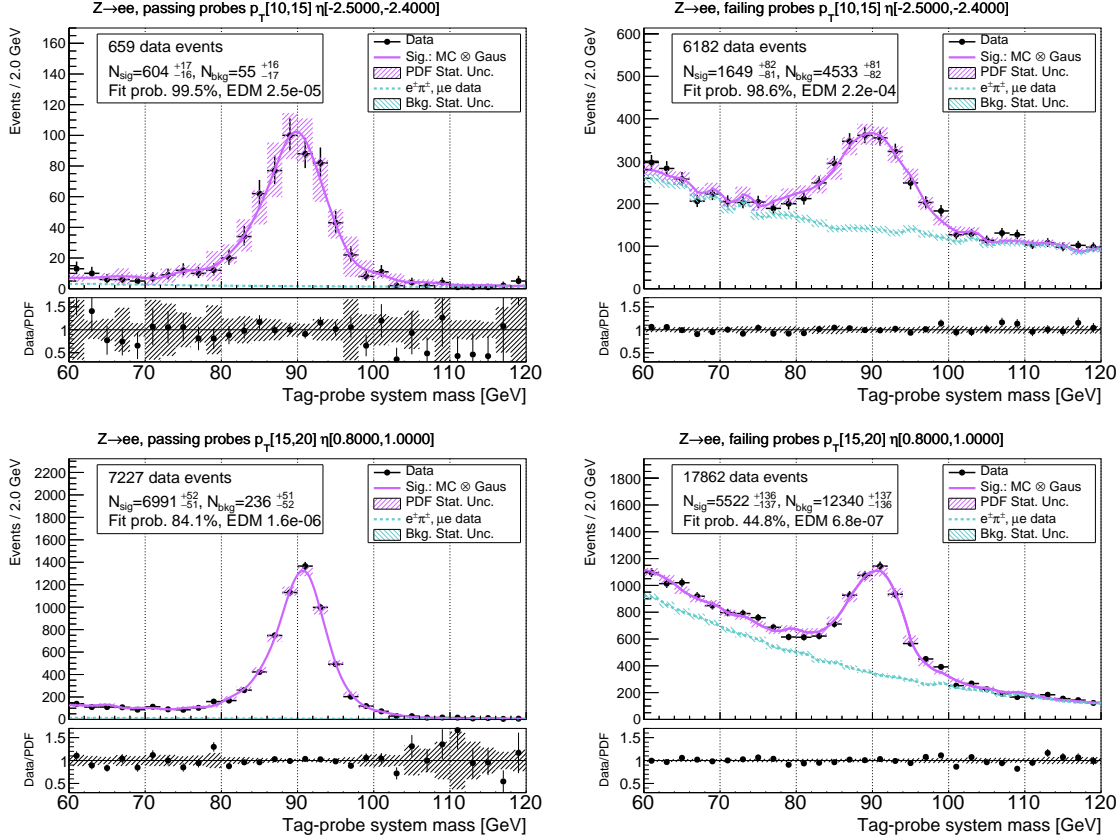


Figure 6-4: Efficiency extraction fits for the Medium electron working point using the data-driven background shape, at low electron transverse momentum.

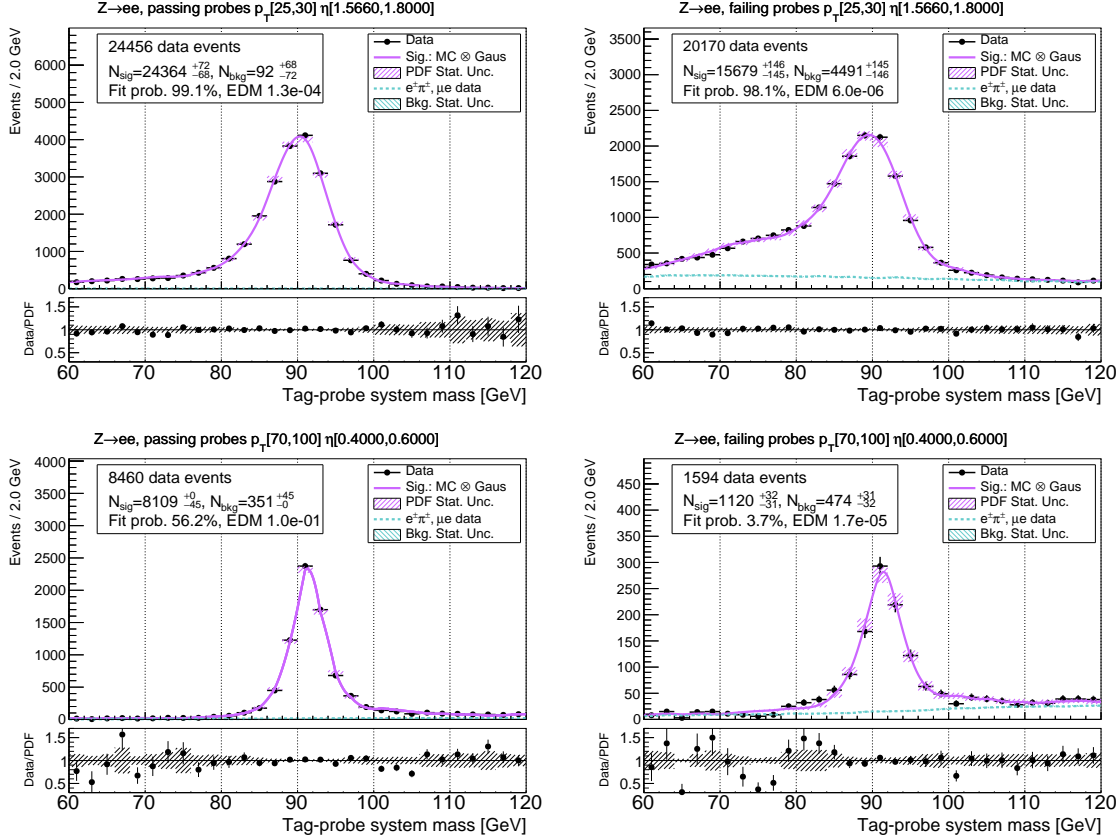


Figure 6-5: Efficiency extraction fits for the Medium electron working point using the data-driven background shape, at higher values of electron transverse momentum.

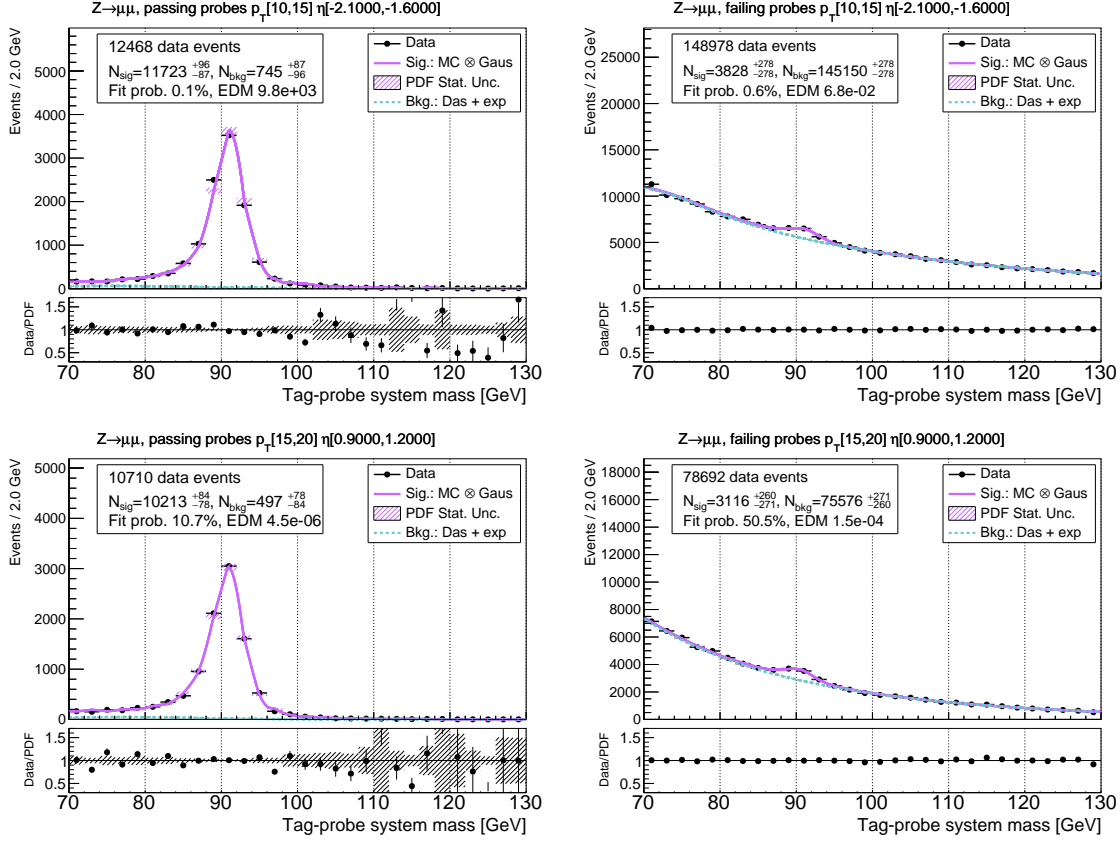


Figure 6-6: Efficiency extraction fits for the Medium muon working point using the alternative analytic background shape, at low muon transverse momentum.

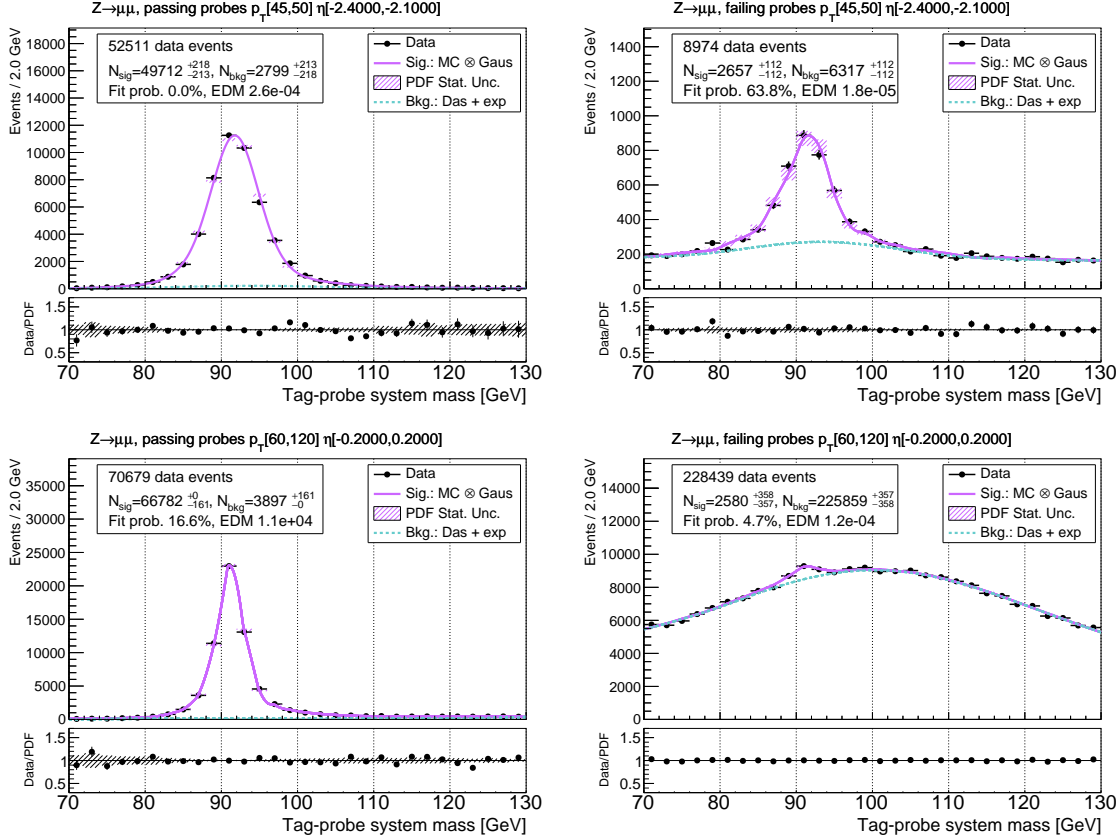


Figure 6-7: Efficiency extraction fits for the Medium muon working point using the alternative analytic background shape, at higher values of muon transverse momentum.

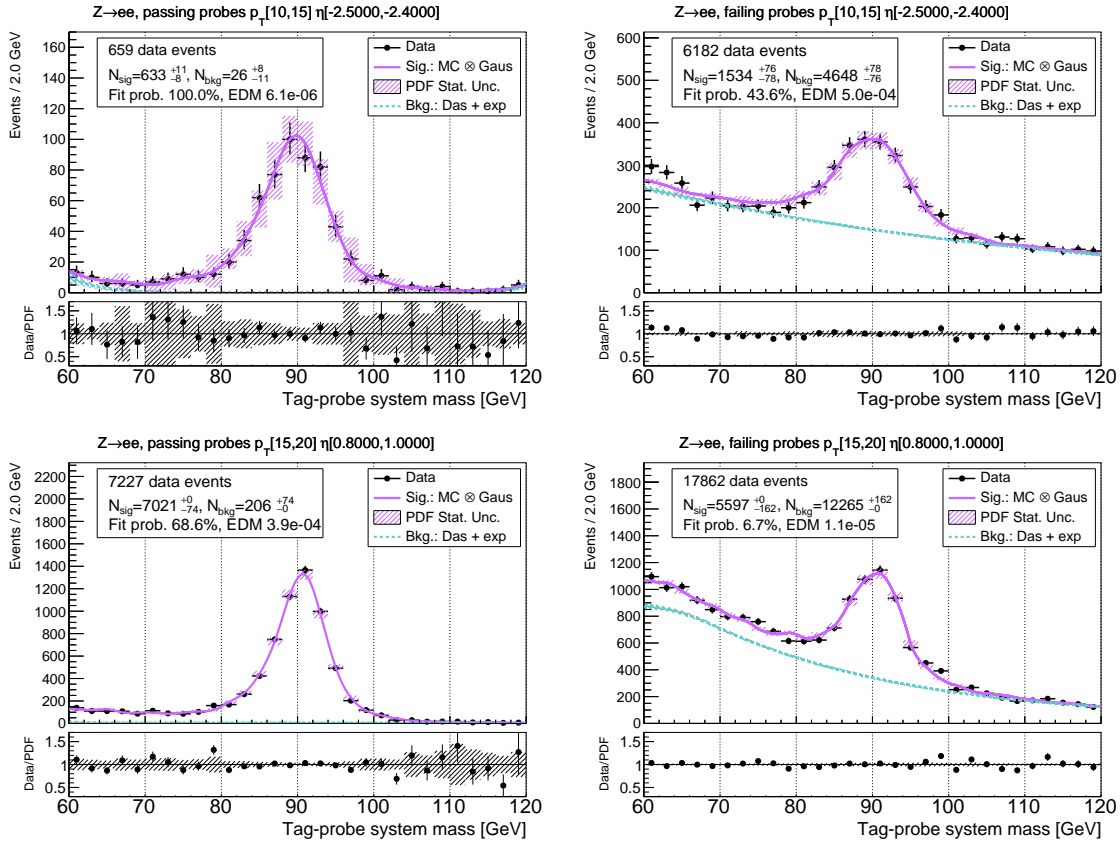


Figure 6-8: Efficiency extraction fits for the Medium electron working point using the alternative analytic background shape, at low electron transverse momentum.

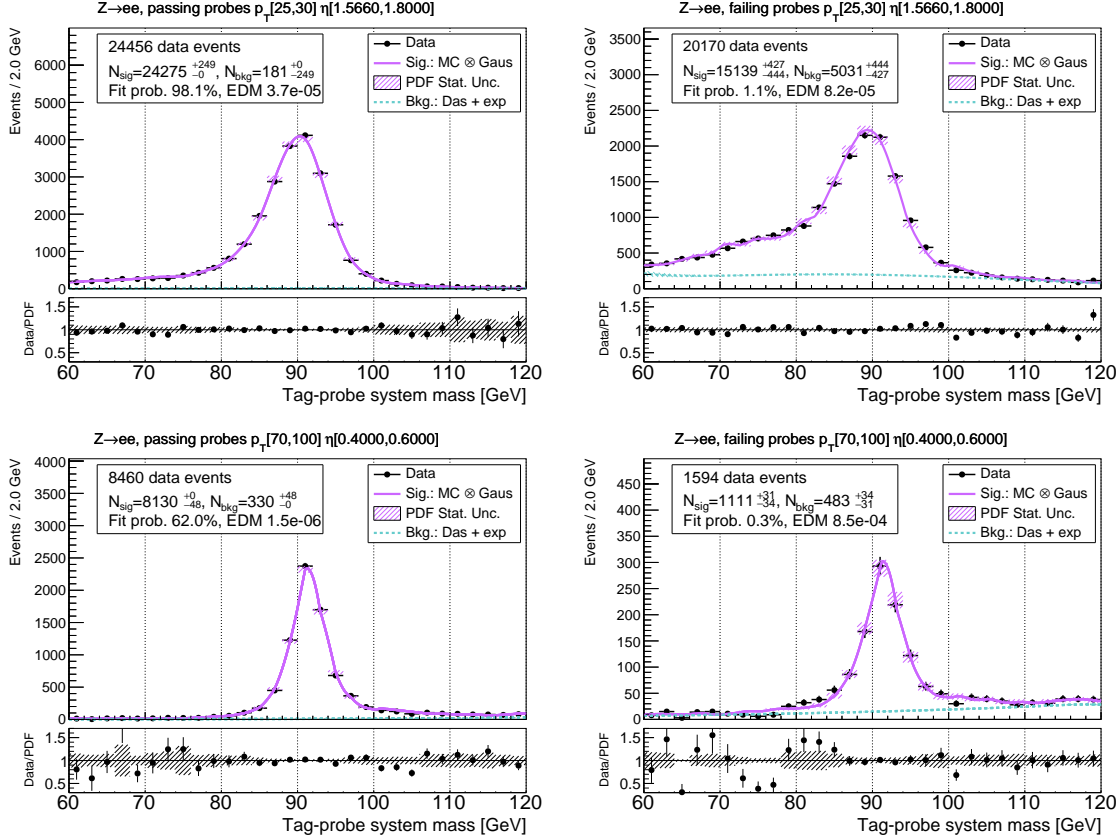


Figure 6-9: Efficiency extraction fits for the Medium electron working point using the alternative analytic background shape, at higher values of electron transverse momentum.

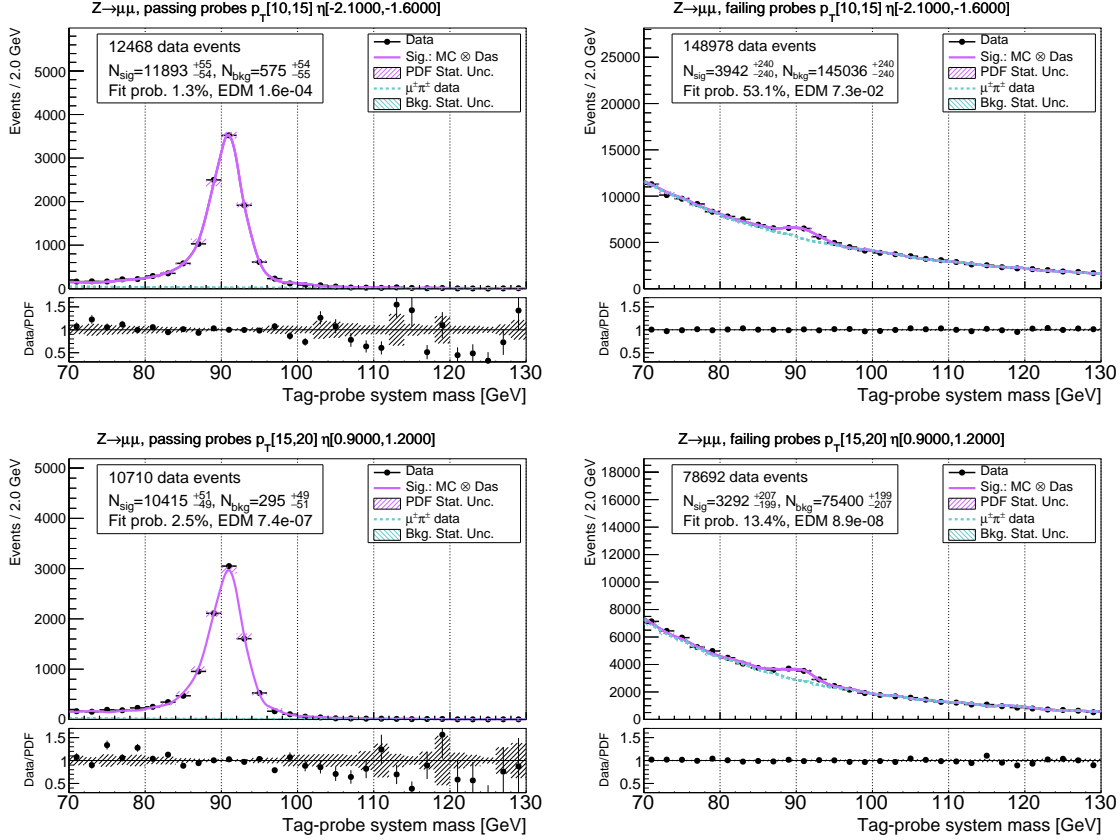


Figure 6-10: Efficiency extraction fits for the Medium muon working point using the analytic detector resolution function, at low muon transverse momentum.

6.4.2 Signal resolution modeling

We consider the uncertainty from using the simulation of the reconstructed Z resonance signal shape by convolution with an analytic function more complex than a Gaussian to try to capture more detector resolution effects. The difference in scale factors derived from the data efficiency extraction fits using the two methods is taken as the systematic uncertainty due to signal resolution modeling. The alternative function is a single Gaussian with asymmetric, exponential tails.

Examples of fits for 2016 run eras B to F with the alternative resolution function are shown for dimuons in Figures 6-10 and 6-11, and for dielectrons in Figures 6-12 and 6-13. These may be compared with the fits using the nominal resolution function in section 6.3. The difference in the Data/MC scale factors derived using the two methods is taken as a systematic; see Figures A-13 and A-14.

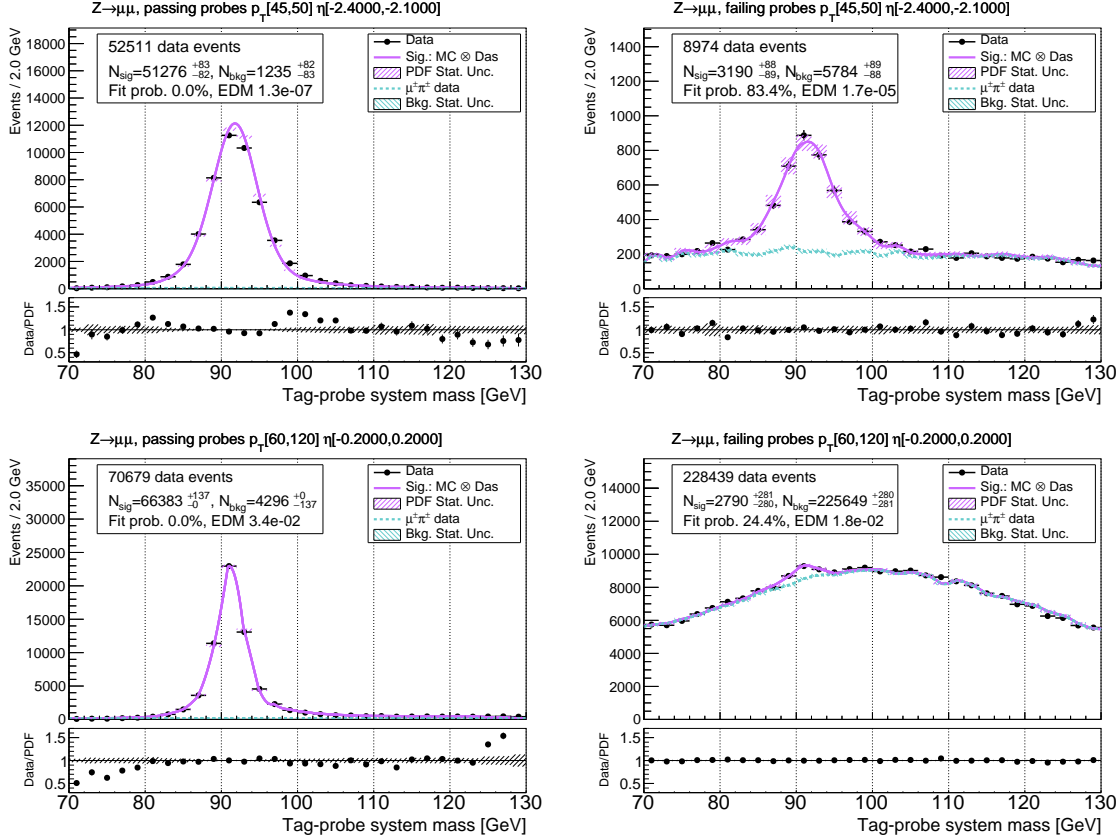


Figure 6-11: Efficiency extraction fits for the Medium muon working point using the analytic detector resolution function, at higher values of muon transverse momentum.

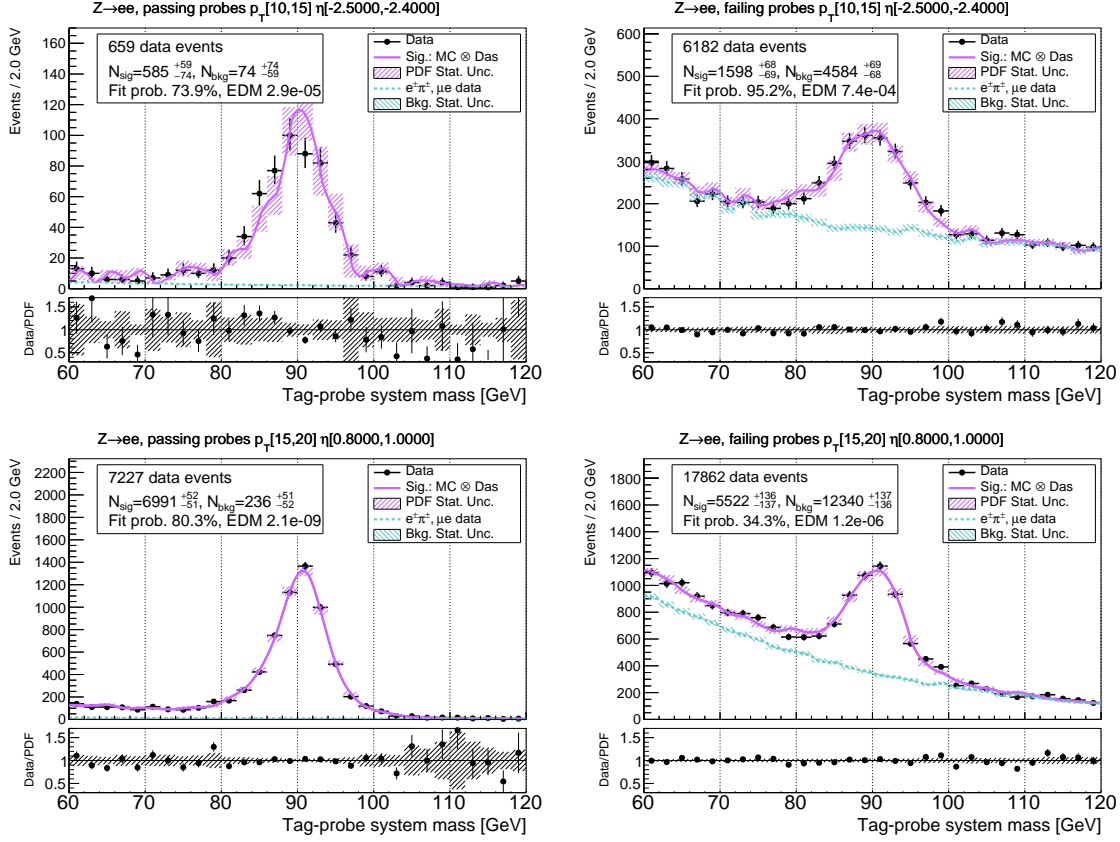


Figure 6-12: Efficiency extraction fits for the Medium electron working point using the analytic detector resolution function, at low electron transverse momentum.

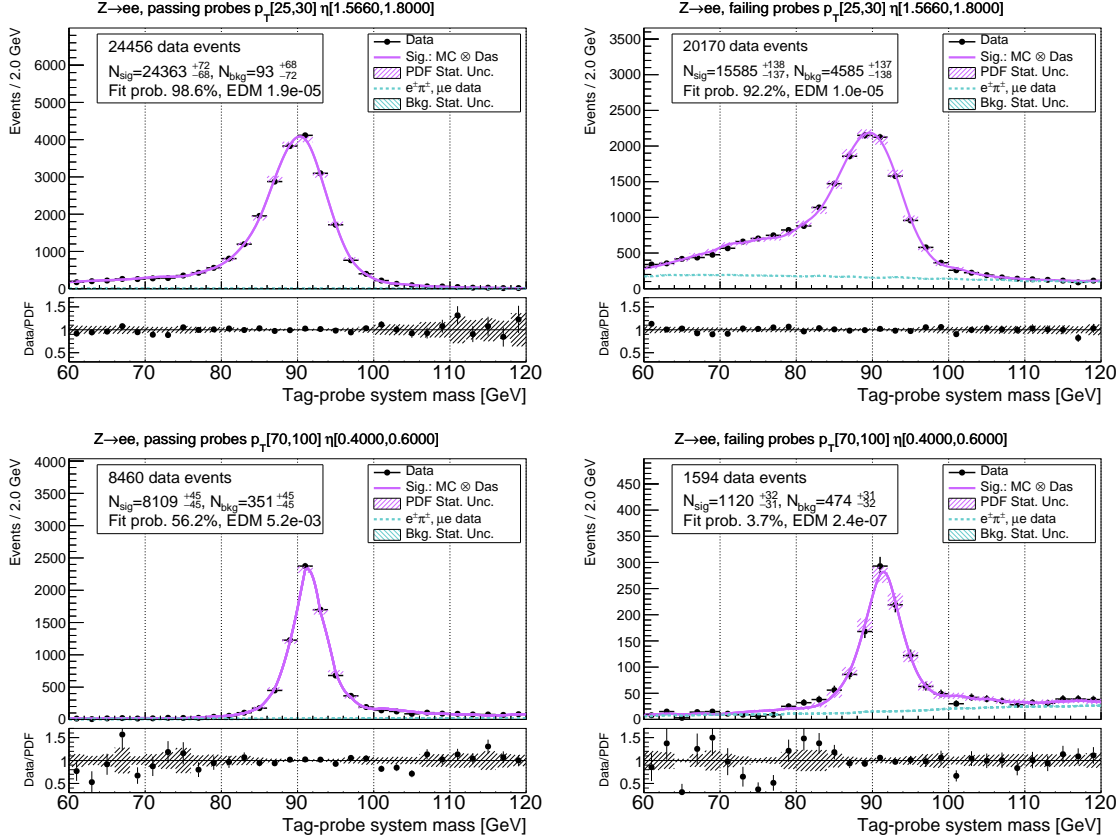


Figure 6-13: Efficiency extraction fits for the Medium electron working point using the analytic detector resolution function, at higher values of electron transverse momentum.

6.4.3 Signal final state radiation modeling

The reconstructed dilepton mass shape has a fat tail on the left side because of the effect of final state radiation (FSR). In these tail events, at least one of the final state leptons radiates a photon, reducing the energy of the dilepton system and changing the momentum of the emitting lepton. It is more prevalent for electrons than for muons because bremsstrahlung is suppressed as the fourth power of lepton mass.

Simulation addresses the phenomenon of FSR well in Z boson reconstruction, but we must assess the uncertainty on how FSR is modeled in the MC generator, which is only an approximation. To do this, we consider an alternative showering program called PHOTOS. See Ref. [154]. The goal is to compare the efficiencies obtained from fitting templates with different showering algorithm provenances. Due to technical reasons, our NLO QCD generator of choice for the nominal fit model (aMC@NLO) could not be made to work with the PHOTOS showering algorithm. Instead, we decided to use POWHEG and then pursue a reweighting procedure to capture the effect.

First, we generated Monte Carlo events using POWHEG+PYTHIA8 (the nominal showering algorithm) and POWHEG+PHOTOS (the alternative showering algorithm). In carrying out a private production only up to the GEN-SIM data tier, we were able to generate order of 10 million events for each showering choice. Next, the events constituting the templates from the nominal generator were reweighted as a function of their generator-level mass to the corresponding distribution in the POWHEG+X samples, where X represents PYTHIA8 or PHOTOS. The generator-level mass is an appropriate variable for this procedure because radiated photons carrying off substantial energy, as modeled by the generator, will reduce the generator mass. The altered weights were propagated to the histograms used as fitting templates, and fits were performed using the alternative POWHEG+X shapes.

Examples of these fits for 2016 run eras B to F are shown for dimuons in Figures 6-14, 6-15, 6-16, and 6-17; and for dielectrons in Figures 6-18, 6-19, 6-20, and 6-21. These may be compared with the fits using the nominally simulated FSR tail.

To get alternative scale factors, the efficiencies extracted from data are divided by the respective cut-and-count Monte Carlo efficiency derived from the reweighted templates. In other words, the data efficiency obtained by fitting with reweighted POWHEG+PYTHIA8 is divided by the cut-and-count MC efficiency from reweighted POWHEG+PYTHIA8, to get a scale factor. Then, the systematic uncertainty in a kinematic bin is defined as the absolute difference between the POWHEG+X scale factors, in that bin:

$$\delta_{\text{FSR}} = \left| \frac{\varepsilon_{\text{Data}}^{\text{PYTHIA8}}}{\varepsilon_{\text{MC}}^{\text{PYTHIA8}}} - \frac{\varepsilon_{\text{Data}}^{\text{PHOTOS}}}{\varepsilon_{\text{MC}}^{\text{PHOTOS}}} \right| \quad (6.2)$$

For 2D maps of the systematic uncertainty that results from this method, see Figures A-15 and A-16.

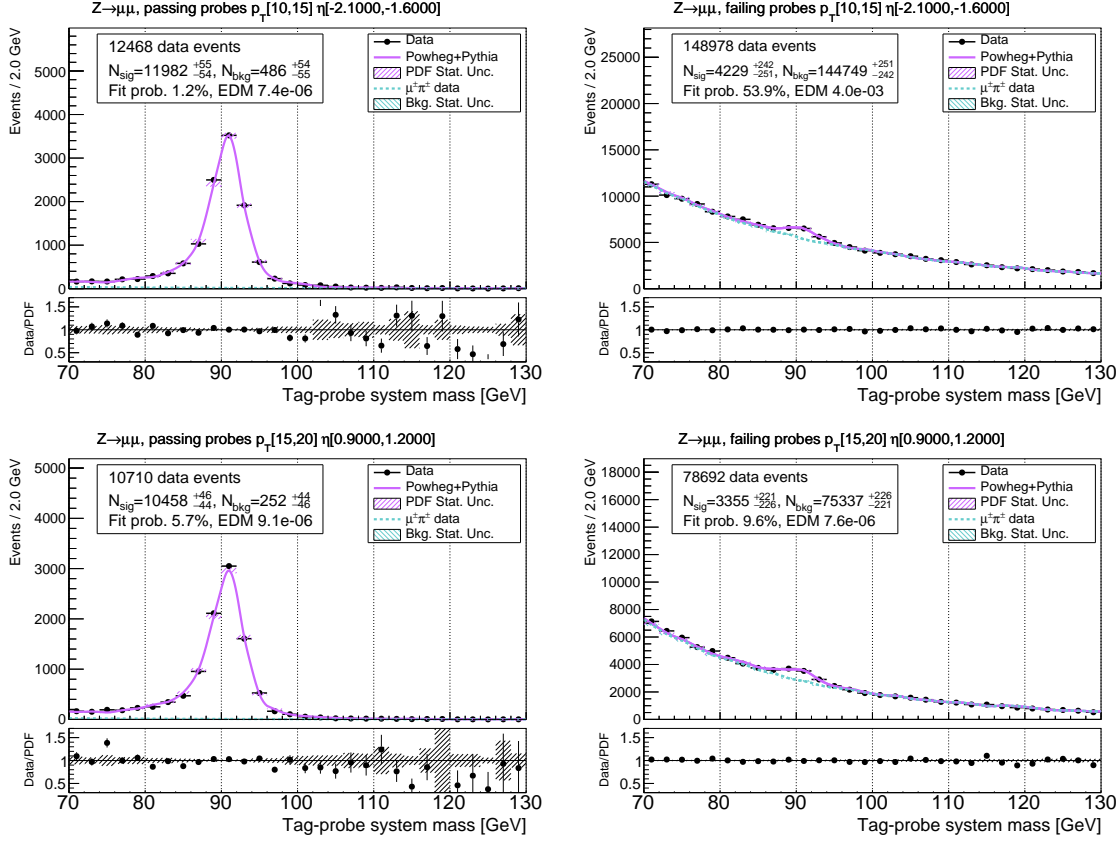


Figure 6-14: Efficiency extraction fits for the Medium muon working point using POWHEG and PYTHIA8, at low muon transverse momentum.

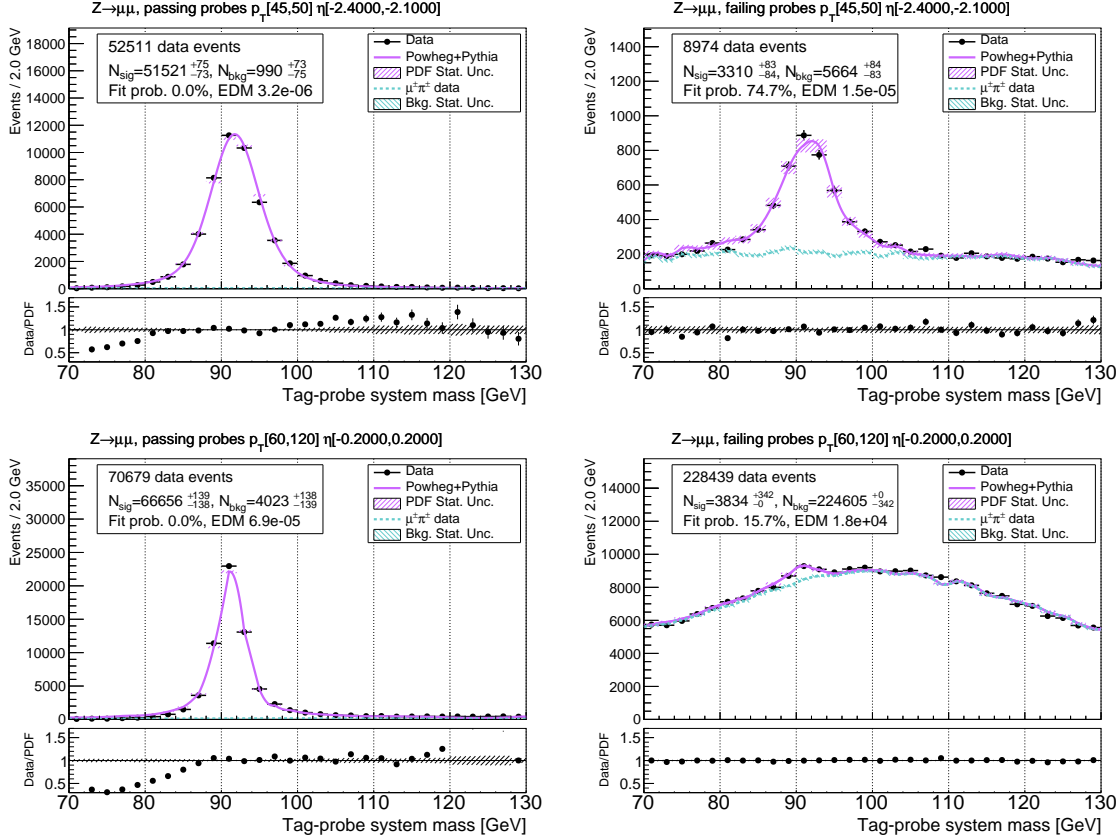


Figure 6-15: Efficiency extraction fits for the Medium muon working point using POWHEG and PYTHIA8, at higher values of muon transverse momentum.

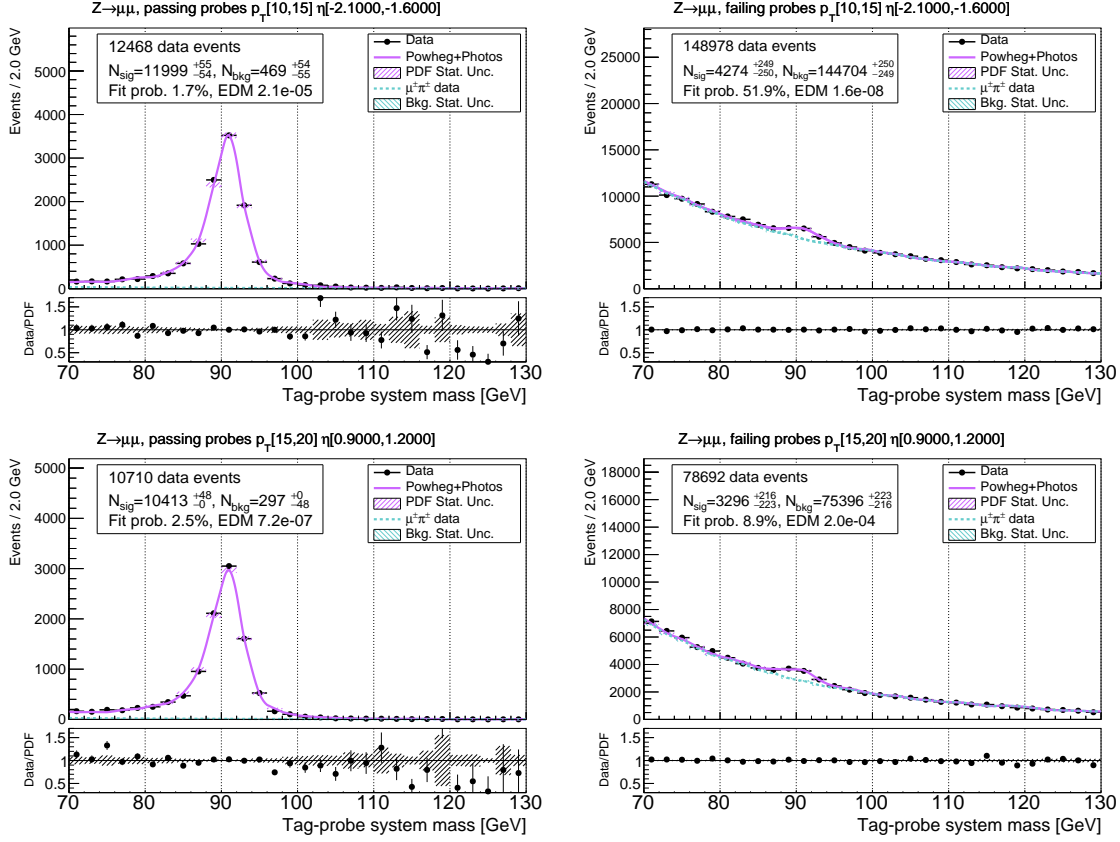


Figure 6-16: Efficiency extraction fits for the Medium muon working point using POWHEG and PHOTOS, at low muon transverse momentum.

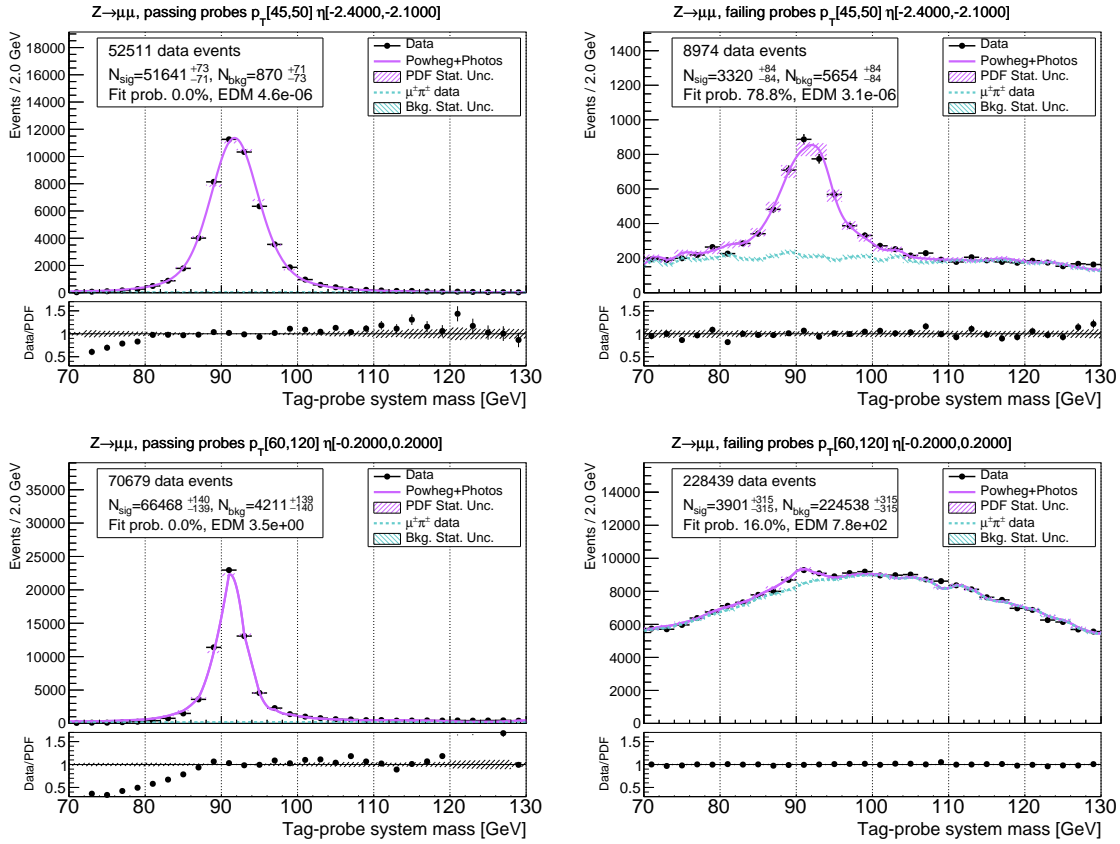


Figure 6-17: Efficiency extraction fits for the Medium muon working point using POWHEG and PHOTOS, at higher values of muon transverse momentum.

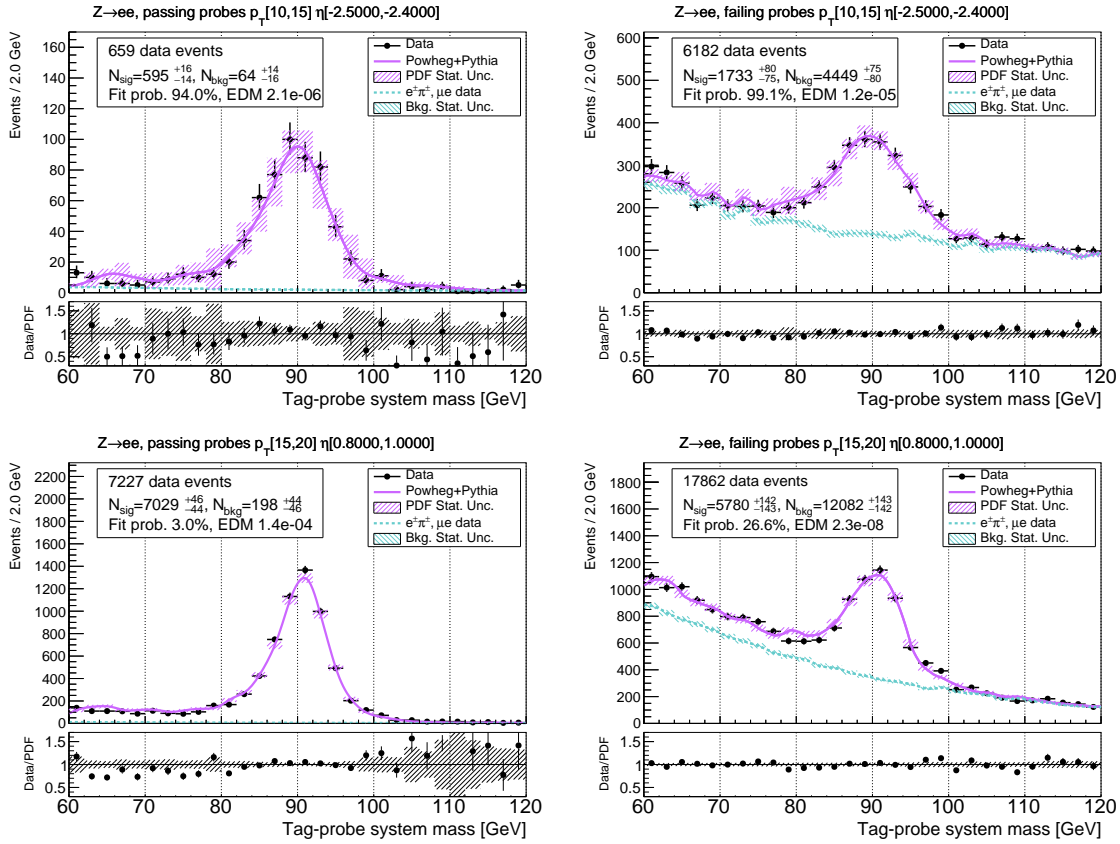


Figure 6-18: Efficiency extraction fits for the Medium electron working point using POWHEG and PYTHIA8, at low electron transverse momentum.

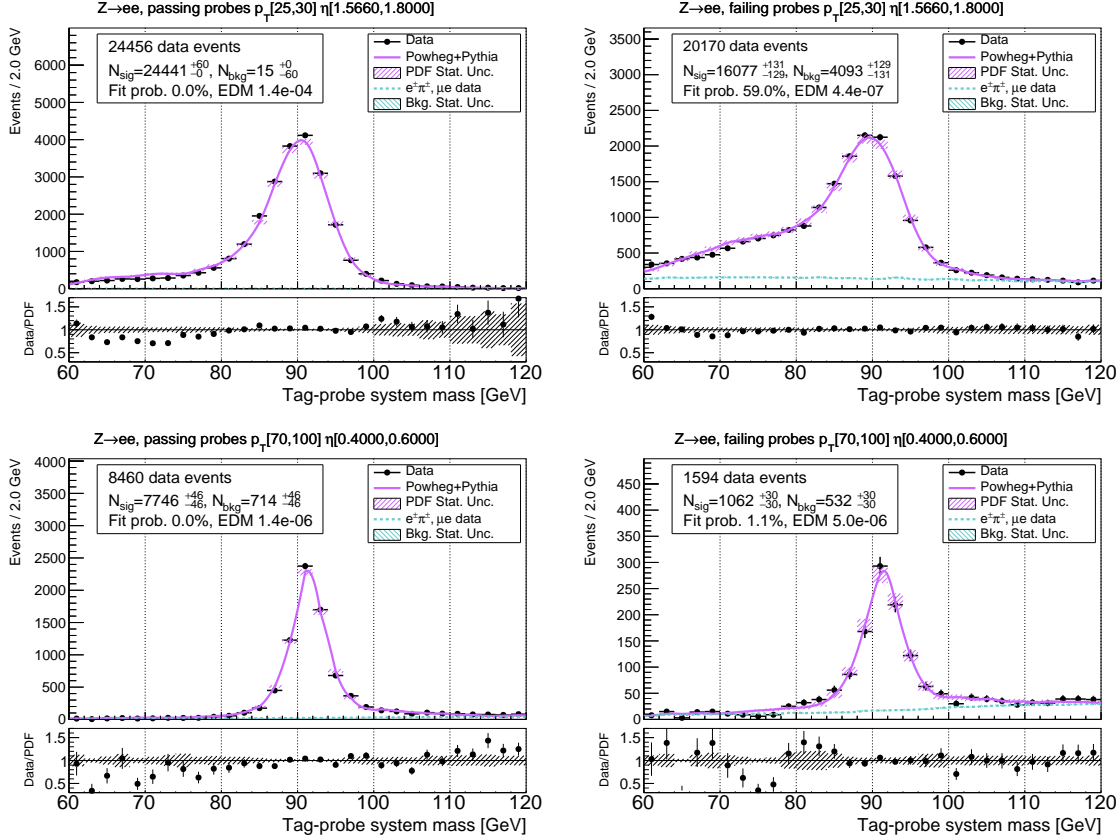


Figure 6-19: Efficiency extraction fits for the Medium electron working point using POWHEG and PYTHIA8, at higher values of electron transverse momentum.

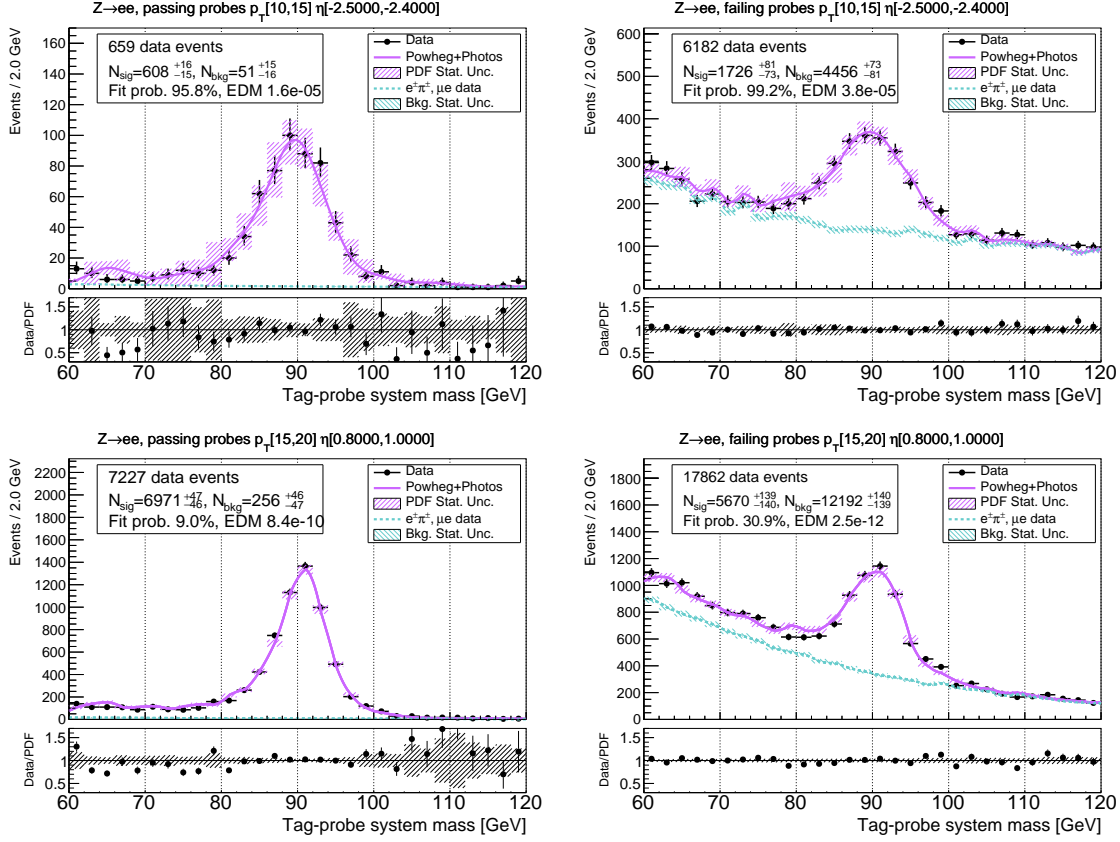


Figure 6-20: Efficiency extraction fits for the Medium electron working point using POWHEG and PHOTOS, at low electron transverse momentum.

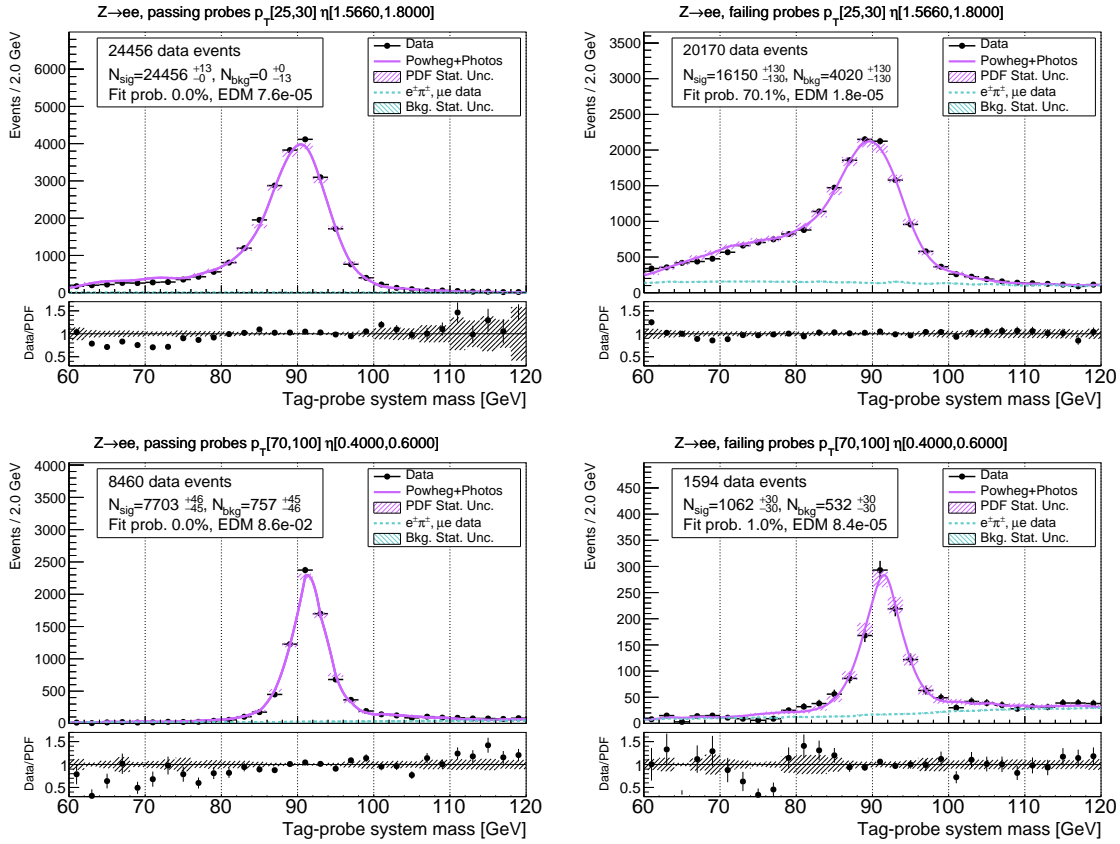


Figure 6-21: Efficiency extraction fits for the Medium electron working point using POWHEG and PHOTOS, at higher values of electron transverse momentum.

6.4.4 Choice of generator

The choice of generator used to determine the MC before the showering can affect the scale factor determination. The differences in generator implementations, including leading-order versus next-to-leading order simulation, can affect the fraction of passing and failing probes, and the truth-matching efficiency. Therefore, we use a different implementation (MADGRAPH5 at leading-order) instead of the nominal (MADGRAPH5_AMC@NLO) to extract the efficiency from data. This data efficiency is divided by the nominal NLO MC efficiency to give an alternative scale factor. We do not substitute the leading-order MC efficiency here because, for the purposes of a precision measurement, the difference in the data efficiency is the real effect. We take the size of the difference in the scale factors as the symmetric systematic uncertainty from the choice of generator. See Figures A-17 and A-18.

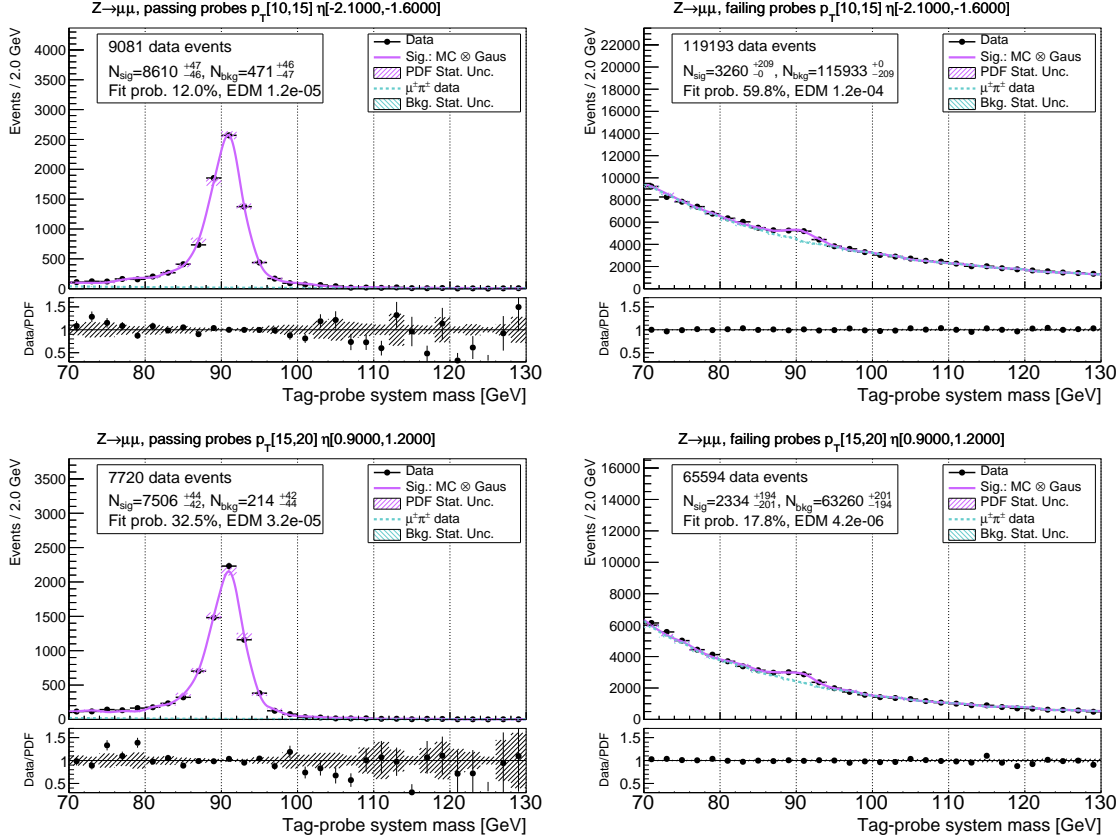


Figure 6-22: Efficiency extraction fits for the Medium muon working point using the alternative tag selection, at low muon transverse momentum.

6.4.5 Bias from choice of tag selection

The choice of tag selection cuts is motivated by the realities of the experiment, such as detector acceptance and trigger p_T thresholds. The tag selection can bias the data efficiency, so we account for this by observing the change in the Data/MC scale factors when the tag selection is changed. The alternative tag selection has a p_T threshold 5 GeV higher, and uses the Medium working point for identification and isolation.

Examples of fits for 2016 run eras B to F with the alternative tag selection applied to Data and MC are shown for dimuons in Figures 6-22 and 6-23, and for dielectrons in Figures 6-24 and 6-25. These may be compared with the fits using the nominal tag selection in section 6.3. The difference in the Data/MC scale factors derived using the two methods is taken as a systematic; see Figures A-19 and A-20.

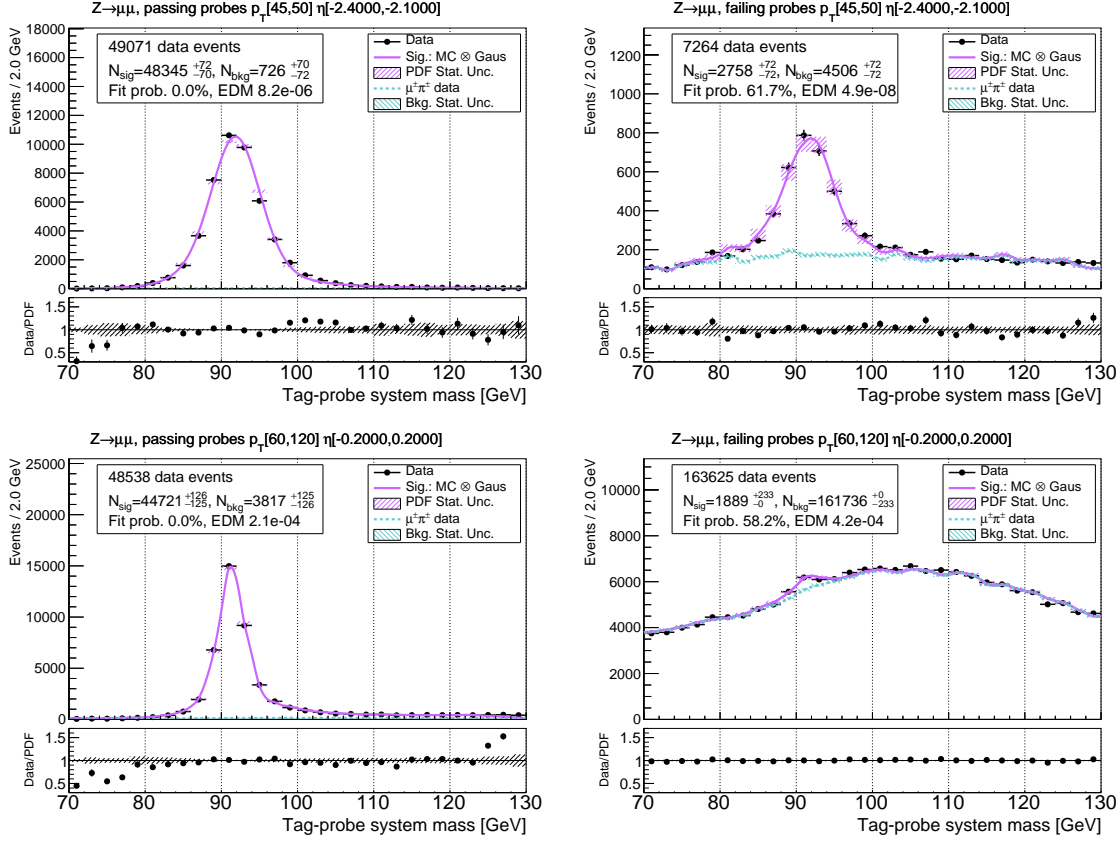


Figure 6-23: Efficiency extraction fits for the Medium muon working point using the alternative tag selection, at higher values of muon transverse momentum.

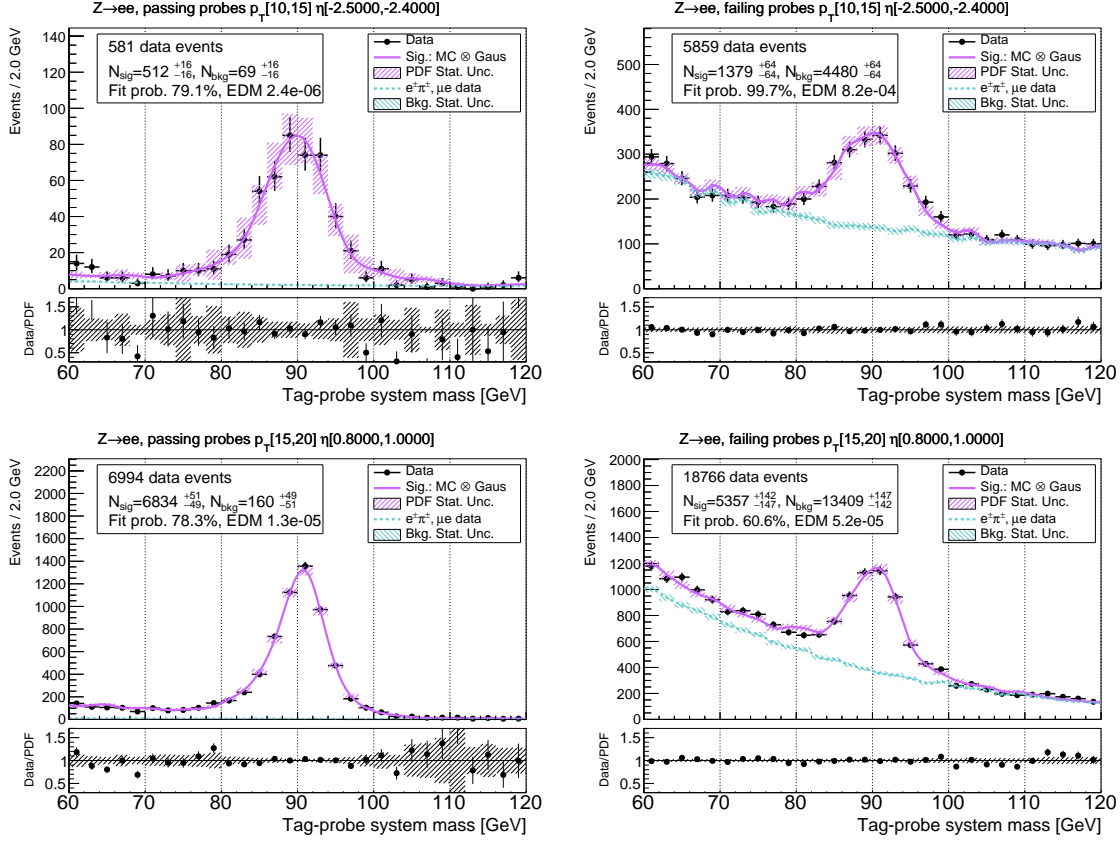


Figure 6-24: Efficiency extraction fits for the Medium electron working point using the alternative tag selection, at low electron transverse momentum.

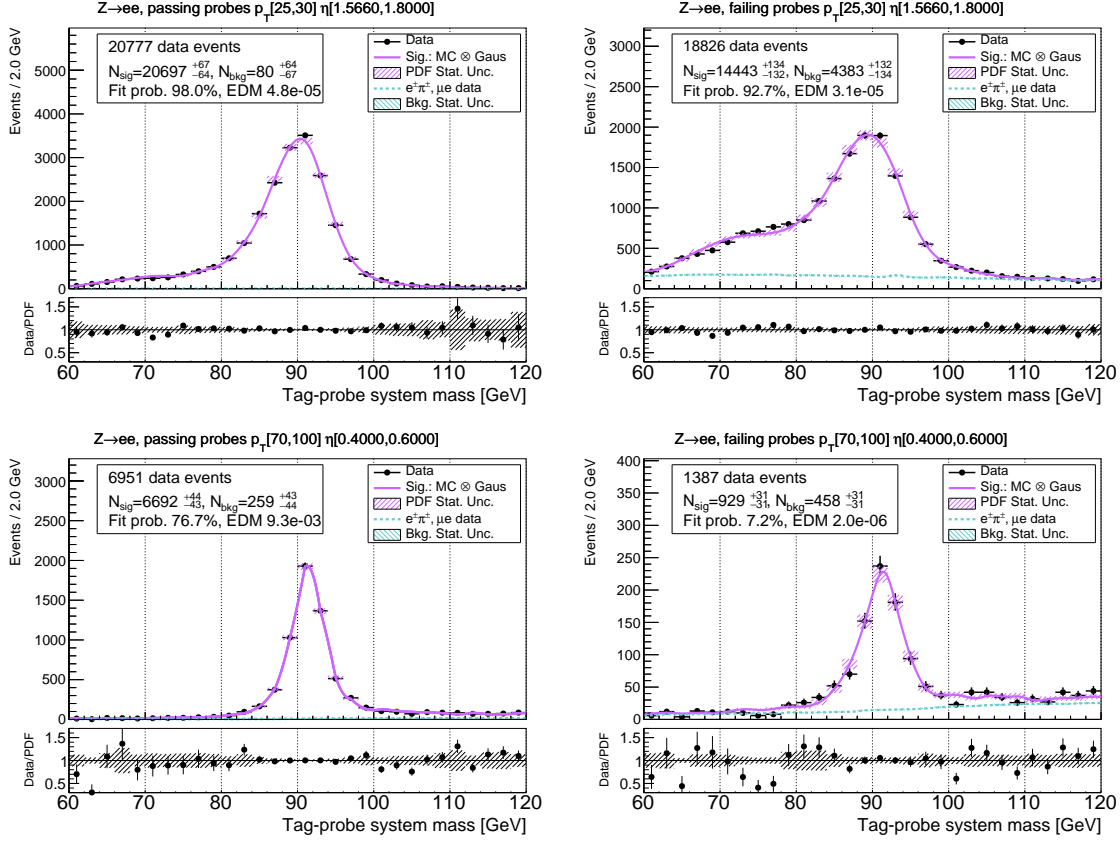


Figure 6-25: Efficiency extraction fits for the Medium electron working point using the alternative tag selection, at higher values of electron transverse momentum.

6.4.6 Total impact of systematic uncertainties

The percent impacts of each source of uncertainty on the inclusive $Z(\ell\ell)$ cross section are shown in Table 6.1. Pre-HIP mitigation scenario in 2016 is assumed.

Source of Uncertainty	Z(ee) Yield % Impact	Z($\mu\mu$) Yield % Impact
Background shape	0.48	0.57
Signal resolution	0.04	0.26
Signal FSR model	0.09	0.07
Generator choice	0.34	0.19
Tag selection	0.44	0.26
Total scale factor impact	0.74	0.71

Table 6.1: Impact of the scale factor uncertainties on the inclusive cross section.

Chapter 7

Measurements of differential Z boson production cross sections

In this chapter I present the measurements of the differential Z boson production cross section in three observables: Z boson transverse momentum, Z boson rapidity, and the ϕ^* observable. The rapidity of the Z boson in pp collisions is strongly correlated with the Bjorken-x of the initial partons and provides constraints on the PDFs of the proton. The precision of the Z boson p_T measurements is limited by the uncertainties in the measurements of the transverse momenta of charged leptons from Z boson decays. The observable ϕ^* [155, 156, 157], defined by the expression

$$\begin{aligned}\phi^* &= \tan\left(\frac{\pi - \Delta\phi}{2}\right) \sin(\theta_\eta^*) \\ \cos(\theta_\eta^*) &= \tanh\left(\frac{\eta^- - \eta^+}{2}\right),\end{aligned}\tag{7.1}$$

where $\Delta\phi$ is the opening angle between the leptons in the plane transverse to the beam, and η^\pm refers to the pseudorapidity of the two leptons, is proportional to the ratio of Z boson p_T to dilepton mass. The variable θ_η^* indicates the scattering angle of the dileptons with respect to the beam in the boosted frame where the leptons are aligned. The observable ϕ^* follows the approximate relationship $\phi^* \sim p_T^Z/m_{\ell\ell}$ that the range $\phi^* \leq 1$ corresponds to p_T^Z up to about 100 GeV for a lepton-pair mass close to the nominal Z boson mass.

The measurement resolution of ϕ^* is better than that of p_T since it depends only on the angular variables of the leptons and benefits from the excellent spatial resolution of the CMS inner tracking system. The Z boson ϕ^* distribution has been previously measured by the D0, ATLAS, CMS, and LHCb collaborations [35, 19, 158, 30].

In all, I will show inclusive fiducial and differential production cross sections of the Z boson as functions of p_T , ϕ^* , and rapidity.

7.1 Event selection

The leptonic final state in the $Z/\gamma^* \rightarrow \ell^+\ell^-$ channel consists of two opposite charged same-flavor high p_T isolated leptons, muons or electrons, compatible with a Z boson decay. Therefore, the selection of the Z boson candidates are required to have either two muons or two electrons with a reconstructed mass ($m_{\ell\ell}$) within 15 GeV the nominal Z boson mass. In addition, both leptons are required to have $p_T > 25$ GeV to ensure $\sim 100\%$ trigger efficiency, and $|\eta| < 2.4$ for muons and electrons. After applying this selection the background level from non single-Z boson processes is below 1%. A few distributions at the reconstruction level for dimuons and dielectrons after applying the full selection are shown in Figures 7-1 and 7-2. Figures 7-3, 7-4, 7-5, and 7-6 show the generator-level correlations between p_T^Z , ϕ^* , y^Z , and the opening angles between the lepton pairs $\Delta\phi$, Δy , and $\Delta R = \sqrt{\Delta\phi^2 + \Delta\eta^2}$.

7.2 Background estimation

After the full selection, the amount of background processes in the data sample is rather small thanks to the clean signature and the relatively tight selection. The background processes is split into two components: the resonant background and the nonresonant background. The resonant background comes from events with a real Z boson in the final state, e.g. WZ diboson production; while the nonresonant background comes from events which do not have a Z boson in the final state. The first set of backgrounds is estimated using a simulated events, as described in Section 5.2.

Nonresonant backgrounds (NRB) consist mainly of leptonic W decays in $t\bar{t}$, tW decays and WW events. Small contributions from single top-quark events produced from s -channel and t -channel processes, and $Z \rightarrow \tau\tau$ events are also considered in this NRB estimation. This contribution of the nonresonant backgrounds is estimated from a control sample of dilepton events of different flavor ($e^\pm\mu^\mp$) that pass all other selection criteria. The method has been previously used in many analyses and assumes the lepton flavor symmetry in the final states of these processes. Since the leptonic decay branching ratios for the ee , $\mu\mu$ and $e\mu$ final states from NRB are 1:1:2, the $e\mu$ events selected inside the Z-mass window is extrapolated to the ee and $\mu\mu$ channels. To account for differences in efficiency for electrons and muons, a correction factor $k_{\mu\mu}$ is derived by comparing the NRB yields in the ee and $\mu\mu$ channels:

$$k_{\mu\mu} = \frac{\epsilon_\mu}{\epsilon_e} \approx \sqrt{\frac{N_{NRB}^{\mu\mu}}{N_{NRB}^{ee}}} \quad (7.2)$$

This again assumes that each lepton leg acts independently. The factor $k_{\mu\mu}$ is found to be about 1.3 for the final selection, consistent between data and simulation. With this correction factor, the relation between the NRB yields in the signal and control

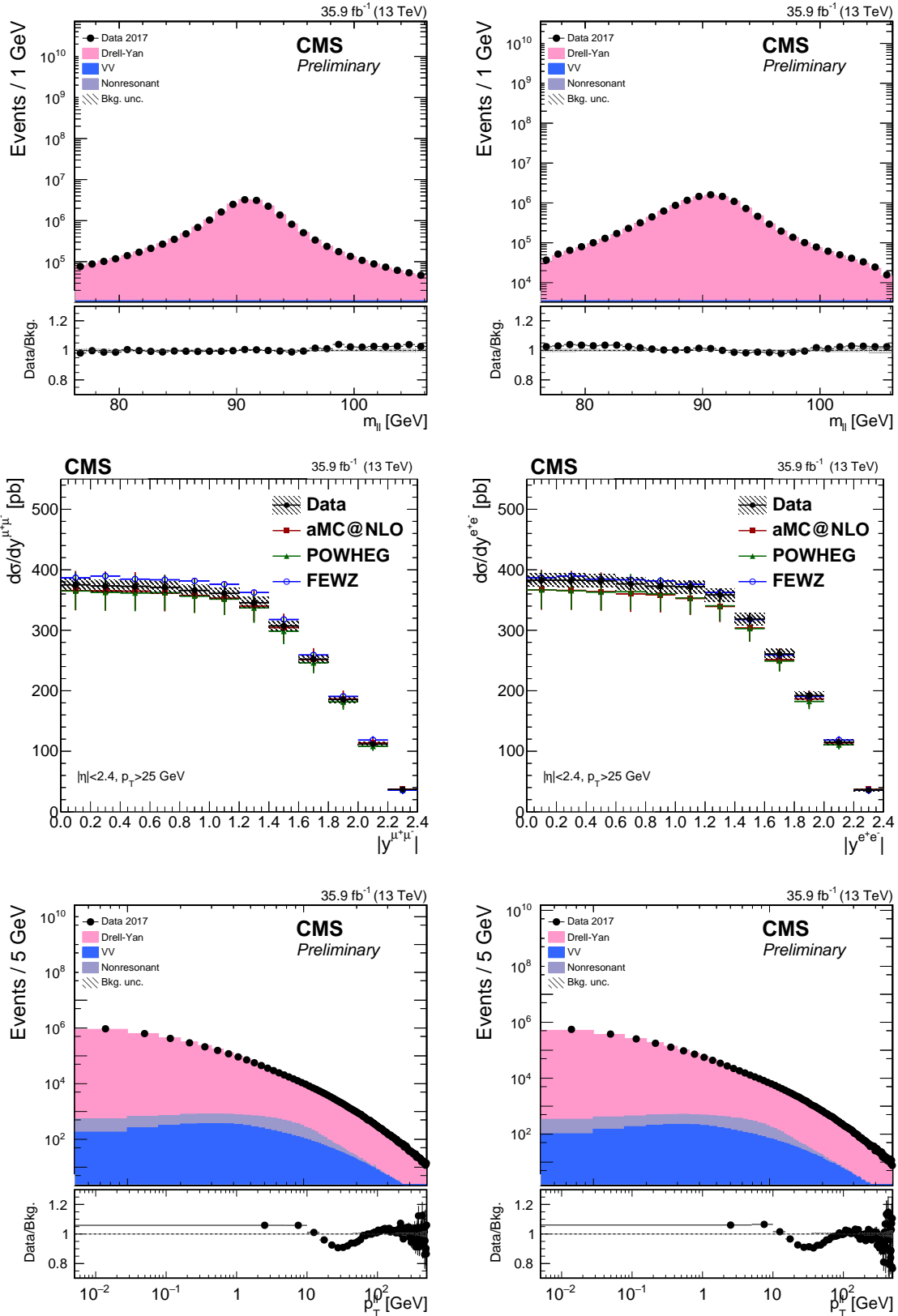


Figure 7-1: Distributions at the reconstruction level of $m_{\ell\ell}$ (top), $|y^Z|$ (center), and p_T^Z (bottom) for dimuons (left) and dielectrons (right) after applying the full selection.

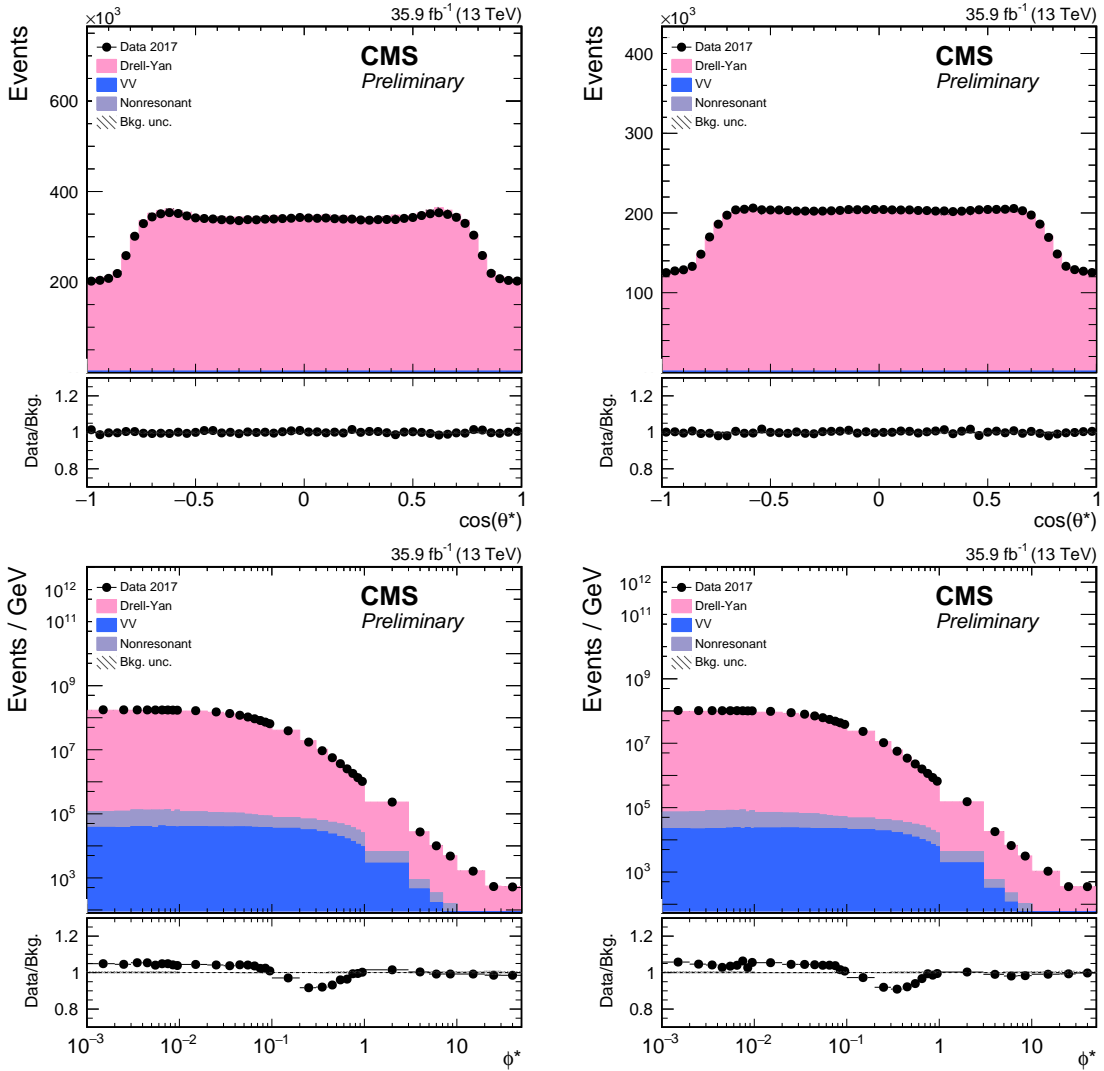


Figure 7-2: Distributions at the reconstruction level of $\cos(\theta^*)$ (top) and ϕ^* (bottom) for dimuons (left) and dielectrons (right) after applying the full selection.

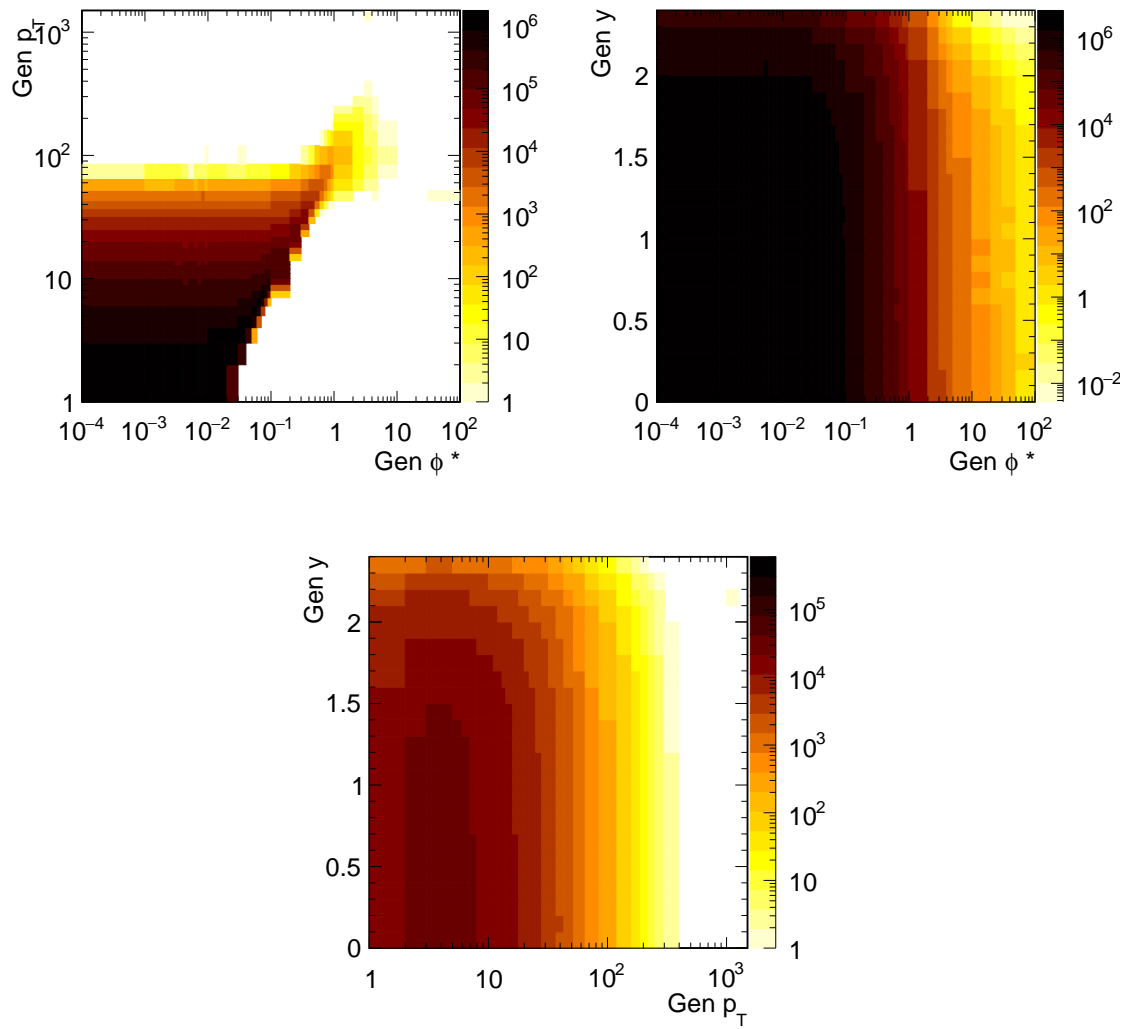


Figure 7-3: Distributions at the generator level of ϕ^* vs p_T^Z (top left), ϕ^* vs y^Z (top right), and p_T^Z vs y^Z (bottom) for dilepton pairs.

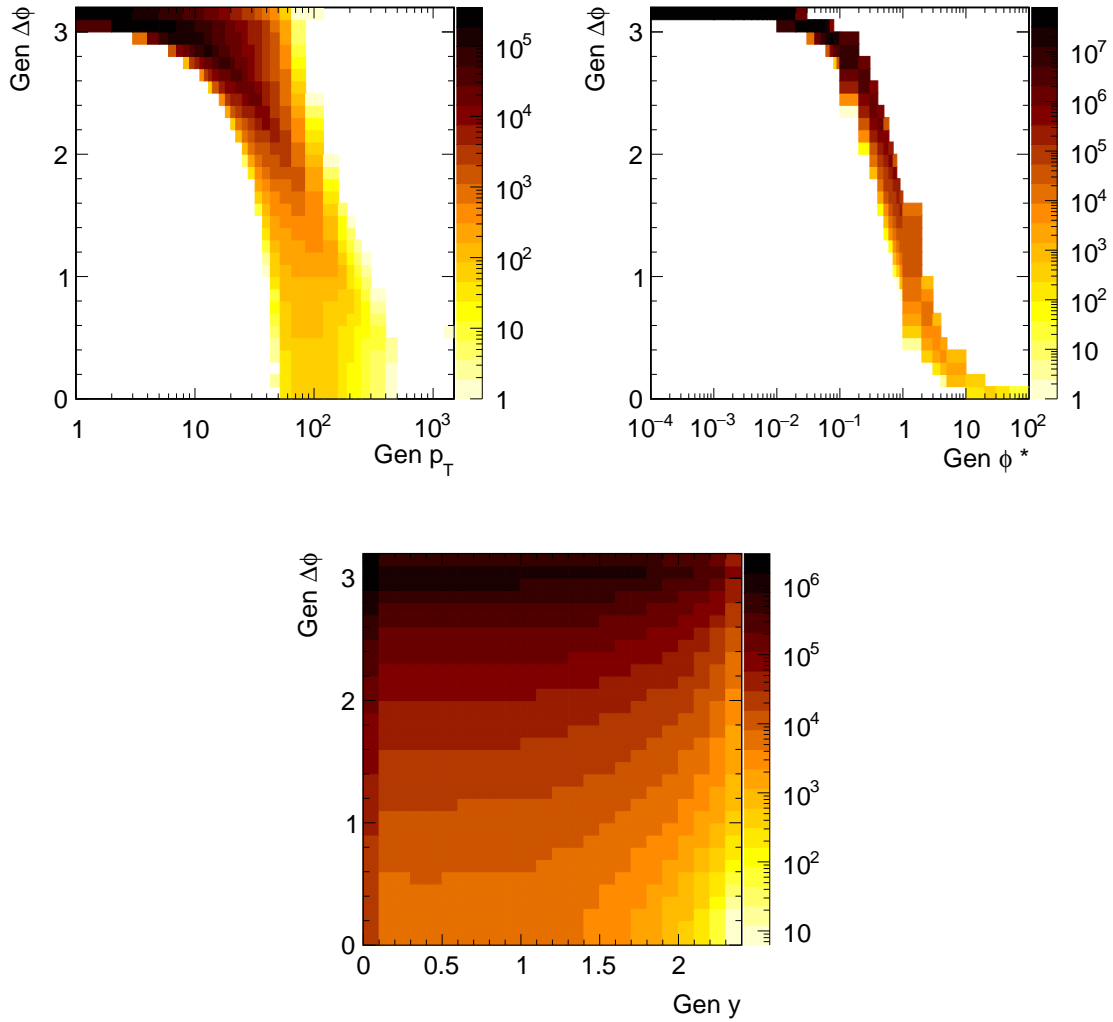


Figure 7-4: Distributions at the generator level of $\Delta\phi$ with p_T^Z (top left), ϕ^* (top right), and y^Z (bottom) for dilepton pairs.

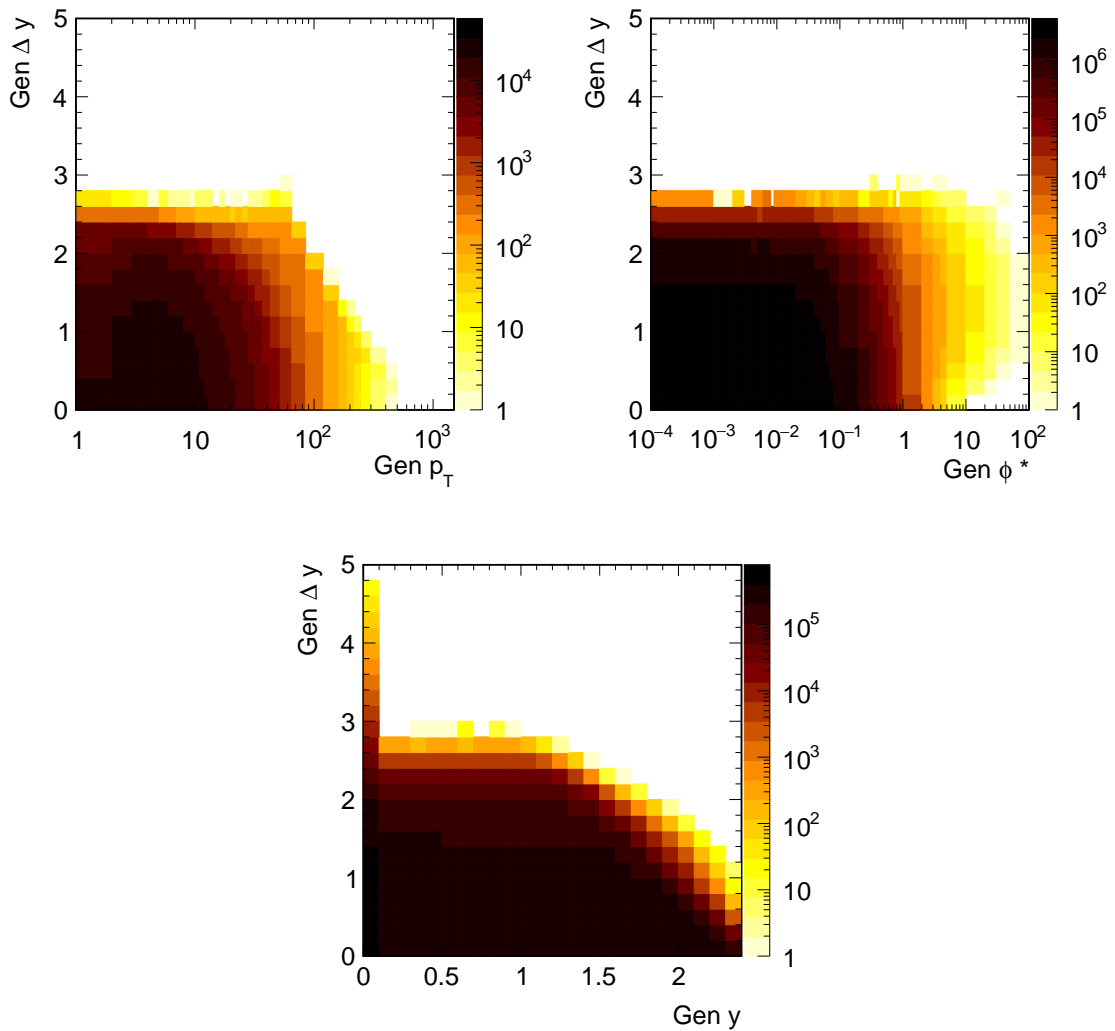


Figure 7-5: Distributions at the generator level of Δy with p_T^Z (top left), ϕ^* (top right), and y^Z (bottom) for dilepton pairs.

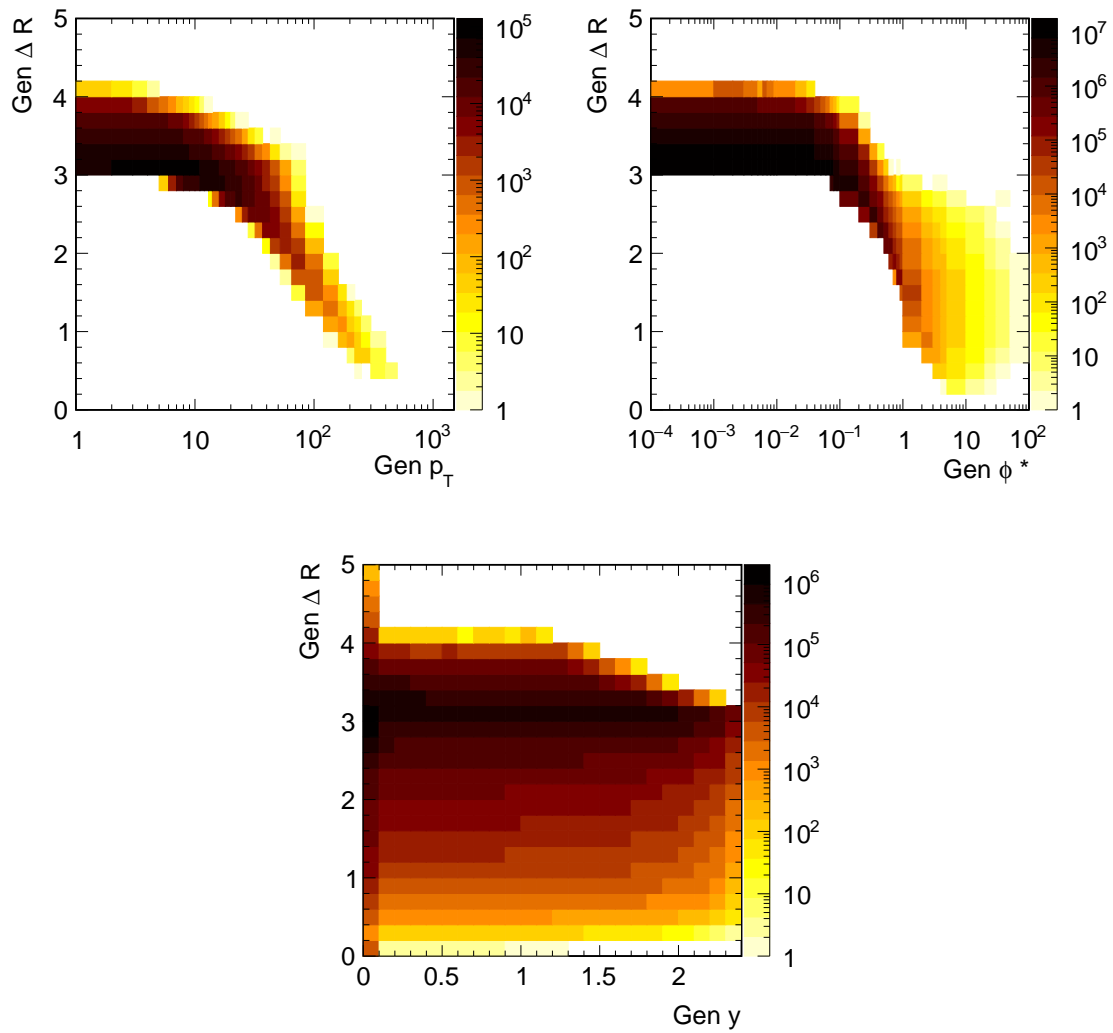


Figure 7-6: Distributions at the generator level of ΔR with p_T^Z (top left), ϕ^* (top right), and y^Z (bottom) for dilepton pairs.

region is:

$$\begin{aligned}
 N_{NRB}^{\mu\mu} &= \frac{1}{2} k_{\mu\mu} N_{NRB}^{e\mu} \\
 N_{NRB}^{ee} &= \frac{1}{2} \frac{1}{k_{\mu\mu}} N_{NRB}^{e\mu} \\
 \rightarrow N_{NRB}^{2\ell} &= \frac{1}{2} \left(k_{\mu\mu} + \frac{1}{k_{\mu\mu}} \right) N_{NRB}^{e\mu}
 \end{aligned} \tag{7.3}$$

A summary of the data, signal, and background yields after the full selection for the dimuon and dielectron final states is shown in Table 7.1.

Final state	Data	$Z \rightarrow \ell\ell$	Resonant bkg.	Nonresonant bkg.
$\mu\mu$	$\sim 20.4 \times 10^6$	$\sim 20.7 \times 10^6$	$\sim 30 \times 10^3$	$\sim 41 \times 10^3$
ee	$\sim 12.1 \times 10^6$	$\sim 12.0 \times 10^6$	$\sim 19 \times 10^3$	$\sim 26 \times 10^3$

Table 7.1: Summary of data, signal, and background yields after the full selection. The signal yields are quoted using `MADGRAPH5_AMC@NLO`.

7.3 Systematic uncertainties

In this section the systematic uncertainties taken into account in the Z differential measurement are summarized. Uncertainties do not only influence the overall normalization (e.g. the uncertainty in the luminosity measurement), but also the distribution of relevant kinematic observables (e.g. the uncertainty in the lepton momentum scale), are treated as shape uncertainties. Their impact is evaluated by performing the full analysis with its value shifted up and down by one standard deviation. For each source of uncertainty, the impact in different bins of the final distribution is thus considered fully correlated, while independent sources of uncertainty are treated as uncorrelated.

7.3.1 Sources of systematic uncertainties

The different sources of the systematic uncertainties are summarized in this section

Luminosity

The assigned uncertainty to the integrated luminosity measurement for the data set used in this analysis is 2.5%.

Trigger, lepton reconstruction and identification efficiencies

Discrepancies in the lepton reconstruction and identification efficiencies between data and simulation are corrected by applying to all MC samples data-to-simulation scale

factors measured using $Z/\gamma^* \rightarrow \ell^+\ell^-$ events in the Z peak region [159] that are recorded with unbiased triggers. These factors depend on the lepton p_T and η and are within 2% for electrons and muons. The uncertainty in the determination of the trigger efficiency leads to an uncertainty smaller than 1% in the expected signal yield. Residual difference between the analysis lepton requirements with respect to the trigger selections is well covered by the uncertainty in the trigger efficiency. The uncertainty due to the muon (electron) reconstruction efficiency varies between 0.1% (0.2%) in the central part of the detector up to (0.4%) (1.0%) at large $|\eta|$ values. The uncertainty due to the lepton identification selection is about 0.4% per muon leg, and about 1.1% per electron leg, although with a sizable dependence on η and p_T . The precise methodology of determining these identification scale factors has been expounded above, in Chapter 6. The trigger and reconstruction efficiencies are measured in similar ways, but the fitting procedure is comparatively trivial due to high purity.

Lepton momentum scale and resolution

The lepton momentum scale uncertainty is computed by varying the momentum of the leptons by their uncertainties. The effect on the analysis is rather small, except for very low or very high dilepton p_T .

L1 pre-firing trigger inefficiency

The L1 pre-firing trigger inefficiency is an experimental issue in the data recorded in 2016 which reduces the number of selected events. In addition, it introduces a sizable uncertainty since it is not easy to precisely measure this effect.

The root of the problem is the ECAL trigger primitive (TP) timing. When an ECAL TP pre-fires, its entire energy is assigned to the bunch crossing numbered -1 (BX-1). The trigger rules dictate that after a L1 trigger firing, the next 2 bunch crossings are not available for firing. Thus, if the energy of the TP is large enough to pre-fire a L1 trigger in BX-1, any physics event in BX0 or BX1 is lost. In contrast, if the BX-1 is not accepted, a residual effect on BX0 is present because a null energy is associated with the early TP. Finally, the TP inputs are used by the ECAL selective readout units (SRPs) to decide whether a certain region of the detector needs to be fully readout or zero-suppressed. Crystals associated with the early TP will be readout in zero-suppression mode, injecting a bias in the HLT/offline energy measurement.

The effect can be measured in data by selecting un-prefirable events at BX0, where the L1 trigger fired in BX-3. In that case, by the trigger rules BX-2 and BX-1 cannot possibly have fired the L1 trigger, so BX0 is a clean slate. Unfortunately, the rate of un-prefirable events is rather small compared to the total data sample, about 0.1%, and therefore the statistical precision of that effect is a concern.

Overall, the recommended uncertainty is about 20% of the correction. This translates to a rather small impact on the inclusive analysis, but it leads to a sizable impact on the Z boson rapidity measurement.

Because this effect directly affects the lepton and event reconstruction, the corresponding uncertainty has been merged together with the standard lepton reconstruction efficiency uncertainties.

Background subtraction

The resonant background processes are estimated from simulation, so the uncertainties on the normalization are derived from variations of the QCD scale, α_s and parton distribution functions (PDFs) variations [160, 161, 162, 163, 164, 139]. The PDF and α_s uncertainties for signal and background processes are estimated from the standard deviation of weights from the replicas provided in the NNPDF3.0 parton distribution set [98].

The procedure for estimating uncertainties arising from Parton Distribution Functions (PDF uncertainties) follows the recommendations issued by the PDF4LHC group [165]. For the second run of the LHC, the PDF4LHC group has provides a set of combined PDF sets – the PDF4LHC pdf sets – which are used in the following for the estimation of PDF uncertainty.

The uncertainty in the nonresonant background is estimated to be about 5%, which is rather conservative, but it makes barely any difference in this analysis.

Model dependence in unfolding

The model dependence of unfolding is due to the convolution of the detector resolution effects with the expected spectra. Unfolding is expected to work properly if these differences are small. The predicted amount by which events migrate between bins in the observed distribution must be close to the actual amount of migration. In order to quantify the uncertainty from this effect, a different matrix can be constructed starting from a different MC generator, using fully reconstructed events in order to correctly account for the bin migrations. Alternatively, one could try to reweight the MC to match other predicted spectra. Model dependence is evaluated unfolding the data with the different models and symmetrizing the uncertainties.

Statistical uncertainty estimation

The computation of the statistical uncertainty estimation after unfolding is complicated by the bias introduced by the unfolding itself. A “proper” way of doing this step is not fully established from the statistical point of view, making this an active field of research [166, 167]. Different toys and resampling techniques are available in order to perform such operation, that usually provide a better coverage with respect to the analytical error propagation. The toy generation is performed by ROOUNFOLD, smearing the data distribution using Gaussian uncertainties corresponding to the histogram errors.

7.3.2 Correlations

The correlations among the different bins and the two final states used in the analysis are described in this section.

All the systematic uncertainties are considered to be correlated among the different bins for a single variable, with the exception of the uncertainties with statistical nature. The statistical uncertainties of the MC samples are treated as uncorrelated quantities among the different bins. In addition, the statistical uncertainties in the lepton efficiency scale factors for each lepton η and p_T bin used for such measurements are treated as uncorrelated quantities.

When combining the muon and electron channels, the luminosity, background estimation, and modelling uncertainties are treated as correlated parameters, all others are considered as uncorrelated between them.

7.3.3 Total systematic uncertainty

A graphical representation of the different contributions to the systematic uncertainty is shown in Figures 7-7, 7-8, and 7-9. A summary of the systematic uncertainties related to the lepton efficiency measurements of muons and electrons is shown in Figure 7-10.

The differential cross section measurements can also be performed with respect to the inclusive cross section. Therefore, in that case the uncertainties are largely reduced, in particular the lepton reconstruction selection efficiency mostly cancel out, and the effect due to the integrated luminosity completely cancel out. Those uncertainties are summarized in Figure 7-11.

7.4 Results

7.4.1 Inclusive fiducial cross section measurements

The inclusive fiducial cross section is measured in the muon-pair and electron-pair final states. The combined cross section is obtained by treating the systematic uncertainties, except the uncertainties due to the integrated luminosity and background estimation, as uncorrelated between the two final states. The luminosity and background estimation uncertainties are treated as fully correlated in the combined measurement. The uncertainties are dominated by the uncertainty in the integrated luminosity and the lepton efficiency. A summary of the systematic uncertainties is shown in Table 7.2. The measured cross sections are shown in Table 7.3.

The measured cross section values agree with the theoretical predictions. The predicted values are $\sigma_{Z \rightarrow \ell\ell} = 682 \pm 55$ pb with MADGRAPH5_AMC@NLO using the NNPDF 3.0 [98] NLO PDF set, and $\sigma_{Z \rightarrow \ell\ell} = 719 \pm 8$ pb with fixed order FEWZ [168, 169, 170, 171] at NNLO accuracy in QCD using the NNPDF 3.1 [172] NNLO PDF set. The theoretical uncertainties for MADGRAPH5_AMC@NLO and FEWZ include statistical, PDF, and scale uncertainties. The scale uncertainties are estimated by varying the renormalization and factorization scales independently up and down by a

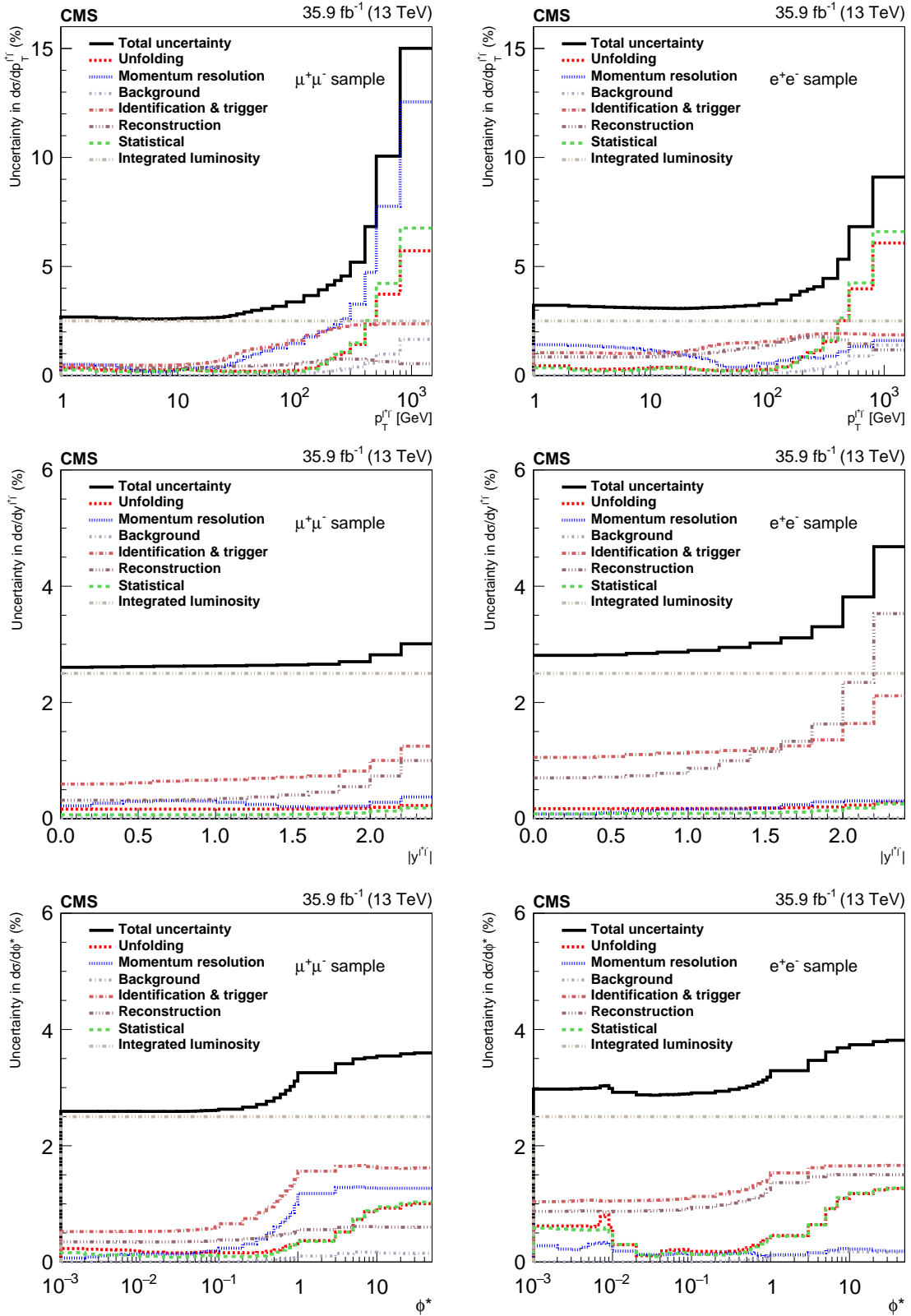


Figure 7-7: Summary of the systematic uncertainties of muons (left) and electrons (right) for the p_T^Z analysis (top), the $|y^Z|$ analysis (center), and the ϕ^* analysis (bottom).

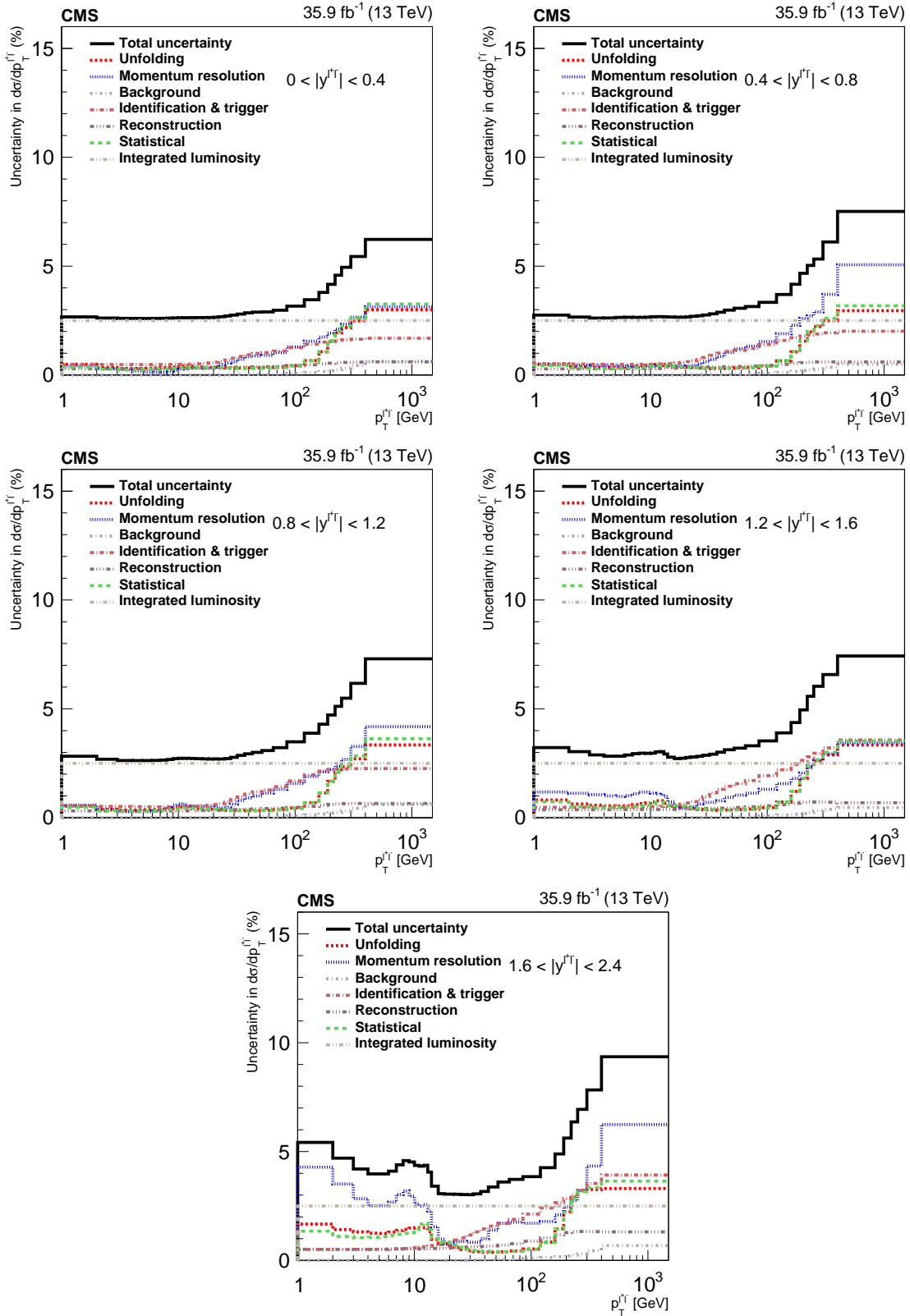


Figure 7-8: Summary of the systematic uncertainties for the p_T^Z analysis of muons in the $0.0 < |y^Z| < 0.4$ region (top left), $0.4 < |y^Z| < 0.8$ region (top right), $0.8 < |y^Z| < 1.2$ region (center left), $1.2 < |y^Z| < 1.6$ region (center right), and $1.6 < |y^Z| < 2.4$ region (bottom).

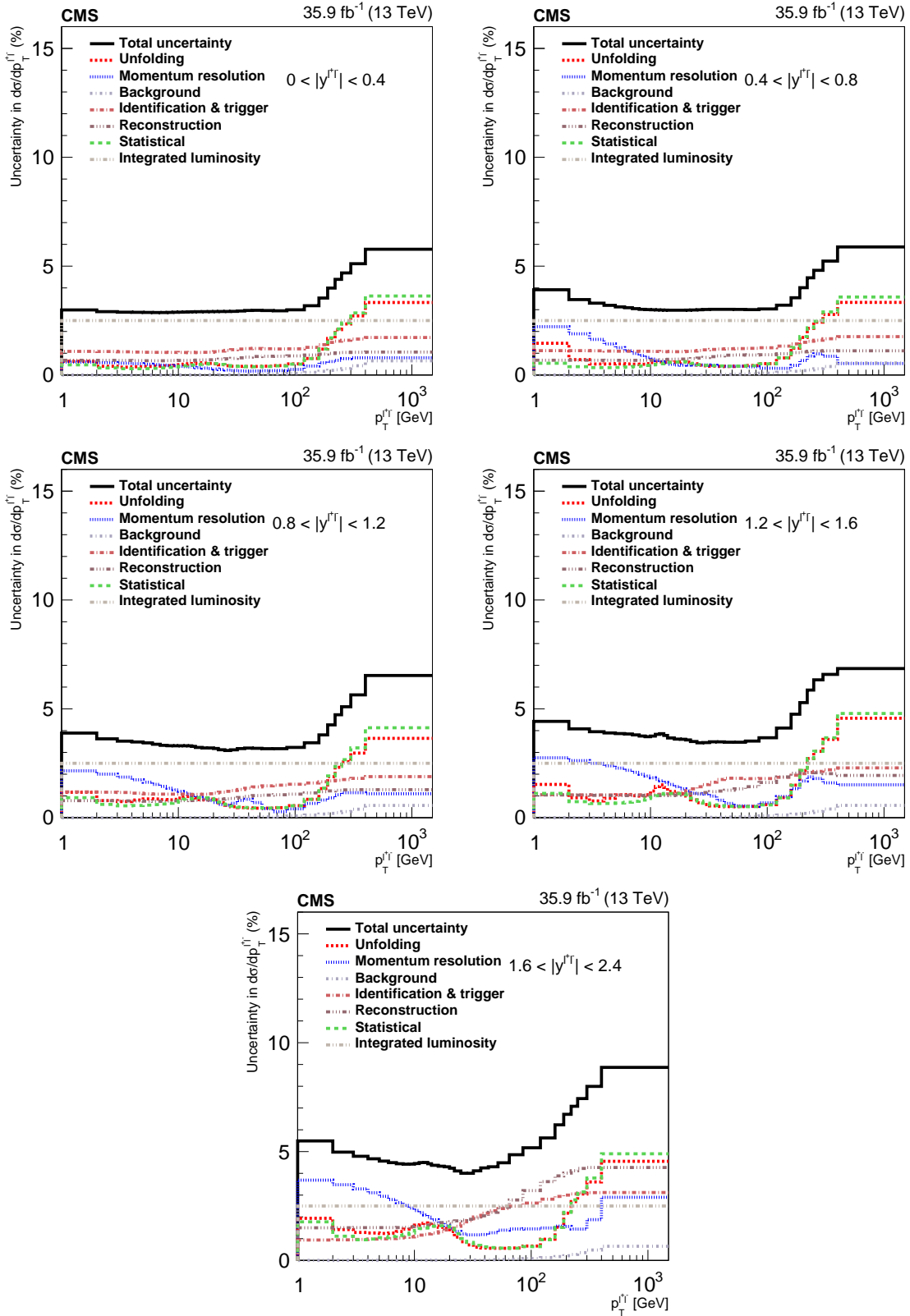


Figure 7-9: Summary of the systematic uncertainties for the p_T^Z analysis of electrons in the $0.0 < |y^Z| < 0.4$ region (top left), $0.4 < |y^Z| < 0.8$ region (top right), $0.8 < |y^Z| < 1.2$ region (center left), $1.2 < |y^Z| < 1.6$ region (center right), and $1.6 < |y^Z| < 2.4$ region (bottom).

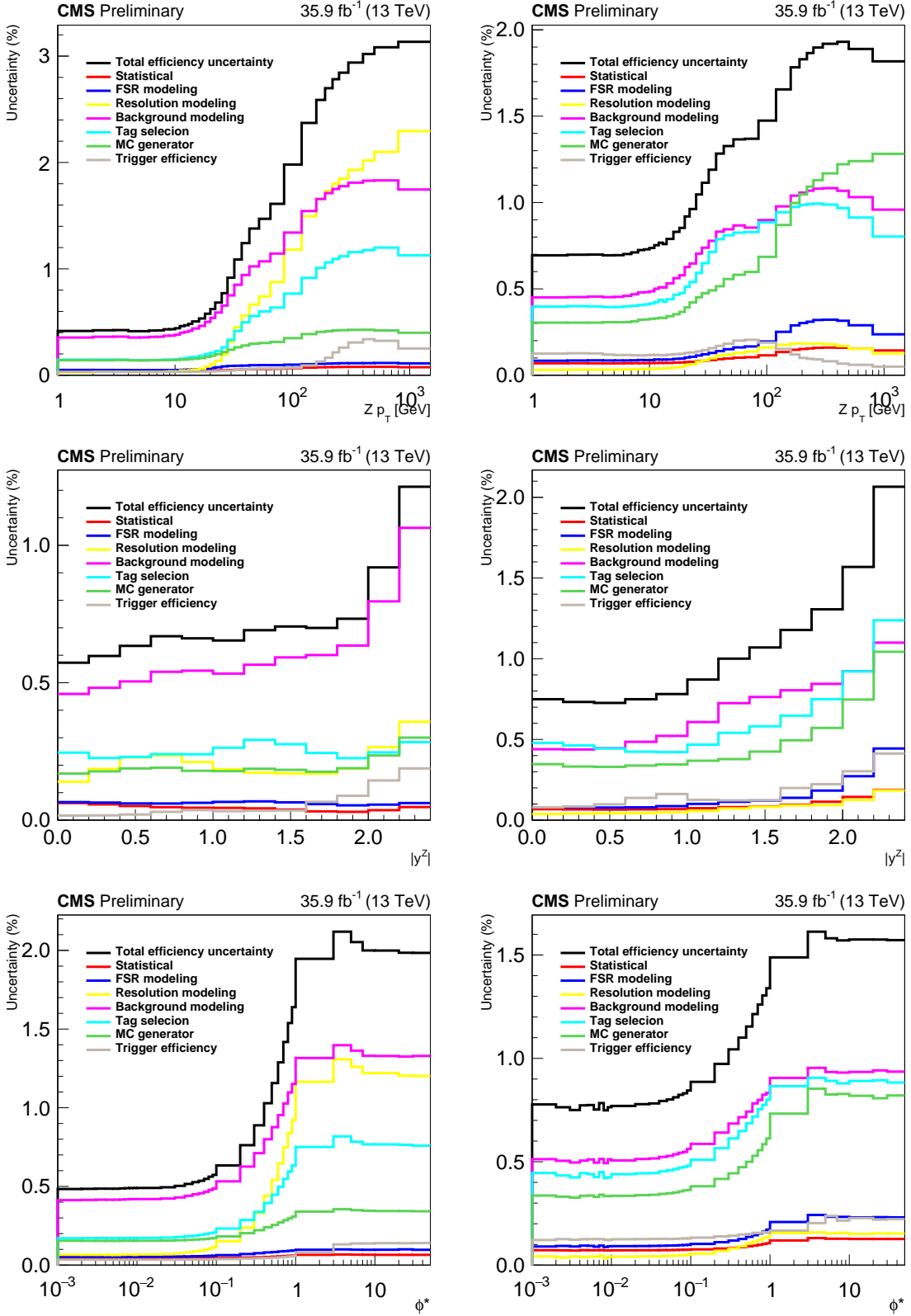


Figure 7-10: Summary of the systematic uncertainties related to the lepton efficiency measurements of muons (left) and electrons (right) for the p_T^Z analysis (top), the $|y^Z|$ analysis (center), and the ϕ^* analysis (bottom).

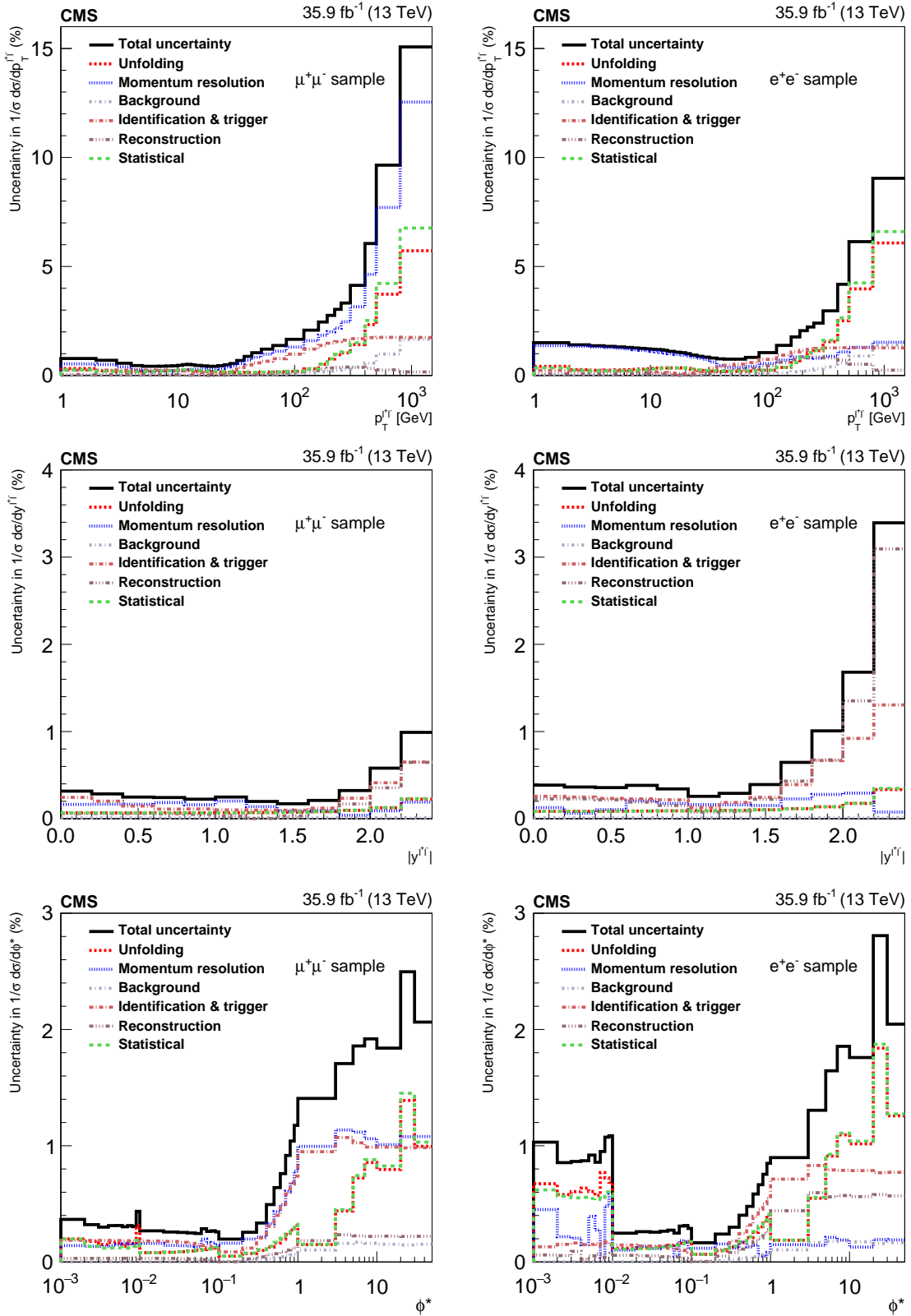


Figure 7-11: Summary of the systematic uncertainties of muons (left) and electrons (right) for the p_T^Z analysis (top), the $|y^Z|$ analysis (center), and the ϕ^* analysis (bottom) for the differential cross section measurements with respect to the inclusive cross section.

Source	$Z \rightarrow \mu\mu$ (%)	$Z \rightarrow ee$ (%)
Luminosity	2.5	2.5
Muon reconstruction efficiency	0.4	-
Muon selection efficiency	0.7	-
Muon momentum scale	0.1	-
Electron reconstruction efficiency	-	0.9
Electron selection efficiency	-	0.9
Electron momentum scale	-	0.2
Background estimation	< 0.1	< 0.1
Total (excluding luminosity)	0.8	1.3

Table 7.2: Summary of the systematic uncertainties for the inclusive fiducial cross section measurements.

Cross section	$\sigma \mathcal{B}$ [pb]
$\sigma_{Z \rightarrow \mu\mu}$	694 ± 6 (syst) ± 17 (lumi)
$\sigma_{Z \rightarrow ee}$	711 ± 9 (syst) ± 18 (lumi)
$\sigma_{Z \rightarrow \ell\ell}$	699 ± 5 (syst) ± 17 (lumi)

Table 7.3: The measured inclusive fiducial cross sections in the muon-pair and electron-pair final states. The combined measurement is also shown.

factor of two from their nominal values (removing combinations where both variations differ by a factor of four) and taking the largest variations as the uncertainty.

7.4.2 Differential cross section measurements

The measured differential cross sections corrected for detector effects are compared to various theoretical predictions. The measured absolute cross sections in bins of $|y^Z|$ are shown in Figure 7-12. The measurement is compared to predictions using parton shower modeling with both MADGRAPH5_AMC@NLO and POWHEG at NLO accuracy in QCD using the NNPDF 3.0 PDF set. A comparison with fixed order prediction at NNLO accuracy with FEWZ using the NNPDF 3.1 NNLO PDF set is also shown. The MADGRAPH5_AMC@NLO and POWHEG predictions are consistent with the data within the theoretical uncertainties. The FEWZ prediction with the NNPDF 3.1 PDF set is within 5% of the measurement over the entire $|y^Z|$ range.

Figure 7-13 shows the measured absolute cross sections in bins of p_T^Z . The measurement is compared to predictions using parton shower modeling with MADGRAPH5_AMC@NLO and POWHEG. A comparison with POWHEG using the MiNLO procedure and using the NNPDF 3.1 NLO PDF set is also shown. The predictions are consistent with the data within the theoretical uncertainties. The POWHEG predictions at high- p_T (above 100 GeV) disagree with the data. The higher order accuracy of the MADGRAPH5_AMC@NLO and POWHEG-MiNLO predictions at high- p_T lead to an improved agreement with the data.

Figure 7-14 (left) shows comparisons to resummed calculations with RESBOS [173, 174, 175] and GENEVA [176]. A comparison to the MADGRAPH5_AMC@NLO prediction is also included as a reference. The RESBOS predictions are obtained using the *CP* version at NNLL accuracy with CT14 NNLO PDF set and are consistent with the data within the theoretical uncertainties at low- p_T but disagree with the measurements at high- p_T . The GENEVA predictions include resummation to NNLL accuracy where the resulting parton-level events are further combined with parton showering and hadronization provided by PYTHIA8. The GENEVA predictions are generally consistent with the data within the theoretical uncertainties but disagree with the data at low p_T (below 30 GeV). The CUETP8M1 tune is used for the underlying-event modeling for the shown GENEVA predictions. A dedicated tune for the underlying-event modeling will lead to improved agreement with the data.

The p_T^Z distribution for $p_T > 30$ GeV is compared to fixed order predictions as shown in Figure 7-14 (right). A comparison to the MADGRAPH5_AMC@NLO prediction is included as a reference. The data is compared to the FEWZ predictions at NNLO in QCD and to the complete NNLO predictions of vector boson production in association with a jet [7, 8]. The central renormalization and factorization scale values were chosen to be $\mu_{R/F} = \sqrt{(P_{TZ}^2 + M_{ll}^2)}$ for the FEWZ and Z+1 jet at NNLO predictions. The scale uncertainties are estimated by varying the renormalization and factorization scales up and down together within a factor of two. The CT14 [177] NNLO PDF set is used for the Z+1 jet at NNLO predictions. The predictions are consistent with the data within the theoretical uncertainties. As can be seen the Z+1 jet at NNLO calculations significantly reduce the factorization and renormalization scale uncertainties. EW corrections are important at high- p_T with correction factors

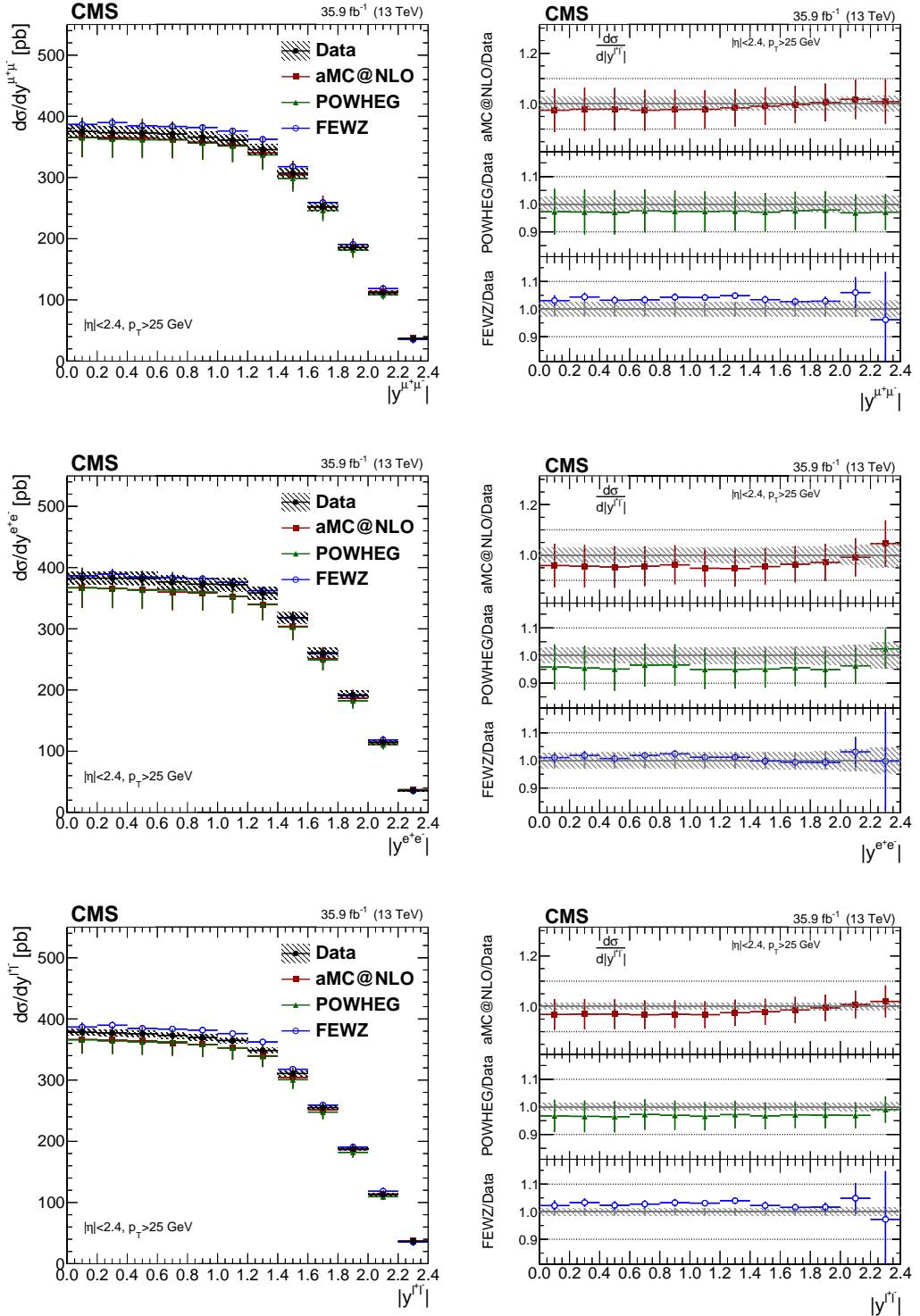


Figure 7-12: The measured absolute cross sections (left) in bins of $|y^Z|$ for the muon-pair (top) and electron-pair (middle) final states, and for the combination (bottom). The ratios of the predictions to the data are also shown (right). The shaded band around the data points (black) correspond to the total experimental uncertainty. The measurement is compared to predictions with `MADGRAPH5_AMC@NLO` (square red markers), `POWHEG` (green triangles), and `FEWZ` (blue circles). The error bands around the predictions correspond to the statistical, PDF, and scale uncertainties.

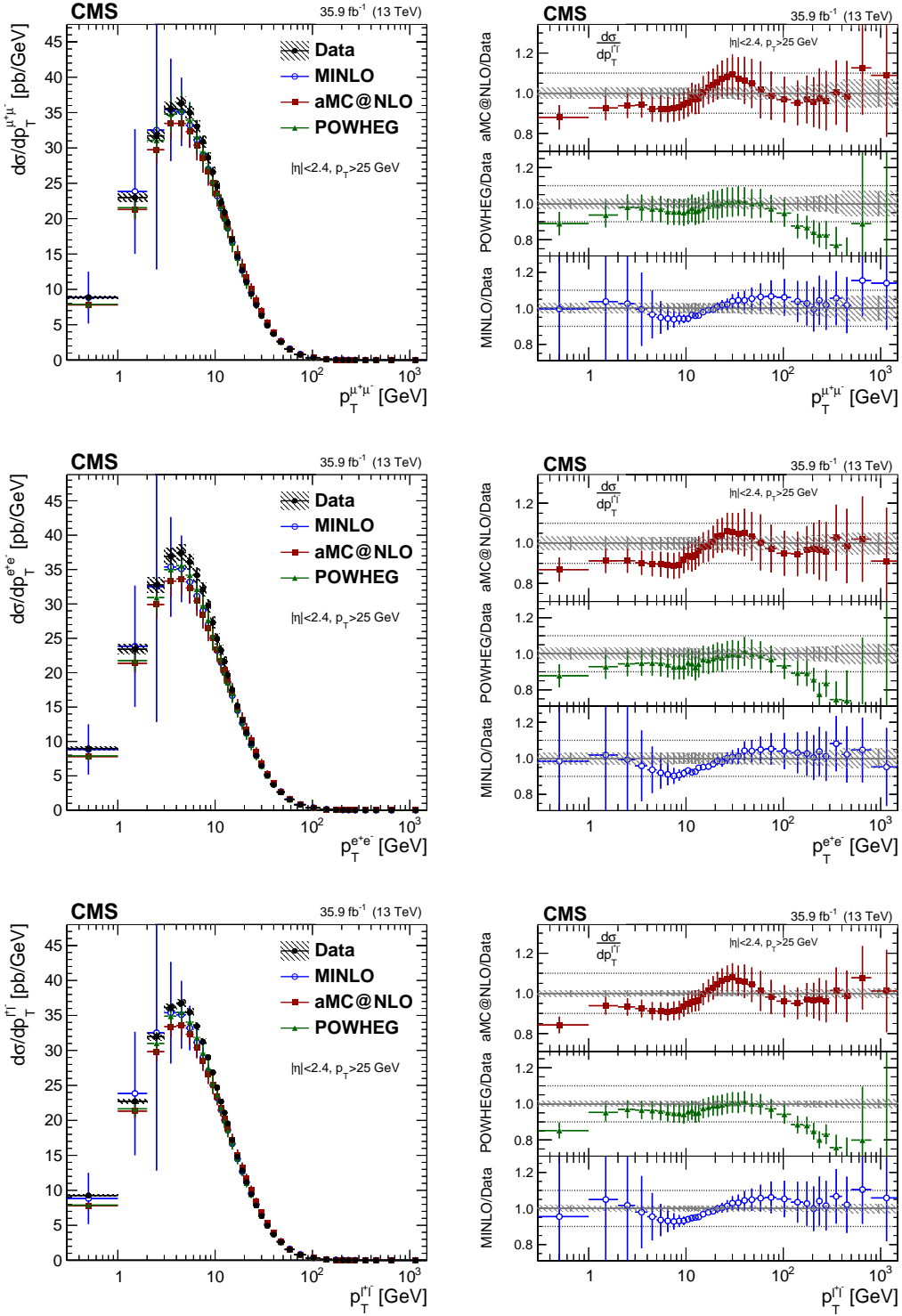


Figure 7-13: The measured absolute cross sections (left) in bins of p_T^Z for the muon-pair (top) and electron-pair (bottom) final states, and for the combination (bottom). The ratios of the predictions to the data are also shown (right). The shaded band around the data points (black) correspond to the total experimental uncertainty. The measurement is compared to predictions with MADGRAPH5_AMC@NLO (square red markers), POWHEG (green triangles), and POWHEG-MINLO (blue circles). The error bands around the predictions correspond to the statistical, PDF, and scale uncertainties.

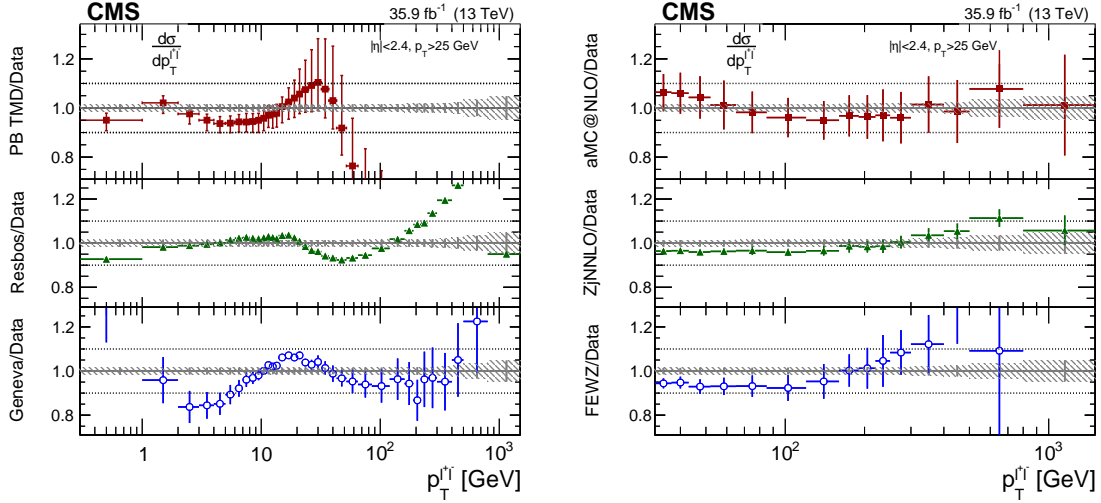


Figure 7-14: The ratios of the predictions to the data in bins of p_T^Z for the combination of the muon-pair and electron-pair final states. The shaded band around the data points (black) correspond to the total experimental uncertainty. The left plot shows comparisons to predictions with `MADGRAPH5_AMC@NLO` (square red markers), `Resbos` (green triangles), and `GENEVA` (blue circles). The right plot shows the p_T^Z distribution for $p_T > 30$ GeV compared to predictions with `MADGRAPH5_AMC@NLO` (square red markers), $Z + 1$ jet at `NNLO` (green triangles), and `FEWZ` (blue circles). The error bands around the predictions correspond to the statistical, PDF, and scale uncertainties.

of up to 0.9 at $p_T = 500$ GeV and 0.8 at $p_T = 1000$ GeV [9, 10]. The EW corrections are not included in the predictions shown in Figure 7-14.

Figure 7-15 shows the measured absolute cross sections in bins of ϕ^* . The measurements is compared to predictions from `MADGRAPH5_AMC@NLO`, `POWHEG`, and `POWHEG-MINLO`. The predictions are consistent with the data within the theoretical uncertainties and describe data well at low p_T .

Summaries of the absolute double-differential cross section measurements in p_T^Z and $|y^Z|$ are shown in Figures 7-16–7-20. The normalized cross section measurements in bins of p_T^Z and ϕ^* are shown in Figure 7-21. The measured normalized cross section uncertainties are smaller than 0.5% for $\phi^* < 0.5$ and for $p_T^Z < 50$ GeV. Summaries of the normalized double-differential cross section measurements in p_T^Z and $|y^Z|$ are shown in Figures 7-23–7-27. The measurements are compared to predictions using parton shower modeling with `MADGRAPH5_AMC@NLO`, `POWHEG`, and `POWHEG-MINLO`. The predictions are consistent with the data within the theoretical uncertainties.

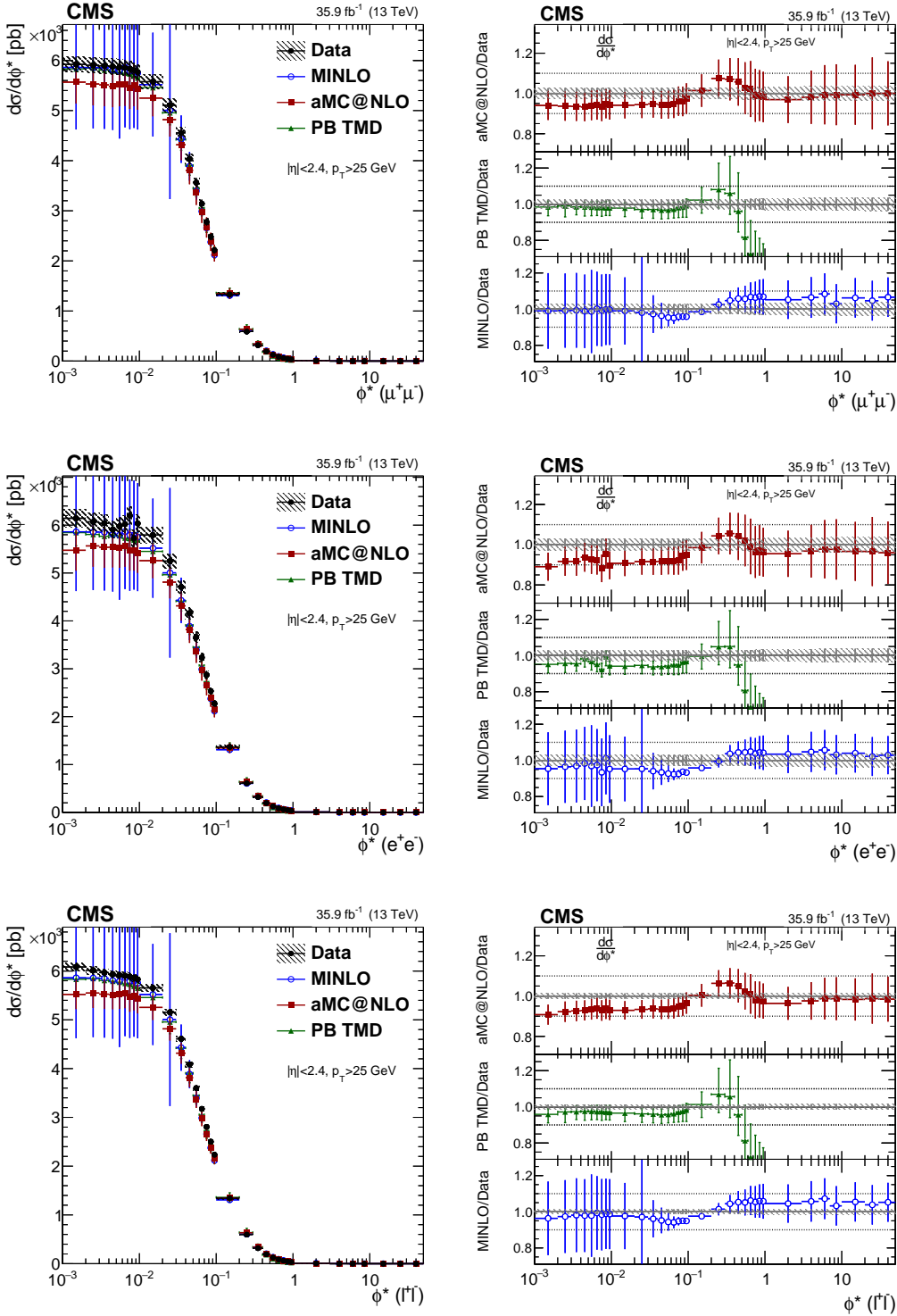


Figure 7-15: The measured absolute cross sections (left) in bins of ϕ^* for the muon-pair (top) and electron-pair (bottom) final states, and for the combination (bottom). The ratios of the predictions to the data are also shown (right). The shaded band around the data points (black) correspond to the total experimental uncertainty. The measurement is compared to predictions with MADGRAPH5_AMC@NLO (square red markers), POWHEG (green triangles), and POWHEG-MINLO (blue circles). The error bands around the predictions correspond to the statistical, PDF, and scale uncertainties.

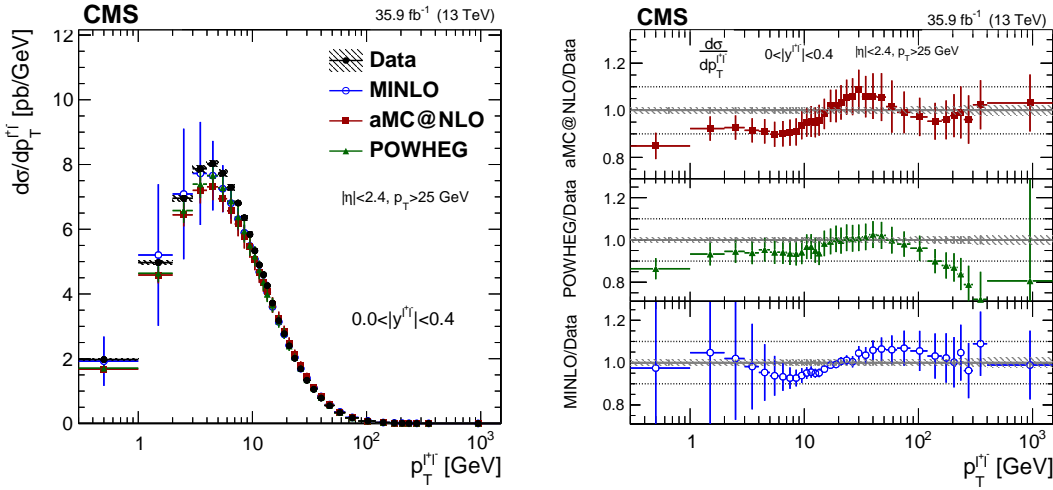


Figure 7-16: The measured absolute cross sections (left) in bins of p_T^Z for the $0.0 < |y^Z| < 0.4$ region. The ratios of the predictions to the data are also shown (right). The shaded bands around the data points (black) correspond to the total experimental uncertainty. The measurement is compared to the predictions with `MADGRAPH5_AMC@NLO` (square red markers), `POWHEG` (green triangles), and `POWHEG-MINLO` (blue circles). The error bands around the predictions correspond to the combined statistical, PDF, and scale uncertainties.

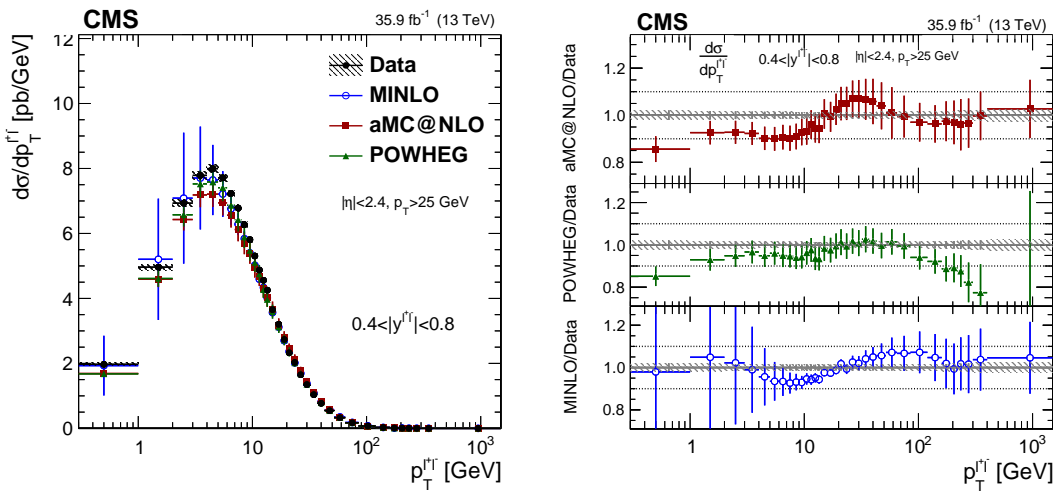


Figure 7-17: The measured absolute cross sections (left) in bins of p_T^Z for the $0.4 < |y^Z| < 0.8$ region. The ratios of the predictions to the data are also shown (right). The shaded bands around the data points (black) correspond to the total experimental uncertainty. The measurement is compared to the predictions with `MADGRAPH5_AMC@NLO` (square red markers), `POWHEG` (green triangles), and `POWHEG-MINLO` (blue circles). The error bands around the predictions correspond to the combined statistical, PDF, and scale uncertainties.

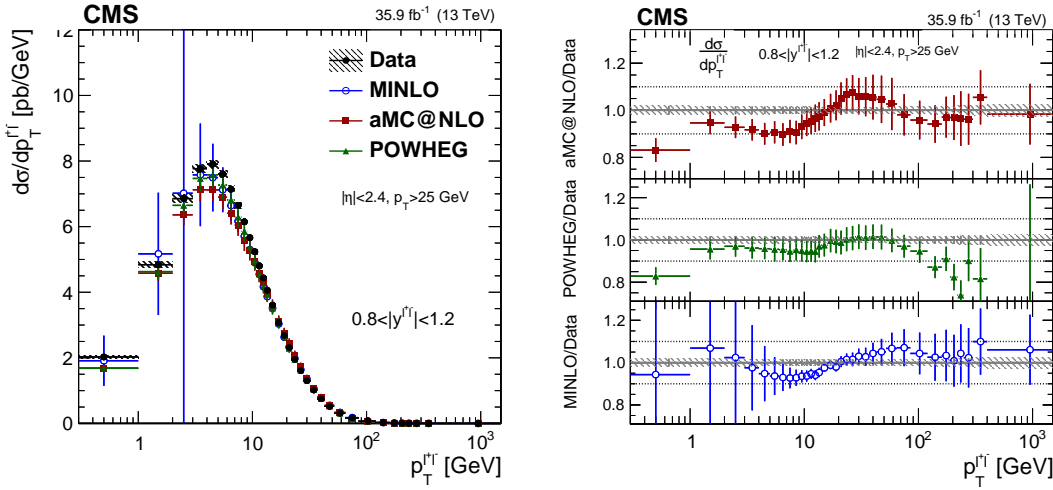


Figure 7-18: The measured absolute cross sections (left) in bins of p_T^Z for the $0.8 < |y^Z| < 1.2$ region. The ratios of the predictions to the data are also shown (right). The shaded bands around the data points (black) correspond to the total experimental uncertainty. The measurement is compared to the predictions with `MADGRAPH5_AMC@NLO` (square red markers), `POWHEG` (green triangles), and `POWHEG-MINLO` (blue circles). The error bands around the predictions correspond to the combined statistical, PDF, and scale uncertainties.

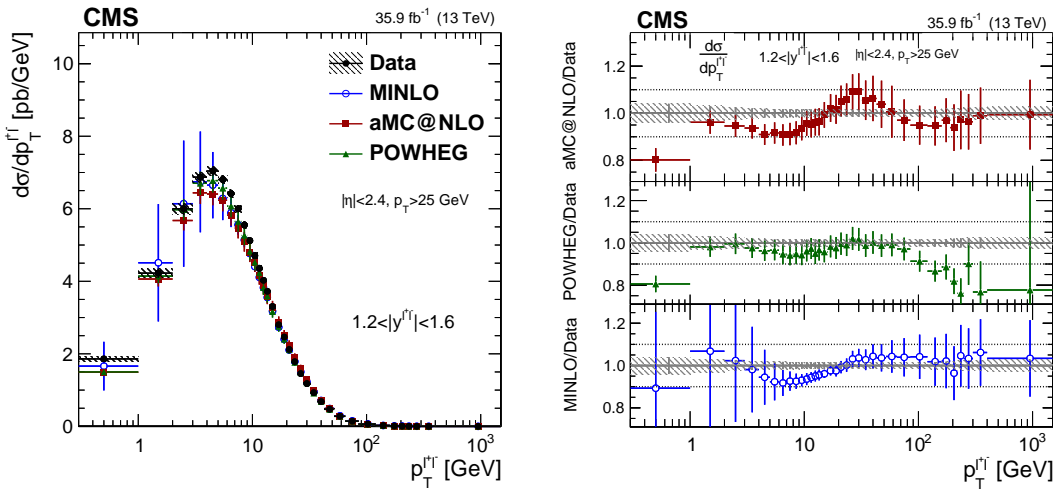


Figure 7-19: The measured absolute cross sections (left) in bins of p_T^Z for the $1.2 < |y^Z| < 1.6$ region. The ratios of the predictions to the data are also shown (right). The shaded bands around the data points (black) correspond to the total experimental uncertainty. The measurement is compared to the predictions with `MADGRAPH5_AMC@NLO` (square red markers), `POWHEG` (green triangles), and `POWHEG-MINLO` (blue circles). The error bands around the predictions correspond to the combined statistical, PDF, and scale uncertainties.

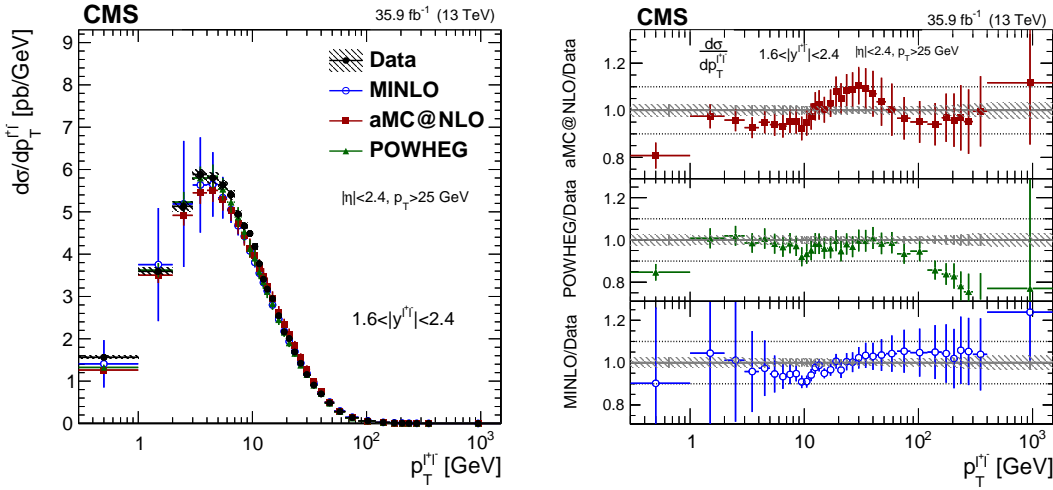


Figure 7-20: The measured absolute cross sections (left) in bins of p_T^Z for the $1.6 < |y^Z| < 2.4$ region. The ratios of the predictions to the data are also shown (right). The shaded bands around the data points (black) correspond to the total experimental uncertainty. The measurement is compared to the predictions with `MADGRAPH5_AMC@NLO` (square red markers), `POWHEG` (green triangles), and `POWHEG-MINLO` (blue circles). The error bands around the predictions correspond to the combined statistical, PDF, and scale uncertainties.

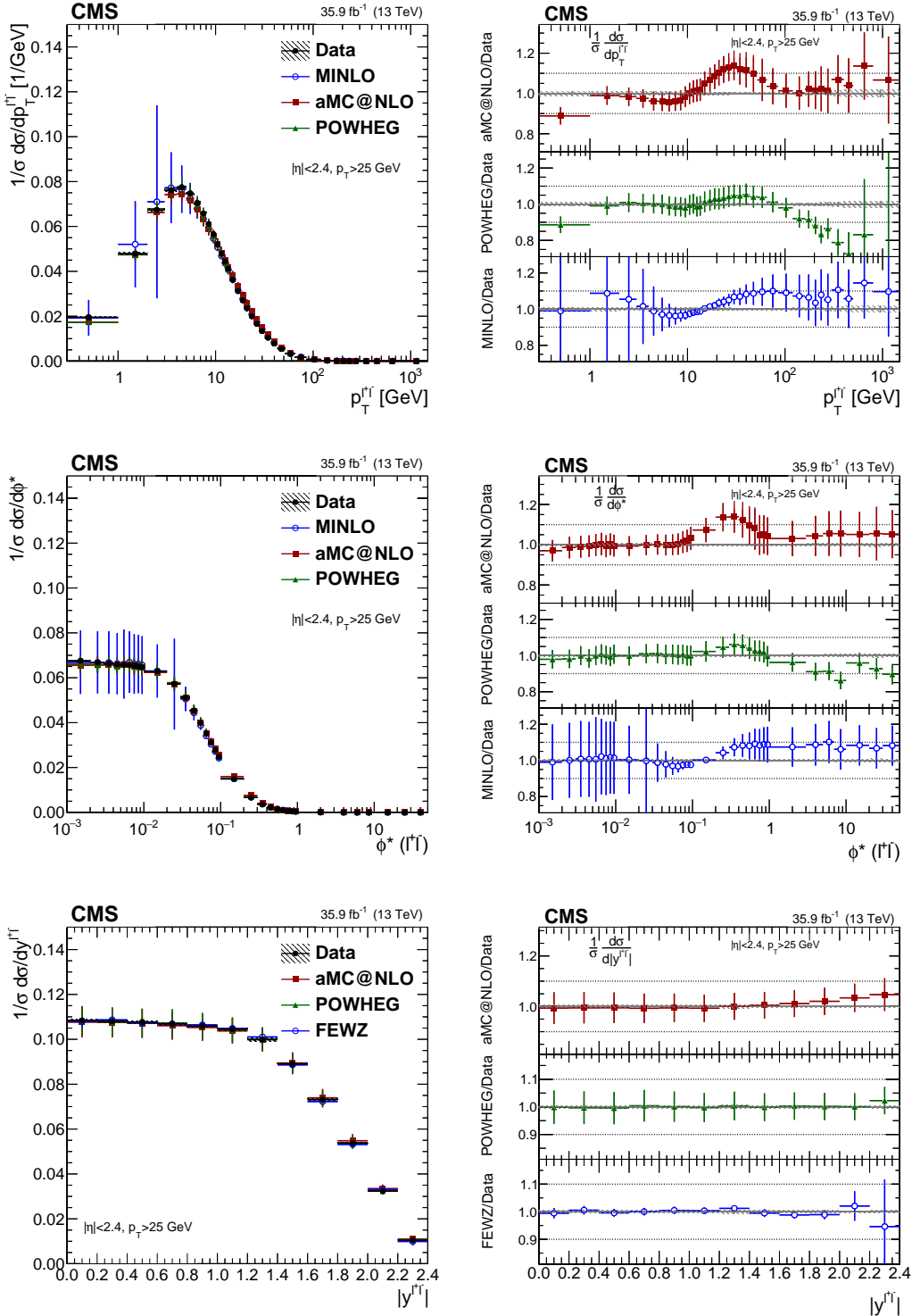


Figure 7-21: The measured normalized cross sections (left) in bins of p_T^Z (upper), ϕ^* (middle), and $|y^Z|$ (lower) for the combined measurement. The ratios of the predictions to the data are also shown (right). The shaded bands around the data points (black) correspond to the total experimental uncertainty. The p_T^Z and ϕ^* measurements are compared to the predictions with MADGRAPH5_AMC@NLO (square red markers), POWHEG (green triangles), and POWHEG-MINLO (blue circles). The $|y^Z|$ measurement is compared to the predictions with MADGRAPH5_AMC@NLO (square red markers), POWHEG (green triangles), and FEWZ (blue circles). The error bars around the predictions correspond to the combined statistical, PDF, and scale uncertainties.

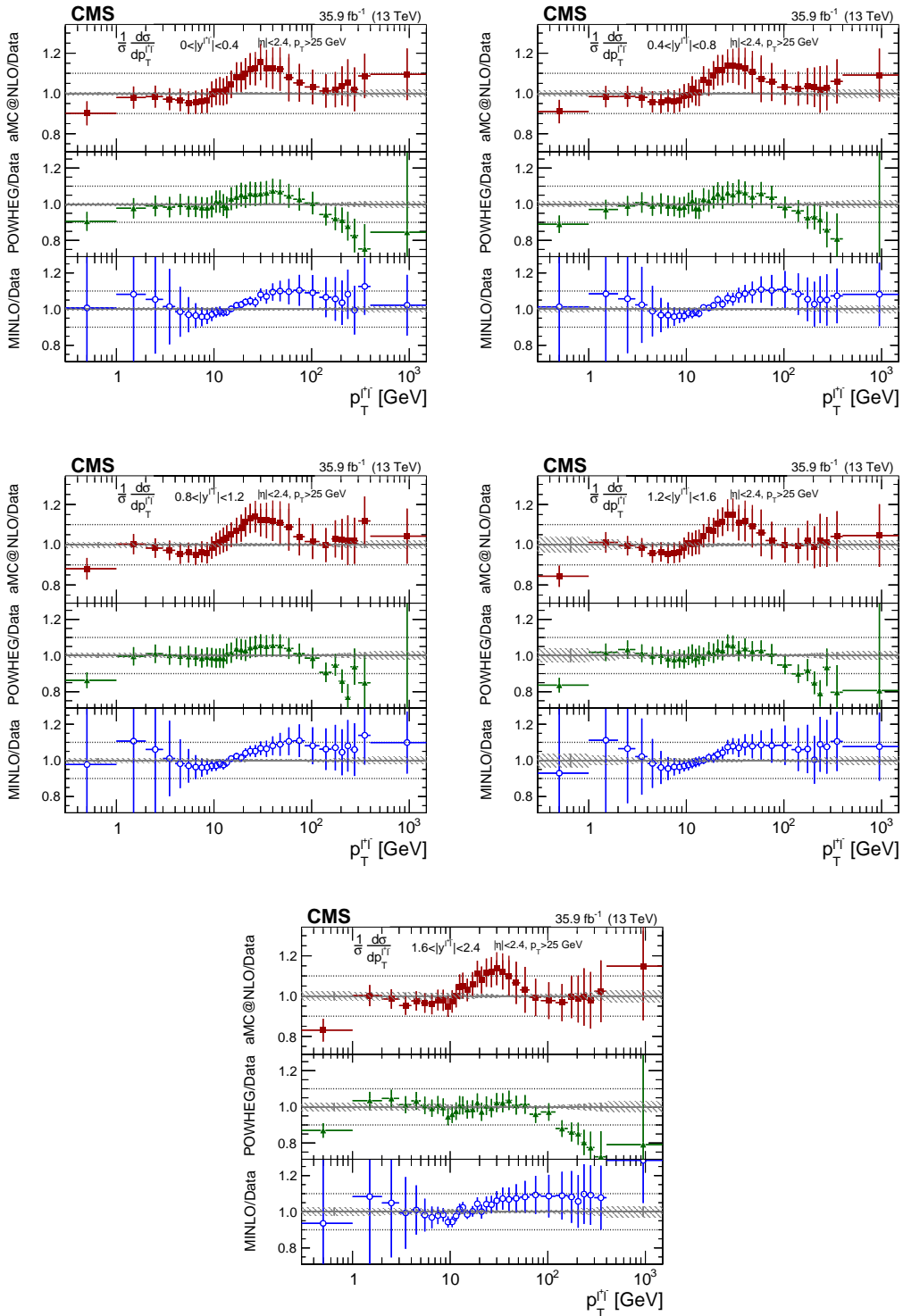


Figure 7-22: The ratios of the predictions to the data for the combined measurements of the normalized cross sections in bins of p_T^Z for the $0.0 < |y^Z| < 0.4$ bin (top left), $0.4 < |y^Z| < 0.8$ bin (top right), $0.8 < |y^Z| < 1.2$ bin (middle left), $1.2 < |y^Z| < 1.6$ bin (middle right), and $1.6 < |y^Z| < 2.4$ bin (bottom). The measurement is compared to predictions with `MADGRAPH5_AMC@NLO` (square red markers), `POWHEG` (green triangles), and `POWHEG-MinLO` (blue circles).

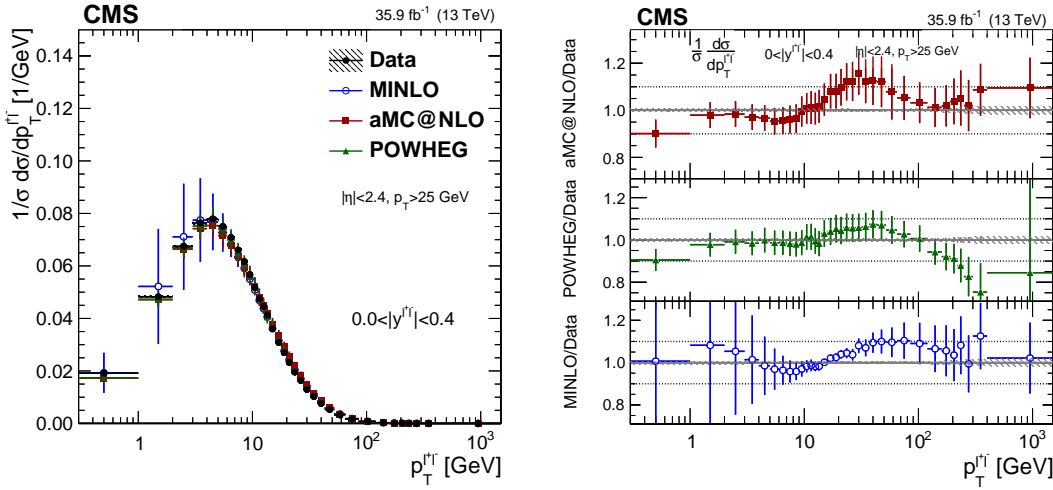


Figure 7-23: The measured normalized cross sections (left) in bins of p_T^Z for the $0.0 < |y^Z| < 0.4$ region. The ratios of the predictions to the data are also shown (right). The shaded bands around the data points (black) correspond to the total experimental uncertainty. The measurement is compared to the predictions with MADGRAPH5_AMC@NLO (square red markers), POWHEG (green triangles), and POWHEG-MINLO (blue circles). The error bands around the predictions correspond to the combined statistical, PDF, and scale uncertainties.

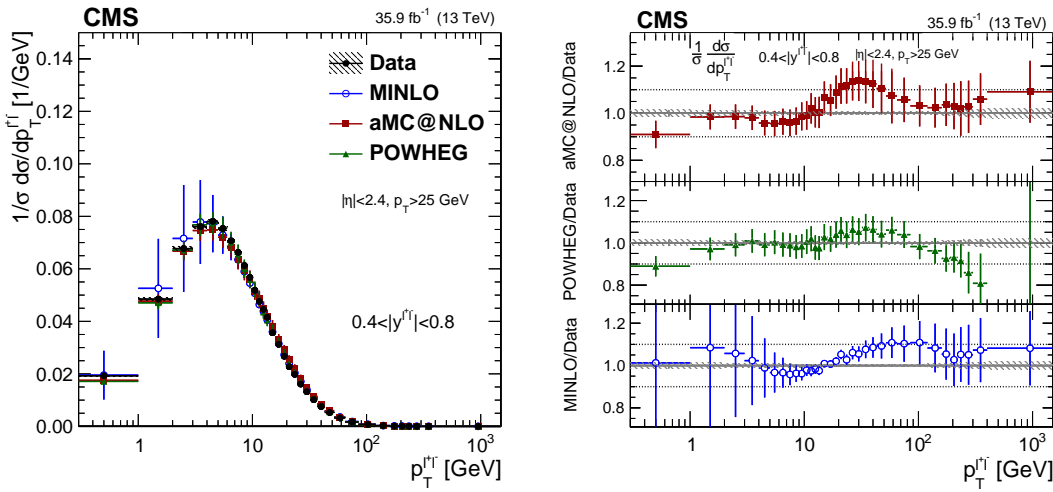


Figure 7-24: The measured normalized cross sections (left) in bins of p_T^Z for the $0.4 < |y^Z| < 0.8$ region. The ratios of the predictions to the data are also shown (right). The shaded bands around the data points (black) correspond to the total experimental uncertainty. The measurement is compared to the predictions with MADGRAPH5_AMC@NLO (square red markers), POWHEG (green triangles), and POWHEG-MINLO (blue circles). The error bands around the predictions correspond to the combined statistical, PDF, and scale uncertainties.

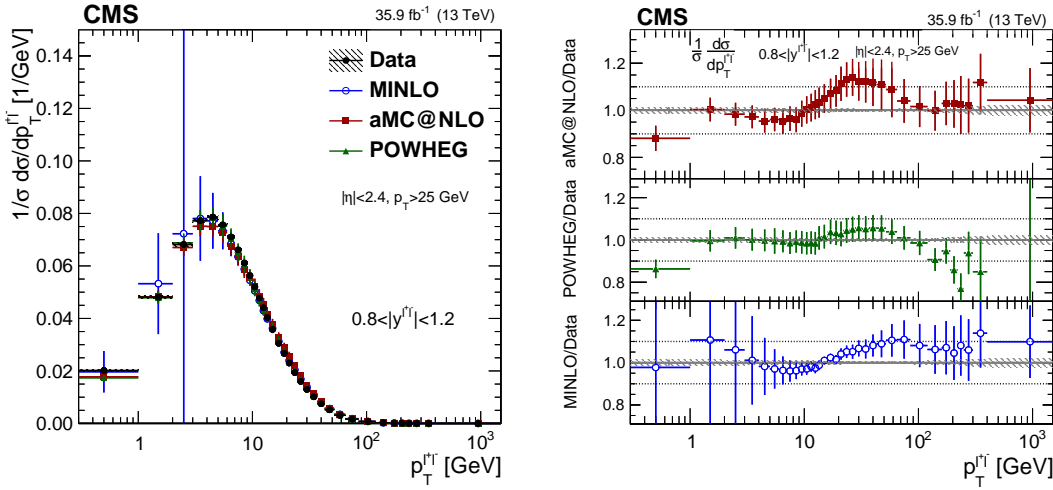


Figure 7-25: The measured normalized cross sections (left) in bins of p_T^Z for the $0.8 < |y^Z| < 1.2$ region. The ratios of the predictions to the data are also shown (right). The shaded bands around the data points (black) correspond to the total experimental uncertainty. The measurement is compared to the predictions with MADGRAPH5_AMC@NLO (square red markers), POWHEG (green triangles), and POWHEG-MINLO (blue circles). The error bands around the predictions correspond to the combined statistical, PDF, and scale uncertainties.

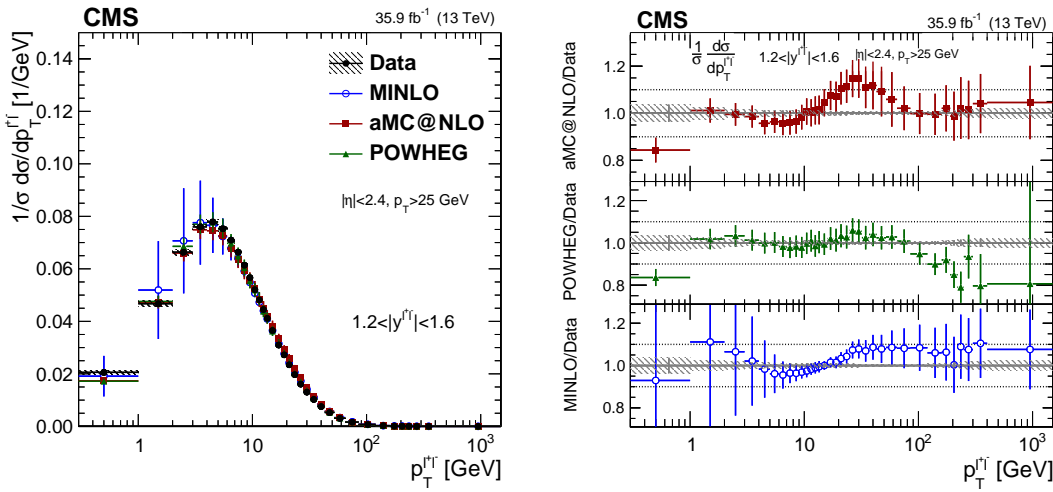


Figure 7-26: The measured normalized cross sections (left) in bins of p_T^Z for the $1.2 < |y^Z| < 1.6$ region. The ratios of the predictions to the data are also shown (right). The shaded bands around the data points (black) correspond to the total experimental uncertainty. The measurement is compared to the predictions with MADGRAPH5_AMC@NLO (square red markers), POWHEG (green triangles), and POWHEG-MINLO (blue circles). The error bands around the predictions correspond to the combined statistical, PDF, and scale uncertainties.

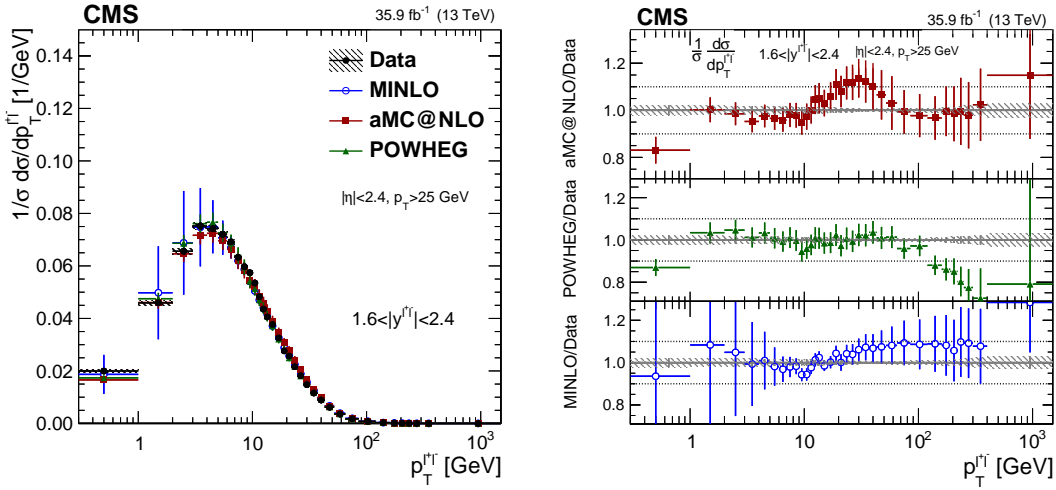


Figure 7-27: The measured normalized cross sections (left) in bins of p_T^Z for the $1.6 < |y^Z| < 2.4$ region. The ratios of the predictions to the data are also shown (right). The shaded bands around the data points (black) correspond to the total experimental uncertainty. The measurement is compared to the predictions with MADGRAPH5_AMC@NLO (square red markers), POWHEG (green triangles), and POWHEG-MINLO (blue circles). The error bands around the predictions correspond to the combined statistical, PDF, and scale uncertainties.

Chapter 8

Diboson studies

In dark matter searches involving a Z boson in the final state, the resonant diboson processes ZZ and WZ are an irreducible background. In the case of hadronic Z boson decays, they are not a major worry, since other hadronic background processes such as pure QCD totally beat out the diboson processes based on the cross-sections [178]. On the other hand, in final states with little hadronic activity, the other background processes which contribute substantially are easy to reject. These diboson processes are the main problem due to the limitations of theoretical calculations.

In this chapter, I survey the current status of the diboson theoretical calculations. The picture is bleak, but there is a silver lining: it is possible to control the cumbersome theoretical uncertainties by exploring the experimental data. I will discuss two separate analysis selections to obtain pure samples of experimental data with fully visible ZZ and WZ processes. These data are interesting on their own to compare to the simulation as a precision electroweak measurement. In the context of this work, they are also a crucial ingredient for the dark matter search of Chapter 9.

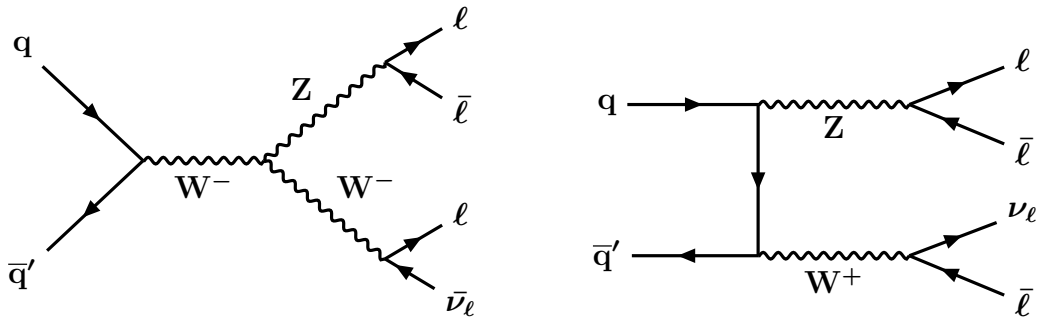


Figure 8-1: Leading order WZ production mechanisms in the s -channel and the t -channel.

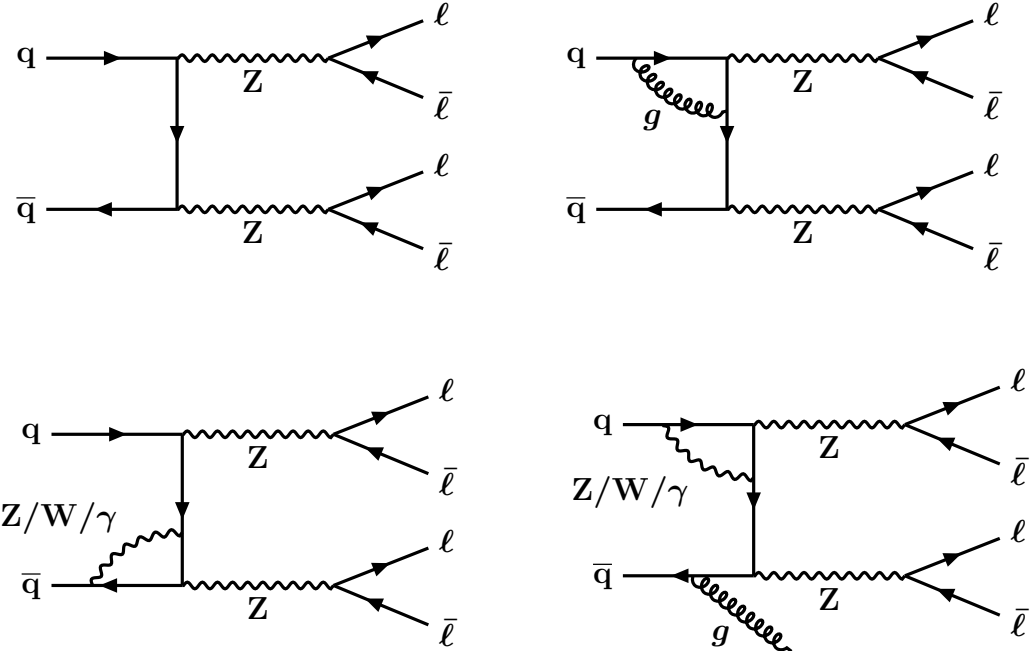


Figure 8-2: Clockwise from upper left: ZZ production at leading order; ZZ production at NLO in QCD; ZZ production at NLO in both QCD and EW; ZZ production at NLO only in EW.

8.1 Theoretical uncertainties in diboson calculations

All simulated physics processes in this work are susceptible to uncertainties due to: the proton parton distribution functions; the QCD scale, α_s ; and the renormalization and factorization scales in the quantum field theory. Consistent with the other processes, these effects are propagated to both the overall cross sections and the transverse momentum spectra of the ZZ and WZ processes. For the purposes of this chapter, it suffices to say that the effect of these is roughly 10%.

8.1.1 Electroweak corrections

Electroweak corrections for the ZZ process are implemented on the basis of a table given by the authors of Refs. [179, 180]. They are a function of the flavour of the quarks which initiated the hard process (u , d or b , treating s as d and c as u), and of the Mandelstam variables \hat{s} and \hat{t} computed in the center-of-mass frame.

The computation of these electroweak corrections has been realized in the approximation where the transverse momentum of complementary jets is small with respect to that of the Z bosons. In this case, the kinematics of the process are completely described by the \hat{s} and \hat{t} variables. The variables \hat{s} and \hat{t} are computed at generator-level. Since \hat{s} is the center-of-mass energy squared, it is computed as the generator-level diboson mass m_{ZZ} .

In an interaction of the type $1 + 2 \rightarrow 3 + 4$, one has $\hat{t} = (p_1 - p_3)^2$. Let us denote the 4-momentum of the first initial state quark as p_{q1}^* , and that of the first Z boson

produced as $p_{Z_1}^*$. Neglecting the quarks' bare masses, this gives:

$$\begin{aligned}\hat{t} &= (p_{q_1}^* - p_{Z_1}^*)^2 = p_{q_1}^{*2} + p_{Z_1}^{*2} - 2p_{q_1}^* \cdot p_{Z_1}^* \\ &\simeq 0 + m_Z^2 - 2\left(\frac{\hat{s}}{4} - \frac{\sqrt{\hat{s}}}{2} \cos \theta \sqrt{\frac{\hat{s}}{4} - m_Z^2}\right) \\ &= m_Z^2 - \frac{\hat{s}}{2} + \cos \theta \sqrt{\frac{\hat{s}^2}{4} - m_Z^2 \hat{s}},\end{aligned}\tag{8.1}$$

The angle θ is determined as the angle between the Z boson considered and the direction of the incident quarks in the center-of-mass frame of the two Z bosons. However, to take into account the radiation of gluons emitted at small angles, the direction of the incident quarks is computed as the direction of the difference of the momenta of the two quarks, normalized to unity. This follows the method originally proposed by Ref. [180]:

$$\cos \theta = \frac{\hat{p}_{q_1 b} - \hat{p}_{q_2 b}}{\left|(\hat{p}_{q_1 b} - \hat{p}_{q_2 b})\right|} \cdot \hat{p}_{Z_1 b},\tag{8.2}$$

where $\hat{p}_{q_i/Z_i b}$ represents the unitary vector of the i th quark/ Z boson after the Lorentz boost. Notice that in the lab frame, the momenta of the incident quarks are computed as the fraction of momentum of the incident protons.

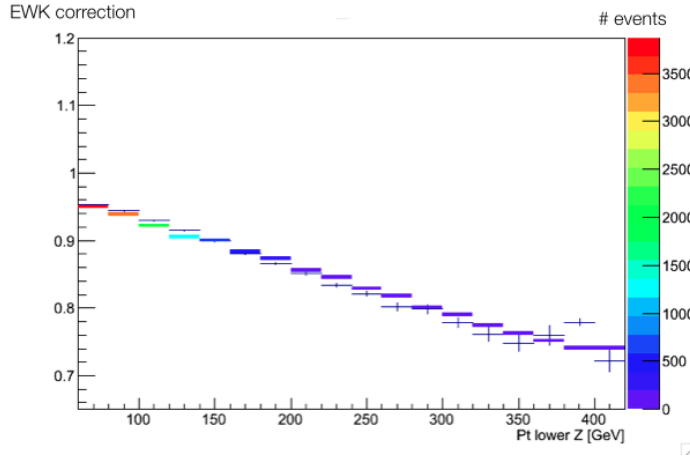


Figure 8-3: Electroweak corrections to the ZZ process, provided by the authors of Ref. [179]. The cross-shaped markers are the corrections applied as a function of \hat{s} , \hat{t} , and the quark flavours. The colored lines are the corrections applied as a function of trailing boson p_T . Since they agree, it is sufficient for our purposes to apply the corrections based on trailing boson p_T .

In this work, an event-by-event reweighting is performed with correction weights binned in the generator-level p_T of the trailing boson. See Figure 8-3. This correction results in a net reduction of the overall ZZ yield of about 10%, although with a strong dependence on the trailing boson p_T . For the $ZZ \rightarrow 2\ell 2\nu$ decay channel, the E_T^{miss} spectrum becomes softer, with a correction of down to -40% for a trailing-Z boson

p_T of 700 GeV.

Electroweak corrections to the WZ process are also considered. These come in two different contributions: virtual and photon-induced. See Figure 8-4. The virtual part, leading to a negative correction, is computed in the same way as for ZZ. The photon-induced part, leading to a positive correction, is estimated by generating events with MadGraph5_aMC@NLO using the LUXqed photon PDF [181]. This correction is applied as a function of the diboson mass m_{WZ} computed at generator-level. The focus of this work is on the high-momentum signature of the dibosons, so a cut of 100 GeV on the transverse momentum of the W and the Z is applied when computing the photon induced contribution. The correction factors for the virtual and the photon induced part are combined to give the total electroweak correction factor:

$$K_{EW}^{\text{NLO}} = (1 + \delta_{\gamma\text{-induced}}) \times (1 + \delta_{\text{virtual}}) \quad (8.3)$$

The distribution of K_{EW}^{NLO} as well as $(1 + \delta_{\text{virtual}})$ are shown in Figure 8-5 as a function of m_{WZ} and p_T^W . The virtual part δ_{virtual} is taken from a table as a function of the Mandelstam variables \hat{s} and \hat{t} , computed in the rest frame of the two incoming partons which initiate the interaction.

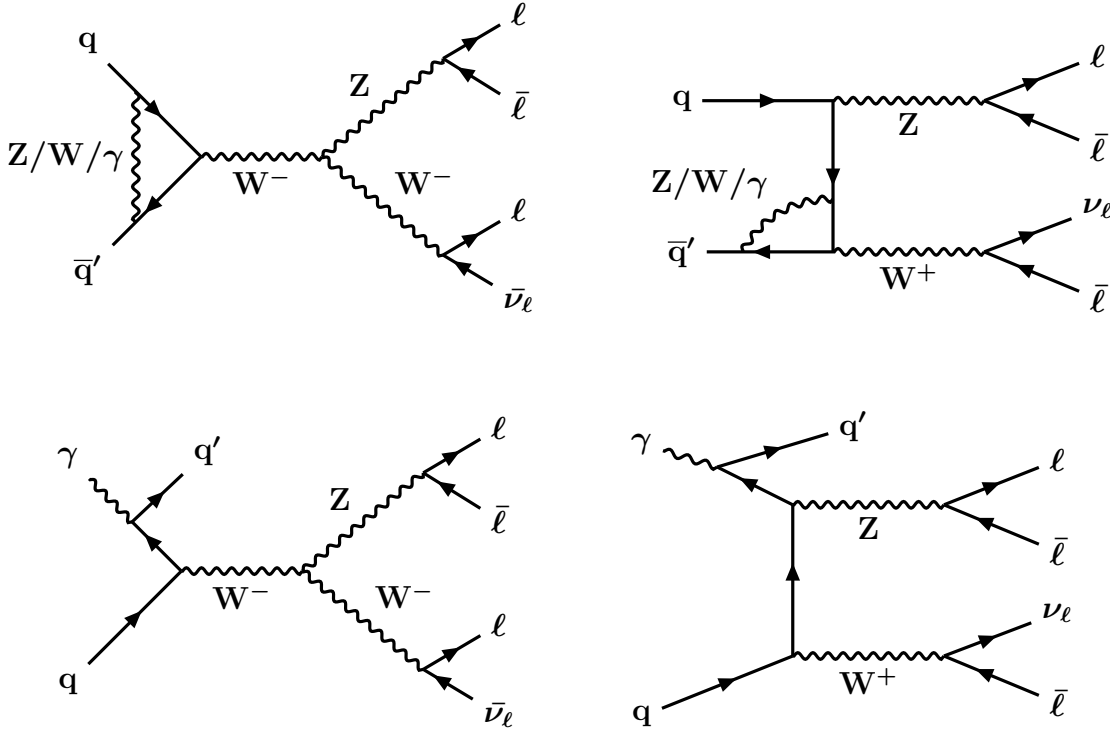


Figure 8-4: WZ production at NLO in EW by internal loop processes (upper row) and photon-quark induced processes (lower row).

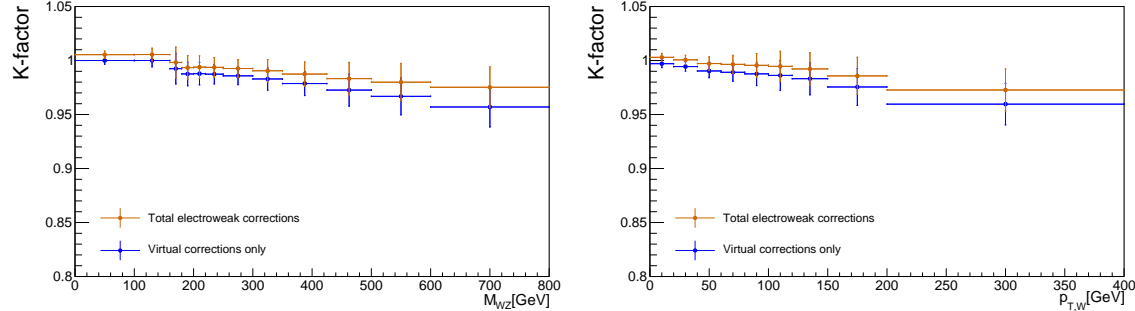


Figure 8-5: Evolution of the NLO electroweak corrections K-factor on $pp \rightarrow W^+Z$ as a function of m_{WZ} (left) and $p_{T,W}$ (right), using only virtual corrections (blue) or using both virtual and photon-induced corrections (brown).

8.1.2 QCD corrections

For quark-induced ZZ production, a QCD NLO to NNLO (next-to-next-to-leading order) correction factor is applied as a function of the mass of the two Z bosons, m_{ZZ} , at generator-level. Figure 8-6 shows the differential cross section. The correction is obtained using settings similar to the CMS simulation (dilepton mass requirements, parton distribution function sets) to ensure its accuracy. See Ref. [182]. In the case of the WZ process, a flat correction factor from QCD NLO to NNLO is applied. Its value is **1.109**; for details see Reference [183].

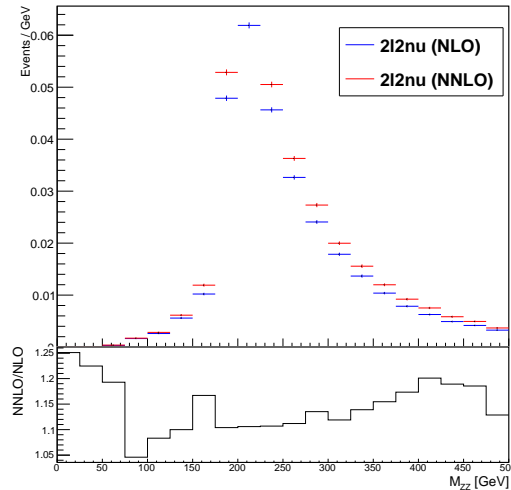


Figure 8-6: Evolution of the NNLO QCD corrections K-factor for $pp \rightarrow ZZ \rightarrow 2\ell 2\nu$ as a function of m_{ZZ} at generator-level.

8.1.3 Cross terms

As discussed in Refs. [179, 180], terms purely of higher order in α_{EW} are expected to be negligible. A significant uncertainty, instead, stems from missing QCD-EW combined corrections, e.g. involving two-loop terms of order $\alpha_S \alpha_{EW}$. So far, this

contribution from diagrams at NLO in both QCD and electroweak has been ignored. This is the source of the so-called “QCD-electroweak cross-term.”

The electroweak and QCD corrections are both large in magnitude, for the ZZ process, so the QCD-electroweak cross-term cannot be neglected. For the majority of ZZ events which have little hadronic activity, the uncertainty from such missing QCD-EW combined corrections is estimated from the product of the NLO QCD corrections ($1 + \delta_{\text{QCD}}$) and NLO EW corrections ($1 + \delta_{\text{EW}}$), as $\delta_{\text{QCD}}\delta_{\text{EW}}$. To compute this uncertainty, a flat δ_{QCD} value of 0.6 is considered , while δ_{EW} is computed event-by-event as a function of the lower- Zp_T (cf. Sec. 5.4.5), then we vary the event weight by a factor $(1 + \delta_{\text{QCD}}\delta_{\text{EW}})$.

Since the EW k -factors for the ZZ are strictly valid only when the hadronic activity in the event is moderate, a variable ρ is built to estimate the level of hadronic activity in the event, following Ref. [180]. It is calculated by considering the balance of the generated leptons’ transverse momenta:

$$\rho = \frac{|\vec{p}_T(\ell_1) + \vec{p}_T(\ell_2) + \vec{p}_T(\ell_3) + \vec{p}_T(\ell_4)|}{|\vec{p}_T(\ell_1)| + |\vec{p}_T(\ell_2)| + |\vec{p}_T(\ell_3)| + |\vec{p}_T(\ell_4)|} \quad (8.4)$$

At high boson momentum, less than 1% of the ZZ events have $\rho > 0.3$. For these events, there is a significant imbalance in the transverse momenta of the four leptons due to the presence of jets. Here, the QCD contribution to the uncertainty is poorly understood, so δ_{QCD} is taken as 1. The factor used for computing the variations of the event weights is then $(1 + \delta_{\text{EW}})$. The total impact of this uncertainty across the whole spectrum of ρ is at the level of 25%.

The overall electroweak NLO correction to the WZ process is relatively small [179, 180, 184]. This is because the virtual corrections and photon-induced corrections partially cancel. Therefore, the NLO QCD-electroweak cross-term for the WZ process is also small. The uncertainties on the NLO electroweak calculation can be estimated as the size of the NLO QCD-electroweak cross terms [181, 140, 185, 186].

Yet another conservative step is taken regarding the NNLO QCD corrections. For lack of a better method, the PDF and QCD scale uncertainties from the original POWHEG calculation at NLO in QCD are carried forward, even though the final distributions are corrected to NNLO in QCD.

8.2 Visible ZZ process

Here, I will describe how events are selected to observe the fully visible ZZ process. Two Z boson candidates are each formed from a pair of opposite-charge electrons or muons, where the mass of each dilepton system lies within 15 GeV of the Z boson mass resonance (91.1876 GeV). The Z candidate whose reconstructed mass is closer to the Z mass is denoted as Z_1 ; the other, as Z_2 . In total, there are four well-identified leptons, giving a very high purity selection. Neither hadronic τ nor b-jet vetoes are applied. The minimum dilepton mass, considering all pairs, must be greater than 4 GeV. The purpose of this requirement is to reject the so-called “nonprompt” backgrounds, which I will explain next.

There is triboson contamination which is the resonant contribution from three bosons (WWZ, WZZ, ZZZ), or two top quarks and a Z boson. There is also a small amount of contamination from the nonprompt backgrounds, including but not limited to the Drell-Yan process, semileptonic diboson decays, leptonic WW decays, and ditop production. From these, it is still possible to end up with four charged leptons or fake lepton signatures after the hard process. These have been mostly suppressed by the minimum dilepton mass requirement. Last but not least, there are Standard Model Higgs boson decays to four leptons via $H \rightarrow ZZ^* \rightarrow 4\ell$, but the cross section is comparatively small.

The selection yields in simulation and data for this ZZ analysis are shown in Table 8.1. Distributions of illustrative variables after the selection are shown in Figures 8-7, 8-8, and 8-9.

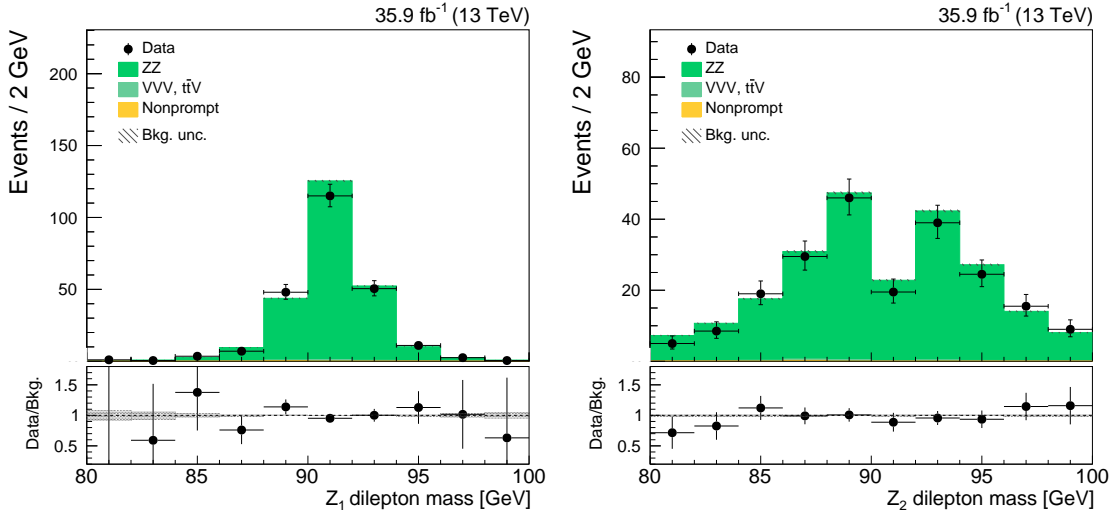


Figure 8-7: The dilepton masses of the two Z candidates. In the right plot, the distribution of Z_2 has a cavity close to the Z mass pole because of how $Z_{1,2}$ are defined.

Process	$4e$	4μ	$2e2\mu$	Total
ZZ	77.6 ± 0.6	171.4 ± 1.0	243.0 ± 1.1	492.0 ± 1.6
VVV	1.0 ± 0.1	1.9 ± 0.2	2.5 ± 0.2	5.5 ± 0.3
Nonprompt bkg.	0.1 ± 0.1	0.1 ± 0.1	0.7 ± 0.4	0.9 ± 0.4
Higgs	0.1 ± 0.1	0.4 ± 0.2	0.3 ± 0.2	0.8 ± 0.3
Total	78.7 ± 0.7	173.4 ± 1.0	246.5 ± 1.2	499.2 ± 1.7
Data	81	175	224	480

Table 8.1: Predicted and observed number of events for the ZZ four-lepton selection using 35.9 fb^{-1} . Only statistical uncertainties are reported.

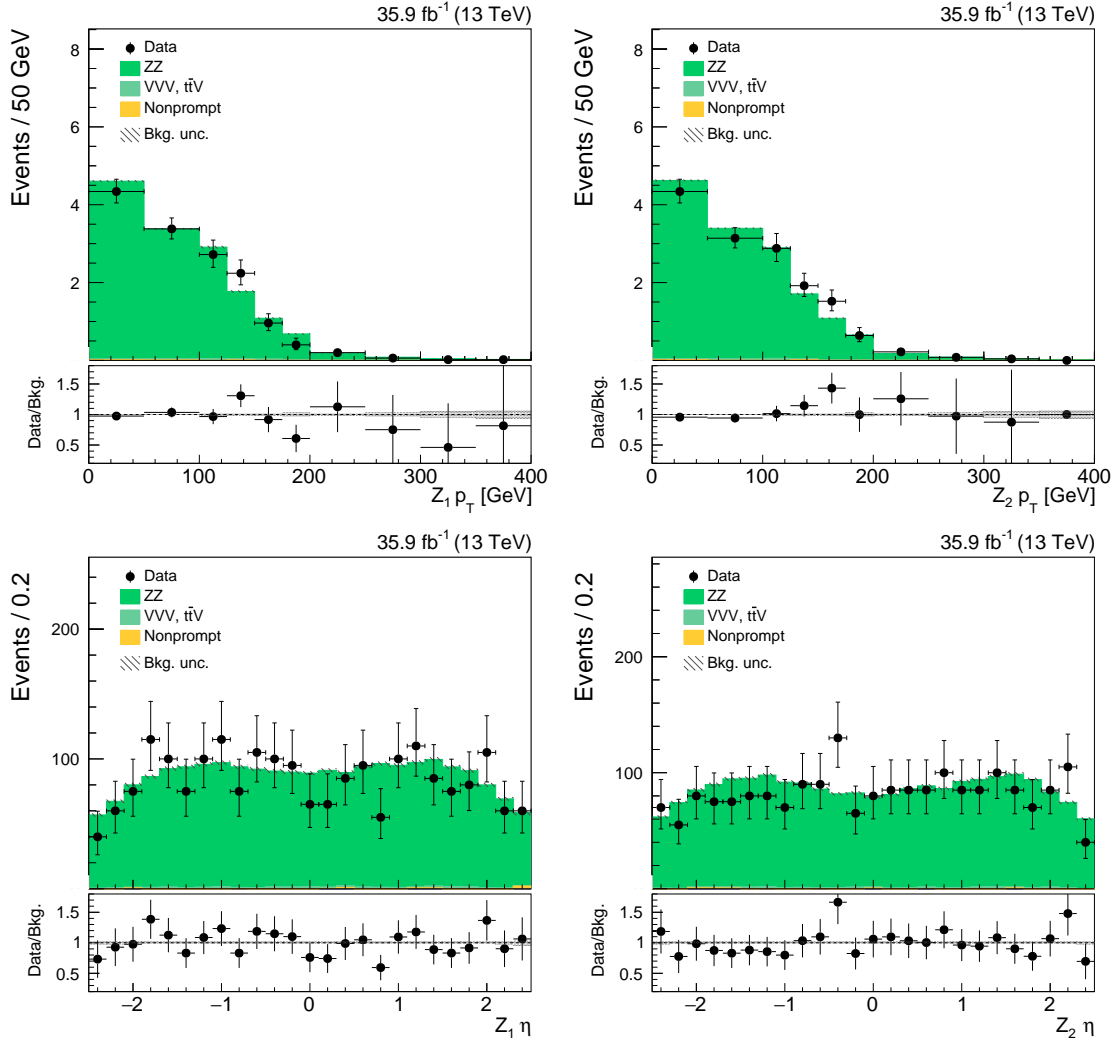


Figure 8-8: Kinematics of the Z candidates. Top: transverse momenta. Bottom: pseudorapidities.

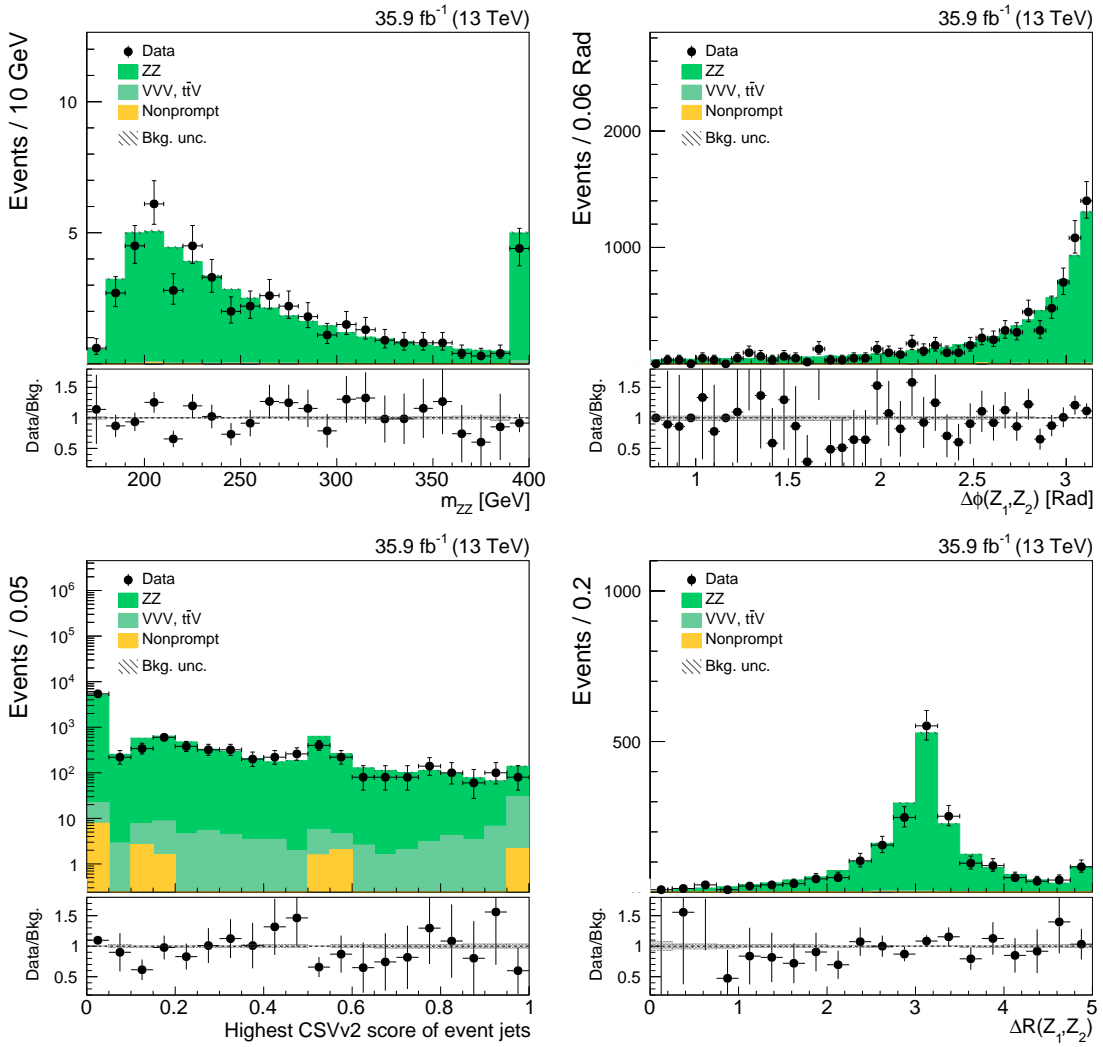


Figure 8-9: More plots of the ZZ data sample. Clockwise from upper left: diboson mass; azimuthal separation between bosons; the maximum b-tag score of any jet in the event; angular separation between bosons. The last bin includes the overflow events.

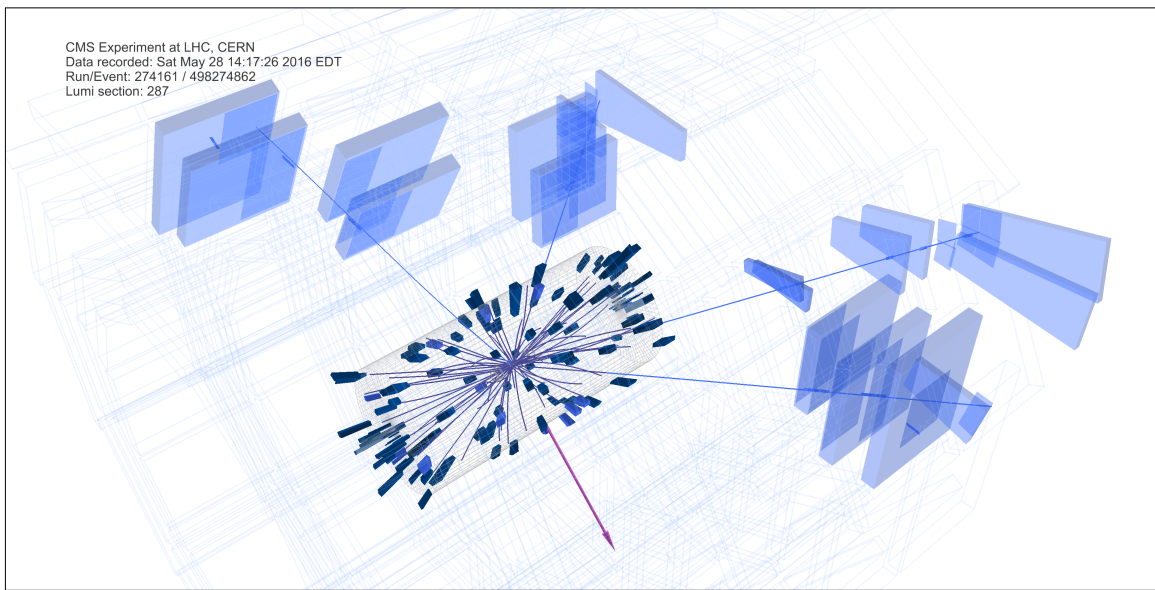
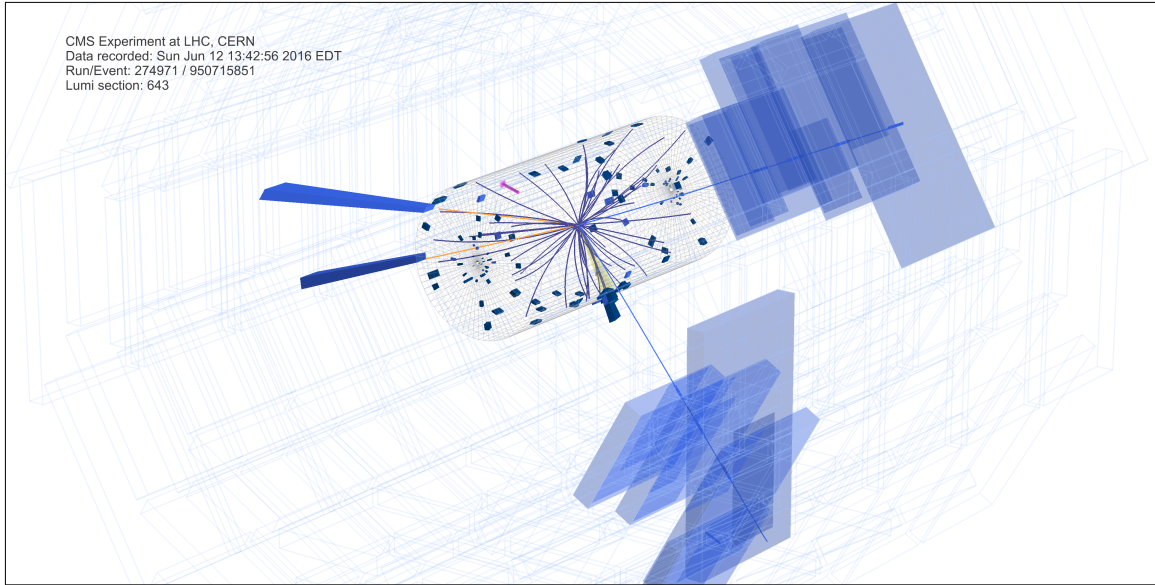


Figure 8-10: 3D event displays of $Z Z(4\ell)$ events with $Z p_T > 200 \text{ GeV}$. The charged particle trajectories are in indigo. The E_T^{miss} is the magenta arrow. The electrons are in gold. Photons are shown as yellow light rays. The HCAL and ECAL deposits associated with PF candidates are the darker cobalt blue prisms and the lighter royal blue prisms, respectively; their length represents energy. The distant wireframe and blue boxes represent the muon systems.

8.3 Visible WZ process

Below, I describe how events are selected to observe fully visible WZ production. The events must have three well-reconstructed leptons and a nominal amount of E_T^{miss} . A single Z boson candidate is formed from a pair of opposite-charge electrons or muons, the mass of which must lie within 15 GeV of the Z boson mass. Additionally, a third well-identified electron or muon is required, representing the W^\pm boson. In the case where there are three electrons or muons, the Z candidate is chosen unambiguously as the opposite-sign dilepton pair whose mass is closest to the Z boson mass.

True WZ events are expected to have an undetectable neutrino in the final state, thus E_T^{miss} of at least 30 GeV is required. To exclude a region where production of Z bosons with final-state radiation may contribute, the trilepton mass is required to be more than 100 GeV. Due to theoretical problems with collinear emission of same-flavor opposite-sign dilepton pairs, the mass of any opposite-sign lepton pair ($m_{2\ell}$) is required to be larger than 4 GeV. These requirements follow precedent for the measurement of the WZ production cross section with CMS [187].

Since there is no danger of contamination, no veto on additional hadronically-decaying τ leptons is applied. A relaxed b-jet veto is applied, only rejecting events where a jet passes the Tight CSVv2 working point (0.9535) previously discussed in Section 4.3.3. This, along with the Z candidate mass requirement, is useful for rejecting ditop background. The Medium CSVv2 working point (0.8484) was not used to maximize efficiency of selecting real WZ events.

The selection yields in simulation and data for the WZ analysis are shown in Table 8.2. Kinematic variables of the bosons, and variables used in the selection, are shown in Figures 8-11, 8-12, and 8-13. In particular, note the presence of the expected Jacobian peak in the W^\pm boson transverse mass distribution in Figure 8-13. The transverse mass is calculated in the transverse (r, ϕ) plane using the third lepton (\vec{p}_T^ℓ) and missing energy (\vec{p}_T^{miss}) vectors:

$$\begin{aligned} m_T &= \sqrt{m_\ell^2 + m_\nu^2 + 2(E_\ell E_\nu - \vec{p}_T^\ell \cdot \vec{p}_T^{\text{miss}})} \\ &\approx \sqrt{2 |\vec{p}_T^\ell| |\vec{p}_T^{\text{miss}}| (1 - \cos \Delta\phi)} \quad \text{for } m_\ell, m_\nu \approx 0 \end{aligned} \tag{8.5}$$

where $\Delta\phi$ is the azimuthal separation between those vectors.

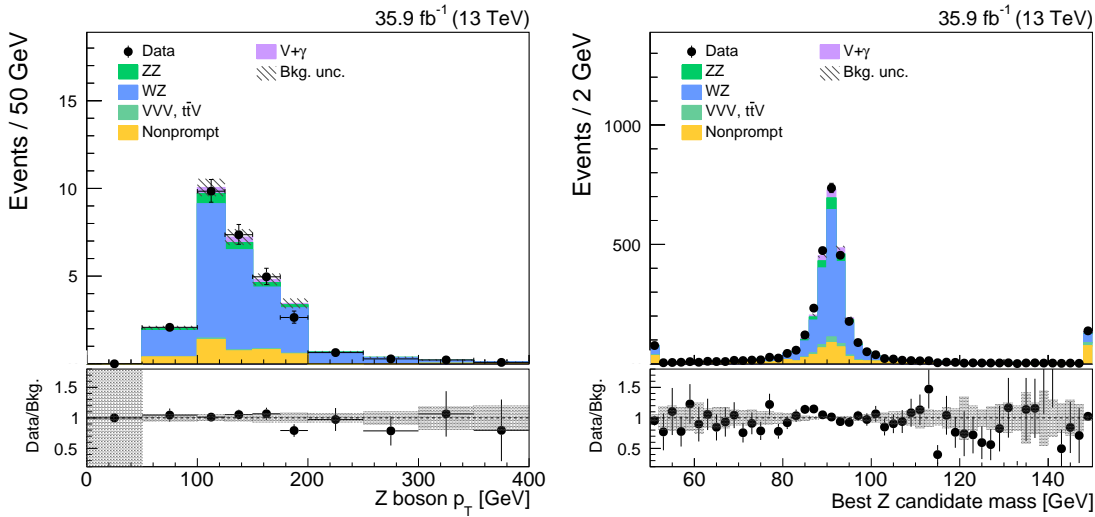


Figure 8-11: The transverse momentum and mass of the reconstructed Z boson candidates. The last bin includes the overflow events.

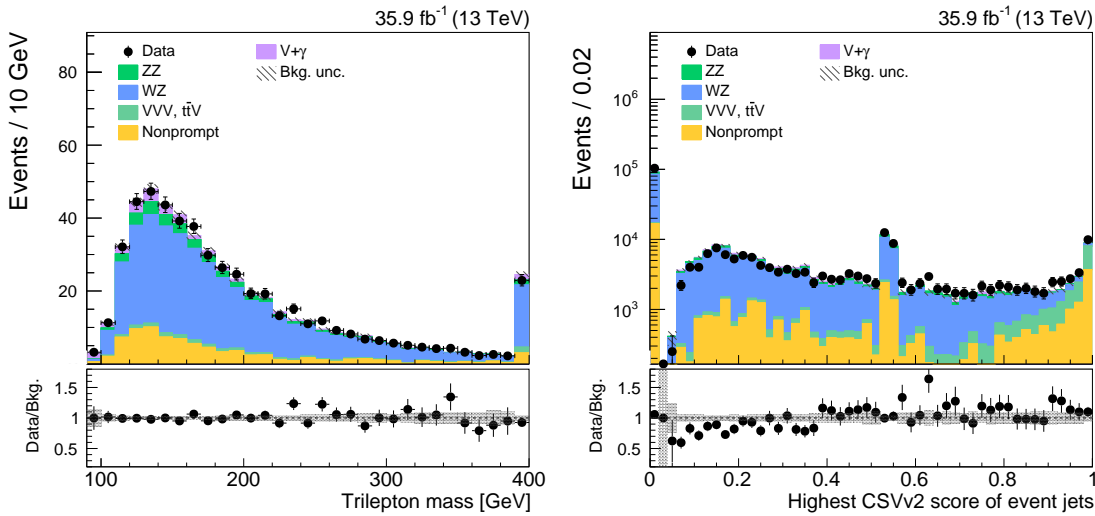


Figure 8-12: Trilepton mass and the maximum b-tag score of any jet in the event at final selection level. The last bin includes the overflow events. Events with a well b-tagged jet (> 0.9535) are rejected.

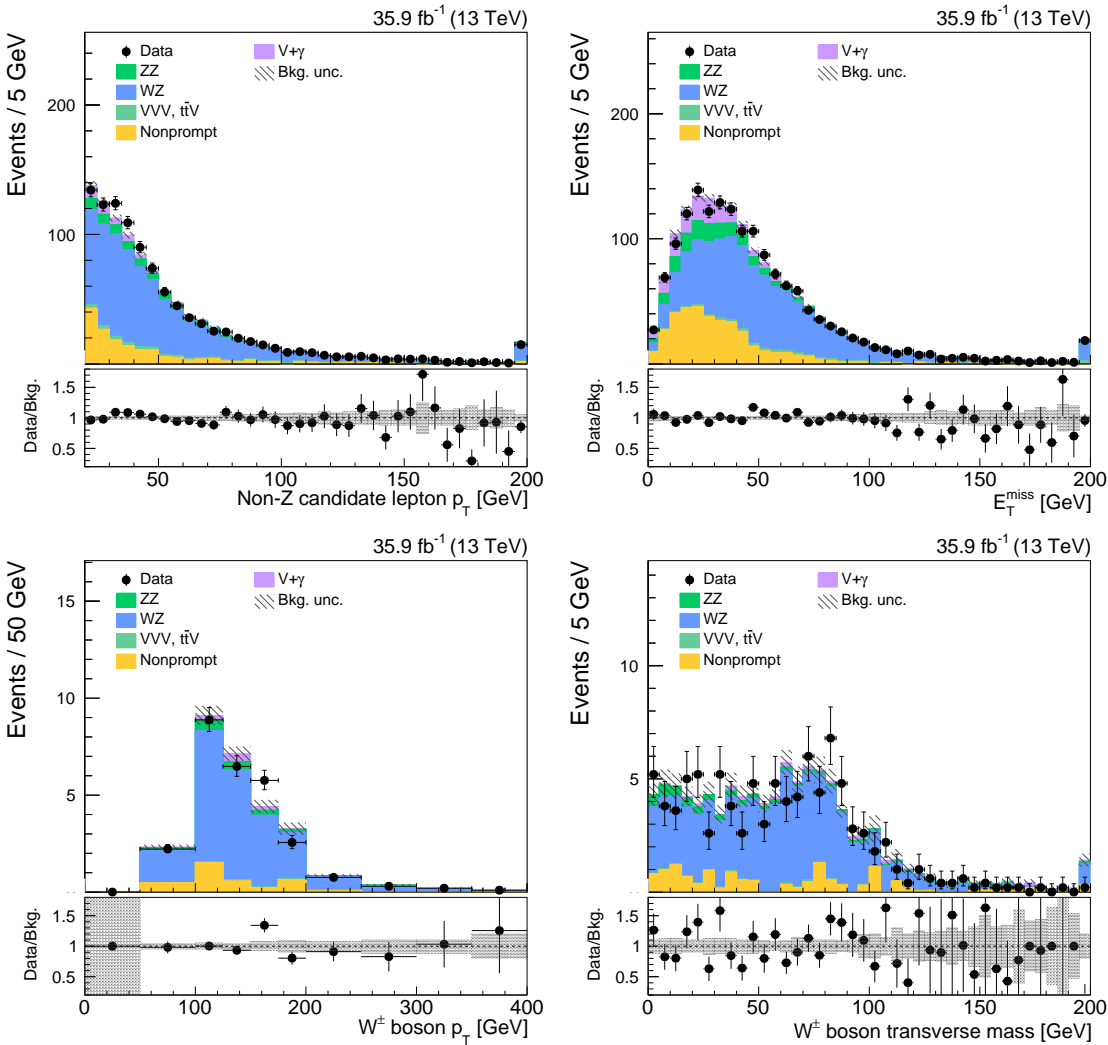


Figure 8-13: Kinematics of the reconstructed W^\pm boson at final selection level. Clockwise from upper left: p_T of the lepton associated with the W^\pm boson; E_T^{miss} in the event; transverse mass of the W^\pm boson; and p_T of the W^\pm boson. Note the Jacobian peak in the transverse mass distribution. The last bin includes the overflow events.

Process	$W(\mu\nu)Z(\mu\mu)$	$W(\mu\nu)Z(ee)$	$W(e\nu)Z(\mu\mu)$	$W(e\nu)Z(ee)$	Total
WZ	117.1 ± 3.1	89.5 ± 2.7	89.5 ± 2.7	67.3 ± 2.3	363.5 ± 5.5
Nonprompt bkg.	11.0 ± 2.5	25.3 ± 7.1	12.3 ± 3.1	16.3 ± 6.2	64.9 ± 10.2
ZZ	9.4 ± 0.2	7.0 ± 0.2	7.0 ± 0.2	4.6 ± 0.2	28.0 ± 0.4
VVV	1.7 ± 0.2	1.1 ± 0.2	1.2 ± 0.2	1.0 ± 0.2	5.0 ± 0.3
$V+\gamma$	0.4 ± 0.4	0.0 ± 0.5	8.3 ± 2.1	6.9 ± 1.8	15.5 ± 2.9
Total	139.6 ± 4.1	123.1 ± 7.7	118.3 ± 4.7	96.0 ± 6.9	477.0 ± 12.0
Data	146	112	111	108	477

Table 8.2: Predicted and observed number of events for the WZ three-lepton selection using 35.9 fb^{-1} . Only statistical uncertainties are reported.

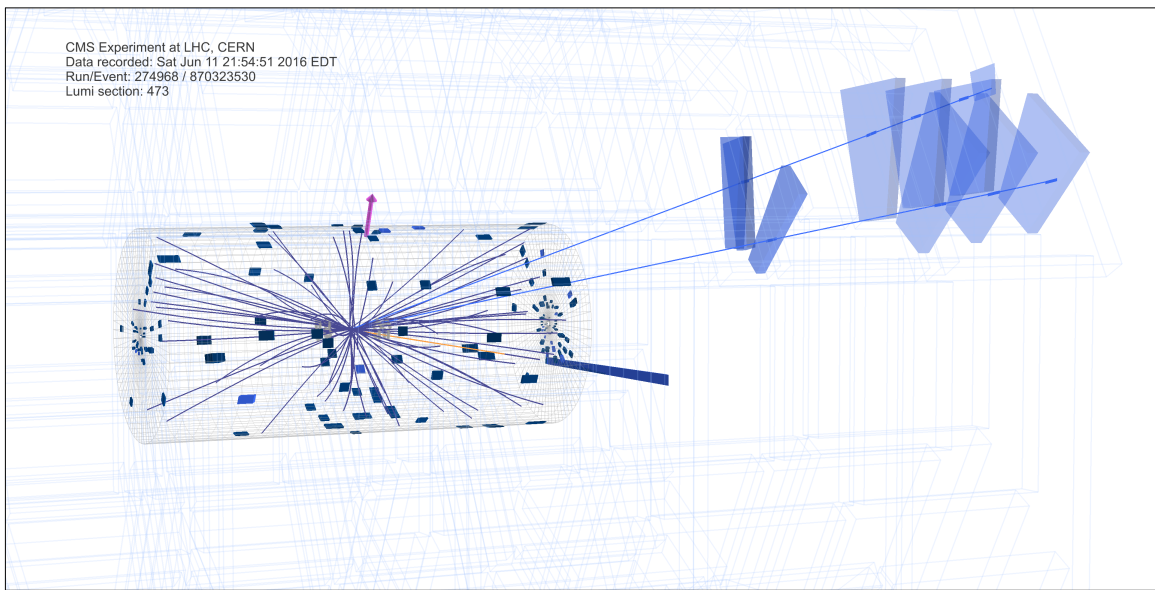
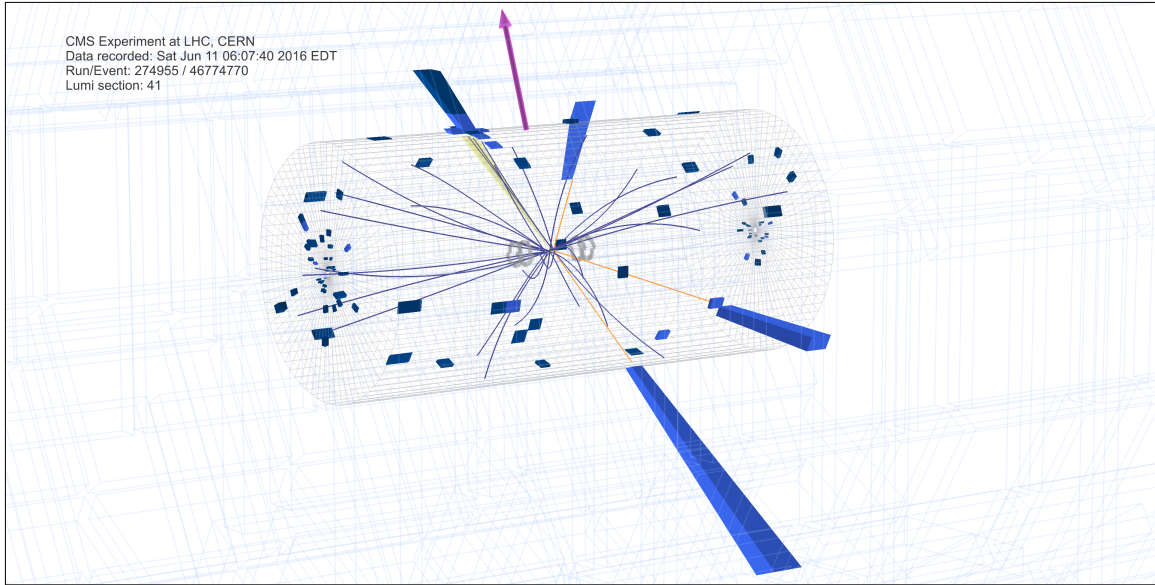


Figure 8-14: 3D event displays of $W(\ell\nu)Z(\ell\ell)$ events with $Z p_T > 200 \text{ GeV}$. The charged particle trajectories are in indigo. The E_T^{miss} is the magenta arrow. The electrons are in gold. Photons are shown as yellow light rays. The HCAL and ECAL deposits associated with PF candidates are the darker cobalt blue prisms and the lighter royal blue prisms, respectively; their length represents energy. The distant wireframe and blue boxes represent the muon systems.

Chapter 9

Search for dark matter produced in association with a boosted Z boson

In this chapter, I will describe the analysis for the dark matter search from start to finish. The final state in this search is a Z boson candidate decaying to charged leptons, recoiling against a lot of missing energy from the undetectable particles. Suppose that significantly more of these events were to be observed compared to the Standard Model prediction. Then we could interpret that result under a variety of theoretical models (described in Section 2.4).

An event selection is constructed to analyze the events collected using the leptonic triggers. The relevant background processes are estimated using either real data or simulated events. After assessing the systematic uncertainties in the methodology, a maximum likelihood fit is performed to test the Standard Model versus the exotic predictions. I will discuss the pursuit of a multivariate analysis to maximize our sensitivity to the invisible Higgs model. Finally, the results are quoted for the search.

9.1 Event selection

In this section, I describe the criteria applied to events in order to select and extract a possible dark matter signature from the data. A preselection is applied to attest to the veracity of the Drell-Yan simulation. Then, the full selection is applied, to kill off the reducible backgrounds and enhance the purity of the dark matter signal as much as possible.

9.1.1 Preselection

First, Z candidates are selected by choosing events with at least two electrons or muons. They must be opposite-charged electrons (muons) each with $p_T > 25$ (20) GeV. The mass of the dilepton system ($m_{\ell\ell}$) is required to be $|m_{\ell\ell} - m_Z| < 15$ GeV, consistent with the decay of a Z boson of mass 91.1876 GeV. Plots showing

basic event-level variables such as the number of jets or leptons after the Z candidate selection stage are shown in Figures 9-1-9-4.

Next, topological criteria are imposed to move closer to the dark matter signature. The E_T^{miss} is required to be larger than 40 GeV and the dilepton p_T ($p_T^{\ell\ell}$) is required to be larger than 60 GeV, in order to reject the bulk of the background from the Drell-Yan process. A few distributions for each flavor channel after this stage are shown in Figures 9-5 to 9-7.

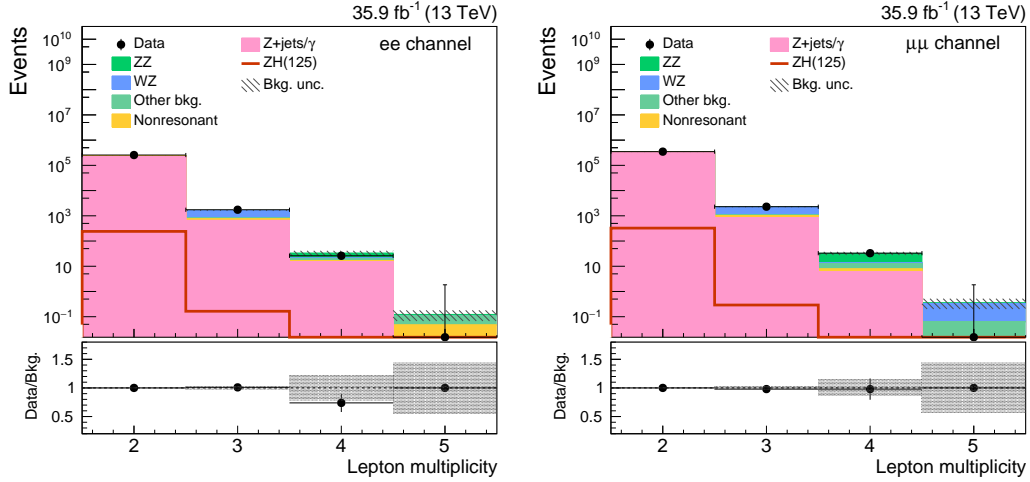


Figure 9-1: Lepton multiplicity for each flavor channel in $Z \rightarrow \ell^+ \ell^-$ candidate events. The uncertainty band corresponds to the statistical uncertainty only. Left: dielectron channel. Right: dimuon channel.

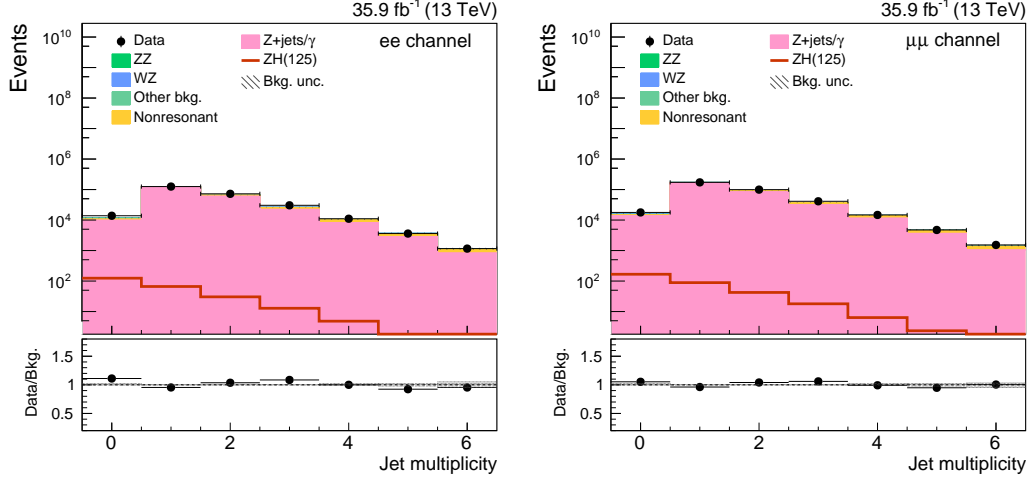


Figure 9-2: Jet multiplicity for each flavor channel in $Z \rightarrow \ell^+ \ell^-$ candidate events. The uncertainty band corresponds to the statistical uncertainty only. Left: dielectron channel. Right: dimuon channel.

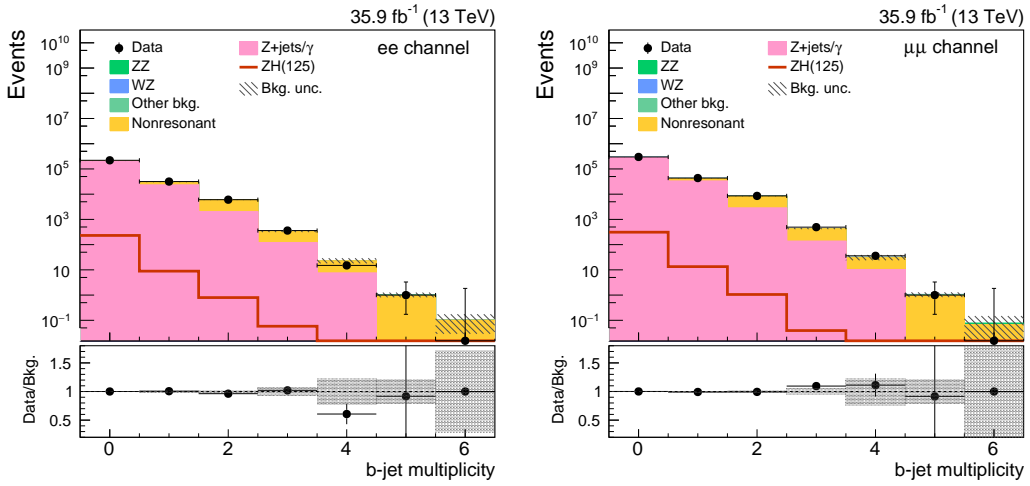


Figure 9-3: Number of jets passing the requirements for b-tagging for each flavor channel in $Z \rightarrow \ell^+ \ell^-$ candidate events. The uncertainty band corresponds to the statistical uncertainty only. Left: dielectron channel. Right: dimuon channel.

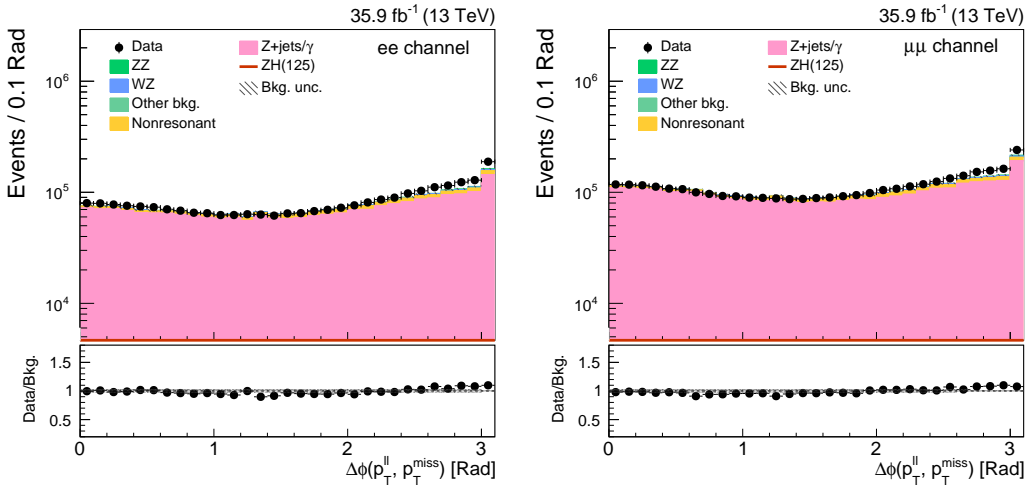


Figure 9-4: Azimuthal separation between the dilepton system and the missing transverse energy for each flavor channel in $Z \rightarrow \ell^+ \ell^-$ candidate events. The uncertainty band corresponds to the statistical uncertainty only. Left: dielectron channel. Right: dimuon channel.

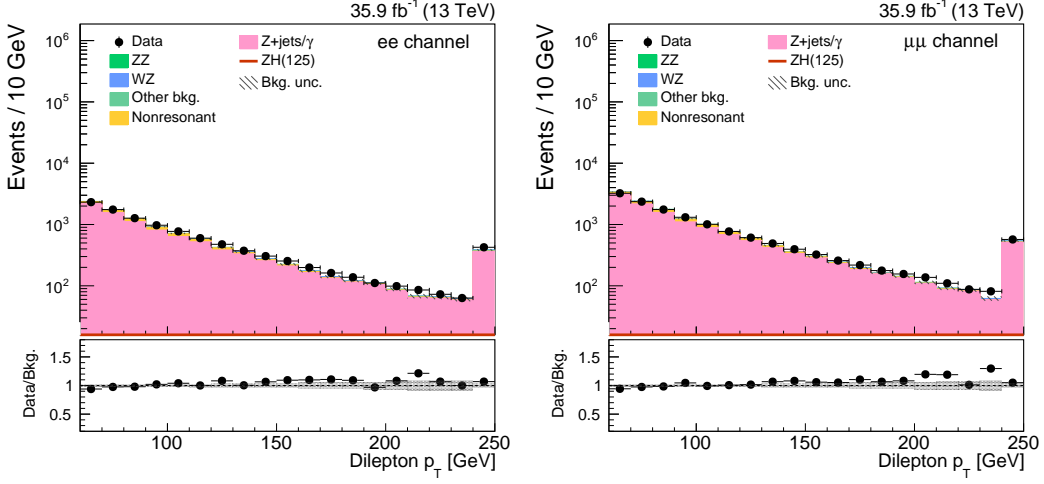


Figure 9-5: Distributions of the $p_T^{\ell\ell}$ for each flavor channel in $Z \rightarrow \ell^+\ell^-$ events with $p_T^{\ell\ell} > 60$ GeV and $E_T^{\text{miss}} > 40$ GeV. The uncertainty band corresponds to the statistical uncertainty only. Left: dielectron channel. Right: dimuon channel.

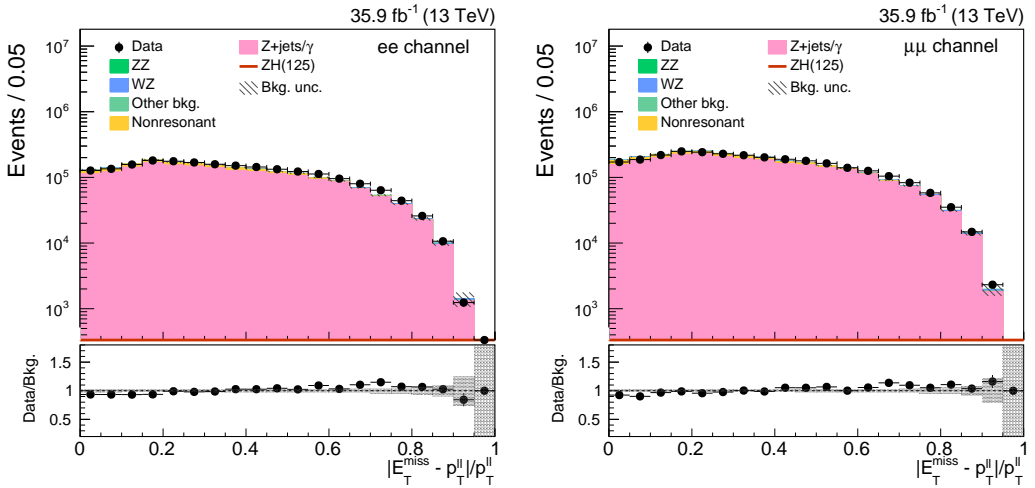


Figure 9-6: Distributions of the balance variable $|E_T^{\text{miss}} - p_T^{\ell\ell}|/p_T^{\ell\ell}$ for each flavor channel in $Z \rightarrow \ell^+\ell^-$ events with $p_T^{\ell\ell} > 60$ GeV and $E_T^{\text{miss}} > 40$ GeV. The uncertainty band corresponds to the statistical uncertainty only. Left: dielectron channel. Right: dimuon channel.

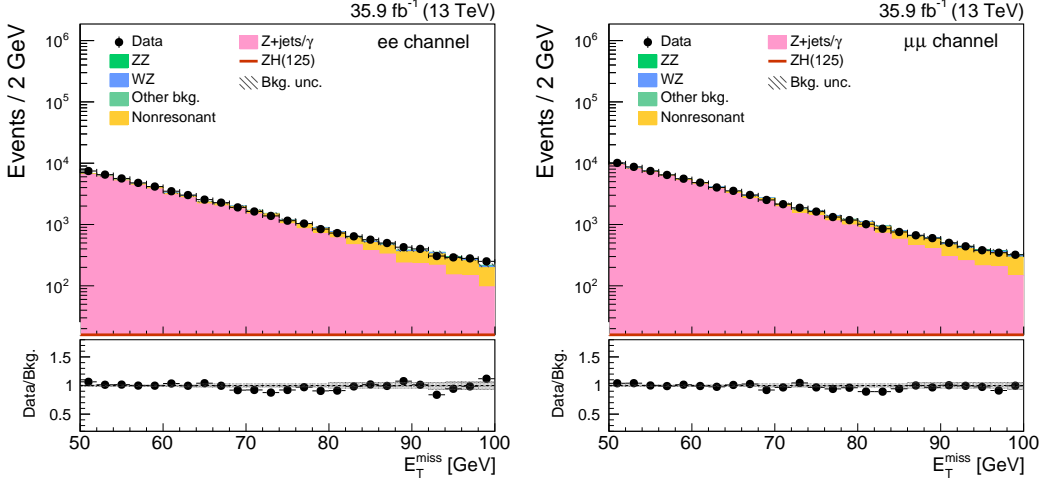


Figure 9-7: Distributions of the missing transverse energy for each flavor channel in $Z \rightarrow \ell^+\ell^-$ events with $p_T^{\ell\ell} > 60$ GeV and $E_T^{\text{miss}} > 40$ GeV. The uncertainty band corresponds to the statistical uncertainty only. Left: dielectron channel. Right: dimuon channel.

9.1.2 Signal selection

After the preselection, more stringent criteria are applied to enhance the significance of a dark matter signal. Firstly, events with more than two well-identified charged leptons are rejected. There are nonresonant background processes which do not have anything to do with a Z boson, but they can end up looking like a signal event by way of combinatorics. A great example of this is two independent objects each eventually producing a charged lepton and missing energy, such as leptonic WW decays. Another example is top-quark backgrounds such as the ubiquitous ditop production. There, each top-quark decays to a b-quark and a W^\pm boson, which decays leptonically. These nonresonant backgrounds are already partially mitigated by the Z candidate mass window requirement in the preselection. It can be further reduced by requiring a small angular separation of the leptons, $\Delta R < 1.8$.

All of the dark matter models considered are quark-induced processes with no extra quarks or gluons produced in the final state. Refer to the diagrams in Figure 2-8. Hadronic activity in a dark matter signal event is minimal and only arises from the initial-state radiation of a gluon or secondary pileup interactions. Top-quark backgrounds are not quark-induced, and produce b-jets from the top-quark decays as well as extra jets in general. They are easily reduced by requiring that events have no more than one jet with $p_T^j > 30$ GeV and $|\eta| < 2.4$. Furthermore, a b-jet veto is imposed. Events are rejected if a central jet is found which passes the “Medium” working point of the CSVv2 b-tagging algorithm (> 0.8484).

Events are rejected if a third, additional electron or muon is reconstructed with $p_T > 10$ GeV using a loose selection; or if they contain a reconstructed hadronically decaying τ lepton with $p_T > 18$ GeV. These criteria reduce the background contribution from WZ events where the lepton originating from the W boson decay is not

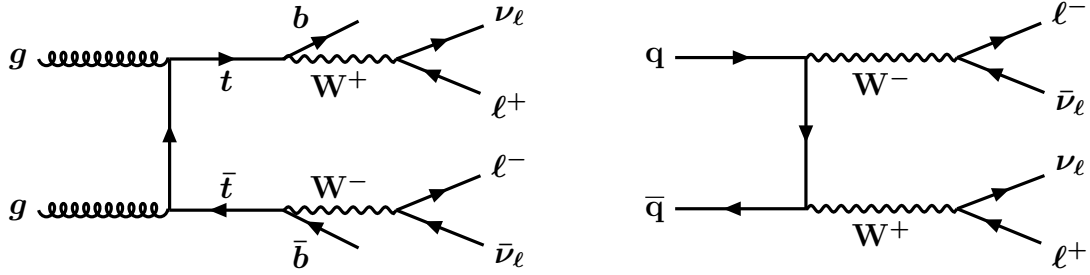


Figure 9-8: Nonresonant backgrounds. Left: ditop production resulting in two b -jets, two charged leptons, and missing energy. Right: WW production producing two charged leptons and missing energy.

reconstructed.

Last but not least, the Drell-Yan process must still be dealt with. It is important to note that the Drell-Yan process cannot generate real missing energy. It can only look like a signal event due to detector acceptance effects and mismeasurement of jets. This is handled in the signal selection in several ways. The Z candidate and the missing transverse energy are required to be back-to-back in the transverse plane: $\Delta\phi_{\ell\ell, E_T^{\text{miss}}} > 2.6$. Their momenta in the transverse plane must also be balanced¹: $|E_T^{\text{miss}} - p_T^{\ell\ell}|/p_T^{\ell\ell} < 0.4$. A mismeasurement of an energetic jet will induce missing energy in the same angular direction of the jet. So if there is a jet in the event, it must not be in the same azimuthal direction as the jet: $\Delta\phi_{\text{jet}, E_T^{\text{miss}}} > 0.5$ Rad. This also helps deal with the aforementioned lost WZ , in the case that the lepton is mistakenly reconstructed as a jet or the τ lepton reconstruction fails. Finally, since the missing energy distribution of the Drell-Yan background is a sharply falling spectrum, events must have E_T^{miss} larger than 100 GeV.

A summary of the criteria for the signal region are given in Table 9.1. Following this selection, a dark matter signature could, in principle, appear prominently in the spectrum of missing transverse energy. A maximum likelihood fit is performed to test the compatibility of the observed spectrum with signal+background and background-only hypotheses. The likelihood is described below in Section 9.4.

¹This is frequently referred to as “the balance.”

Variable	Selection	Rejection Target
N_ℓ	$= 2$	WZ, VVV
p_T^ℓ	$> 25/20 \text{ GeV (electrons)}$ $> 20 \text{ GeV (muons)}$	QCD QCD
Z boson requirement (GeV)	$ m_{\ell\ell} - m_Z < 15 \text{ GeV}$	WW, top-quark
Jet counting	$\leq 1 \text{ jet with } p_T^j > 30 \text{ GeV}$	$Z/\gamma^* \rightarrow \ell^+ \ell^-$, top-quark, VVV
$p_T^{\ell\ell}$ (GeV)	> 60	$Z/\gamma^* \rightarrow \ell^+ \ell^-$
B-tagging veto	$\text{CSVv2} < 0.8484$	Top-quark, VVV
Tau veto	$0 \tau_h$ candidates with $p_T^\tau > 18 \text{ GeV}$	WZ
E_T^{miss} (GeV)	> 100	$Z/\gamma^* \rightarrow \ell^+ \ell^-$, WW, top-quark
$\Delta\phi_{\ell\ell, E_T^{\text{miss}}}$	> 2.6	$Z/\gamma^* \rightarrow \ell^+ \ell^-$
$ E_T^{\text{miss}} - p_T^{\ell\ell} /p_T^{\ell\ell}$	< 0.4	$Z/\gamma^* \rightarrow \ell^+ \ell^-$
$\Delta\phi_{\text{jet}, E_T^{\text{miss}}}$	> 0.5	$Z/\gamma^* \rightarrow \ell^+ \ell^-$, WZ
$\Delta R_{\ell\ell}$	< 1.8	WW, top-quark

Table 9.1: Summary of the kinematic selection requirements for the E_T^{miss} -based analysis.

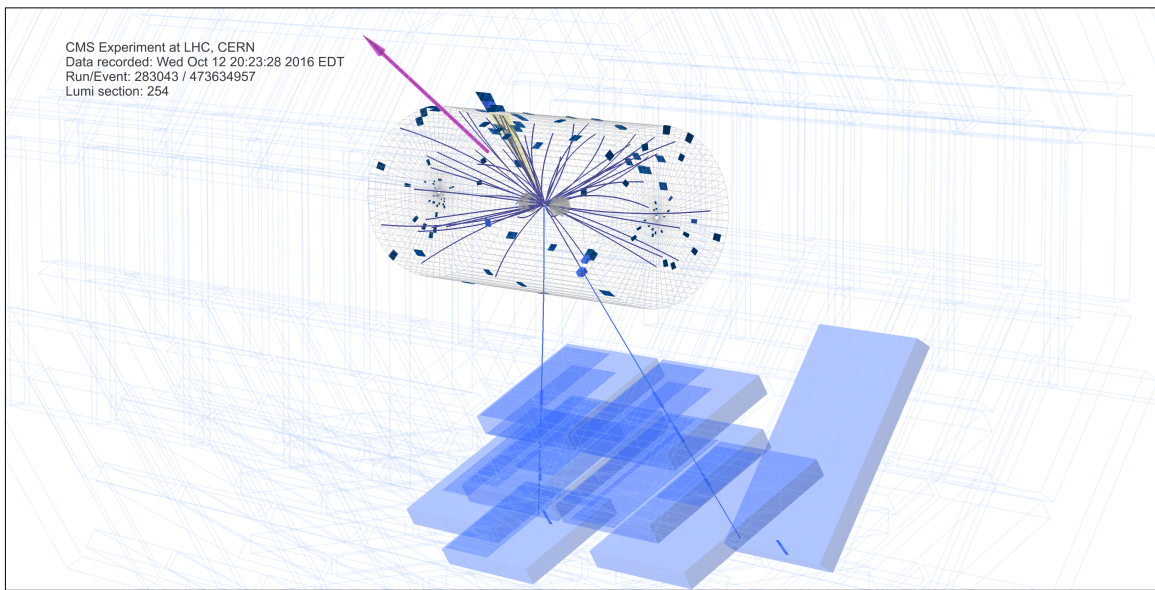
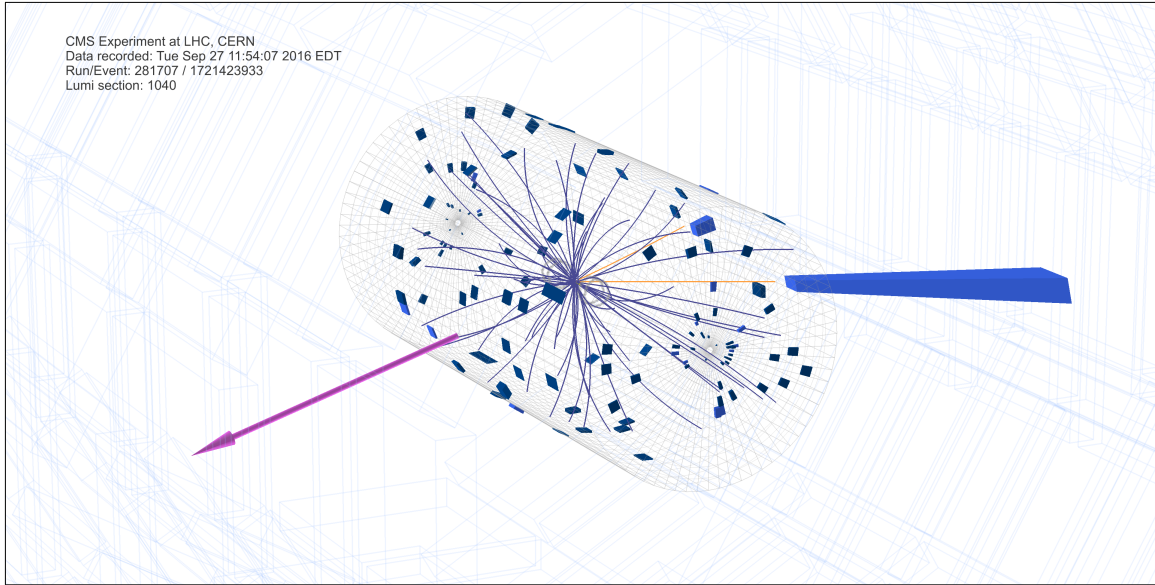


Figure 9-9: 3D event displays of $Z(\ell\ell)$ events with $E_T^{\text{miss}} > 300 \text{ GeV}$. The charged particle trajectories are in indigo. The E_T^{miss} is the magenta arrow. The electrons are in gold. Photons are shown as yellow light rays. The HCAL and ECAL deposits associated with PF candidates are the darker cobalt blue prisms and the lighter royal blue prisms, respectively; their length represents energy. The distant wireframe and blue boxes represent the muon systems.

9.2 Background estimation

A combination of data-driven methods and detailed simulated studies is used to estimate background contributions. The spectra of diboson processes are taken from simulation with conservative systematic uncertainties, but the ratio of ZZ/WZ is measured from data. The nonresonant background processes may just as well produce different-flavor lepton pairs, so we extrapolate from those data events to estimate the yield of same-flavor lepton pairs. The Drell-Yan process is estimated from a side-band of low E_T^{miss} . Its contribution for higher values of E_T^{miss} is very small, but in order to verify the accurate simulation of the E_T^{miss} spectrum, several cross-checks are performed.

9.2.1 Diboson processes

Contributions from the ZZ and WZ processes are estimated from control regions in data. These processes contribute to the signal region via the $\text{ZZ} \rightarrow \ell\ell\nu\nu$ and $\text{WZ} \rightarrow \ell\ell\ell\nu$ decay modes, respectively. In both cases, the observed E_T^{miss} corresponds to the p_T of one of the bosons. The processes are estimated from the control samples described in Chapter 8, Sections 8.3 and 8.2. The visible decay modes allow us to probe the boson p_T distribution, which is expected to be independent of the decay mode.

Using the pure control samples with three or four leptons, an extrapolation is performed to the missing energy spectra for ZZ and WZ events with only two reconstructed leptons and missing energy in the final state². Extrapolation to the $2\ell + E_T^{\text{miss}}$ final state is accomplished by furnishing a quantity known as the emulated E_T^{miss} . For the WZ process, the fake E_T^{miss} is the true W boson p_T . It is estimated by calculating the vectorial sum of the E_T^{miss} vector and the transverse momentum vector of the third lepton. For the ZZ process, the fake E_T^{miss} comes from taking the sum of any nominal true E_T^{miss} and one of the leptonically-decaying Z bosons. The Z boson which is made to vanish is chosen to be the one whose reconstructed mass is further from the nominal Z boson mass, previously denoted as Z_2 in Section 8.2. The choice of which Z candidate to use for the fake E_T^{miss} is arbitrary, and has almost no effect on the resulting distribution.

After the emulated E_T^{miss} procedure, the kinematic criteria of the selection in Section 9.1 are applied. The resulting emulated E_T^{miss} spectra are shown in Fig. 9-10.

9.2.2 Nonresonant backgrounds

The contribution of the nonresonant flavor symmetric backgrounds is estimated from a control sample of events with dilepton of different flavors ($e^\pm\mu^\mp$) that pass all analysis selections. Nonresonant backgrounds (NRB) consists mainly of leptonic W decays in $t\bar{t}$, tW decays and WW events. Small contributions from single top-quark

²The WZ process can appear this way due to a lost lepton, either from inefficiency in the reconstruction and identification or the non-hermetic tracking acceptance

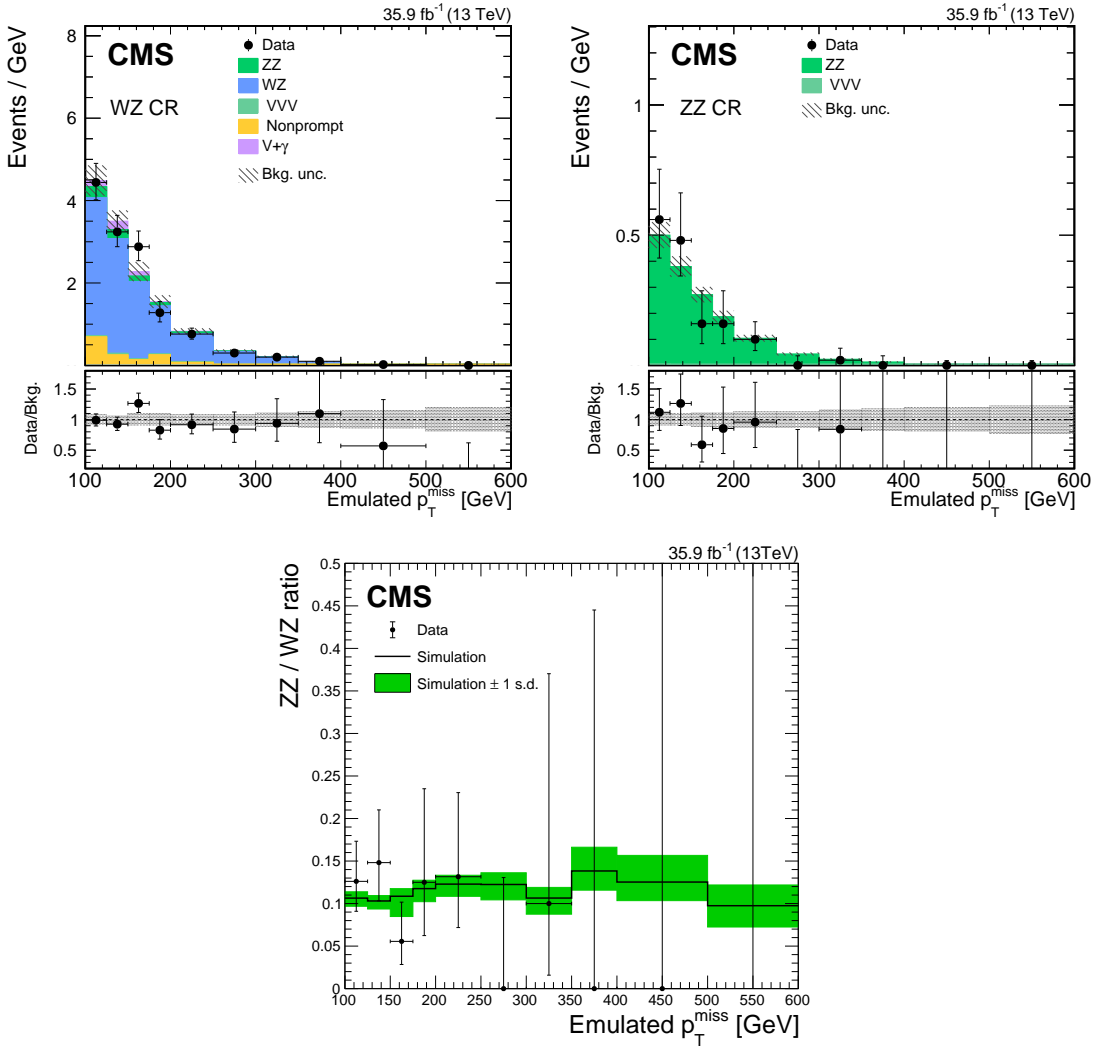


Figure 9-10: Emulated E_T^{miss} distribution for the $\text{WZ} \rightarrow 3\ell\nu$ (top left) and $\text{ZZ} \rightarrow 4\ell$ (top right) control regions, and the ratio between both distributions in data and simulation (bottom). Simulated distributions correspond to the result of the maximum likelihood fit described in Section 9.4. Uncertainty bands correspond to both statistical and systematic uncertainty.

events produced from s -channel and t -channel processes, and $Z \rightarrow \tau\tau$ events in which τ leptons produce light leptons and E_T^{miss} are also considered in this NRB estimation.

The method assumes the lepton flavor symmetry in the final states of these processes. Since the leptonic decay branching ratios for the ee , $\mu\mu$ and $e\mu$ final states from NRB are 1:1:2, the $e\mu$ events selected inside the Z -mass window can be extrapolated to the ee and $\mu\mu$ channels. To account for differences in efficiency for electrons and muons, a correction factor k_{ee} can be derived by comparing the NRB yields in the ee and $\mu\mu$ channels, exactly as is done in Formulas 7.2 and 7.3 from Section 7.2:

$$k_{ee} = \frac{\epsilon_e}{\epsilon_\mu} \approx \sqrt{\frac{N_{NRB}^{ee}}{N_{NRB}^{\mu\mu}}} \quad (9.1)$$

once again under the assumption that each lepton leg acts independently. In simulation, k_{ee} is found to be about 0.88 after all selection criteria are applied. With this correction factor, the relation between the NRB yields in the signal and control region is:

$$\begin{aligned} N_{NRB}^{ee} &= \frac{1}{2} k_{ee} N_{NRB}^{e\mu} \\ N_{NRB}^{\mu\mu} &= \frac{1}{2} \frac{1}{k_{ee}} N_{NRB}^{e\mu} \\ \rightarrow N_{NRB}^{2\ell} &= \frac{1}{2} \left(k_{ee} + \frac{1}{k_{ee}} \right) N_{NRB}^{e\mu} \\ &= f_{NRB} N_{NRB}^{e\mu} \end{aligned} \quad (9.2)$$

This transfer factor f_{NRB} is implied by the MC estimates in the likelihood (Sec. 9.4), and the MC yields are found to be consistent with the derived relation within the statistical uncertainty. Perturbations in the predicted transfer factor are suppressed upon summing the $ee + \mu\mu$ channels, as shown:

$$\begin{aligned} f + \delta f &= \frac{1}{2} \left(k + \delta k + \frac{1}{k + \delta k} \right) \\ &= f + \frac{k^2 - 1}{2k^2} \delta k + \mathcal{O}(\delta^2) \\ &= f + \mathcal{O}(\delta^2) \quad \text{for } k \approx 1 \end{aligned} \quad (9.3)$$

such that the extrapolation uncertainty, taken as a conservative 20%, covers any data-MC discrepancy in the transfer factor.

Note that the $e\mu$ control sample contains a small contribution from $W + \text{jets}$ because of fake leptons. Since the rate of fake electrons and muons is different, this method does not account properly for the $W + \text{jets}$ contribution, leading to an underestimation of $W + \text{jets} \rightarrow ee + X$, and an overestimation of $W + \text{jets} \rightarrow \mu\mu + X$. Given the very small yield expected for such process in the signal region, well below

the systematic uncertainty, the effect is neglected. Moreover, the small biases resulting in the ee and $\mu\mu$ channels partially cancel out, so the overall effect on the $\ell\ell$ channel is even smaller.

As shown in Fig. 9-11, the $e\mu$ system mass, transverse momentum distributions and the E_T^{miss} distribution in the $e\mu$ channel, the dominant sources in the $e\mu$ channel within the Z mass window and in large E_T^{miss} (or $p_T^{\ell\ell}$) region are $t\bar{t}$, tW , WW , $\tau\tau$, and W + jets events. Contributions from the $t\bar{t}Z$ process are deemed negligible. As shown in Fig. 9-12, the shape of the E_T^{miss} spectrum is identical in the $e\mu$ control region and the $\ell\ell$ signal region.

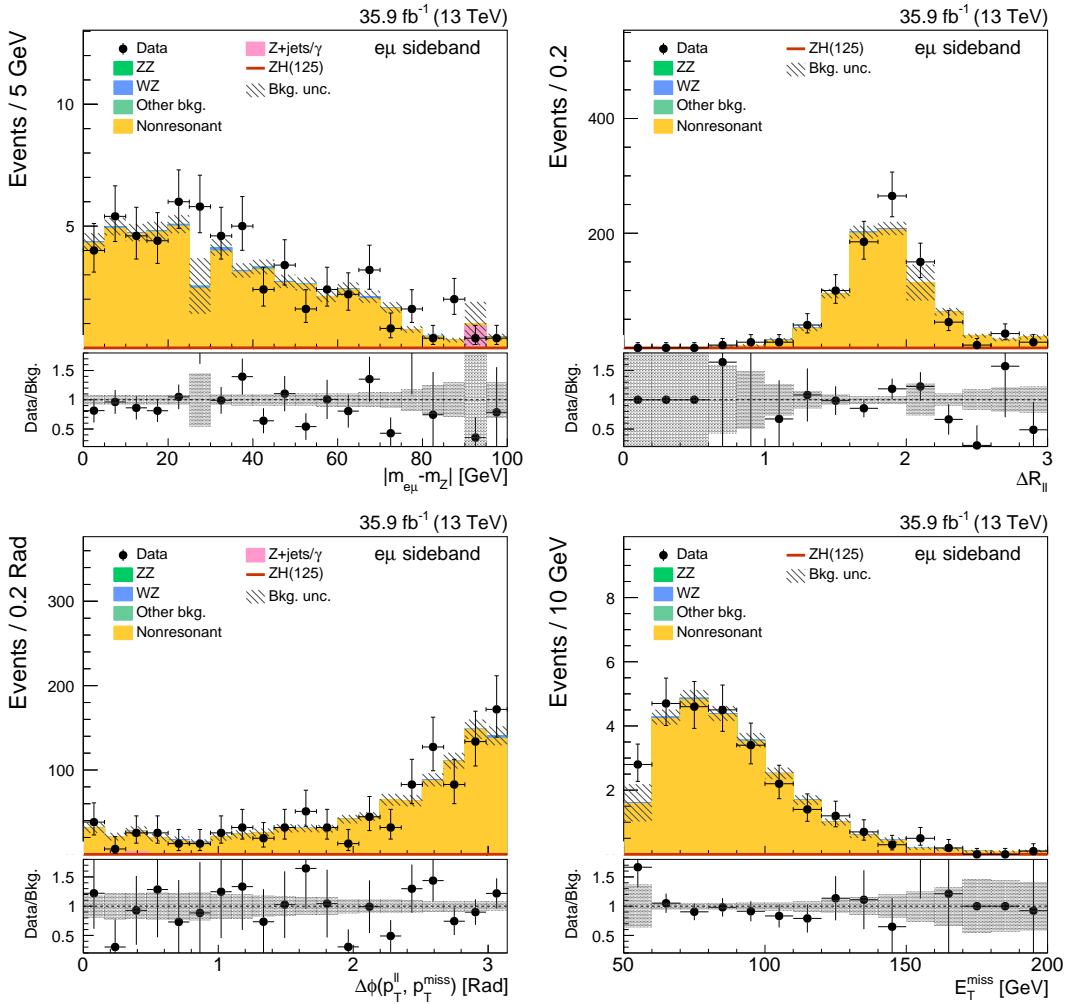


Figure 9-11: Distributions of $|m_{e\mu} - m_Z|$, ΔR_{ll} , $\Delta\phi_{ll, E_T^{\text{miss}}}$, and E_T^{miss} for $e\mu$ events after applying the full selection except the variable itself.

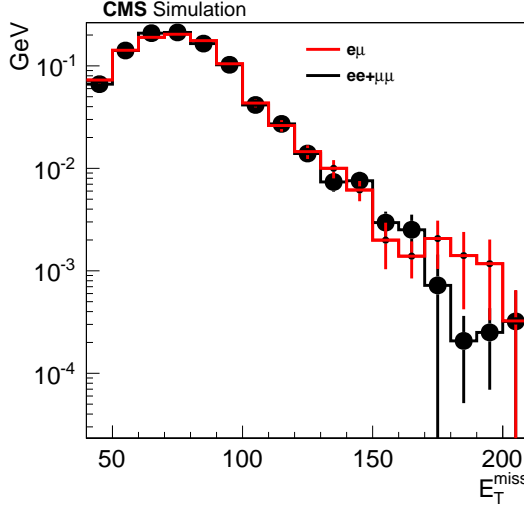


Figure 9-12: Comparison of the E_T^{miss} distributions for $W^+W^- + \text{top-quark}$ simulated events for $e\mu$ versus $ee + \mu\mu$ events.

9.2.3 Drell-Yan background estimation

The Drell-Yan (DY) process is dominant in the region of low E_T^{miss} . This process does not produce undetectable particles, therefore any non-zero E_T^{miss} arises from limited detector acceptance and mismeasurement. The estimation of this background uses simulated DY events, which are normalized to data in a control region. A scale factor is obtained by measuring the number of DY events in a E_T^{miss} sideband of [50, 100] GeV, and is included in the maximum likelihood fit, as shown in Sec. 9.4.

A 100% uncertainty is assigned to the DY estimate in order to cover the extrapolation from the low- E_T^{miss} region to the higher- E_T^{miss} signal region. This uncertainty has little effect on the results due to the small overall contribution from the DY process. Extensive checks are performed to ensure that the estimation method is sensible. By defining control regions where E_T^{miss} mismodeling issues are expected to have a large impact, and confirming that the estimate from simulation for these regions still holds within the uncertainties, it is shown in Fig. 9-13 that E_T^{miss} mismodeling is under control.

For example, it is possible to calculate missing energy multiple ways and assess how well they corroborate one another. The nominal E_T^{miss} quantity used in this work uses all the information from the Particle Flow reconstruction, and is called PF E_T^{miss} . The so-called “Calo E_T^{miss} ” is the calculation of missing energy only using the calorimeter deposits. A large difference between the two indicates fake missing energy e.g. from mismeasurement of a jet. The focus is how well the simulation describes the distribution in data of that disagreement, especially at high values.

Additionally, an independent estimation method using a $\gamma + E_T^{\text{miss}}$ control region is implemented, and the results are confirmed to be consistent between the two methods, further increasing confidence in the approach chosen here.

Spurious muons and mismeasured electrons were observed in the re-reconstruction

of the 2016 data, due to the relaxed tracking and PF requirements of the ‘HIP mitigation’ described earlier in Section 5.1.1. A re-analysis of the data was performed to identify and clean or correct the data for these objects. These issues are not expected to affect our analysis in a significant manner, mainly due to our third lepton veto. Nevertheless, the effect is negligible in our signal region. A correlation plot showing the effect of this cleaning is shown in Fig. 9-13.

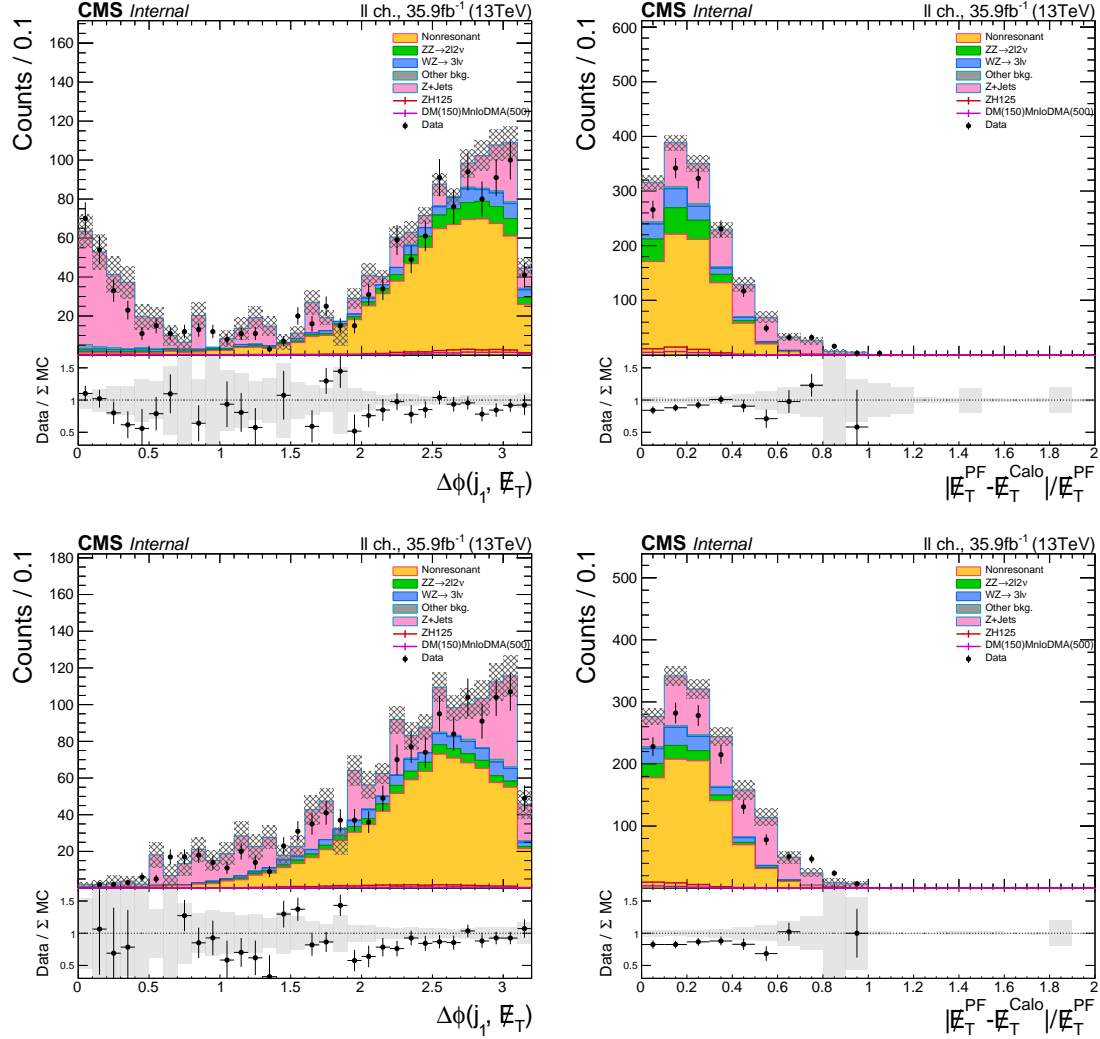


Figure 9-13: Selection of E_T^{miss} mismodeling control regions, after a loose selection: m_Z window, $p_T^{\ell\ell} > 60 \text{ GeV}$, < 2 Jets, $E_T^{\text{miss}} > 100 \text{ GeV}$. Top row: Events failing E_T^{miss} Balance cut, $\Delta\phi(j, E_T^{\text{miss}})$ and the PF to Calo E_T^{miss} ratio are plotted. Second row: Events failing $\Delta\phi(Z, E_T^{\text{miss}})$ cut, $\Delta\phi(j, E_T^{\text{miss}})$ and the PF to Calo E_T^{miss} ratio are plotted.

9.3 Systematic uncertainties

Systematic uncertainties in the data-based background estimates are described in Section 9.2. Here I will list all of the uncertainties which are taken into account in

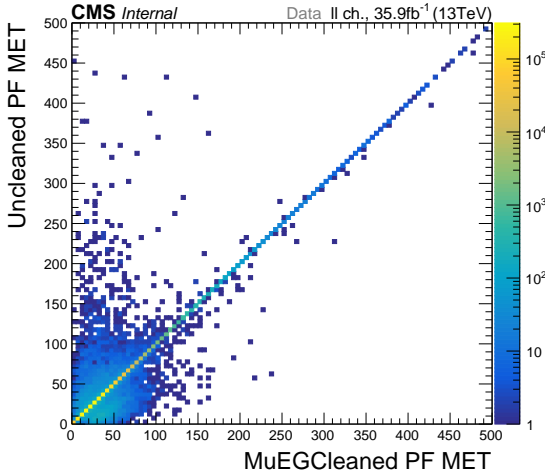


Figure 9-14: Joint distribution of the E_T^{miss} and the cleaned E_T^{miss} , showing the effect of the cleaning.

the fit to the E_T^{miss} shapes. Uncertainties which do not only influence the overall normalization (e.g. the uncertainty in the luminosity measurement), but also the distribution of relevant kinematic observables (e.g. the uncertainty in the jet energy scale), are treated as shape uncertainties. Their impact is evaluated by performing the full analysis not only for the central value of the relevant parameter, but also with its value shifted up and down by one standard deviation. The final varied E_T^{miss} -distributions are used as input for the limit calculation. For each source of uncertainty, the impact in different bins of the E_T^{miss} -distribution is thus considered fully correlated, while independent sources of uncertainty are treated as uncorrelated.

9.3.1 Luminosity

The assigned uncertainty to the integrated luminosity measurement for the data set used in this analysis is 2.5% [150].

9.3.2 Trigger, lepton reconstruction and identification efficiencies

Discrepancies in the lepton reconstruction and identification efficiencies between data and simulation are corrected by applying to all MC samples data-to-simulation scale factors measured using $Z/\gamma^* \rightarrow \ell^+\ell^-$ events in the Z peak region [159] that are recorded with unbiased triggers. These factors depend on the lepton p_T and η and are within a few percent for electrons and muons. The uncertainty in the determination of the trigger efficiency leads to an uncertainty smaller than 1% in the expected signal yield. Residual difference between the analysis lepton requirements with respect to the trigger selections is well covered by the uncertainty in the trigger efficiency.

9.3.3 Lepton momentum and electron energy scale

The lepton momentum scale uncertainty is computed by varying the momentum of the leptons by their uncertainties. The uncertainty on the muon and electron transverse momenta is assumed to be 1%.

9.3.4 Jet energy scale (JES) and resolution (JER)

The uncertainty in the calibration of the jet energy scale and resolution directly affects the acceptance of the requirement < 2 jets, the E_T^{miss} computation, and all the cuts related to jets.

The estimate of the jet energy scale uncertainty is performed varying the jet energy scale up and down by 1σ . The variation corresponds to a simple re-scaling of the jet four-momentum as $P \rightarrow P \cdot (1 \pm \delta p_T^{\text{JES}}/p_T)$, where δp_T^{JES} is the absolute uncertainty on the jet energy scale which is parametrized as function of the p_T and η of the jet. For more details on the jet energy scale prescription, see Ref. [188].

In order to account for the systematic uncertainty of the jet resolution smearing procedure, the resolution scale factors are varied up and down within their uncertainty.

9.3.5 B-tagging efficiency

In this analysis, b-tagging is used to reject events with real b-jets in the final state since the signal events have little b-jet content. For numerous reasons, the b-tagging efficiency of light flavor, c-quark, and b-quark jets varies between data and simulation. To account for this, a recommendation provided by the collaboration’s B-Tagging and Vertexing Group is used to reweight the b-tagging (in)efficiencies of the selected jets [131].

The b-tagging efficiency determination relies on a data sample of jets enriched in heavy flavor content. This is obtained by requiring a primary AK4 jet containing a soft muon, along with a secondary “away-jet” having separation $\Delta R > 1.5$ with respect to the first jet. Fit templates for the different jet flavors are built from muon-enriched simulated samples of QCD processes. Various systematic uncertainties are considered for this method:

- Relative contribution of gluon splitting
- Modelling of b-quark fragmentation
- Relative contribution of light jets and c-quark jets
- Pileup
- Muon selection
- Away-jet selection
- Jet energy scale

The impact of these systematic uncertainties on the sensitivity of this analysis is only 0.1%.

9.3.6 Pileup

As discussed in Sec. 5.4.1, MC samples are re-weighted to reproduce the pileup conditions observed in data. To compute the uncertainty related to this re-weighting procedure, the pileup distribution is computed not only for the nominal value of the minimum bias cross-section, but also for $\pm 5\%$ variations of it. The resulting variations in weights are propagated through the analysis chain, and the varied E_T^{miss} spectra are used to as input to the maximum likelihood fit. The variation of the final yields induced by this procedure is less than 1% in MC-estimated processes.

9.3.7 Theoretical uncertainties

Uncertainties on the normalization for ZZ, WZ and signal processes are derived from variations of the QCD scale, α_s and parton distribution functions (PDFs) variations [160, 161, 162, 163, 164, 139].

The PDF and α_s uncertainties for signal and background processes are estimated from the standard deviation of weights from the replicas provided in the NNPDF3.0 parton distribution set [98].

The samples for the signals and leading backgrounds were generated at NLO in QCD, and the scale uncertainties are estimated using the weights stored in the respective samples. For the ZZ process, this procedure is rather conservative in the sense that the prediction is corrected to NNLO in QCD, but the assumed uncertainty reflects the precision of the NLO generator.

The PDF uncertainties for the PDF4LHC PDF sets are assessed in the following way. The final distribution for the variable of interest is reweighted bin-by-bin using the PDF4LHC PDF sets. This produces $1 + N_{\text{mem}}$ distributions, where N_{mem} is the number of alternative PDF sets used. The uncertainty $\delta^{\text{PDF}}\sigma$ on the cross section σ is calculated in a bin-by-bin approach via

$$\delta^{\text{PDF}}\sigma = \sqrt{\frac{1}{N_{\text{mem}} - 1} \sum_{k=1}^{N_{\text{mem}}} (\sigma^{(k)} - \langle \sigma \rangle)^2}, \quad (9.4)$$

whereby the mean value of the cross section σ is given by

$$\langle \sigma \rangle = \frac{1}{N_{\text{mem}}} \sum_{k=1}^{N_{\text{mem}}} \sigma^{(k)}, \quad (9.5)$$

Now, let us return to the discussion of diboson theory introduced in Chapter 8, Section 8.1. The uncertainties from the higher order theoretical calculations are propagated to the E_T^{miss} distribution. The NLO electroweak and NNLO QCD corrections

each carry a “shape uncertainty,” meaning the corresponding nuisance parameters in each bin of E_T^{miss} are fully correlated for the purposes of the maximum likelihood fit.

9.3.8 MC statistical uncertainty

All background estimation procedures in this analysis rely on some degree of simulation shape information. For the DY and NRB processes, the final shape is taken directly from simulation, while the WZ and ZZ estimates only depend on the ratio of the MC expectations for the processes. In any case, the limited number of simulated events gives rise to a statistical uncertainty. This uncertainty is treated as fully uncorrelated for each process classification and distribution bin.

9.3.9 Summary

The summary of all systematic uncertainties and their correlations is shown in Table 9.2. The following uncertainties are considered for the shape variation:

- lepton efficiencies and momentum resolution
- missing transverse energy
- jet energy scale and resolution
- b-tagging efficiency
- pileup reweighting
- limited number of Monte Carlo events
- missing mixed QCD-EW corrections
- missing QCD higher-order corrections
- PDF

The overall signal efficiency uncertainty is estimated to be about 11% and is dominated by the theoretical uncertainty due to missing higher-order corrections and PDF uncertainties. The total uncertainty in the background estimations in the signal region is about 10%, which is dominated by the theoretical uncertainties in the ZZ and WZ processes.

The post-fit pulls and the impacts of the top 30 uncertainties, ordered by decreasing importance, are shown in Figure 9-15.

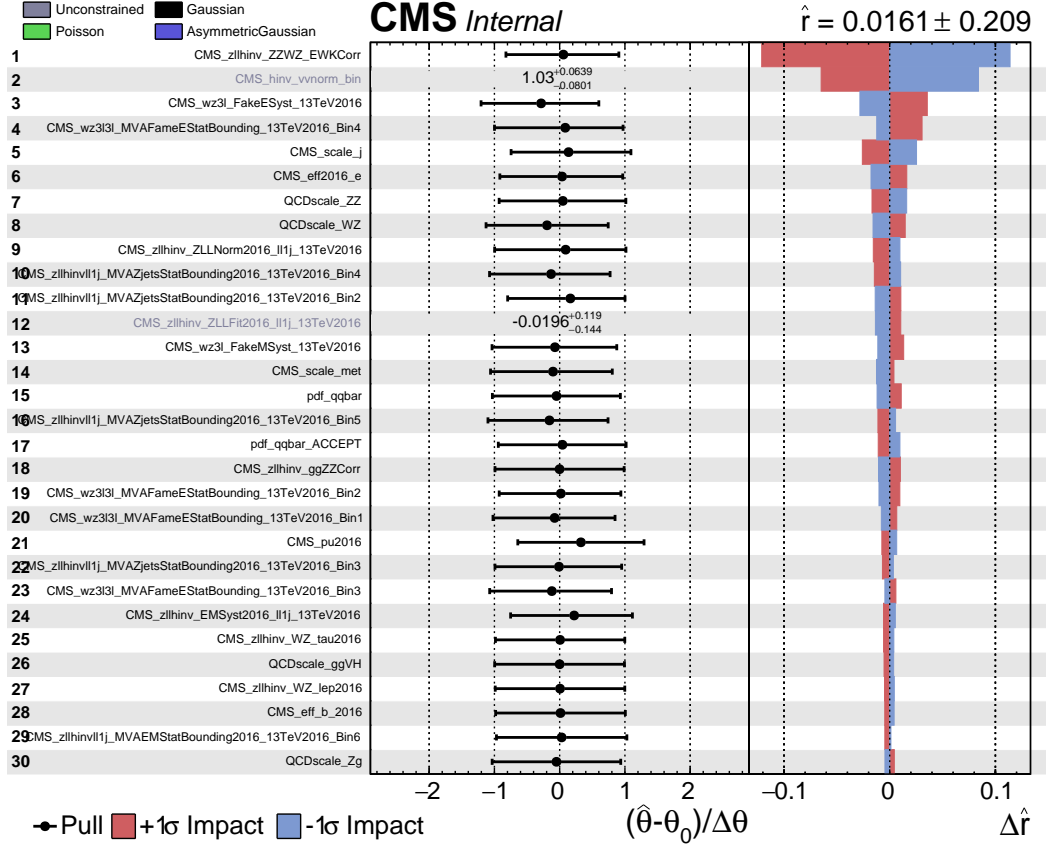


Figure 9-15: Top uncertainties at 35.9 fb^{-1} for a 125 GeV scalar boson mediator, ranked by decreasing importance. The codenames are explained as follows: CMS_zllhinv_ZZWZ_EWKCorr is the diboson electroweak uncertainties. CMS_hinv_vvnorm_bin is the ZZ/WZ ratio parameter from Section 9.4. CMS_wz3l_FakeESyst_13TeV2016 is the uncertainty on MC simulation for producing an electron fake to give 3 leptons in the 3-lepton control sample. CMS_wz3l3l_MVAFameEStatBounding_13TeV2016_Bin4 is a statistical nuisance on a bin of this electron fake process. CMS_scale_j is the jet energy scale uncertainty. CMS_eff2016_e is the uncertainty on the electron identification efficiency. QCDscale_ZZ is the effect of the QCD scale on the ZZ process. QCDscale_WZ is the effect of the QCD scale on the WZ process. CMS_zllhinv_ZLLNorm2016_ll1j_13TeV2016 is the effect of the 100% uncertainty on the Drell-Yan + fake E_T^{miss} process extrapolating from the low- E_T^{miss} sideband to the signal region.

Source of uncertainty	Effect (%)					Impact on exp. limit
	Signal	ZZ	WZ	NRB	DY	
* VV Electroweak Corrections	-	10	-4	-	-	-
* QCD Scale, VV backgrounds	-	9	4	-	-	-
* QCD Scale, Higgs Signal	3.5	-	-	-	-	-
* QCD Scale, Dark Matter Signal	5	-	-	-	-	-
* PDF, WZ background	-	-	1.5	-	-	-
* PDF, ZZ background	-	1.5	-	-	-	2 %
* PDF, Higgs Signal	1.5	-	-	-	-	-
* PDF, Dark Matter Signal	1-2	-	-	-	-	-
* MC Statistics, Nonresonant	-	-	-	5	-	-
* MC Statistics, Drell-Yan	-	-	-	-	30	-
* MC Statistics, ZZ	-	0.1	-	-	-	1 %
* MC Statistics, WZ	-	-	2	-	-	-
* MC Statistics, Higgs Signal	1	-	-	-	-	-
* MC Statistics, DmSimp Signals	3	-	-	-	-	-
NRB extrapolation to signal region	-	-	-	20	-	< 1 %
Drell-Yan extrapolation to signal region	-	-	-	-	100	-
Non-prompt backgrounds (signal region)	-	-	3	-	-	< 1 %
Non-prompt backgrounds (WZ control region)	-	-	-	-	30	< 1 %
Luminosity					2.6	< 1 %
* Electron Efficiency					1.5	
* Muon Efficiency					1	
* Electron energy scale					1-2	
* Muon energy scale					1-2	
* Jet Energy Scale				1-3 (typically anti-correlated with yield)		1 %
* Jet Energy Resolution				1 (typ. anti-correlated)		
* Unclustered Energy Scale (MET)				1-4 (typ. anti-correlated), strong in DY		
* Pileup				1 (typ. anti-correlated)		
* B-tagging fake efficiency				0.1		

Table 9.2: Summary of systematic uncertainties. Each uncertainty represents the variation of the relative yields of the processes in the signal region. A particular uncertainty is fully correlated across processes for which it contributes, including those processes which are also present in control regions. The symbol “-” indicates that the systematic uncertainty does not contribute or is deemed negligible. For shape uncertainties (indicated with a *), the numbers correspond to the overall effect of the shape variation on yield or acceptance. The impact on the expected limit, i.e. the relative decrease in the median expected upper limit on signal strength upon removing the nuisance, is also evaluated with respect to the SM Higgs signal.

9.4 Maximum likelihood fit

The likelihood \mathcal{L} is constructed as follows:

$$\begin{aligned}
\mathcal{L} = \prod_i \mathcal{P} & \left[N_{obs,i}^{2\ell} \middle| \boldsymbol{\mu}_{DY} N_{DY,i}^{2\ell}(\boldsymbol{\theta}) + \boldsymbol{\mu}_{NRB} N_{NRB,i}^{2\ell}(\boldsymbol{\theta}) \right. \\
& \left. + N_{other,i}^{2\ell}(\boldsymbol{\theta}) + \boldsymbol{\mu}_i^{VV} (N_{ZZ,i}^{2\ell}(\boldsymbol{\theta}) + N_{WZ,i}^{2\ell}(\boldsymbol{\theta})) + \boldsymbol{\mu} N_{Sig,i}^{2\ell}(\boldsymbol{\theta}) \right] \\
& \times \prod_i \mathcal{P} \left[N_{obs,i}^{3\ell} \middle| N_{other,i}^{3\ell}(\boldsymbol{\theta}) + \boldsymbol{\mu}_i^{VV} N_{WZ,i}^{3\ell}(\boldsymbol{\theta}) \right] \\
& \times \prod_i \mathcal{P} \left[N_{obs,i}^{4\ell} \middle| N_{other,i}^{4\ell}(\boldsymbol{\theta}) + \boldsymbol{\mu}_i^{VV} N_{ZZ,i}^{4\ell}(\boldsymbol{\theta}) \right] \\
& \times \mathcal{P} \left[N_{obs}^{e\mu} \middle| \boldsymbol{\mu}_{NRB} N_{NRB}^{e\mu}(\boldsymbol{\theta}) + N_{other}^{e\mu}(\boldsymbol{\theta}) \right] \\
& \times \mathcal{P} \left[N_{obs}^{DYsb} \middle| \boldsymbol{\mu}_{DY} N_{DY}^{DYsb}(\boldsymbol{\theta}) + \boldsymbol{\mu}_{NRB} N_{NRB}^{DYsb}(\boldsymbol{\theta}) + N_{other}^{DYsb}(\boldsymbol{\theta}) \right. \\
& \left. + \boldsymbol{\mu}_i^{VV} (N_{ZZ}^{DYsb}(\boldsymbol{\theta}) + N_{WZ}^{DYsb}(\boldsymbol{\theta})) + \boldsymbol{\mu} N_{Sig}^{DYsb}(\boldsymbol{\theta}) \right] \times e^{-(\boldsymbol{\theta}-\hat{\boldsymbol{\theta}})^2/2}
\end{aligned} \tag{9.6}$$

where $\mathcal{P}(N|\lambda)$ is the Poisson probability, $\boldsymbol{\theta}$ are nuisance parameters for the systematics as described in Section 9.3, $\boldsymbol{\mu}$ is the signal strength, $\boldsymbol{\mu}_i^{VV}$ is the diboson process normalization in bin i , $\boldsymbol{\mu}_{DY}$ is the Drell-Yan normalization, $\boldsymbol{\mu}_{NRB}$ is the nonresonant background (NRB) normalization, $N_x^{2\ell}$ is the MC prediction for the yield of process x in the signal region, $N_x^{3\ell}$ is the MC prediction for the yield of process x in the WZ control region, $N_x^{4\ell}$ is the MC prediction for the yield of process x in the ZZ control region, $N_x^{e\mu}$ is the MC prediction for the yield of process x in the NRB control region, and N_x^{DYsb} is the MC prediction for the yield of process x in the 2ℓ Drell-Yan sideband ($[50, 100]$ GeV) region.

9.4.1 The ZZ/WZ ratio

The ZZ and WZ control samples are included as separate control regions in the maximum-likelihood fit. A freely floating normalization parameter is used which scales both VV processes. It is correlated across the bins of E_T^{miss} and emulated E_T^{miss} . Systematic uncertainties from the corrections at higher order in electroweak may not fully cancel between the two processes. Thus, a shape uncertainty on the ratio of ZZ to WZ is considered which takes into account the electroweak uncertainty of both processes. The nuisance is bin-dependent, but it is correlated between the E_T^{miss} bins and between the signal and control regions.

9.5 Multivariate analysis

As previously described, the analysis contains several theoretical interpretations, some of which act as representatives for a whole class of models. However, in the case of the invisible Higgs model with Standard Model mass hypothesis of 125 GeV, the well-defined nature of the model permits exploration of multivariate analysis techniques without reducing the discovery potential of the analysis. The main irreducible backgrounds of this analysis consist of an invisible vector boson of mass 80 or 91 GeV recoiling against a leptonic Z, resulting in very similar E_T^{miss} shapes of the invisible Higgs signal hypothesis and the background processes. Thus, it is essential to look for information in reconstructed objects which is related to the spin state of the invisible particle, so as to discriminate the spin-0 Higgs from these spin-1 vector boson backgrounds. Furthermore, any information that is not mutual to important analysis variables such as the E_T^{miss} and the dilepton mass could be capitalized upon using a multivariate approach.

9.5.1 Classifier variables and training

The following set of twelve variables is used to train a Boosted Decision Tree (BDT) classifier:

- $|m_{\ell\ell} - m_Z|$ (dilepton mass)
- $p_T^{\ell 1}$ (leading lepton transverse momentum)
- $p_T^{\ell 2}$ (subleading lepton transverse momentum)
- $p_T^{\ell\ell}$ (dilepton transverse momentum)
- $|\eta^{\ell 1}|$ (leading lepton pseudorapidity)
- $|\eta^{\ell 2}|$ (subleading lepton pseudorapidity)
- E_T^{miss} (missing transverse energy)
- $m_T(p_T^{\ell 1}, E_T^{\text{miss}})$ (leading lepton transverse mass)
- $m_T(p_T^{\ell 2}, E_T^{\text{miss}})$ (subleading lepton transverse mass)
- $\Delta\phi_{\ell\ell, E_T^{\text{miss}}}$ (azimuthal separation between dilepton and missing energy)
- $\Delta R_{\ell\ell}$ (separation between leptons)
- $|\cos\theta_{\ell 1}^{CS}|$ (cosine of Collins-Soper angle for leading lepton)

The Collins-Soper angle $\theta_{\ell 1}^{CS}$ is defined as the angle between the leading lepton trajectory and the Z mother trajectory, in the rest frame of the Z mother [189]. This allows some access to the spin information of the invisible particle and adds discrimination power between the diboson processes and the invisible Higgs hypothesis.

The best performance for this analysis was found in a multiclass BDT with the following parameters: 400 trees, gradient boosting with learning rate 0.5, bagging with fraction 0.5, and tree depth of 4. For a discussion of gradient boosted decision trees, see Appendix B. The multiple classes are: invisible Higgs (Signal); ZZ; WZ; Drell-Yan ($Z+jets$); and flavor-symmetric or non-resonant backgrounds (Non-prompt). The signal likelihood which is used as the final discriminator is the likelihood assigned to the quark- and gluon- induced invisible Higgs process, normalized to the sum of the likelihoods of all processes. The analysis criteria involving jet counting, jet kinematics, or jet vetoes are not considered as input variables, so that the classifier remains unbiased toward selecting events with 0 jets. The training preselection is as follows:

- B-tagging veto
- Tau veto
- Jet multiplicity ≤ 1 jet with $p_T^j > 30$ GeV
- Exactly 2 leptons
- $\Delta\phi_{jet, E_T^{\text{miss}}} > 0.5$ (in events with a jet)
- $E_T^{\text{miss}} > 130$ GeV

The training requirement for the E_T^{miss} was found via a stepwise optimization procedure. Because events with less E_T^{miss} can still be classified as highly signal-like, a looser criterion of $E_T^{\text{miss}} > 100$ GeV is applied for the MVA signal region. The higher training requirement helps to learn about difficult events which are not handled well by the standard analysis. It also happens to be compatible with the 125 GeV Higgs mass.

The pairwise mutual information between the input variables for the different physics process classes is shown in Figure B-1. After applying the training preselection, distributions of these variables are compared between data and simulation in Figures B-2, and B-3.

9.5.2 Analysis selection

The signal region in the multivariate analysis is defined using the training preselection cuts except $E_T^{\text{miss}} > 100$ GeV and classifier value > 0.2 . The Drell-Yan normalization is taken from a control selection similar to the rectangular analysis, admitting events which otherwise pass the signal region selection with $E_T^{\text{miss}} < 100$ GeV or classifier value < 0.2 . The non-resonant background normalization is taken from a control sample applying the signal region selection described in this section, but requiring opposite-flavor events. The diboson control region selections are unchanged from the rectangular analysis. See Figures 9-17 and 9-18 for the classifier spectrum in the signal region and diboson regions.

The signal hypothesis is considered in a shape analysis of the BDT classifier spectrum.

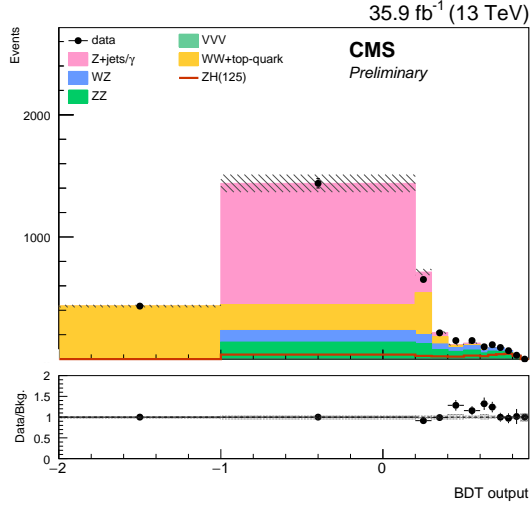


Figure 9-16: Distribution of the BDT classifier in the multivariate analysis before the likelihood fit. The first two bins $[-2, -1]$ and $[-1, 0]$ are a technical artifact of the control region implementation and do not correspond to a BDT score. The first bin contains the nonresonant background sideband of opposite-flavor events. The second bin contains the Drell-Yan sideband of events failing the BDT or E_T^{miss} requirement. The rest of the bins are the signal region BDT bins. Uncertainty bands represent only the statistical uncertainty.

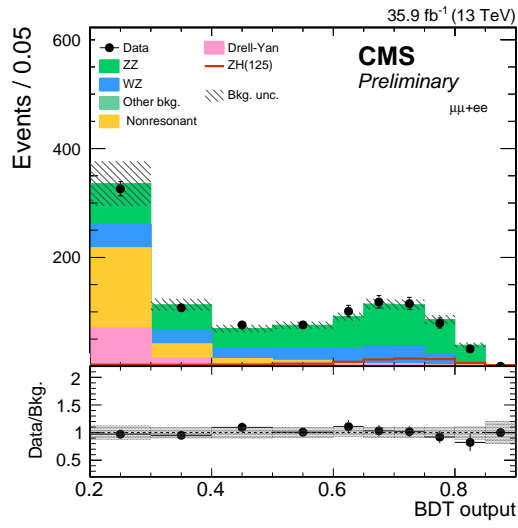


Figure 9-17: Distribution of the BDT classifier in the multivariate analysis signal region after the likelihood fit. Uncertainty bands correspond to both statistical and systematic uncertainty.

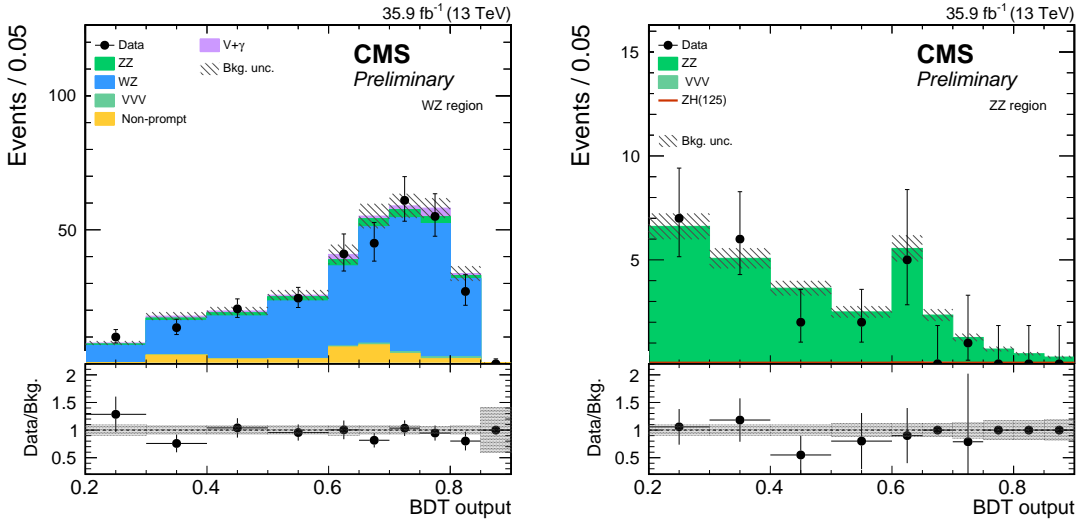


Figure 9-18: Distribution of the BDT classifier in the diboson control regions: WZ three-lepton region at left, ZZ four-lepton region at right. Uncertainty bands correspond to both statistical and systematic uncertainty. These are the same events as in Figure 9-10.

The experimental uncertainties affecting the input values to the BDT are propagated to the corresponding uncertainties on the output distribution of BDT scores in a robust mapping procedure. For a discussion of it, see Section B.3.

9.5.3 Improvement in sensitivity

A maximum likelihood fit is performed in the distribution of BDT scores, akin to the E_T^{miss} analysis prescription described in Section 9.4. The ZZ/WZ ratio is handled in the same way, but the bin-dependent electroweak uncertainty on the ratio of ZZ/WZ is described in bins of BDT score instead of (emulated) E_T^{miss} . Altogether, the BDT analysis improves the invisible Higgs sensitivity by 10%, where the metric is the expected limit on the branching ratio of Higgs boson to invisible particles.

Taking this approach is not nearly as rewarding for the higher mass simplified-model DM signals, where E_T^{miss} is a more powerful discriminant variable. Furthermore, the multivariate analysis strategy described above is dependent on the mediator mass. This would necessitate training and evaluating a different classifier for every mass scenario. These cases require further study before multivariate techniques can be exploited there.

9.6 Search results

The number of observed and expected events after final selection for the E_T^{miss} and BDT analyses are shown in Tables 9.3 and 9.4, respectively. There is no significant difference between the dimuon and dielectron channels in terms of signal-to-background ratio, and hence the two of them are treated together when computing the final results. Figure 9-19 shows the E_T^{miss} distributions after the final selection.

No deviation from the SM background expectations is found. Upper limits on the contribution of events from new physics are computed by using the modified frequentist approach CL_s [190, 191] based on asymptotic formulas [192]. The expected numbers of background events and signal events, scaled by a signal strength modifier, are combined in a profile-likelihood test statistic, in which the systematic uncertainties are incorporated as nuisance parameters. The systematic uncertainties include normalization uncertainties that affect the overall size of contributions and, when a shape analysis is performed, shape uncertainties that alter the shapes of the distributions used in extracting the signal limits.

Process	ee	$\mu\mu$	$\mu\mu+ee$
qqZH(125)	69.3 ± 2.3	89.3 ± 3.1	158.6 ± 5.4
ggZH(125)	18.4 ± 2.0	24.3 ± 2.9	42.7 ± 4.9
ZH(800)	113.1 ± 4.5	152.1 ± 6.1	265.1 ± 10.6
DM(150)MV(500)	40.9 ± 1.6	57.9 ± 2.3	98.8 ± 3.9
DM(150)MA(500)	27.5 ± 1.1	38.0 ± 1.5	65.5 ± 2.6
Nonresonant bkg.	32.1 ± 6.4	41.0 ± 8.2	74.8 ± 15.0
ZZ	162.3 ± 4.0	217.5 ± 5.4	379.8 ± 9.4
$WZ \rightarrow 3l\nu$	70.4 ± 2.9	92.1 ± 3.9	162.5 ± 6.8
Other bkg.	1.1 ± 0.1	1.4 ± 0.1	2.6 ± 0.2
Z+Jets	35.6 ± 14.4	22.9 ± 9.3	72.0 ± 29.2
Total bkg.	310.4 ± 19.5	381.3 ± 15.7	691.7 ± 34.8
Data	292	396	688

Table 9.3: Observed number of events, post-fit background estimates, and signal predictions for the E_T^{miss} analysis using 35.9 fb^{-1} . Both statistical and systematic uncertainties are reported. High-mass Higgs model is scaled to 1 pb (all masses in GeV).

Process	ee	$\mu\mu$	$\mu\mu+ee$
qqZH(125)	89.6 ± 2.5	117.3 ± 3.3	207.0 ± 5.8
ggZH(125)	26.8 ± 2.8	35.9 ± 3.7	62.7 ± 6.5
Nonresonant bkg.	165 ± 20	211 ± 26	375 ± 46
ZZ	309 ± 12	421 ± 17	730 ± 29
$WZ \rightarrow 3l\nu$	142.9 ± 5.2	192.5 ± 7.0	335 ± 12
Other bkg.	2.31 ± 0.15	3.23 ± 0.21	5.54 ± 0.36
Z+Jets	84 ± 25	110 ± 33	194 ± 58
Total bkg.	704 ± 35	936 ± 46	1640 ± 81
Data	682 ± 26	904 ± 30	1586 ± 40

Table 9.4: Observed number of events, post-fit background estimates, and signal predictions for the BDT analysis using 35.9 fb^{-1} . Both statistical and systematic uncertainties are reported. (all masses in GeV).

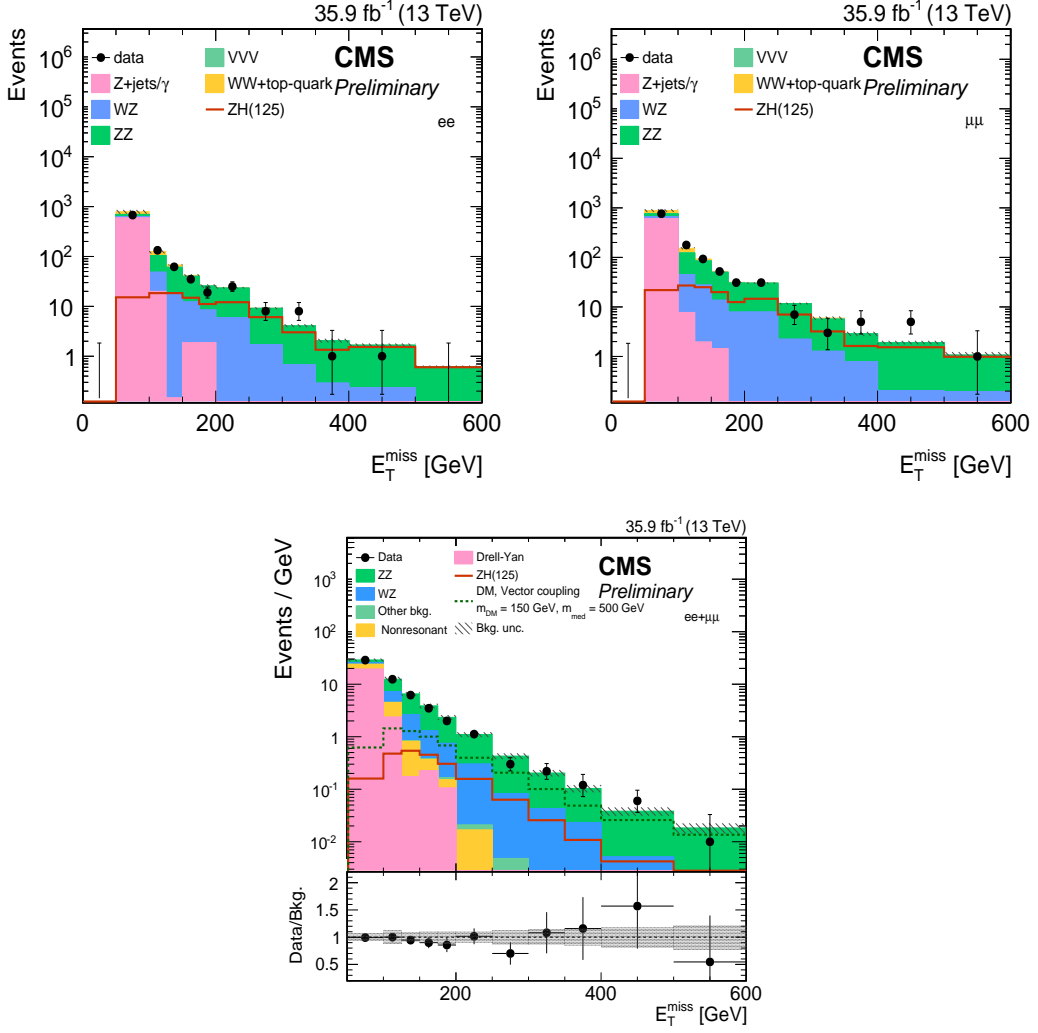


Figure 9-19: Distribution of the E_T^{miss} after the full selection including the region between 50 and 100 GeV. For the ee channel (top left) and $\mu\mu$ channel (top right), the uncertainty band corresponds to the statistical uncertainty only. For the $\ell\ell$ channel (bottom), the plot includes both statistical and systematic uncertainty. The signal normalization is arbitrary.

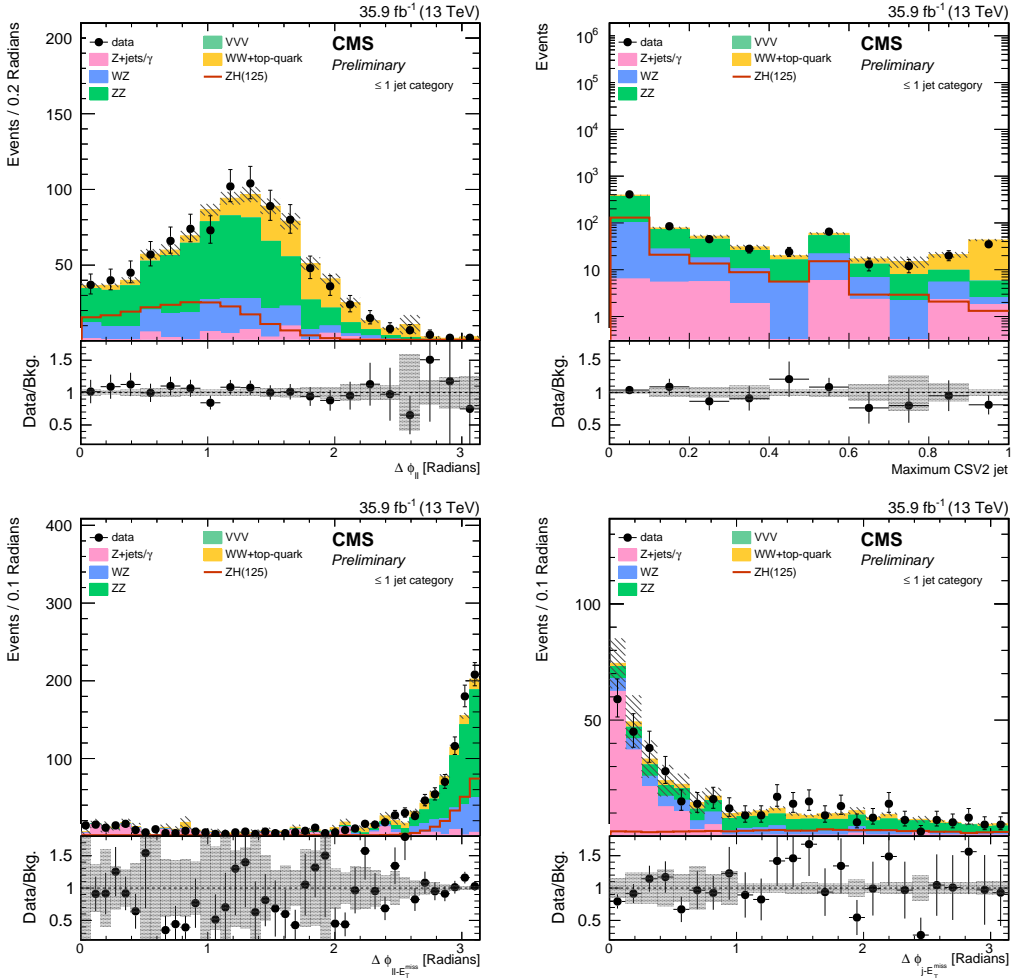


Figure 9-20: Distributions after the full selection except the variable itself. Upper left: $\Delta\phi_{\ell\ell}$. Upper right: maximum CSV2 b-tagging score among the jets. Bottom left: $\Delta\phi_{\ell, E_T^{\text{miss}}}$. Bottom right: $\Delta\phi_{\text{jet}, E_T^{\text{miss}}}$. The uncertainty band corresponds to the statistical uncertainty only.

9.6.1 Invisible Higgs interpretation

No significant excess of events is observed over the SM expectation. Upper limits are derived for the Higgs boson production cross section. For $m_H = 125$ GeV, this is interpreted as the upper limit on the branching ratio of the Higgs boson to invisible particles, assuming the SM production rate. To compute the upper limits, the modified frequentist construction CL_s is used (see [190, 191, 193]). The number of events are modeled as a Poisson random variable, where the mean value is the sum of the contributions from signal and background processes. The 95% observed and median expected CL upper limits on the production cross section times branching ratio, $\sigma_{qq \rightarrow ZH} \times B(H \rightarrow \text{invisible})$, computed with the asymptotic CL_s method are shown in Figure 9-21 for the rectangular analysis in E_T^{miss} . Assuming the SM production rate, the 95% observed (expected) CL upper limit on $B(H \rightarrow \text{invisible})$ is 0.45 (0.44) using the rectangular analysis in E_T^{miss} , and 0.40 (0.42) using the multivariate analysis. The $gg \rightarrow Z(\ell\ell)H$ process has also been considered for the 125 GeV mass point.

The signal strength limits for quark+gluon initiated $ZH(\rightarrow \text{invisible})$ processes is shown in Fig. 9-22. The signal strength limits for only quark-initiated processes is shown in Fig. 9-23.

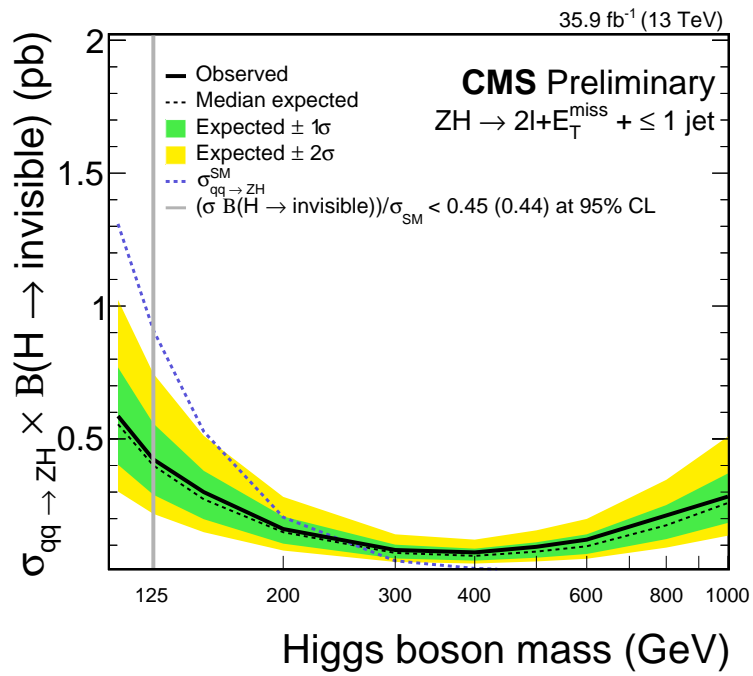


Figure 9-21: Expected and observed 95% CL upper limits on the production cross section times branching ratio, $\sigma_{Z\bar{H}(\rightarrow \text{invisible})} \times \text{BR}(H \rightarrow \text{invisible})$ as a function of the Higgs boson mass.

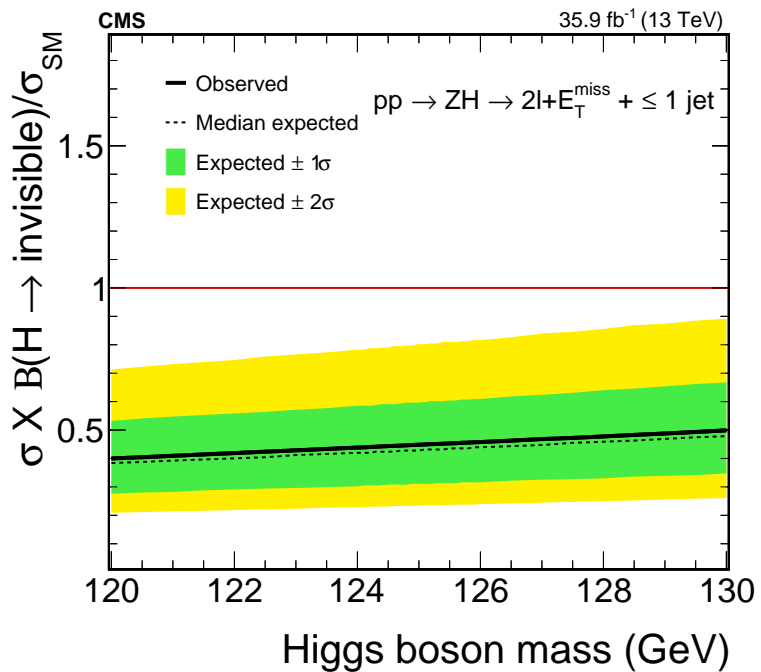


Figure 9-22: Expected and observed 95% CL upper limits on the signal strength, $\sigma_{ZH(\rightarrow\text{invisible})} \times \text{BR}(\text{H} \rightarrow \text{invisible})/\sigma_{SM}$ as a function of the Higgs boson mass. σ_{SM} includes both quark- and gluon-initiated processes.

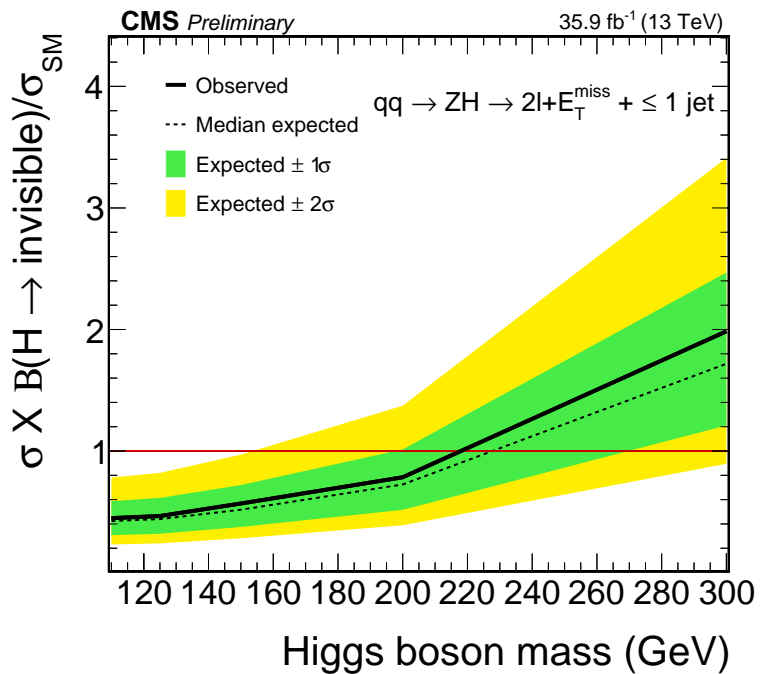


Figure 9-23: Expected and observed 95% CL upper limits on the signal strength, $\sigma_{Z\text{H}(\rightarrow\text{invisible})} \times \text{BR}(\text{H} \rightarrow \text{invisible})/\sigma_{SM}$ as a function of the Higgs boson mass, including only quark-initiated processes.

9.6.2 Simplified Model dark matter interpretation

To compute limits on specific DM models, a shape-based analysis is employed, based on the E_T^{miss} distributions in Fig. 9-19. In this case, the test statistics is a binned likelihood. Figure 9-24 shows the 95% CL expected limits for vector and axial-vector mediated scenarios with couplings $g_\chi = 1$, $g_q = 0.25$. The plane of mediator and dark matter masses is interpolated between the fully simulated points, which are tabulated in Table 9.5. More details on this interpolation procedure may be found in Appendix D.

The limits are compared to the results from direct-detection experiments in Fig. 9-26. Figure 9-25 shows the 95% CL expected limits as a function of m_ϕ for fixed $m_\chi = 1 \text{ GeV}$ with couplings $g_\chi = 1$, $g_q = 1$ for scalar and pseudoscalar-vector mediated scenarios. The expected and observed cross section limits for the different DM signal hypotheses are shown in Tables 9.5, 9.6, 9.7, 9.8.

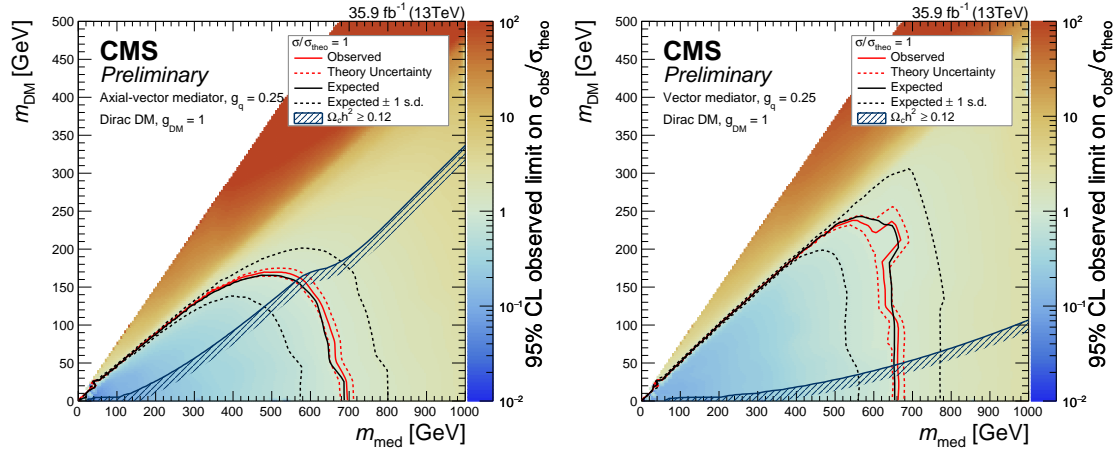


Figure 9-24: The 95% CL expected and observed limits on signal strength $\sigma^{\text{obs}}/\sigma^{\text{th}}$ for the axial (left) and vector (right) mediated DM scenario with $g_q = 0.25$.

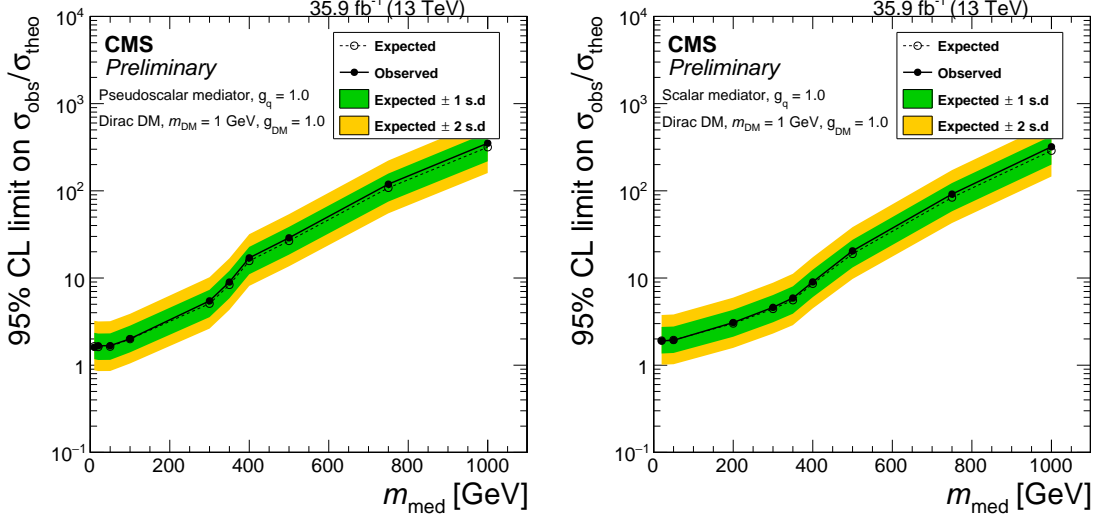


Figure 9-25: The 95% CL expected and observed limits on signal strength σ^{obs}/σ^{th} for the pseudoscalar (left) and scalar (right) mediated DM scenario with $g_q = 1$.

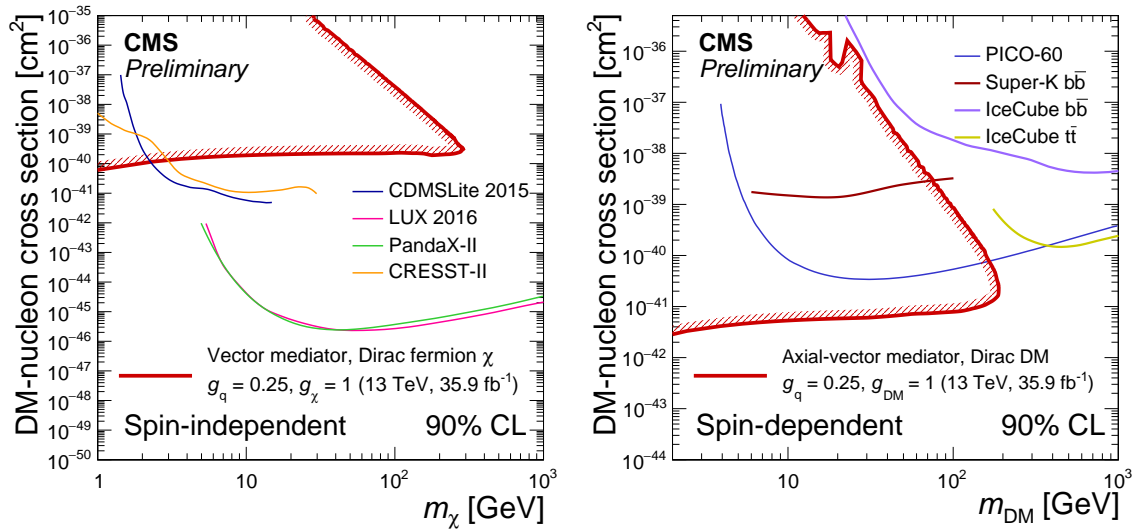


Figure 9-26: Observed 90% CL limits on the DM-nucleon scattering cross sections in both spin-independent (left) and spin-dependent (right) cases, assuming a mediator-quark coupling constant $g_q = 0.25$ and mediator-DM coupling constant $g_\chi = 1$. Limits from the LUX [194], CDMSLite [195], PandaX-II [196], and CRESST-II [197] experiments are shown for the spin-independent case. Limits from the Super-Kamiokande [198], PICO-60 [199], and IceCube [200, 201] experiments are shown for the spin-dependent case.

Short title	μ_{exp}	$\delta^+ \mu_{exp}$	$\delta^- \mu_{exp}$	μ_{obs}	$\sigma \cdot BR [pb]$
DM(100)MnloDMV(300)	0.29	0.4	0.21	0.33	0.0885
DM(10)MnloDMV(10)	1.6	2.3	1.2	1.8	0.0524
DM(10)MnloDMV(100)	0.12	0.16	0.087	0.12	0.515
DM(10)MnloDMV(50)	0.12	0.16	0.085	0.12	0.823
DM(150)MnloDMV(200)	10	15	7.6	12	0.00184
DM(150)MnloDMV(500)	0.72	1	0.53	0.92	0.0278
DM(1)MnloDMV(10)	1.6	2.2	1.2	1.7	0.0545
DM(1)MnloDMV(100)	0.14	0.19	0.1	0.15	0.516
DM(1)MnloDMV(1000)	2.2	3.3	1.5	2.8	0.00402
DM(1)MnloDMV(200)	0.17	0.25	0.13	0.21	0.199
DM(1)MnloDMV(2000)	22	34	15	32	0.000252
DM(1)MnloDMV(300)	0.28	0.39	0.2	0.3	0.0949
DM(1)MnloDMV(50)	0.12	0.17	0.085	0.13	0.841
DM(1)MnloDMV(500)	0.57	0.82	0.41	0.7	0.029
DM(1)MnloDMV(750)	1.2	1.8	0.86	1.5	0.00978
DM(300)MnloDMV(750)	1.4	2	1	1.9	0.00811
DM(40)MnloDMV(100)	0.15	0.21	0.11	0.17	0.445
DM(490)MnloDMV(1000)	5.7	8.5	3.9	8	0.00153
DM(500)MnloDMV(500)	2e+02	3e+02	1.4e+02	2.7e+02	3.63e-05
DM(50)MnloDMV(200)	0.2	0.28	0.15	0.22	0.194
DM(50)MnloDMV(500)	0.59	0.83	0.42	0.68	0.0291
DM(75)MnloDMV(500)	0.65	0.91	0.47	0.8	0.0286
DM(990)MnloDMV(2000)	88	1.3e+02	60	1.2e+02	7.12e-05

Table 9.5: Expected cross-section limits for a Vector mediator with 35.9 fb^{-1} and couplings $g_\chi = 1$, $g_q = 0.25$. μ_{exp} corresponds to the expected cross-section limits divided by the theoretical cross section. Limits are with respect to the NLO DmSimp model [202, 203]

Short title	μ_{exp}	$\delta^+ \mu_{exp}$	$\delta^- \mu_{exp}$	μ_{obs}	$\sigma \cdot BR [pb]$
DM(100)MnloDMA(300)	0.4	0.57	0.28	0.47	0.0594
DM(100)MnloDMA(750)	1.3	1.9	0.96	1.6	0.00925
DM(10)MnloDMA(10)	1.6	2.2	1.1	1.9	0.0418
DM(10)MnloDMA(100)	0.12	0.16	0.084	0.13	0.602
DM(10)MnloDMA(50)	0.054	0.074	0.039	0.051	1.88
DM(140)MnloDMA(300)	2.2	3.2	1.6	2.5	0.0108
DM(150)MnloDMA(1000)	2.6	3.7	1.8	3.4	0.00376
DM(150)MnloDMA(200)	25	35	18	29	0.000693
DM(150)MnloDMA(500)	0.89	1.3	0.65	1.1	0.0204
DM(1)MnloDMA(10)	1.3	1.9	0.95	1.7	0.0532
DM(1)MnloDMA(100)	0.1	0.14	0.074	0.12	0.618
DM(1)MnloDMA(1000)	2.2	3.2	1.5	2.8	0.00407
DM(1)MnloDMA(200)	0.18	0.25	0.13	0.2	0.209
DM(1)MnloDMA(2000)	22	33	15	29	0.000252
DM(1)MnloDMA(300)	0.26	0.36	0.18	0.3	0.0964
DM(1)MnloDMA(50)	0.057	0.079	0.042	0.06	1.9
DM(1)MnloDMA(500)	0.52	0.74	0.36	0.62	0.0307
DM(1)MnloDMA(750)	1.1	1.6	0.76	1.4	0.01
DM(200)MnloDMA(750)	1.7	2.4	1.2	2.2	0.00741
DM(300)MnloDMA(750)	3.5	5.1	2.5	4.2	0.00345
DM(40)MnloDMA(100)	0.24	0.33	0.17	0.29	0.256
DM(490)MnloDMA(1000)	68	1e+02	47	91	0.000136
DM(500)MnloDMA(2000)	33	49	22	45	0.000179
DM(500)MnloDMA(500)	6.3e+02	9.4e+02	4.3e+02	8.6e+02	1.1e-05
DM(50)MnloDMA(200)	0.23	0.33	0.17	0.25	0.164
DM(50)MnloDMA(300)	0.32	0.45	0.23	0.37	0.0896
DM(50)MnloDMA(50)	5.3	7.4	3.8	5.7	0.00591
DM(50)MnloDMA(500)	0.55	0.78	0.39	0.63	0.0294
DM(75)MnloDMA(1000)	2.2	3.3	1.6	3	0.00398
DM(75)MnloDMA(500)	0.63	0.89	0.45	0.75	0.0279
DM(990)MnloDMA(2000)	1.3e+03	2e+03	8.9e+02	1.9e+03	4.64e-06

Table 9.6: Expected cross-section limits for an Axial Vector mediator with 35.9 fb^{-1} and couplings $g_\chi = 1$, $g_q = 0.25$. μ_{exp} corresponds to the expected cross-section limits divided by the theoretical cross section. Limits are with respect to the NLO DmSimp model.

Short title	μ_{exp}	$\delta^+ \mu_{exp}$	$\delta^- \mu_{exp}$	μ_{obs}	$\sigma \cdot BR [pb]$
DM(100)MnloDMP(300)	6.3	8.9	4.6	8.4	0.00255
DM(100)MnloDMP(350)	11	15	7.7	14	0.00138
DM(100)MnloDMP(500)	35	50	25	48	0.000288
DM(100)MnloDMP(750)	1.2e+02	1.7e+02	87	1.7e+02	6.78e-05
DM(10)MnloDMP(10)	33	46	24	41	0.00056
DM(10)MnloDMP(100)	2.3	3.1	1.7	2.7	0.00871
DM(10)MnloDMP(50)	2	2.8	1.5	2.5	0.00972
DM(1)MnloDMP(10)	1.9	2.7	1.4	2.3	0.0102
DM(1)MnloDMP(100)	2.4	3.3	1.7	2.8	0.00879
DM(1)MnloDMP(1000)	3.4e+02	4.9e+02	2.4e+02	4.9e+02	2.16e-05
DM(1)MnloDMP(20)	1.9	2.7	1.4	2.3	0.0101
DM(1)MnloDMP(300)	6	8.4	4.3	7.9	0.00254
DM(1)MnloDMP(350)	9.8	14	7	13	0.00148
DM(1)MnloDMP(400)	18	26	13	25	0.000683
DM(1)MnloDMP(50)	1.9	2.7	1.4	2.3	0.00972
DM(1)MnloDMP(500)	31	44	22	42	0.000323
DM(1)MnloDMP(750)	1.2e+02	1.8e+02	89	1.7e+02	7.02e-05
DM(200)MnloDMP(500)	47	66	34	64	0.000213
DM(350)MnloDMP(1000)	4.7e+02	6.9e+02	3.3e+02	6.8e+02	1.57e-05
DM(350)MnloDMP(750)	2.9e+02	4.2e+02	2.1e+02	4.1e+02	2.99e-05
DM(40)MnloDMP(100)	2.3	3.1	1.6	2.8	0.00876
DM(50)MnloDMP(10)	1e+02	1.5e+02	75	1.3e+02	0.000151
DM(50)MnloDMP(200)	4.3	6	3.1	5.5	0.00418
DM(50)MnloDMP(300)	6	8.4	4.3	7.9	0.00248
DM(50)MnloDMP(350)	10	14	7.2	13	0.00148
DM(50)MnloDMP(400)	17	24	12	23	0.00069
DM(50)MnloDMP(50)	92	1.3e+02	67	1.2e+02	0.000178
DM(50)MnloDMP(500)	32	45	23	44	0.000304

Table 9.7: Expected and observed signal strength limits for NLO Simplified Model Pseudoscalar-mediated Dark Matter samples with 35.9 fb^{-1} . μ_{obs} , and μ_{exp} correspond to the observed and expected cross-section limits divided by the theoretical cross section. The cross section times branching ratio is also listed for reference. The mapping from short title to dataset is as follows: $\text{DM}(m_\chi)\text{MnloDMP}(m_{\text{med}}) \rightarrow \text{DarkMatter_MonoZToLL_NLO_Pseudo_Mx-\$mchi_Mv-\$mmmed_gDM1_gQ1_TuneCUETP8M1_13TeV-madgraph}$

Short title	μ_{exp}	$\delta^+ \mu_{exp}$	$\delta^- \mu_{exp}$	μ_{obs}	$\sigma \cdot BR [pb]$
DM(0)MnloDMS(20)	2.3	3.2	1.7	2.7	0.00739
DM(100)MnloDMS(300)	5.1	7.1	3.7	6.4	0.00257
DM(100)MnloDMS(350)	6.2	8.7	4.5	8.2	0.00192
DM(100)MnloDMS(400)	10	15	7.4	14	0.00105
DM(100)MnloDMS(500)	23	33	17	32	0.00039
DM(10)MnloDMS(10)	45	63	33	56	0.000346
DM(10)MnloDMS(100)	2.6	3.6	1.9	3.2	0.00616
DM(10)MnloDMS(50)	2.3	3.1	1.6	2.7	0.00722
DM(1)MnloDMS(1000)	3.2e+02	4.6e+02	2.3e+02	4.6e+02	2.12e-05
DM(1)MnloDMS(20)	2.3	3.2	1.7	2.7	0.00733
DM(1)MnloDMS(200)	3.5	4.9	2.6	4.4	0.00433
DM(1)MnloDMS(300)	5.2	7.3	3.8	6.7	0.00253
DM(1)MnloDMS(350)	6.5	9.2	4.7	8.6	0.00185
DM(1)MnloDMS(400)	10	14	7.3	13	0.00112
DM(1)MnloDMS(50)	2.3	3.2	1.7	2.8	0.00708
DM(1)MnloDMS(500)	22	32	16	30	0.000421
DM(1)MnloDMS(750)	94	1.4e+02	66	1.3e+02	7.95e-05
DM(200)MnloDMS(500)	48	67	34	65	0.000191
DM(350)MnloDMS(1000)	6.6e+02	9.6e+02	4.6e+02	9.4e+02	9.48e-06
DM(350)MnloDMS(750)	8.9e+02	1.3e+03	6.2e+02	1.3e+03	7.51e-06
DM(40)MnloDMS(100)	2.5	3.5	1.8	3.1	0.0065
DM(450)MnloDMS(1000)	1.9e+03	2.9e+03	1.3e+03	3e+03	2.74e-06
DM(50)MnloDMS(10)	1.7e+02	2.4e+02	1.3e+02	2.2e+02	8.25e-05
DM(50)MnloDMS(200)	3.6	5	2.6	4.5	0.00426
DM(50)MnloDMS(300)	4.9	6.9	3.6	6.4	0.00257
DM(50)MnloDMS(350)	6.2	8.7	4.5	8.1	0.00189
DM(50)MnloDMS(400)	9.5	13	6.8	13	0.00113
DM(50)MnloDMS(50)	1.5e+02	2.1e+02	1.1e+02	1.9e+02	9.31e-05

Table 9.8: Expected and observed signal strength limits for NLO Simplified Model Scalar-mediated Dark Matter samples with 35.9 fb^{-1} . μ_{obs} , and μ_{exp} correspond to the observed and expected cross-section limits divided by the theoretical cross section. The cross section times branching ratio is also listed for reference. The mapping from short title to dataset is as follows: $\text{DM}(\$mchi)\text{MnloDMS}(\$mmed) \rightarrow \text{DarkMatter_MonoZToLL_NLO_Scalar_Mx-\$mchi_Mv-\$mmed_gDM1_gQ1_TuneCUETP8M1_13TeV-madgraph}$

9.6.3 Unparticle interpretation

In the unparticle scenario, a shape analysis of the E_T^{miss} spectrum is performed. Upper limits are set on the Wilson coefficient $\lambda/\Lambda_U^{d_{\text{U}}-1}$ of the unparticle-quark coupling operator. Additionally, lower limits are set on the cutoff scale Λ_U , assuming a fixed value of the coupling $\lambda = 1$.

The limits both variables are calculated at 95% CL and shown in Fig. 9-27 as a function of the scaling dimension d_{U} . Limits on the production cross-section as a function of d_{U} are shown in Fig. 9-28. The exclusion limits for each parameter point are given in Tab. 9.9.

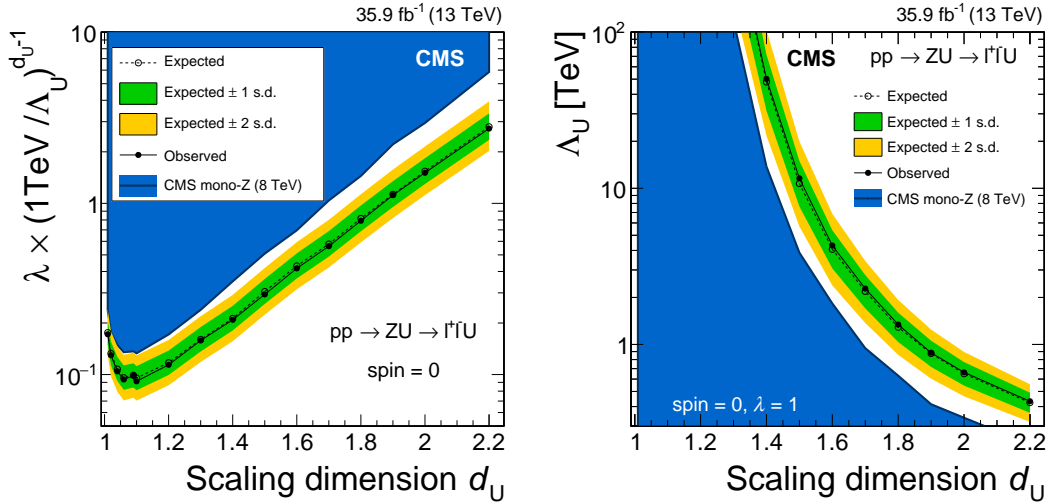


Figure 9-27: Left: The 95% CL upper limits on the Wilson coefficient $\lambda/\Lambda_U^{d_{\text{U}}-1}$ of the unparticle-quark coupling operator. Right: The 95% CL lower limits on unparticle effective cutoff scale Λ_U for a fixed coupling $\lambda = 1$. The results from a previous CMS mono-Z search [46] are shown for comparison.

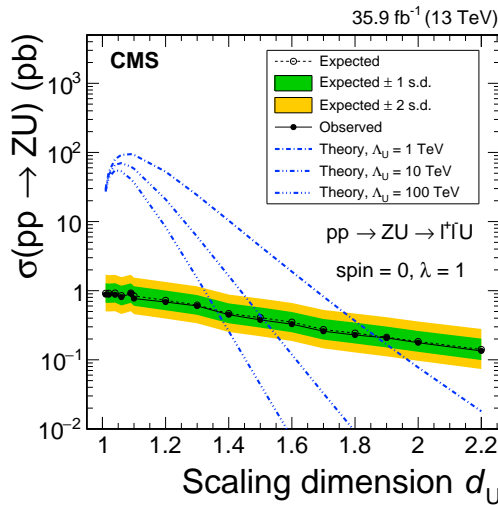


Figure 9-28: The 95% CL upper limits on the cross-section for $pp \rightarrow UZ$ in the unparticle model.

Short title	μ_{exp}	$\delta^+ \mu_{exp}$	$\delta^- \mu_{exp}$	μ_{obs}	σ [pb]
ADD $M_D = 3$ TeV, $n = 2$	0.11	0.17	0.074	0.15	0.0342
ADD $M_D = 3$ TeV, $n = 3$	0.097	0.15	0.065	0.13	0.032
ADD $M_D = 3$ TeV, $n = 4$	0.076	0.12	0.05	0.1	0.0369
ADD $M_D = 3$ TeV, $n = 5$	0.052	0.082	0.035	0.071	0.0472
ADD $M_D = 3$ TeV, $n = 6$	0.037	0.057	0.024	0.05	0.0648
ADD $M_D = 3$ TeV, $n = 7$	0.024	0.038	0.016	0.033	0.0939
Unparticle, $d_U = 1.01$, $\Lambda_U = 15$ TeV	0.033	0.013	0.009	0.031	28.2
Unparticle, $d_U = 1.02$, $\Lambda_U = 15$ TeV	0.020	0.007	0.005	0.019	46.7
Unparticle, $d_U = 1.04$, $\Lambda_U = 15$ TeV	0.014	0.006	0.004	0.014	64.4
Unparticle, $d_U = 1.06$, $\Lambda_U = 15$ TeV	0.013	0.005	0.004	0.012	66.7
Unparticle, $d_U = 1.09$, $\Lambda_U = 15$ TeV	0.016	0.006	0.004	0.016	57.9
Unparticle, $d_U = 1.10$, $\Lambda_U = 15$ TeV	0.016	0.006	0.004	0.014	53.7
Unparticle, $d_U = 1.20$, $\Lambda_U = 15$ TeV	0.041	0.016	0.011	0.038	17.9
Unparticle, $d_U = 1.30$, $\Lambda_U = 15$ TeV	0.13	0.052	0.036	0.13	4.7
Unparticle, $d_U = 1.40$, $\Lambda_U = 15$ TeV	0.40	0.16	0.11	0.38	1.1
Unparticle, $d_U = 1.50$, $\Lambda_U = 15$ TeV	1.4	0.56	0.40	1.30	0.29
Unparticle, $d_U = 1.60$, $\Lambda_U = 15$ TeV	4.8	1.93	1.37	4.5	0.073
Unparticle, $d_U = 1.70$, $\Lambda_U = 15$ TeV	14.8	6.20	4.2	14.0	0.019
Unparticle, $d_U = 1.80$, $\Lambda_U = 15$ TeV	50.7	21.23	14.8	47.6	0.0048
Unparticle, $d_U = 1.90$, $\Lambda_U = 15$ TeV	167	71.1	48.1	163	0.00127
Unparticle, $d_U = 2.00$, $\Lambda_U = 15$ TeV	534	224	155	512	0.000345
Unparticle, $d_U = 2.20$, $\Lambda_U = 15$ TeV	5.2e+3	2.3e+3	1.5e+3	5.0e+3	2.71e-5

Table 9.9: Expected and observed signal strength limits for Large Extra Dimension and Unparticle samples with 35.9 fb^{-1} . μ_{obs} , and μ_{exp} correspond to the observed and expected cross-section limits divided by the theoretical cross section. The cross section times branching ratio is also listed for reference. In both ADD and unparticles the given cross-section is the one produced by pythia for the respective sample. The Z branching fractions are not included. The truncation in the ADD case is also not included. The properly truncated ADD cross-sections are given in Appendix E.

9.6.4 ADD Interpretation

In the framework of the ADD model of extra dimensions, limits are calculated depending on the number of extra dimensions n and M_D . For each value of d , cross-section limits are calculated as a function of M_D (fig. 9-30). By finding the intersection between the theory cross-section line with the observed and expected excluded cross-sections, and projecting that point onto the M_D axis, limits on M_D are found as a function of n (fig. 9-29). The used theoretical cross sections are given in appendix E and shown graphically in fig. 9-31.

The observed (expected) exclusion of M_D ranges between 2.1 and 2.4 TeV (2.3 and 2.6 TeV) for n between 2 and 7.

To illustrate the impact of the truncation procedure, the cross-sections with and without truncation are shown in fig. 9-31. The truncation has a greater impact on scenarios with more extra dimensions. The relative spread between low- n and high- n scenarios is thus greatly reduced by the truncation and the cross-sections converge.

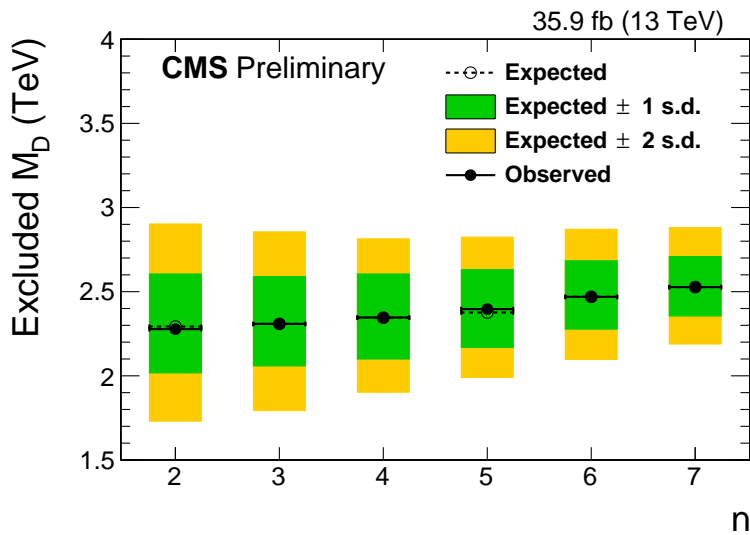


Figure 9-29: Expected and observed exclusion limits on M_D as a function of n .

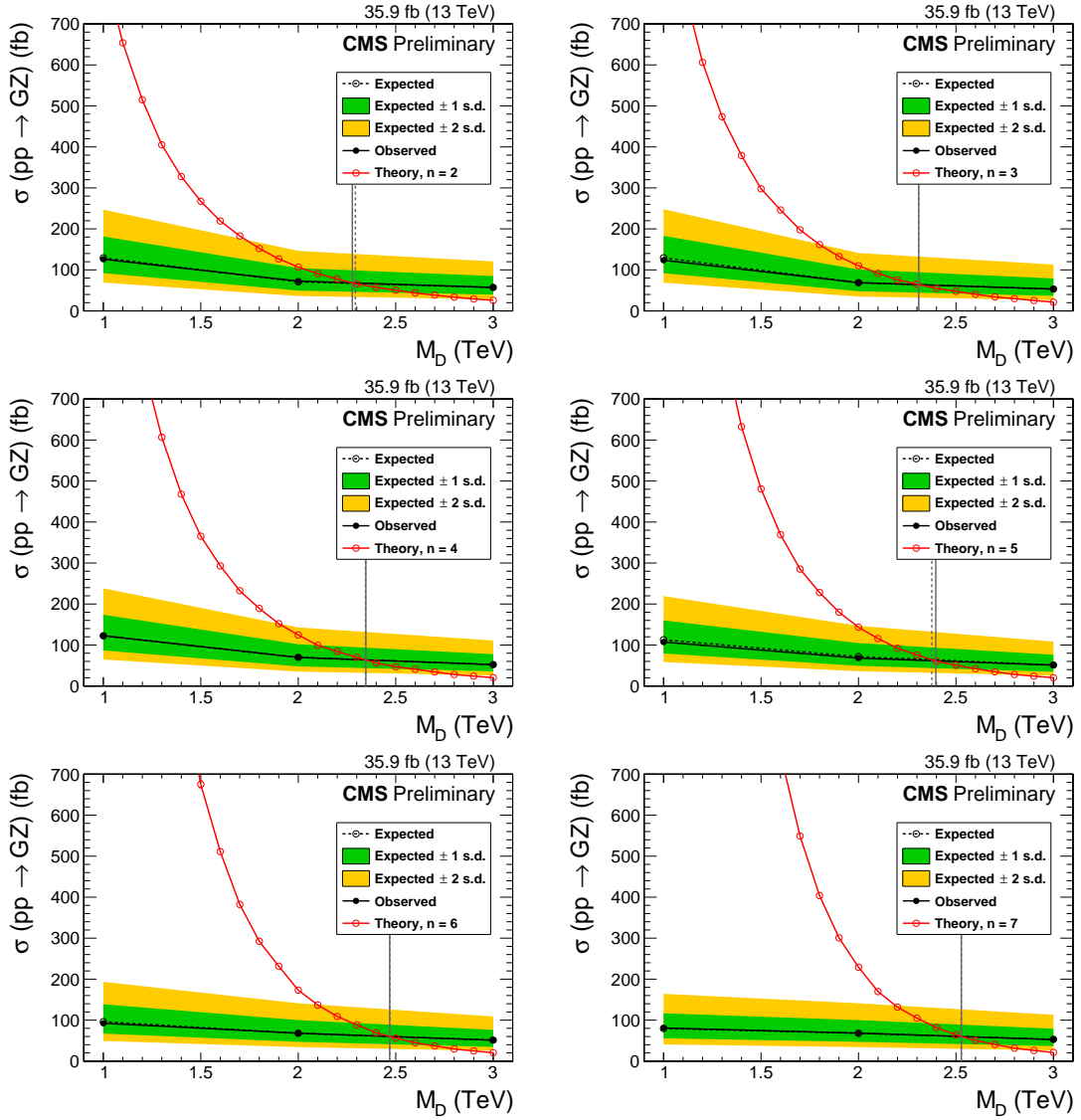


Figure 9-30: Cross-section limits in the ADD scenario as a function of M_D for different values of n . The Red curve shows the theoretical cross-section for given values of n . The cross-sections are calculated for the fiducial phase-space of $p_T(\text{Graviton}) > 50 \text{ GeV}$. Gray lines show the projection of the intersection between theory and expected (observed) exclusion onto the M_D axis.

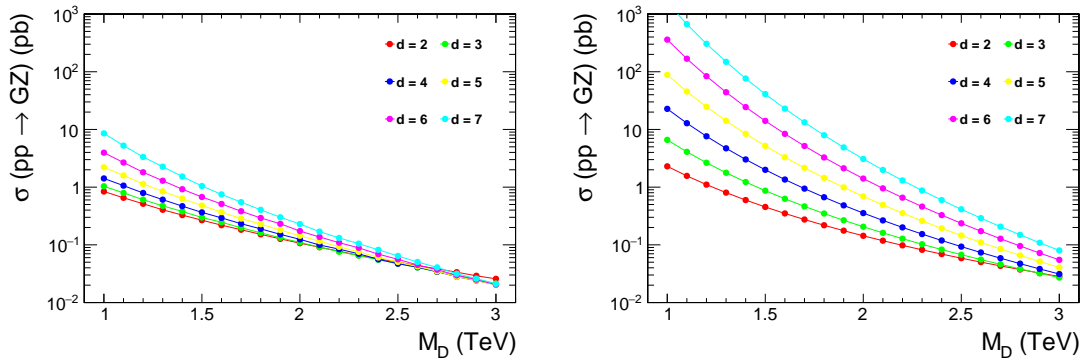


Figure 9-31: Truncated (left) and untruncated (right) cross-sections for the ADD model as a function of M_D . Each curve represents one value of n . The effect of the truncation increases with n . The truncated values are used for limit-setting. The untruncated graphs are shown only for illustration. The cross-sections are calculated for the fiducial phase-space of $p_T(\text{Graviton}) > 50 \text{ GeV}$.

9.6.5 Simplified Likelihood

The observed event yields and total expected background yields in the signal region are tabulated in Tab. 9.10. The correlation between E_T^{miss} bins in the signal region is shown in Fig. 9-32. This allows re-interpretation of the results in this paper according to the simplified likelihood approach, as described in Ref. [204]

To test the validity of the re-interpretation, a closure test was performed using the Higgs invisible signal model. The median expected 95% CL signal strength limit for a Higgs invisible signal was 0.45, as compared to 0.43 for the full likelihood model. A comparison of the likelihood as a function of signal strength μ is shown in Fig. 9-33.

E_T^{miss} Bin	Observed events	Total background prediction
$100 \leq E_T^{\text{miss}} < 125$	311	256 ± 32
$125 \leq E_T^{\text{miss}} < 150$	155	150 ± 12
$150 \leq E_T^{\text{miss}} < 175$	87	86.9 ± 8.4
$175 \leq E_T^{\text{miss}} < 200$	50	52.7 ± 5.3
$200 \leq E_T^{\text{miss}} < 250$	56	50.2 ± 4.9
$250 \leq E_T^{\text{miss}} < 300$	15	19.4 ± 2.2
$300 \leq E_T^{\text{miss}} < 350$	11	9.4 ± 1.2
$350 \leq E_T^{\text{miss}} < 400$	6	4.58 ± 0.66
$400 \leq E_T^{\text{miss}} < 500$	6	3.31 ± 0.54
$500 \leq E_T^{\text{miss}}$	1	1.57 ± 0.33

Table 9.10: Expected event yields in each E_T^{miss} bin for the sum of background processes in the signal region. The background yields and their corresponding uncertainties are obtained after performing a combined fit to data in all control regions, but excluding data in the signal region. The observed events in each bin are also included.

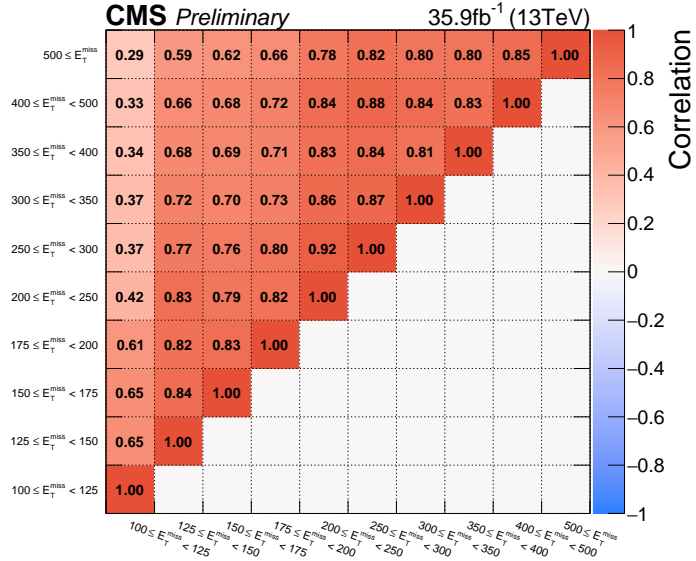


Figure 9-32: Correlations between the uncertainties in the estimated background yields in the signal region E_T^{miss} bins. The correlations are obtained after performing a combined fit to data in all control regions, but excluding data in the signal region.

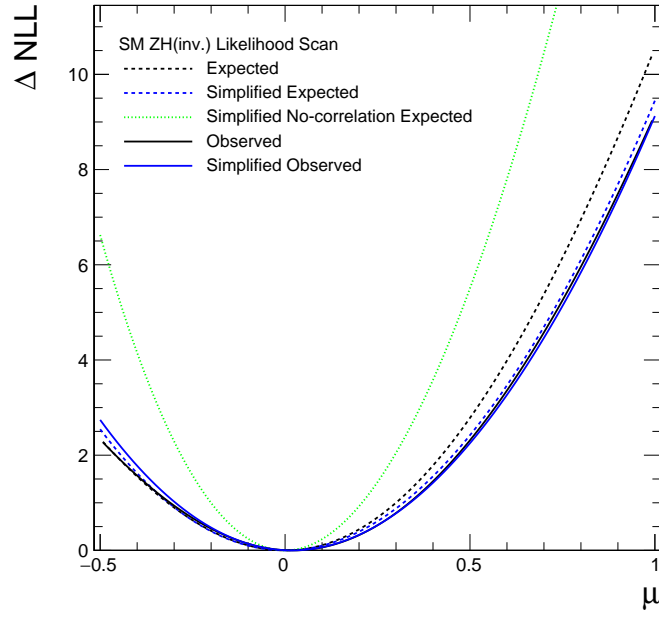


Figure 9-33: Comparison of likelihood scans for the full likelihood model and the simplified likelihood, for the Higgs invisible signal. Good agreement is shown, confirming that the simplified likelihood approximation is valid in this analysis.

Chapter 10

Conclusion and Outlook

In this work, measurements of differential Z/γ^* production cross sections in pp collisions at $\sqrt{s} = 13$ TeV in the electron and muon final state are presented. The dataset was collected with the CMS Detector at the LHC, corresponding to an integrated luminosity of 35.9 fb^{-1} . A total of 32.5×10^6 data events were selected. The measured fiducial inclusive cross section times branching fraction is:

$$\sigma_{Z \rightarrow \ell^+ \ell^-}(\sqrt{s} = 13 \text{ TeV}) = 699 \pm 5 \text{ (syst)} \pm 17 \text{ (lumi)} \text{ pb}$$

The measurement is limited by the systematic uncertainty of the integrated luminosity. It agrees with next-to-next-to-leading-order QCD and next-to-leading order electroweak cross section calculations.

Distributions of the transverse momentum, the angular variable ϕ_η^* , and the rapidity of lepton pairs were also measured and compared to theoretical predictions. The prediction is consistent with the measurements within uncertainties. The differential measurement provides a useful benchmark for ongoing research in the realm of fixed-order calculations. It will also serve as a constraint in future global fits for the determination of the PDFs. In particular, the Drell-Yan process is most useful in constraining the light-quark PDFs.

In the near future, this measurement will be extended to the entire Run-II dataset, representing an integrated luminosity of 150 fb^{-1} . It will also be combined with the decays to hadrons and neutrinos. This will enhance the precision at higher values of momentum approaching 1 TeV.

Using the same dataset, a search for new physics in events with a leptonically decaying Z boson and large missing transverse momentum was performed. Using the cut-based strategy, 688 data events were selected; using the multivariate strategy, 1586 data events were selected. No evidence for physics beyond the standard model was found. Compared to the previous search in the same final state [205], the exclusion limits on dark matter and mediator masses were significantly extended for spin-1 mediators in the simplified model interpretation, and exclusion limits for unparticles were also extended. Results for dark matter production via spin-0 mediators in the

simplified model interpretation, as well as graviton emission in a model with large extra dimensions, have been presented in this final state for the first time.

In the case of invisible decays of a Standard Model-like Higgs boson, we assume the Standard Model production cross section, and set an upper limit of 40% on the invisible branching ratio (at 95% confidence level). This is competitive with the contemporary result from our sister experiment ATLAS [206]. Using the 2016 ATLAS dataset (integrated luminosity 36.1 fb^{-1}), the corresponding upper limit for invisible Higgs boson decays is 67%.

It is important to note that using the same 2016 CMS dataset, another search for invisible Higgs boson decays in the vector boson fusion (VBF) production mode was performed [207]. There, the participant quarks each emit virtual W^\pm or Z bosons which annihilate into a Higgs boson. The corresponding upper limit is 33%. A preliminary combined result was prepared which included the result from this work, that VBF result, and other CMS results [45] using the Run-I datasets. That combination set a limit of 19%, the most stringent to date. By comparison, the Standard Model branching ratio of Higgs to invisible particles (neutrinos) is around 0.1%. Much work remains to be done in order to bridge this gap, and the first step will be a combined analysis of the full Run-II CMS and ATLAS datasets.

Beyond the pursuit of the invisible Higgs, constraints have been placed on other models. For the most generic of models with a massive spin-1 mediator, mediator masses up to order of 500 GeV have been excluded in an electroweak scale coupling scenario. When interpreted in the context of the dark matter-nucleon scattering cross section, this result serves to complement the efforts of the direct detection dark matter experiments. In the context of the ADD extra dimensions model, constraints were calculated on the true Planck scale of the $n + 4$ dimensional spacetime M_D , as a function of the number of extra dimensions n . Between two and seven extra dimensions, values of M_D below approximately 2.3 TeV were excluded.

In the future, this search will be performed with the remainder of the Run-II CMS dataset. It may also be combined with the other search channels to broaden the exclusion of the various exotic models, similar to the existing preliminary combined analysis in Ref. [208].

In closing, we are entering an era where the Standard Model is tested at high precision. The work presented here grants us further insight into the internal structure of the proton, and later we hope to use it to nail down the mass of the W^\pm boson. Meanwhile, the community of theorists have an additional reference point for state-of-the-art quantum field theory calculations. These, along with plans for future colliders, will usher in a new age of precise Higgs boson measurements. As our accumulated knowledge of the fundamental interactions begins to crystallize, there is no guarantee we will observe new physics at the LHC or elsewhere. But we will leave no stone unturned—and we are still on the hunt.

Appendix A

Lepton identification efficiencies and scale factors

A.1 Central values

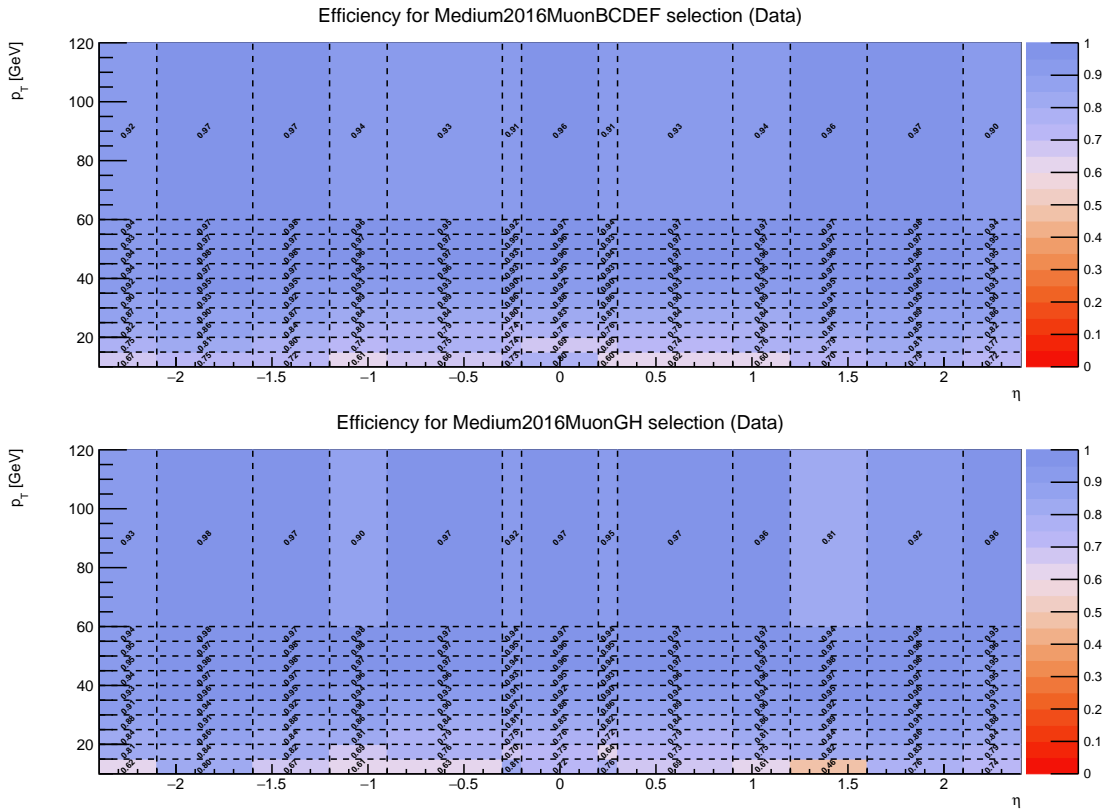


Figure A-1: Efficiencies extracted from data for the Medium muon working point in 2016 run eras B to F, and G to H.

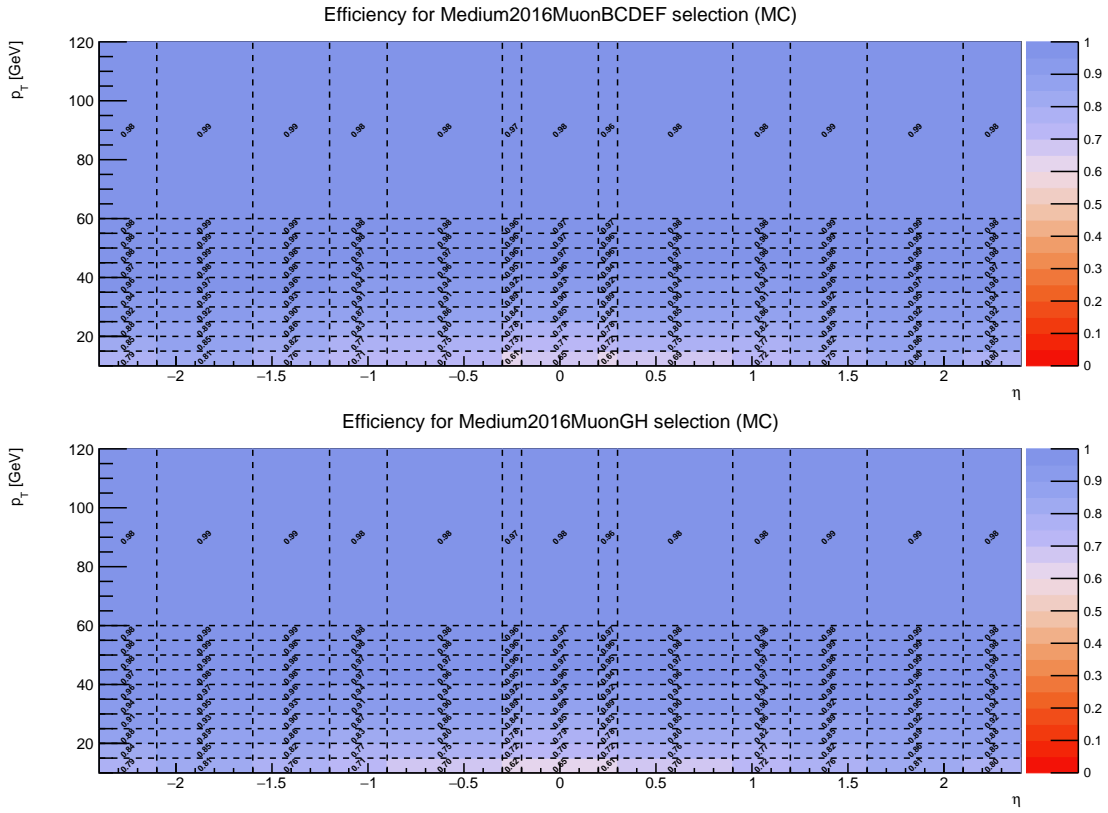


Figure A-2: Efficiencies extracted from MC for the Medium muon working point after reweighting to the pileup profile in 2016 run eras B to F, and G to H.

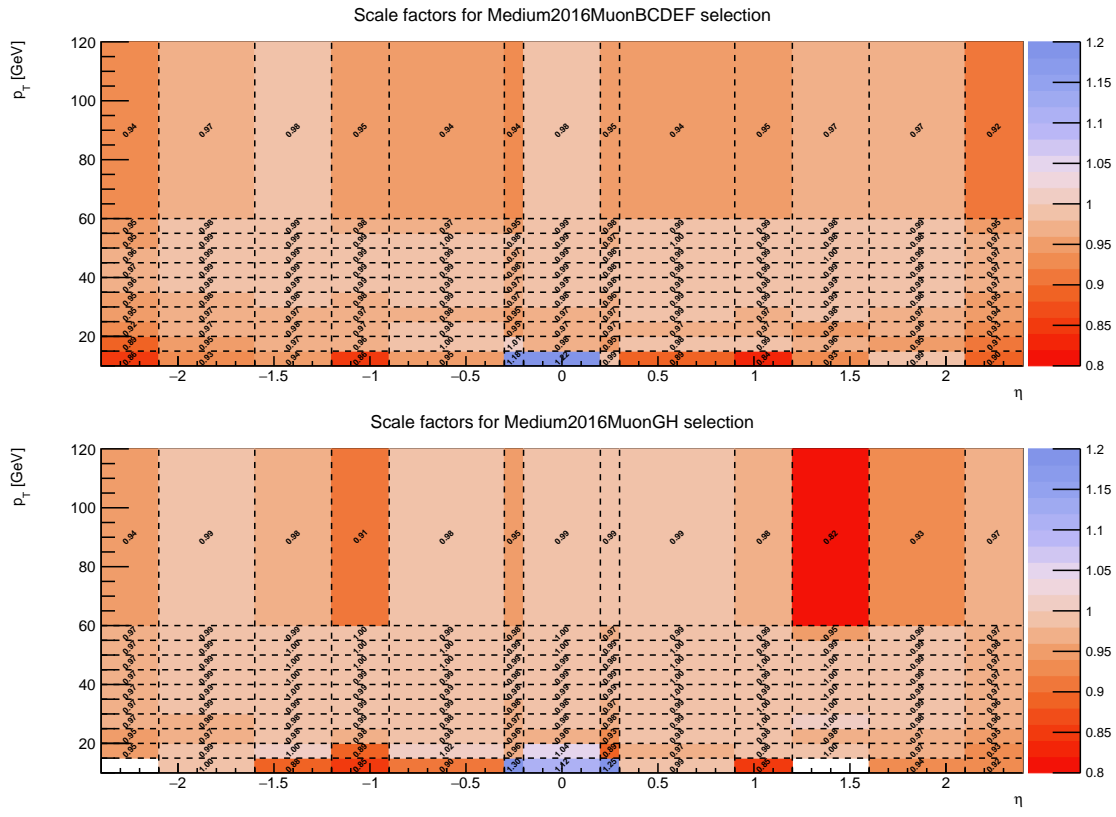


Figure A-3: Scale factors derived from Data/MC efficiencies for the Medium muon working point in 2016 run eras B to F, and G to H.

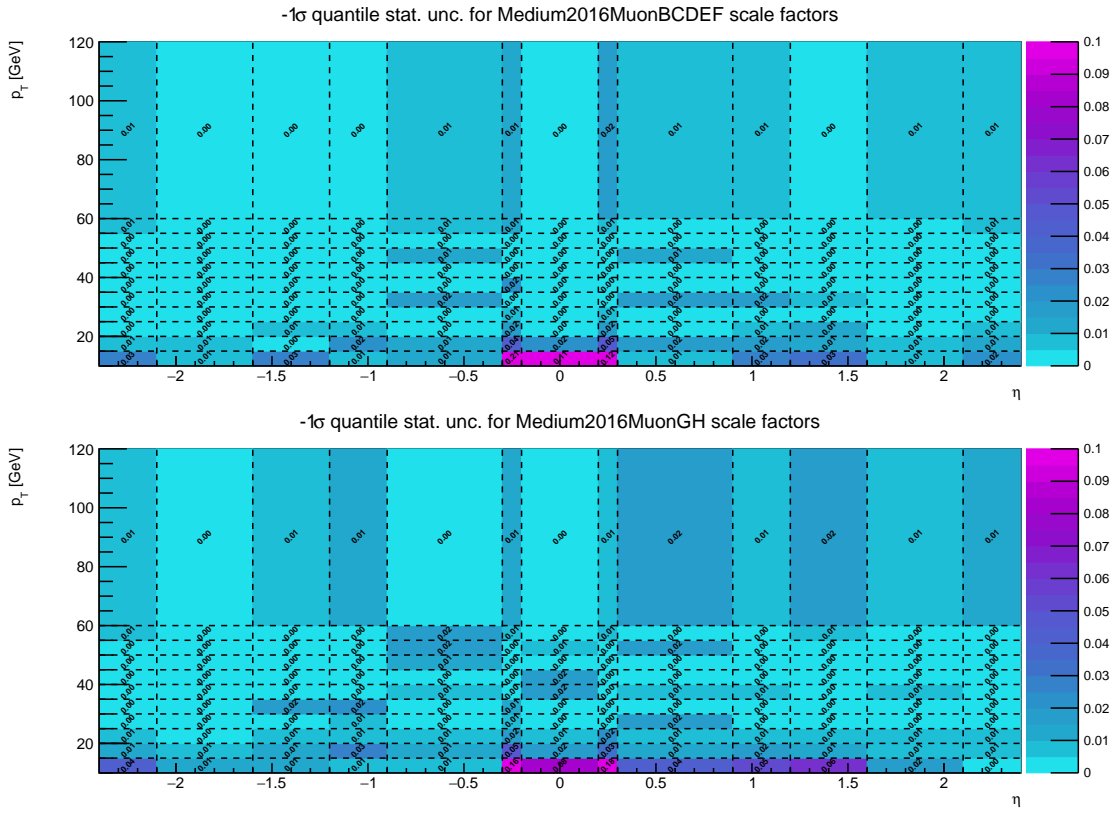


Figure A-4: Statistical uncertainties on the Medium muon scale factors (negative error) in 2016 run eras B to F, and G to H.

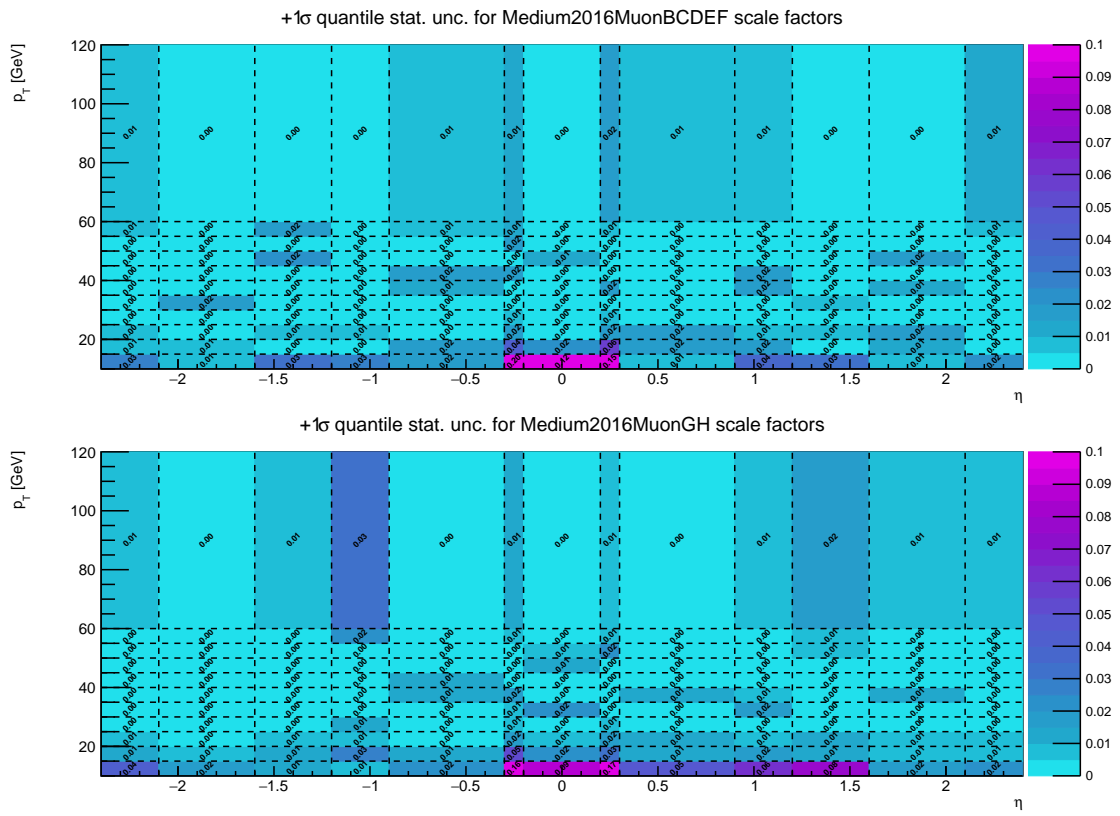


Figure A-5: Statistical uncertainties on the Medium muon scale factors (positive error) in 2016 run eras B to F, and G to H.

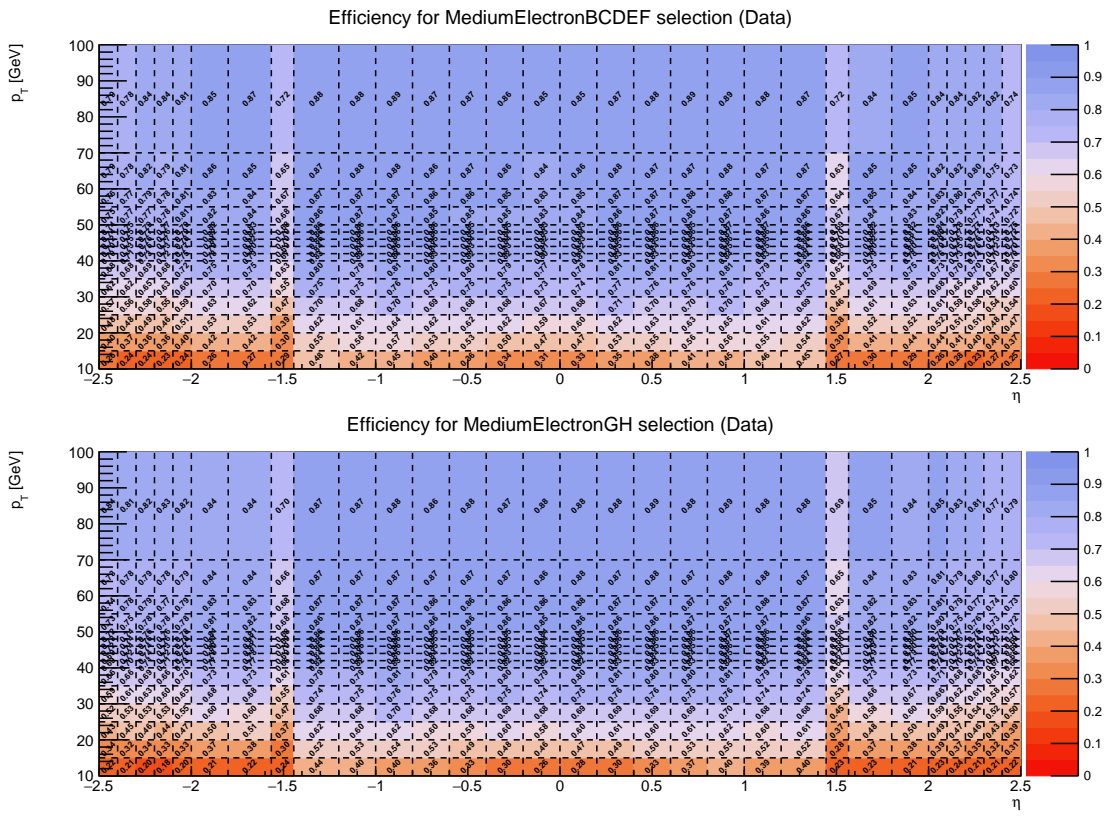


Figure A-6: Efficiencies extracted from data for the Medium electron working point in 2016 run eras B to F, and G to H.

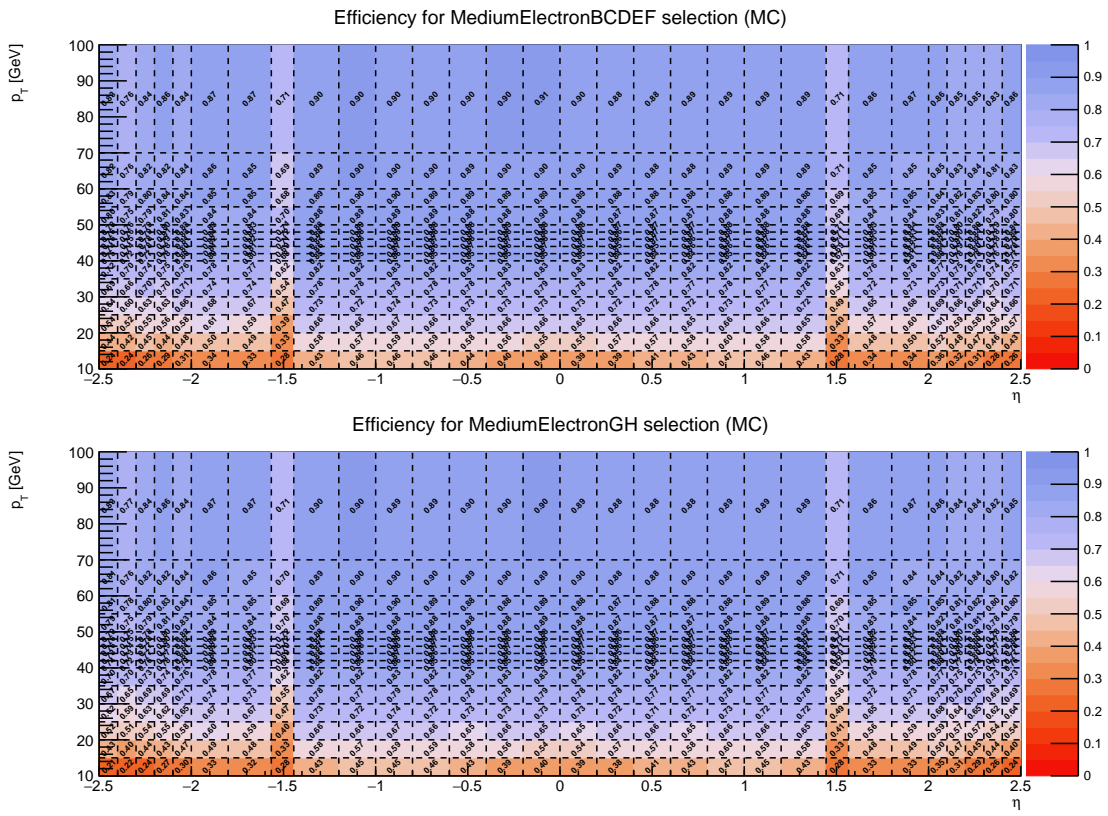


Figure A-7: Efficiencies extracted from MC for the Medium electron working point after reweighting to the pileup profile in 2016 run eras B to F, and G to H.

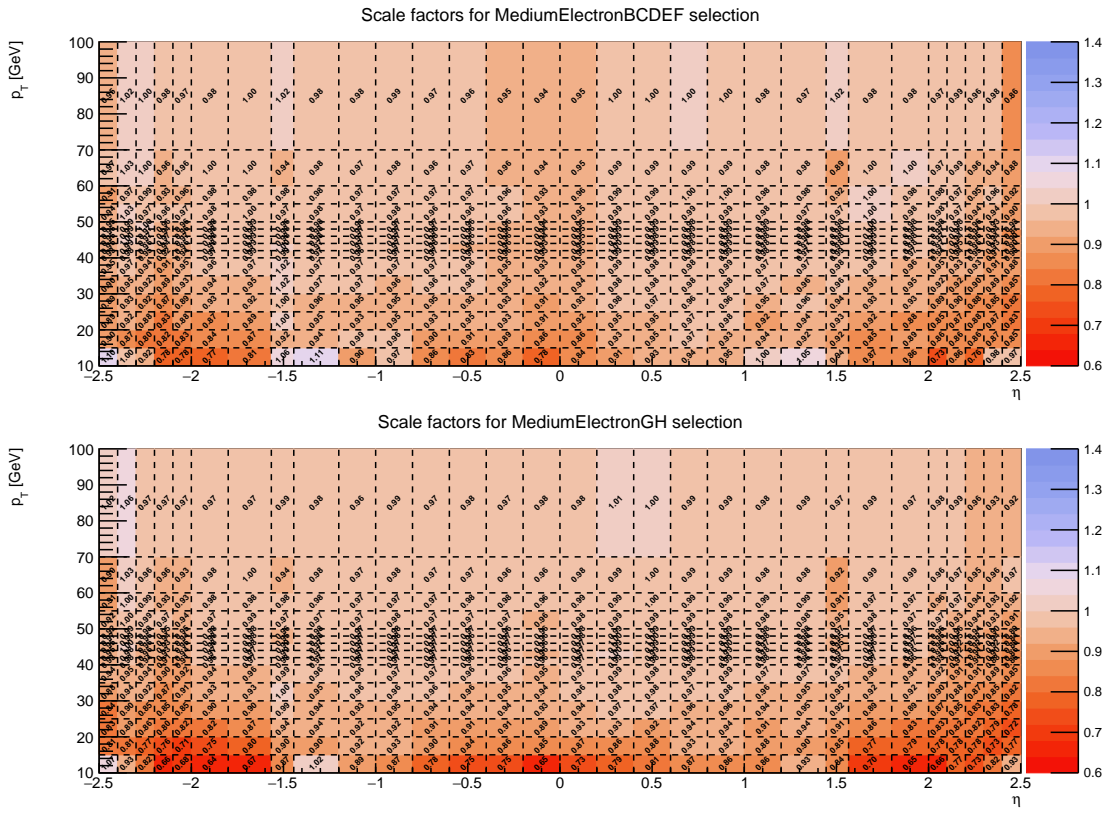


Figure A-8: Scale factors derived from Data/MC efficiencies for the Medium electron working point in 2016 run eras B to F, and G to H.

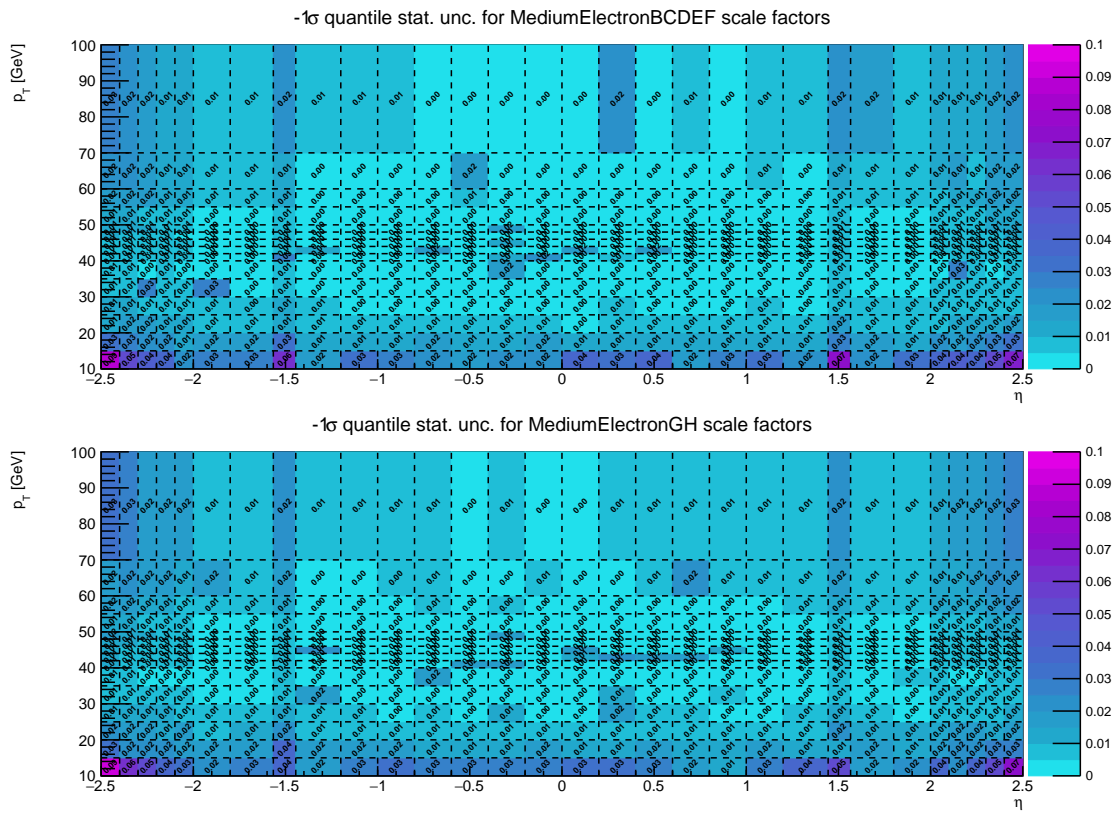


Figure A-9: Statistical uncertainties on the Medium electron scale factors (negative error) in 2016 run eras B to F, and G to H.

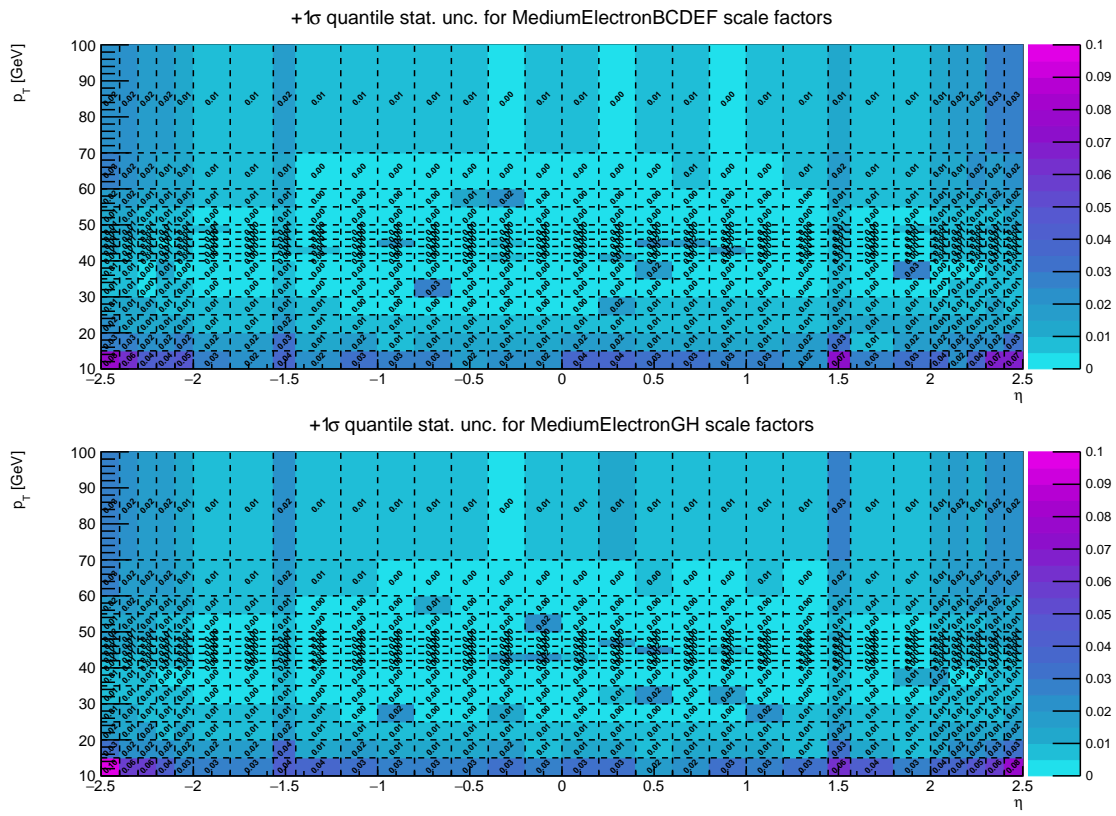


Figure A-10: Statistical uncertainties on the Medium electron scale factors (positive error) in 2016 run eras B to F, and G to H.

A.2 Alternative methods

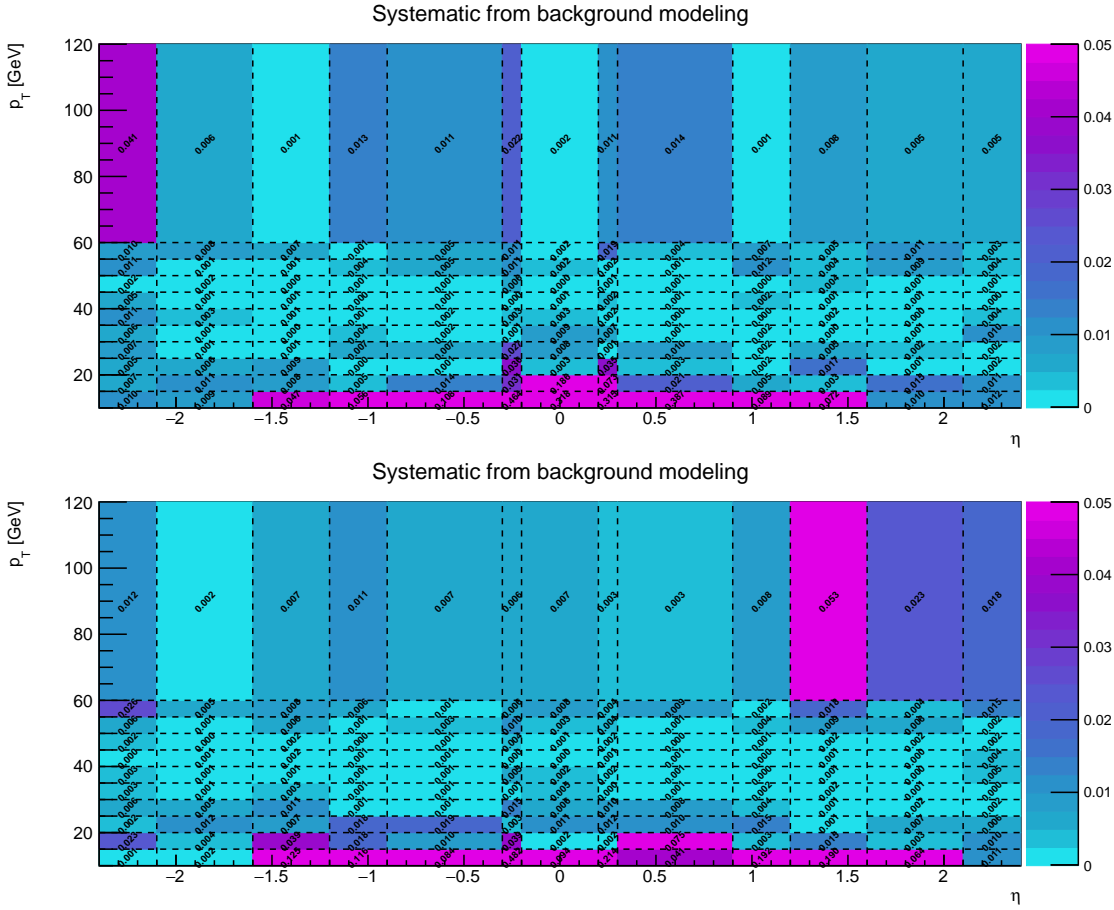


Figure A-11: Systematic uncertainties from choice of background model for the Medium muon scale factors in 2016 run eras B to F (top), and G to H (bottom).

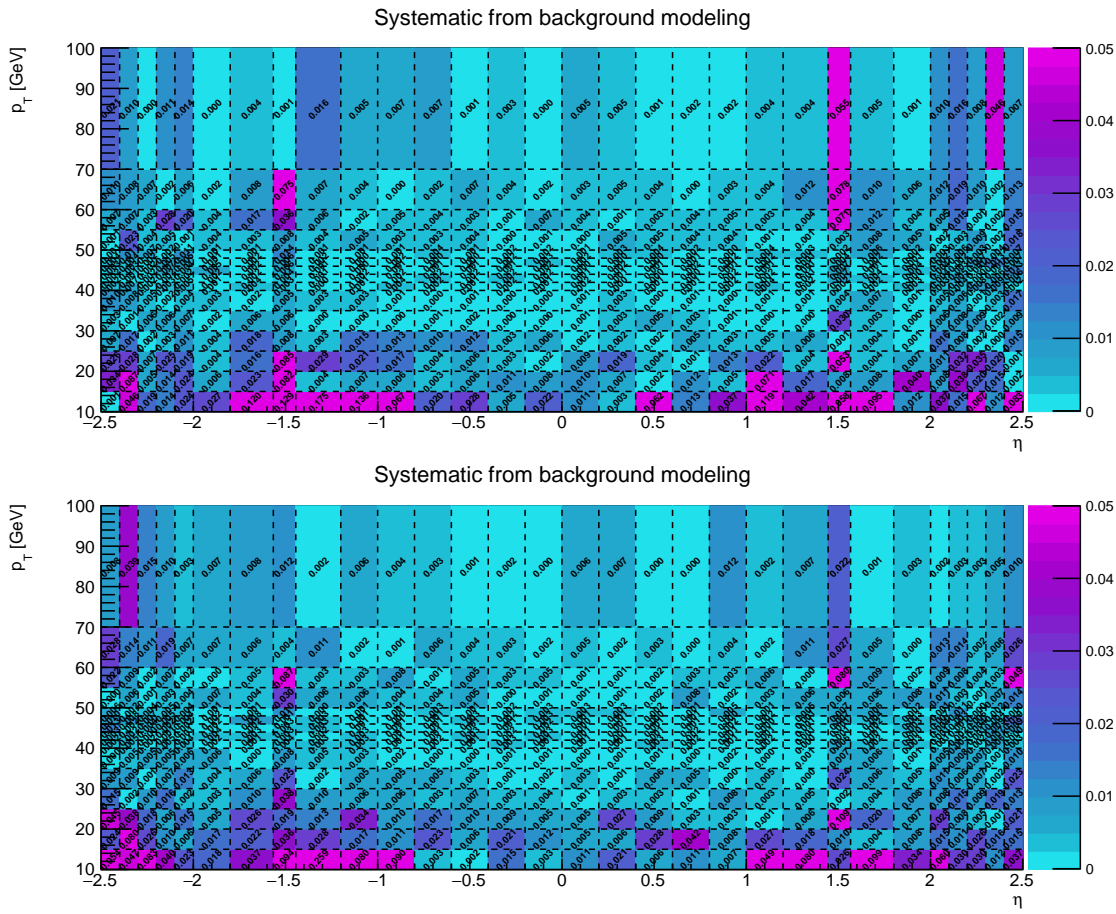


Figure A-12: Systematic uncertainties from choice of background model for the Medium electron scale factors in 2016 run eras B to F (top), and G to H (bottom).

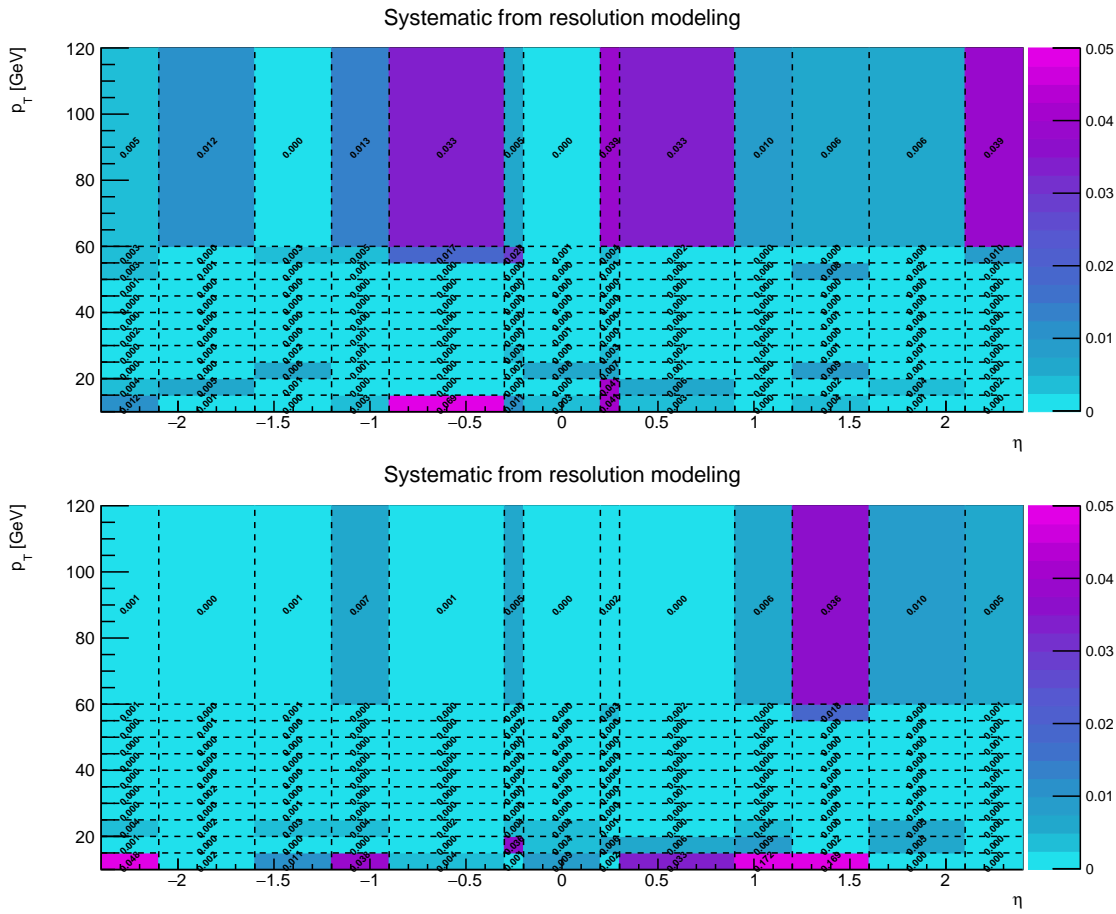


Figure A-13: Systematic uncertainties from signal resolution modeling for the Medium muon scale factors in 2016 run eras B to F (top), and G to H (bottom).

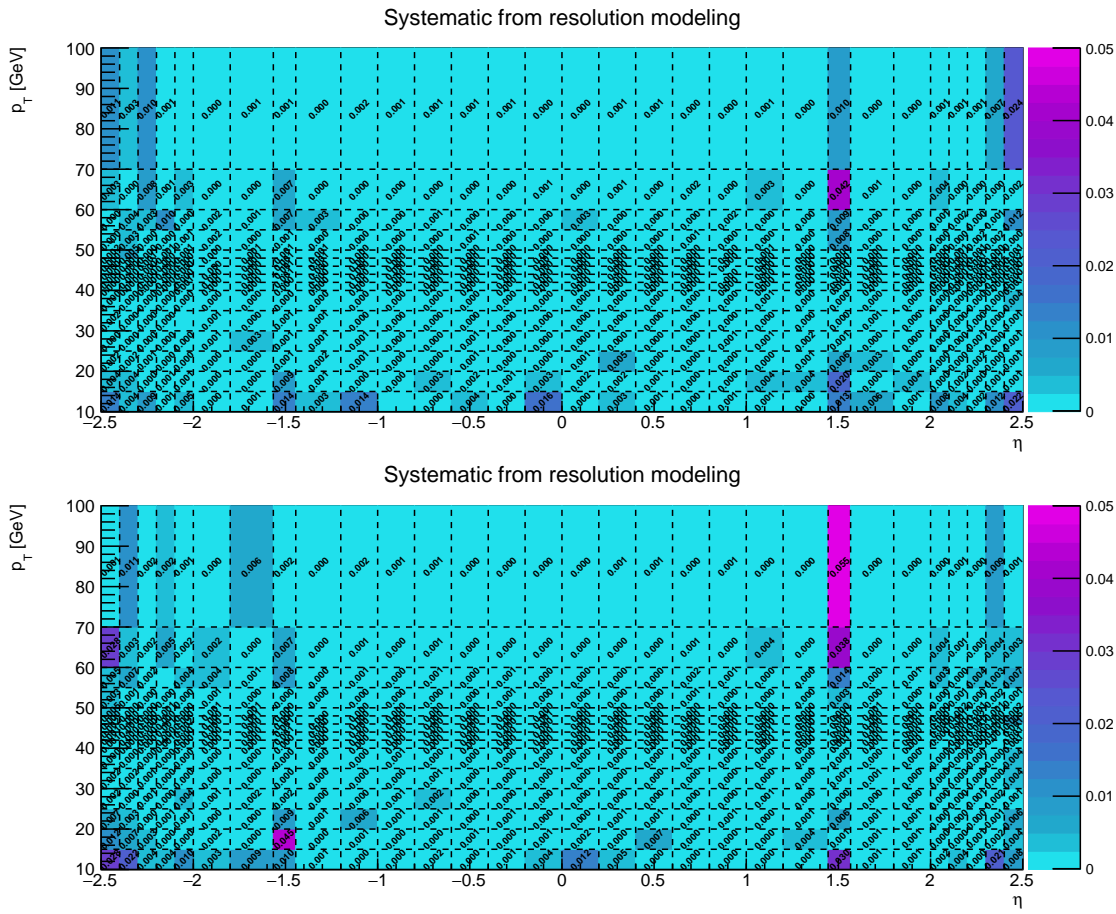


Figure A-14: Systematic uncertainties from signal resolution modeling for the Medium electron scale factors in 2016 run eras B to F (top), and G to H (bottom).

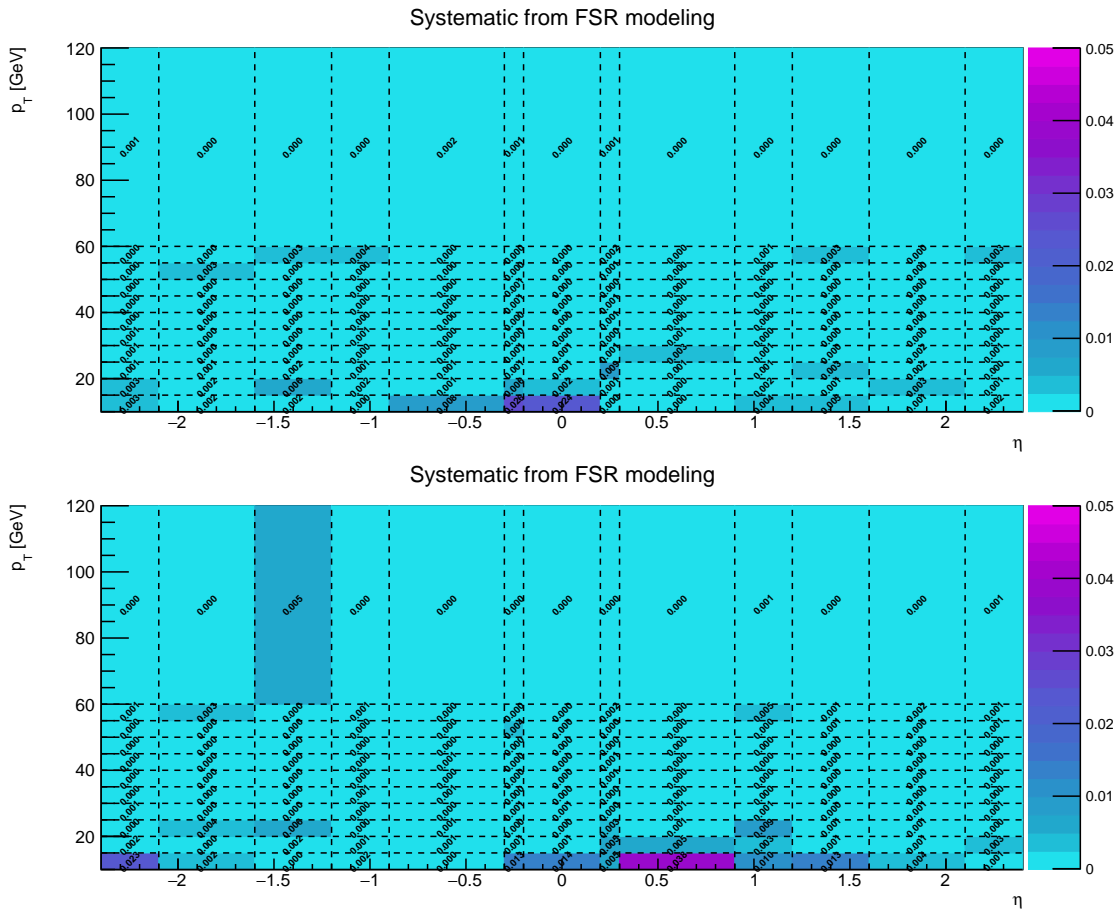


Figure A-15: Systematic uncertainties from signal FSR modeling for the Medium muon scale factors in 2016 run eras B to F (top), and G to H (bottom).

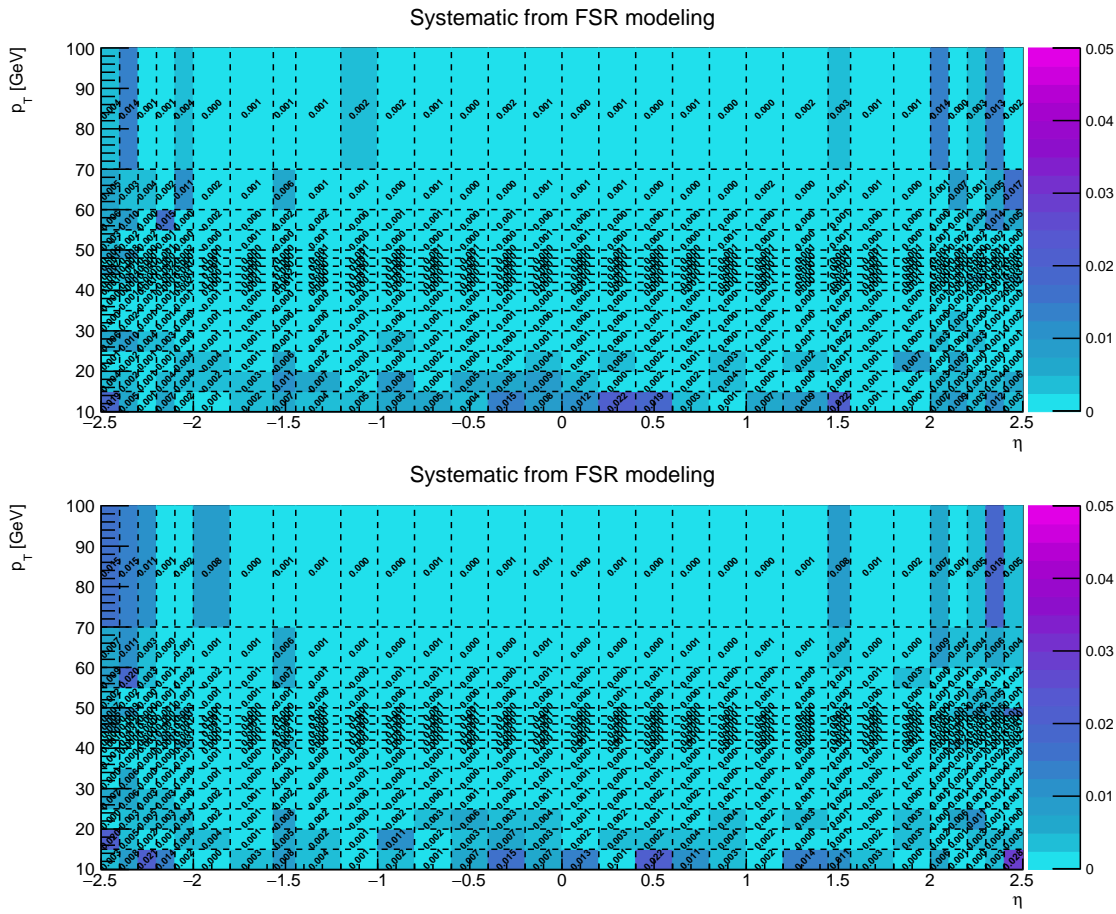


Figure A-16: Systematic uncertainties from signal FSR modeling for the Medium electron scale factors in 2016 run eras B to F (top), and G to H (bottom).

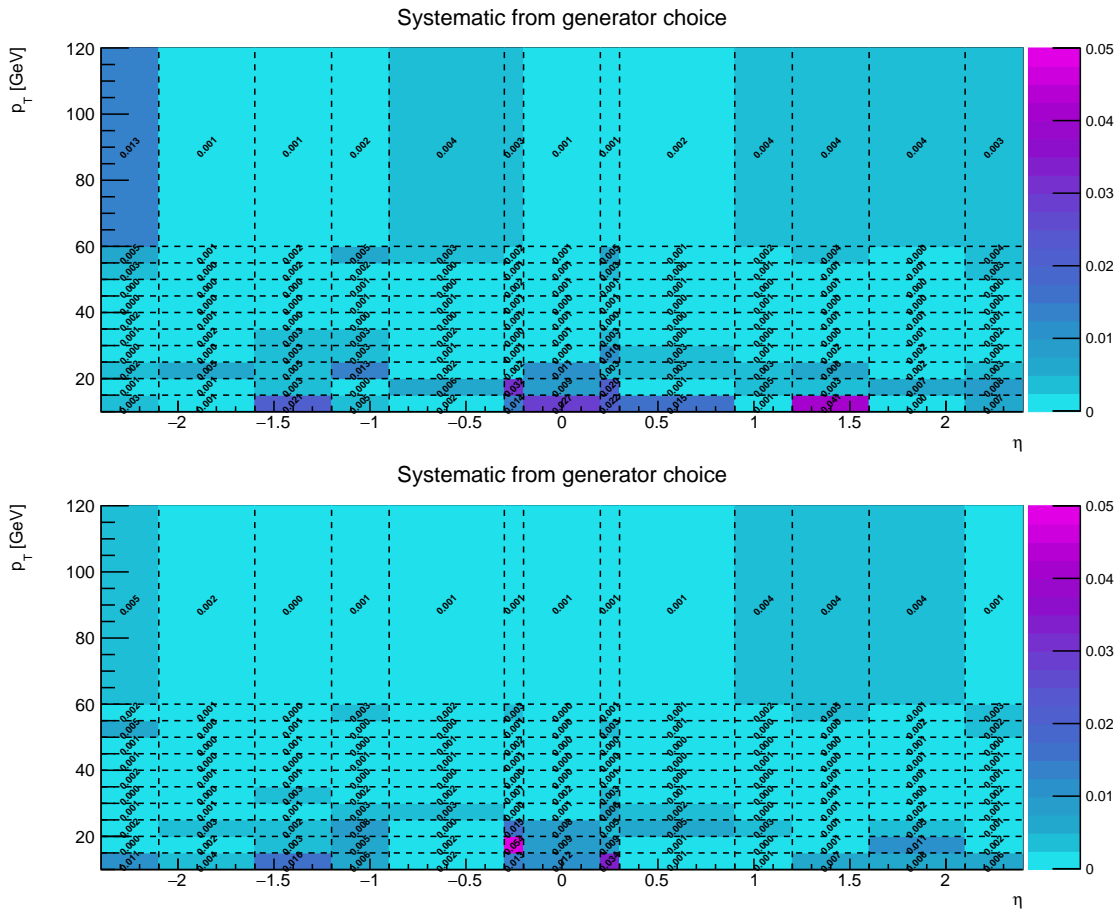


Figure A-17: Systematic uncertainties from generator choice for the Medium muon scale factors in 2016 run eras B to F (top), and G to H (bottom).

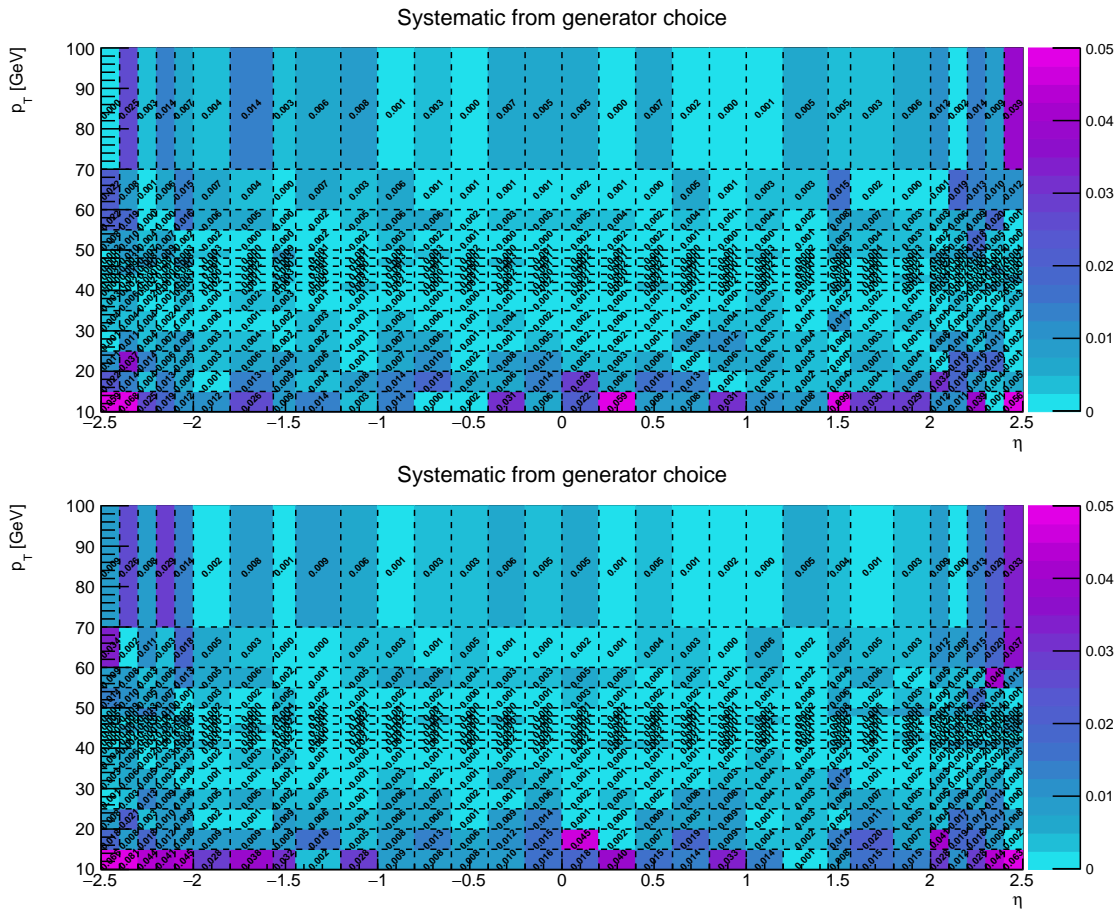


Figure A-18: Systematic uncertainties from generator choice for the Medium electron scale factors in 2016 run eras B to F (top), and G to H (bottom).

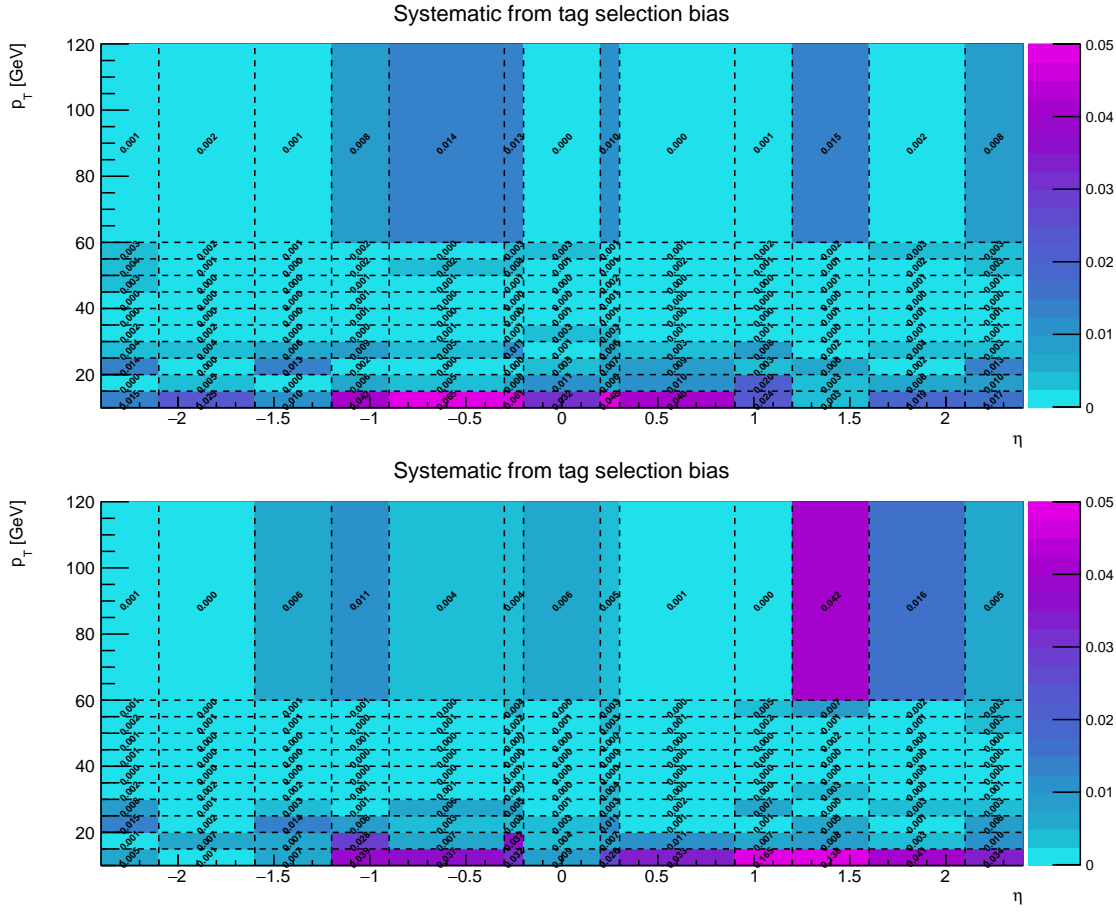


Figure A-19: Systematic uncertainties from choice of tag selection for the Medium muon scale factors in 2016 run eras B to F (top), and G to H (bottom).

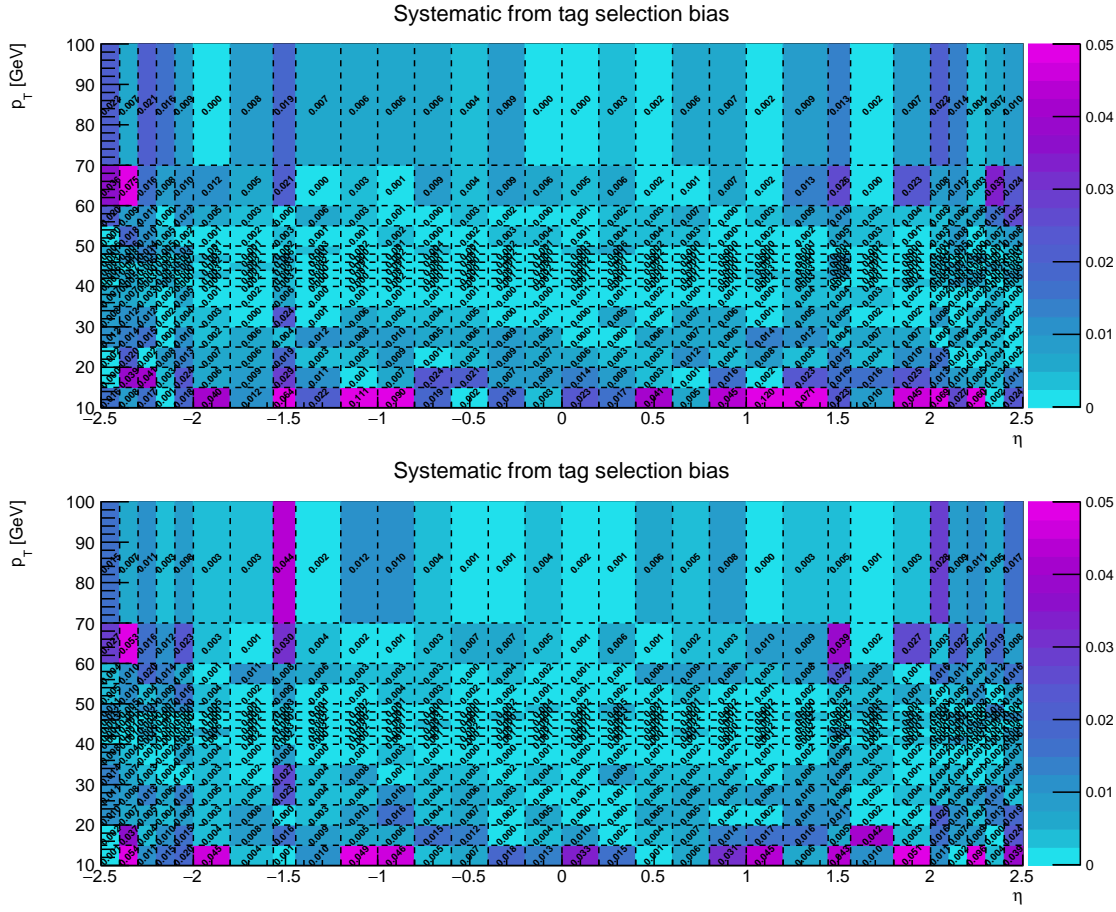


Figure A-20: Systematic uncertainties from choice of tag selection for the Medium electron scale factors in 2016 run eras B to F (top), and G to H (bottom).

Appendix B

Dark matter multivariate analysis

B.1 Boosted decision trees

The multivariate analysis makes use of the implementation of boosted decision trees (BDTs) in the TMVA software package within the ROOT framework [209].

A decision tree is a binary tree structured classifier. Repeated yes/no decisions are taken on a single variable at a time until a stop criterion is fulfilled. The phase space is split this way into many regions that are eventually classified as signal or background, depending on the majority of training events that end up in the final leaf node.

The boosting of a decision tree extends this concept from one tree to several trees which form a forest. The trees are derived from the same training ensemble by reweighting events, and are finally combined into a single classifier which is given by a weighted average of the individual decision trees. Boosting stabilizes the response of the decision trees with respect to fluctuations in the training sample and is able to considerably enhance the performance with respect to a single tree.

B.1.1 Gradient boosting

The idea of function estimation through boosting can be understood by considering a simple additive expansion approach. Consider a particular point \vec{x} in the space of variables describing the dataset. The function $F(\vec{x})$ under consideration is assumed to be a weighted sum of parameterized base functions or *weak learners* $f(\vec{x}; a_m)$. Each base function corresponds to a decision tree

$$F(\vec{x}) = \sum_{m=0}^M \beta_m f(\vec{x}; a_m) \quad P \in \{\beta_m; a_m\}_0^M \quad (\text{B.1})$$

where M is the number of trees in the forest, m represents a particular decision tree, and P is the parameter space of tree weights β_m and tree decisions a_m .

The boosting procedure adjusts the parameters P so that the deviation between the model response $F(\vec{x})$ and the true value y obtained from the training input data

is minimized. For the BDT classifier, the binomial log-likelihood loss function is used for the gradient boosting algorithm:

$$L(F, y) = \ln(1 + e^{-2F(\vec{x})y}) \quad (\text{B.2})$$

The minimization is achieved using an iterative gradient-descent approach. The gradient of the loss function for the current forest, $F_{m-1}(\vec{x})$, is calculated. Then, a new decision tree $h_m(\vec{x})$ is grown to match the mean value of the gradient in each region defined by the tree structure. A coefficient γ_m is found via line search to get the new forest $F_m(\vec{x})$ that minimizes the loss function:

$$F_m(\vec{x}) = F_{m-1}(\vec{x}) + \gamma_m \cdot h_m(\vec{x}) \quad (\text{B.3})$$

Iterating this procedure over several hundred trees yields the desired set of decision trees which minimizes the loss function.

In general, gradient boosting is performed using regularization techniques to avoid overfitting the training data. Here, shrinkage and bagging are used. These are described below. The BDT seen in Chapter 9, Section 9.5 was grown with 400 trees, shrinkage parameter $\nu = 0.5$, and bagging fraction 0.5.

Shrinkage

In the above description, the m^{th} tree used to correct the classifier is directly added to the existing forest with coefficient γ_m . That coefficient can be shrunk by a constant factor ν at each step of the iteration to slow the so-called “learning rate.” The update rule can be modified to reduce the weight of this addition:

$$F_m(\vec{x}) = F_{m-1}(\vec{x}) + \nu \cdot \gamma_m \cdot h_m(\vec{x}) \quad (\text{B.4})$$

With shrinkage, a more generalized model is attained. But more trees are needed to solve the problem, increasing the computational expense of training as well as evaluating the BDT.

Bagging

Random subsamples of the training data can be used for growing the trees. This is called bagging. The bagging fraction is the fraction of training data randomly chosen for the iterations.

B.2 Choice of input variables

The final set of twelve variables was determined using correlation coefficients and the mutual information between the input variables. See Figure B-1. The classifier performance was unchanged by the removal of the least consequential variables. Plots of the variable distributions comparing simulation and data at the training preselection

level is shown in Figures B-2 and B-3. In these plots, the invisible Higgs signal is magnified to illustrate the discriminating power of the variables.

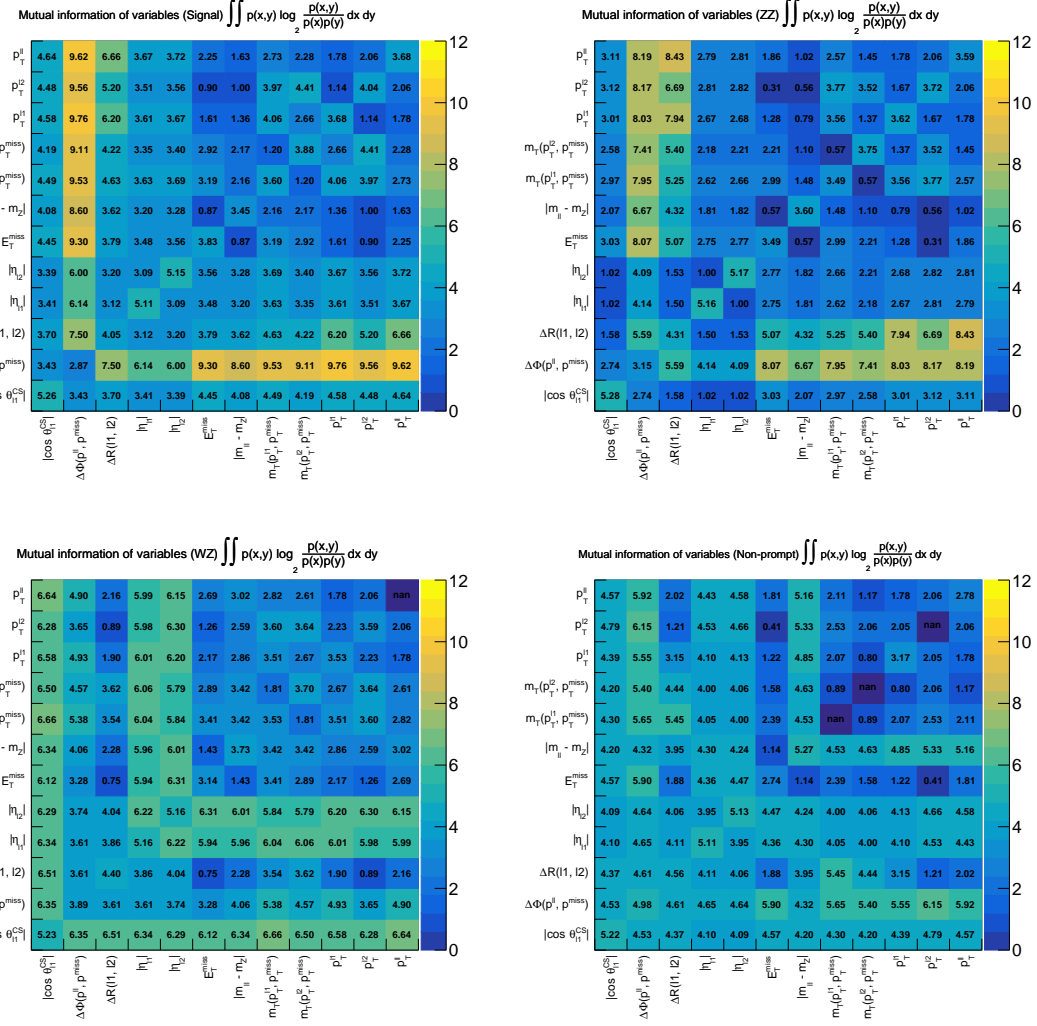


Figure B-1: Mutual information between the twelve BDT input variables for the invisible Higgs, ZZ, WZ, and flavor-symmetric (non-prompt) classes. The matrix for the Drell-Yan class is statistically irrelevant.

B.3 Mapping the experimental uncertainties

In order to perform a shape analysis in the classifier BDT spectrum, the effect of various nuisance parameters must be propagated to the BDT shape. It is not sufficient to simply evaluate different shapes at the extremities of the nuisance variations, because a BDT is not a conformal map. Therefore, we used a toy method to sample the distributions of the relevant nuisance parameters and found the resulting distributions in BDT value. The nuisances considered to be relevant are the uncertainty of

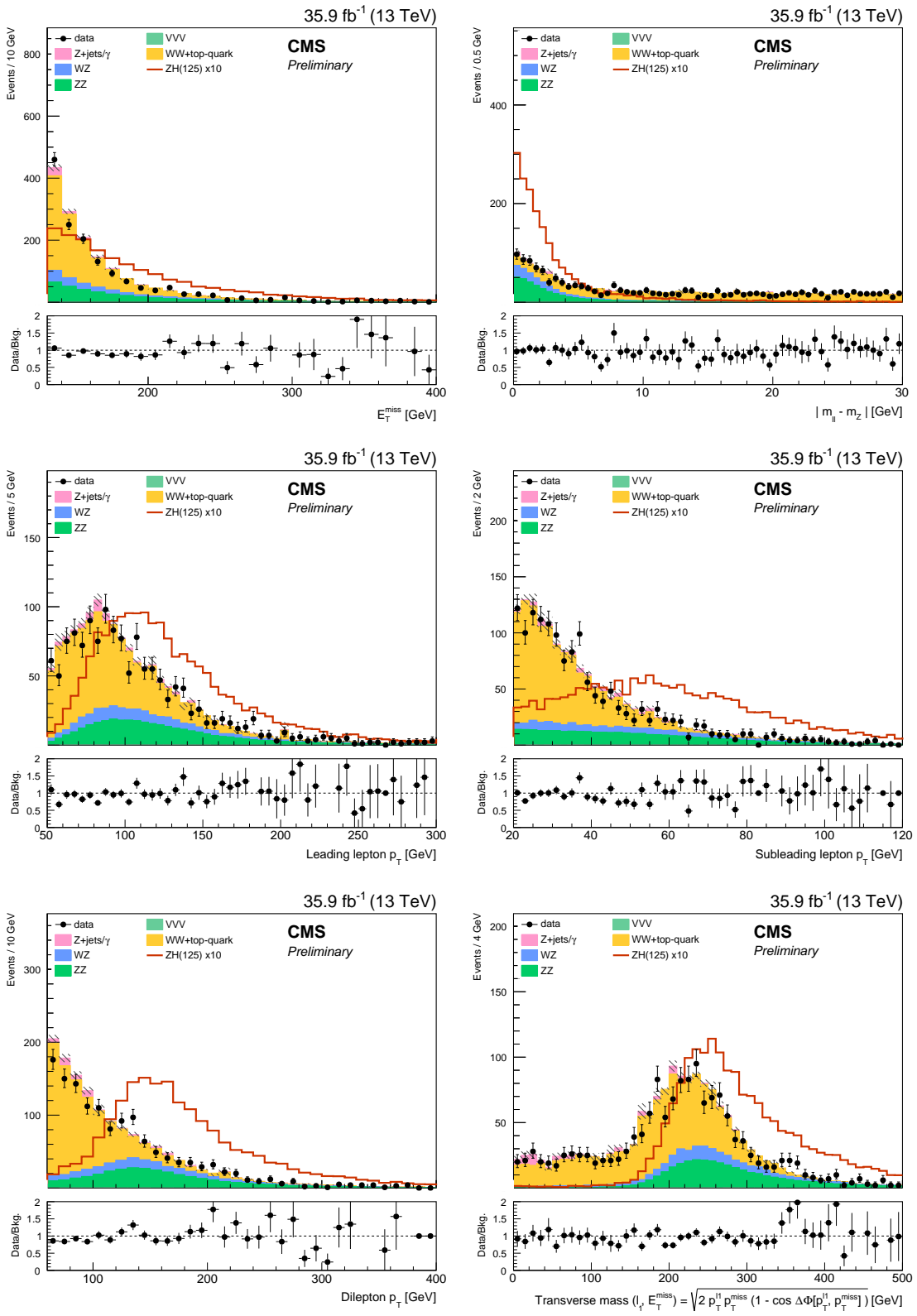


Figure B-2: Comparison of data and prediction in the BDT input variables after applying the training preselection. Signal strength has been enhanced by a factor of 10.

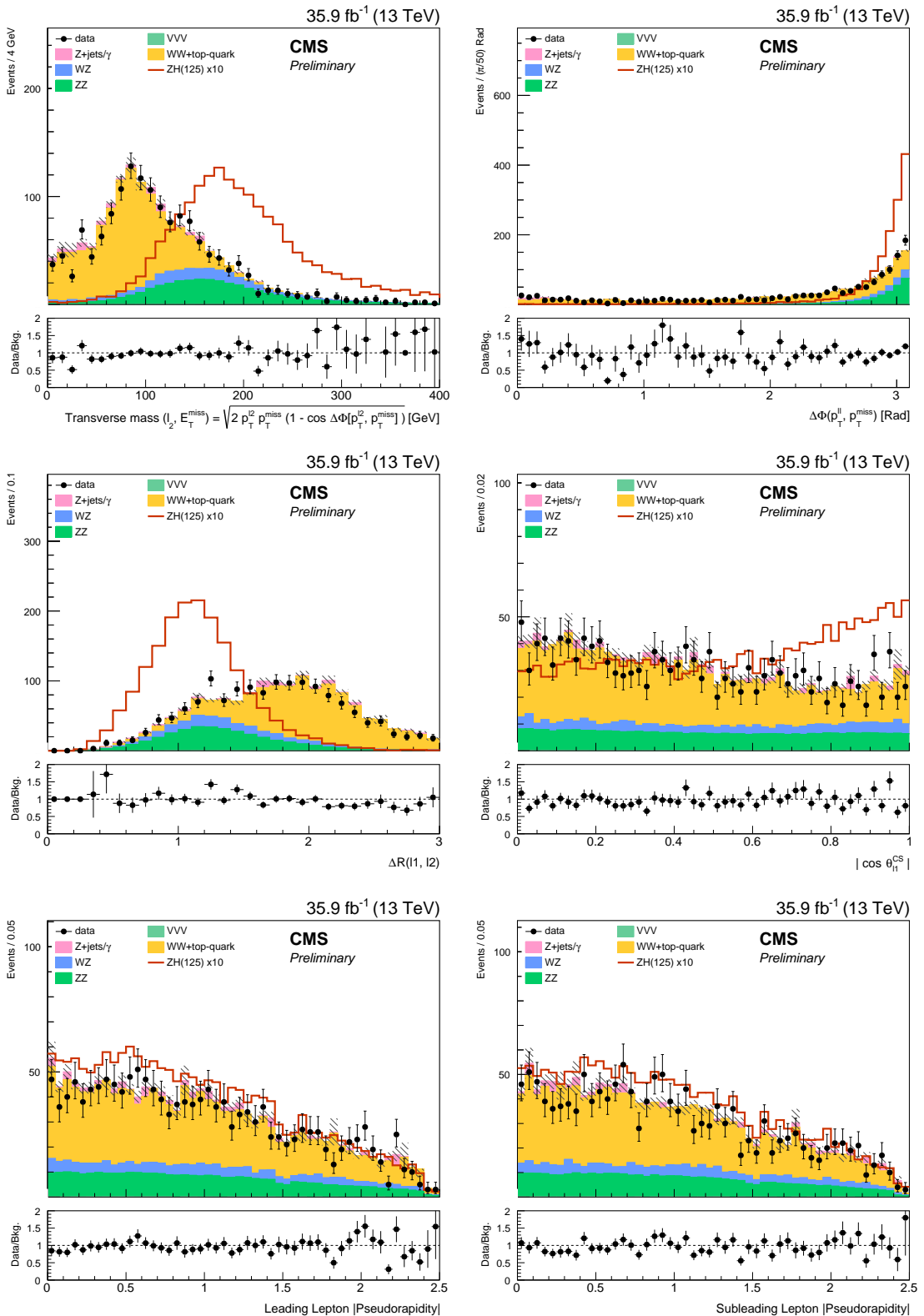


Figure B-3: (continued, 1) Comparison of data and prediction in the BDT input variables after applying the training preselection. Signal strength has been enhanced by a factor of 10.

the lepton momentum scale (see Section 5.4.4) and the uncertainty of missing energy due to the jet energy scale (JES).

The number of random toys used for the uncertainty propagation was 50 due to the high computing cost of many classifier evaluations. The lepton scale variations were sampled from a normal distribution with standard deviation of 0.01. The E_T^{miss} variations were sampled from a normal distribution with standard deviation of 1, then multiplied by the relative size of the jet energy scale effect (this quantity varies per event). Variations in the lepton scale affected the missing energy which was adjusted; variations in the missing energy affected many of the other variables, which were subsequently adjusted.

After performing this procedure for all simulated events, we take the uncertainty bands from the non-normal toy distributions as the distance between the 15.9% and 84.1% quantiles. These are the so-called $\pm 1\sigma$ quantiles of a normal distribution.

Figures B-4, B-5, and B-6 show 2D maps of the nuisance variations with the BDT value on the horizontal axis and the relative variation from the nominal BDT bin yield on the vertical axis. Figures B-7, B-8, and B-9 show the resulting uncertainty shapes that enter the likelihood fit, for the electron scale, muon scale, and E_T^{miss} scale nuisances respectively.

We do not propagate this uncertainty for the non-resonant backgrounds or the Drell-Yan process, because they are not highly signal-like and the other extrapolation uncertainties are sufficiently conservative. Furthermore, when performing the likelihood fit to determine the exclusion limits, we ignore these propagated uncertainties in the ratio of the diboson control regions, and fully correlate them across the shape bins in the signal region.

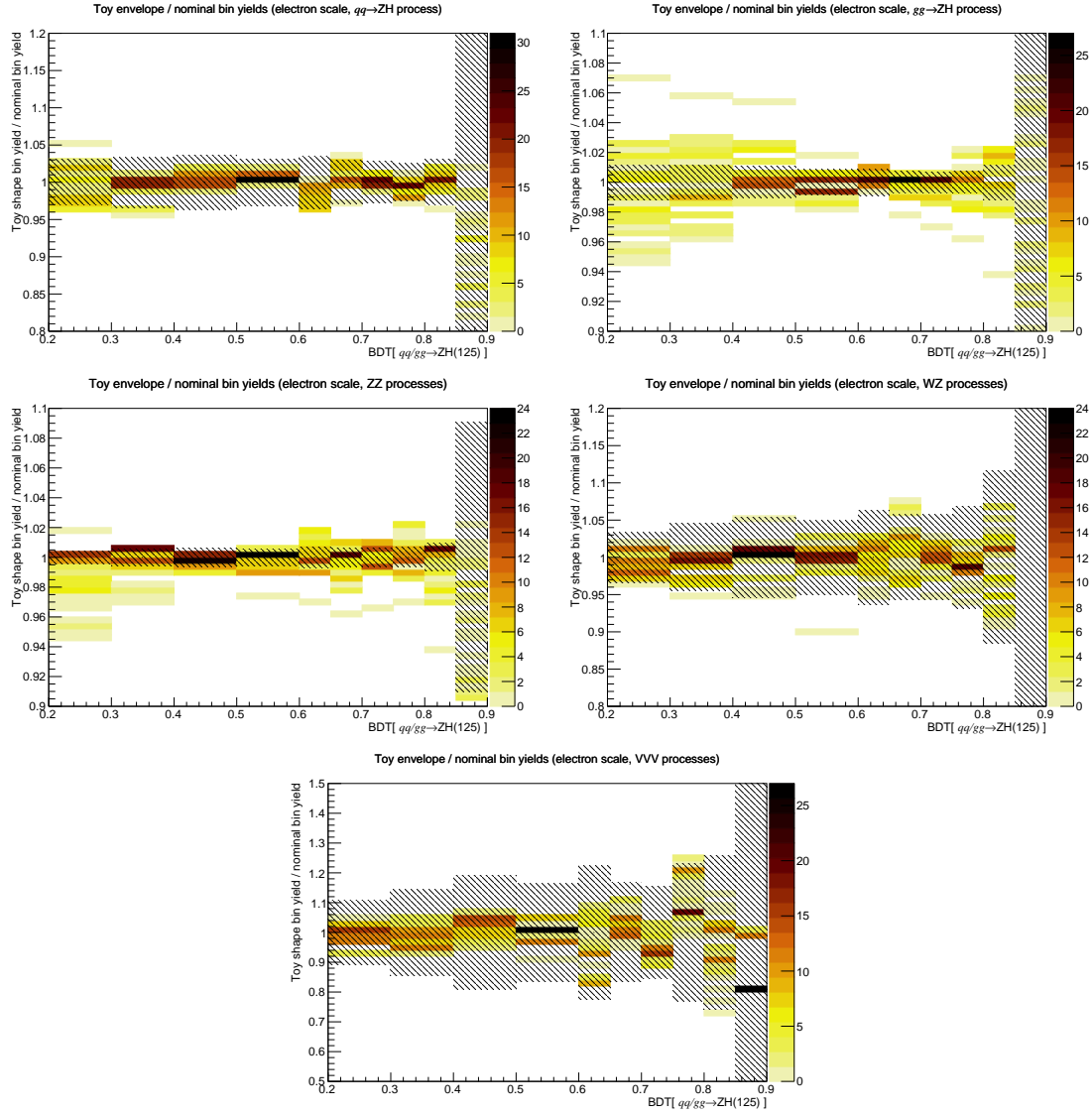


Figure B-4: 2D maps of the relative toy variations from the nominal BDT shape versus the BDT value, for the electron scale. The hashed bands represent statistical uncertainty on the simulated events.

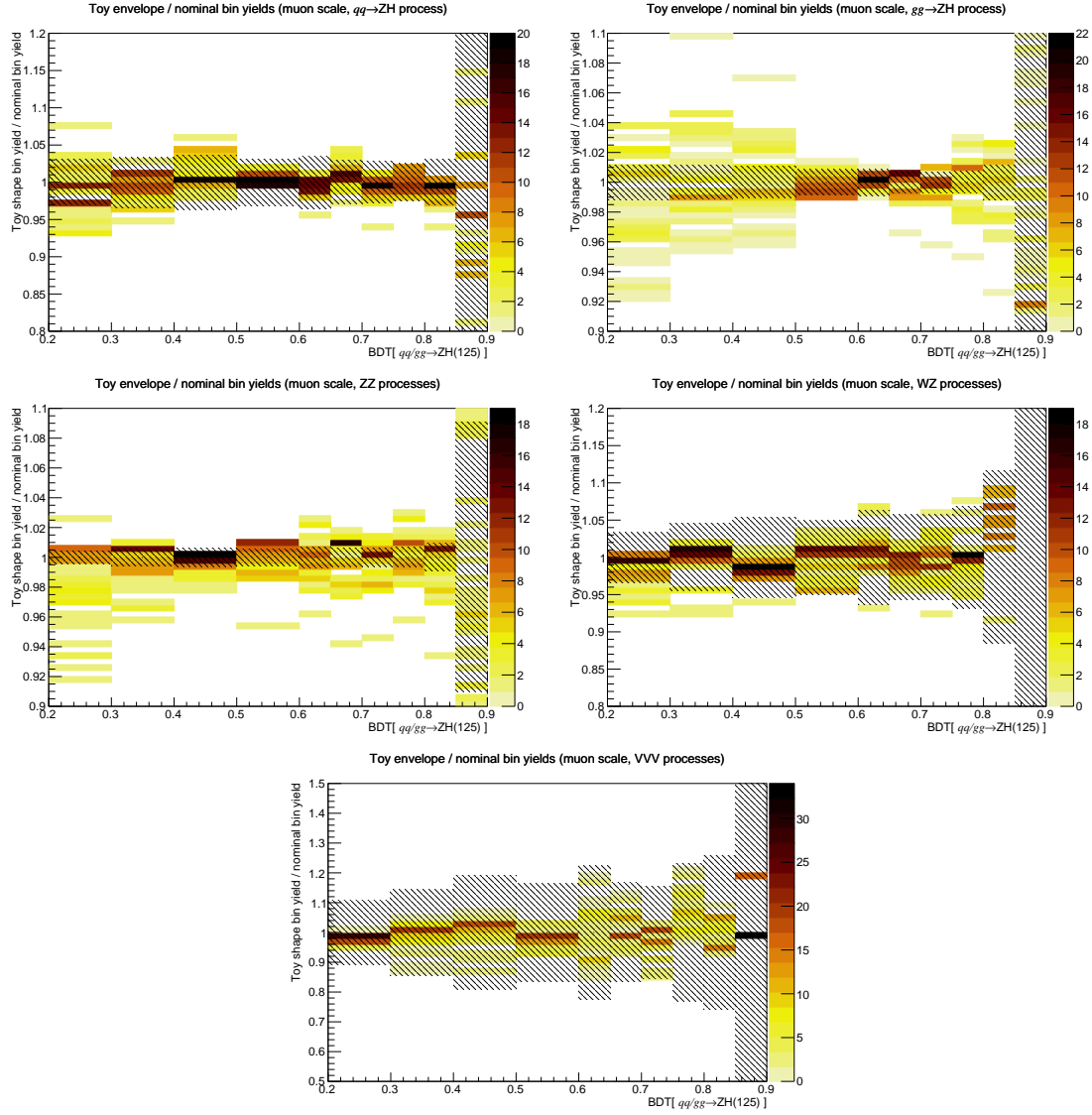


Figure B-5: 2D maps of the relative toy variations from the nominal BDT shape versus the BDT value, for the muon scale. The hashed bands represent statistical uncertainty on the simulated events.

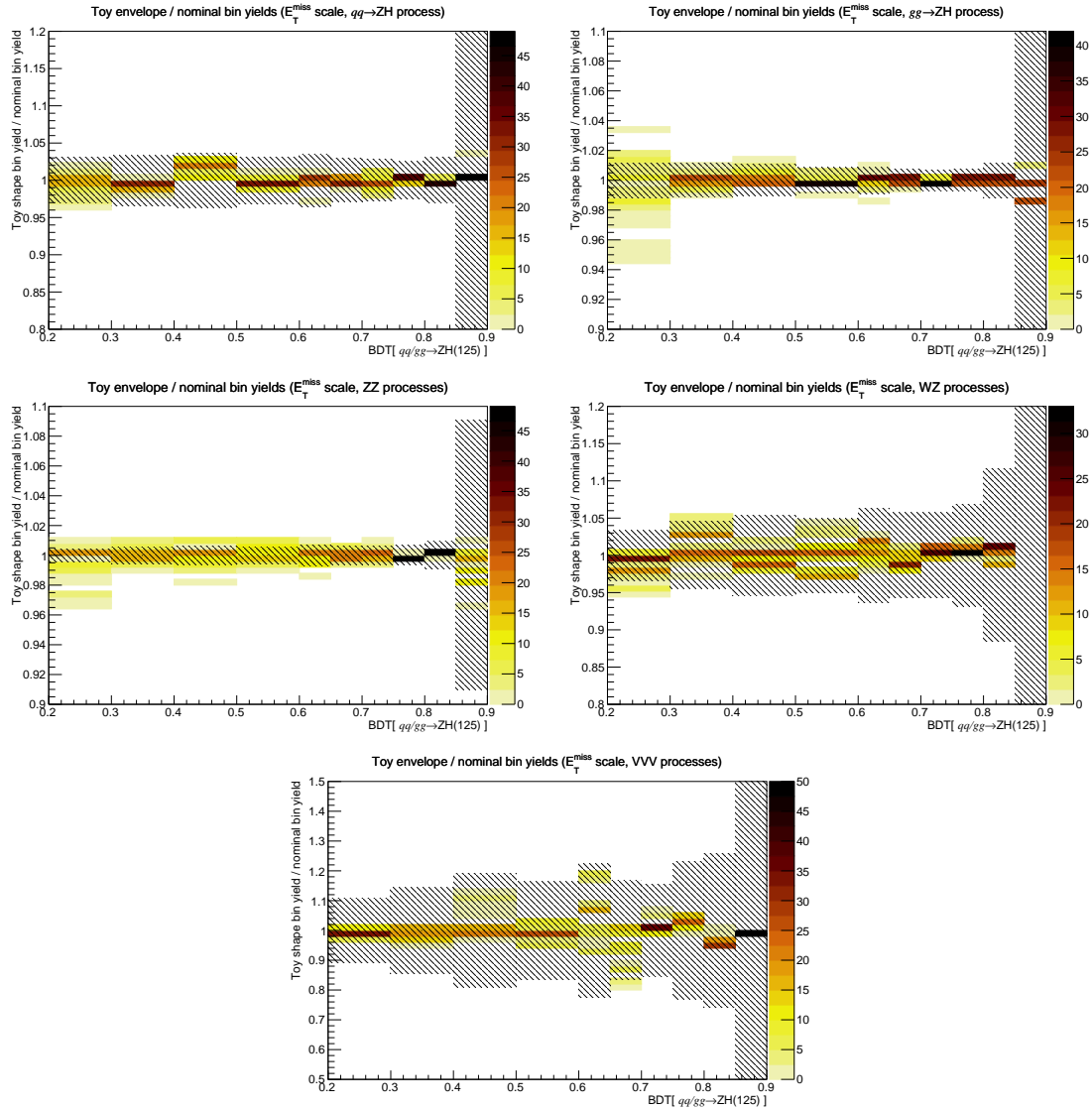


Figure B-6: 2D maps of the relative toy variations from the nominal BDT shape versus the BDT value, for the E_T^{miss} scale due to the JES uncertainty. The hashed bands represent statistical uncertainty on the simulated events.

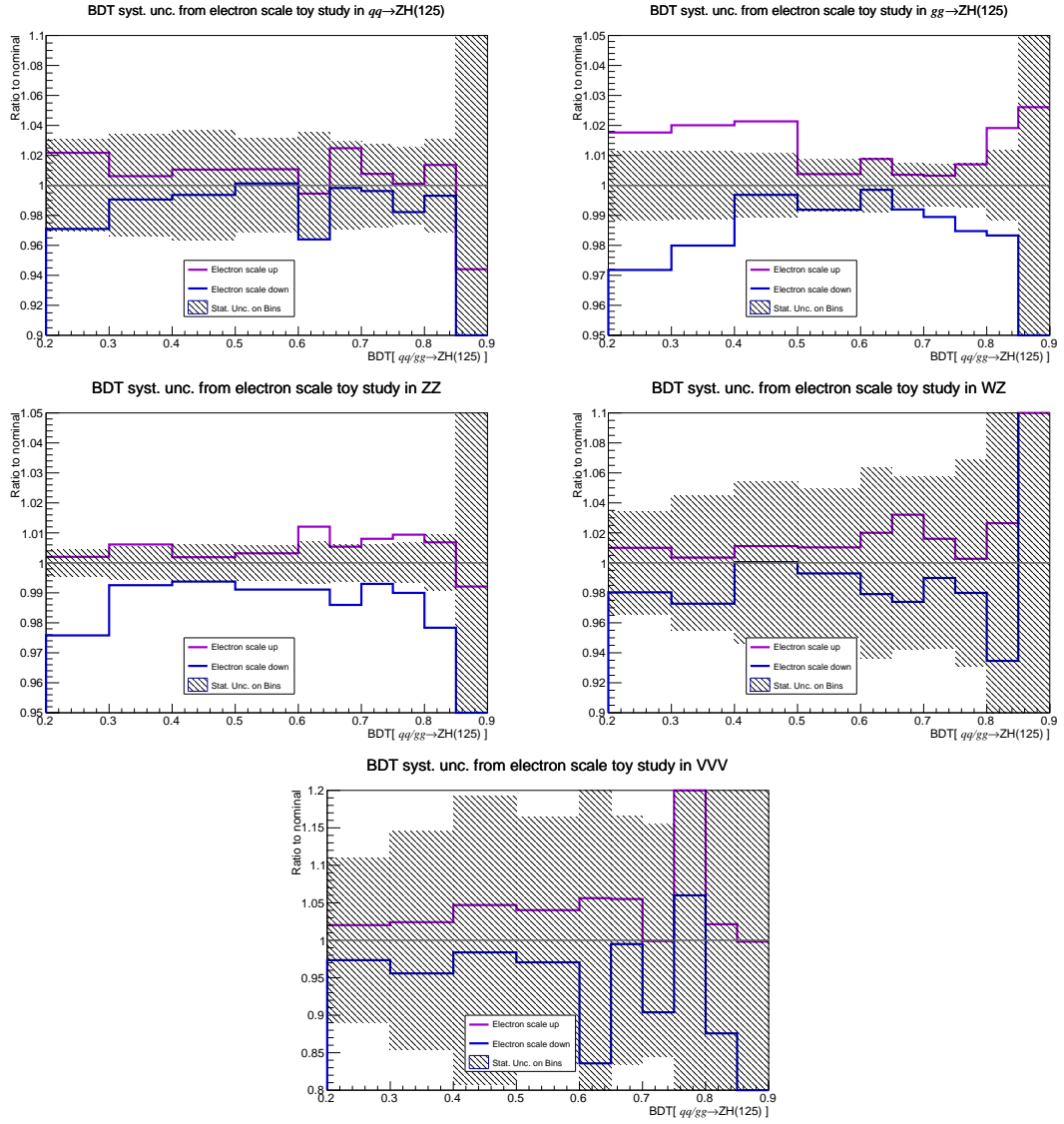


Figure B-7: Uncertainty shapes calculated from the toy method for the electron scale.

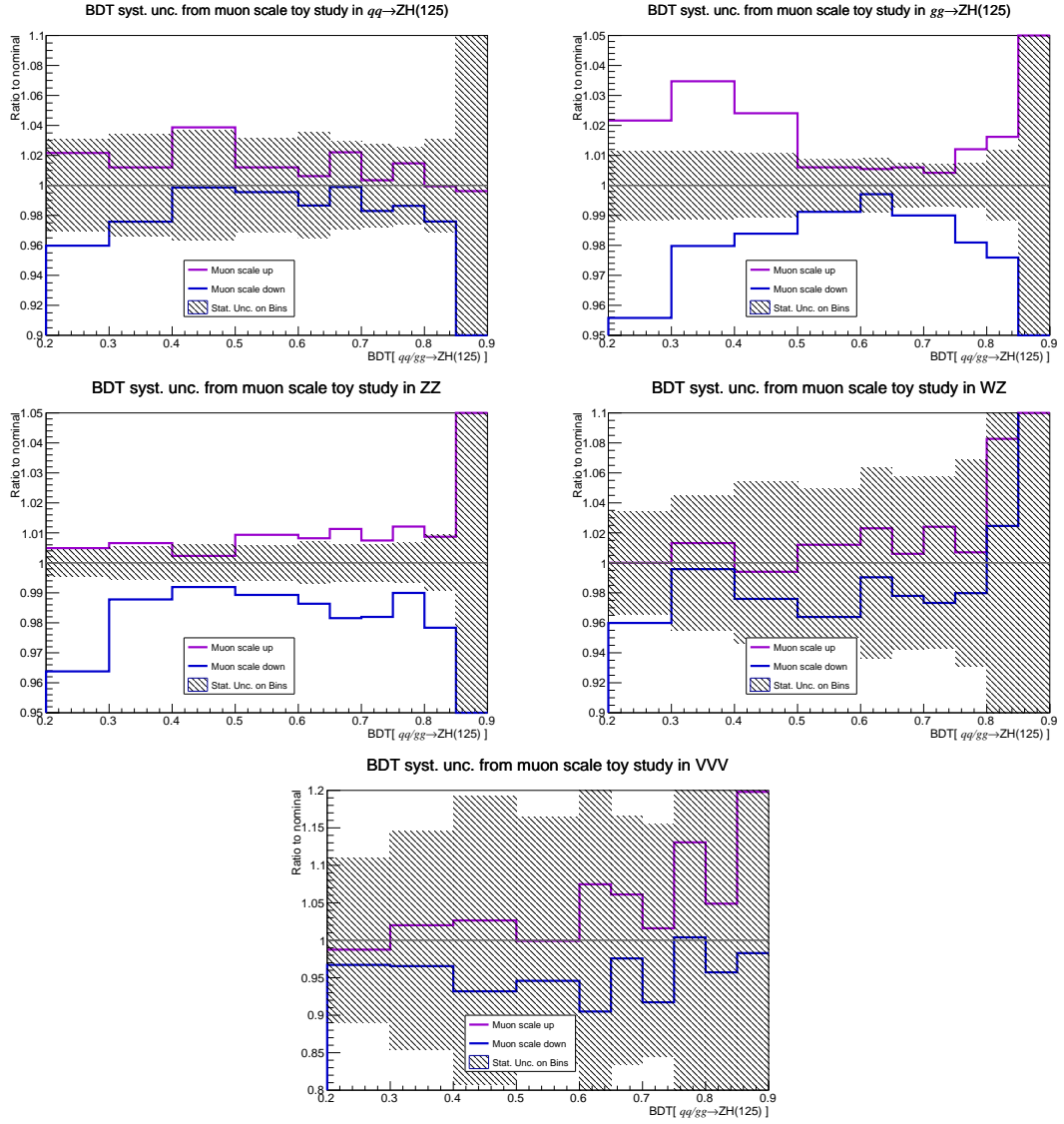


Figure B-8: Uncertainty shapes calculated from the toy method for the muon scale.

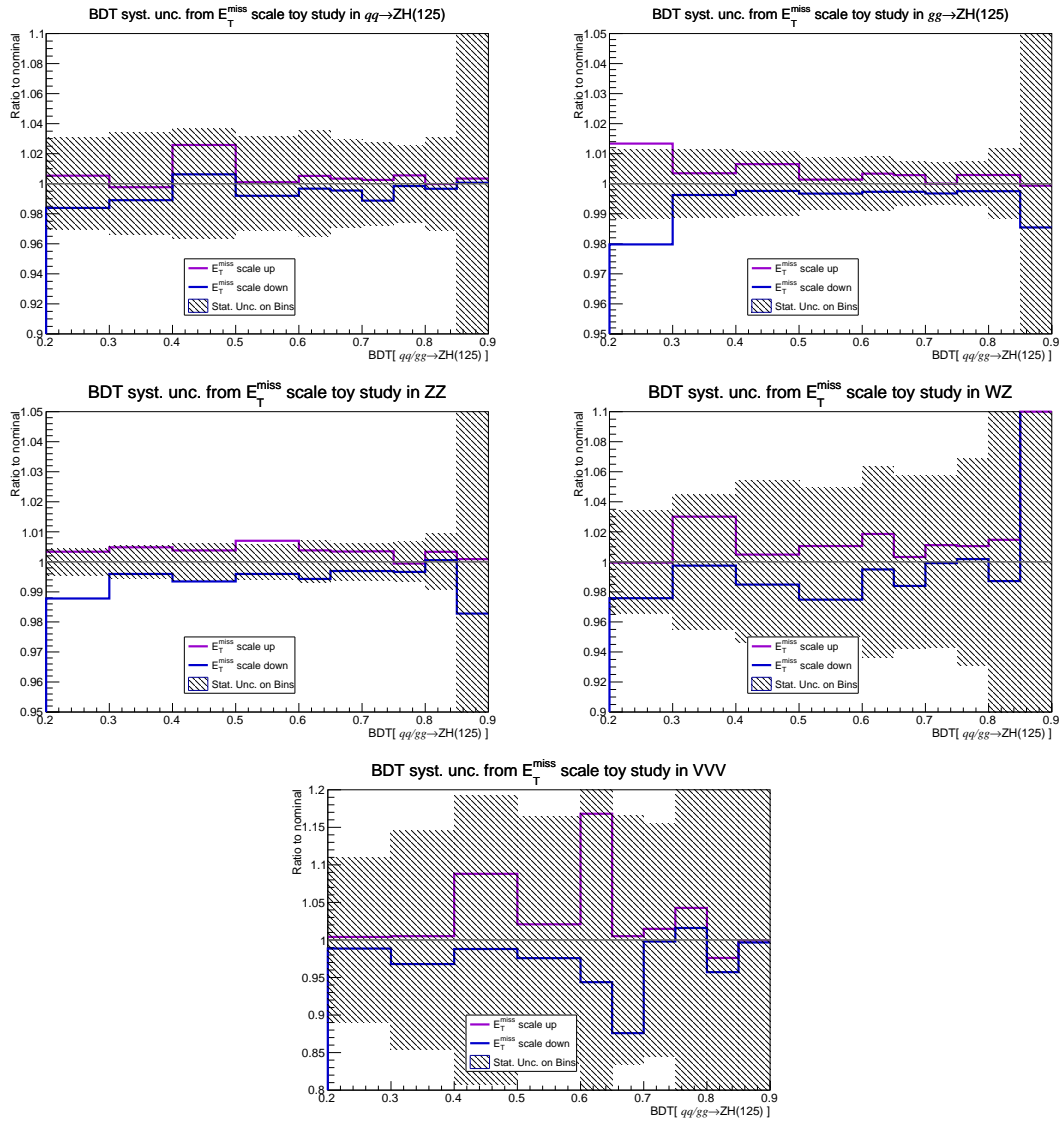


Figure B-9: Uncertainty shapes calculated from the toy method for the E_T^{miss} due to the JES uncertainty.

Appendix C

QCD NNLO/NLO k -factors for $\text{qq} \rightarrow \text{ZZ}$

The NNLO/NLO k -factors for the $\text{qq} \rightarrow \text{ZZ}$ process are available binned in different generator-level variables. They can be applied as a function of either the transverse momentum $p_T(Z, Z)$, mass $M(Z, Z)$ or angular separation $\Delta\phi(Z, Z)$ of the diboson system. While all three versions of the k -factors stem from the same calculation framework and are thus in agreement as far as calculation settings are observed, the binning may impact the result of the corrections. The k -factors are shown in fig. C-1, the distributions of the generator-level variables are shown in fig. C-2. The generator variables are shown for simulated ZZ events after applying the final analysis selection. For both $\Delta\phi(Z, Z)$ and $p_T(Z, Z)$, the signal region events are very strongly peaked in regions where the k -factors are significantly non-flat. Thus, the application of these k -factors depends on the choice of bin sizes. Small variation of the bin sizes may induce large changes in the medium k -factor per bin. To avoid the complications associated with this, the $M(Z, Z)$ binning is used. In this case, the signal region events are not contained in a region of large k -factors variations and the correction is thus more reliable.

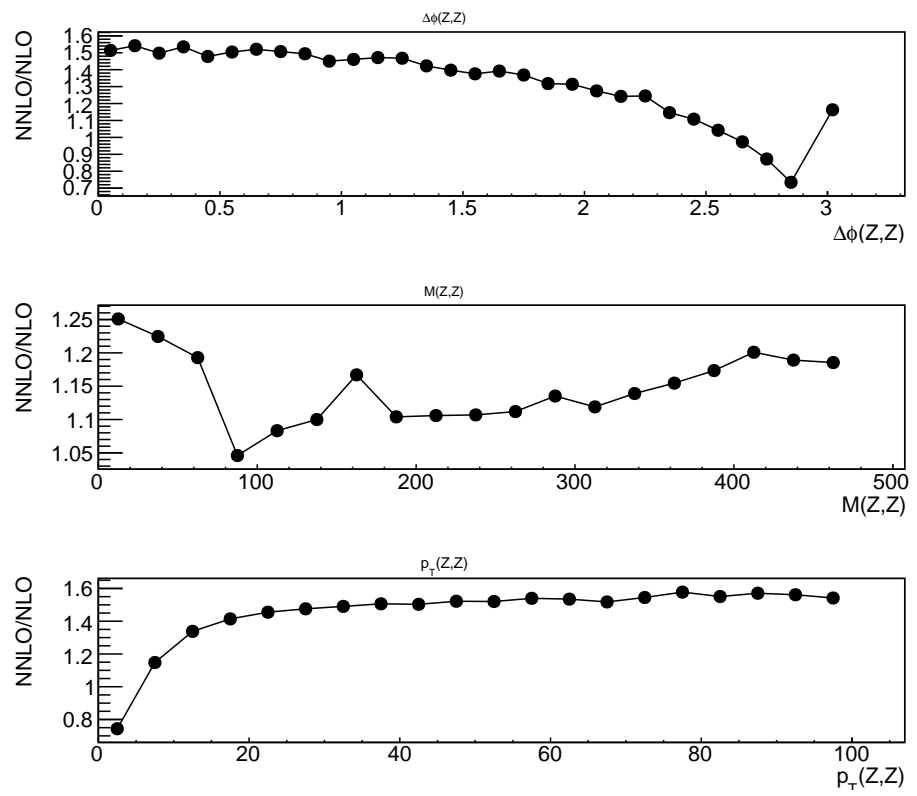


Figure C-1: QCD NNLO/NLO k -factors for the $q\bar{q} \rightarrow ZZ$ process binned in different generator-level kinematic variables of the diboson system.

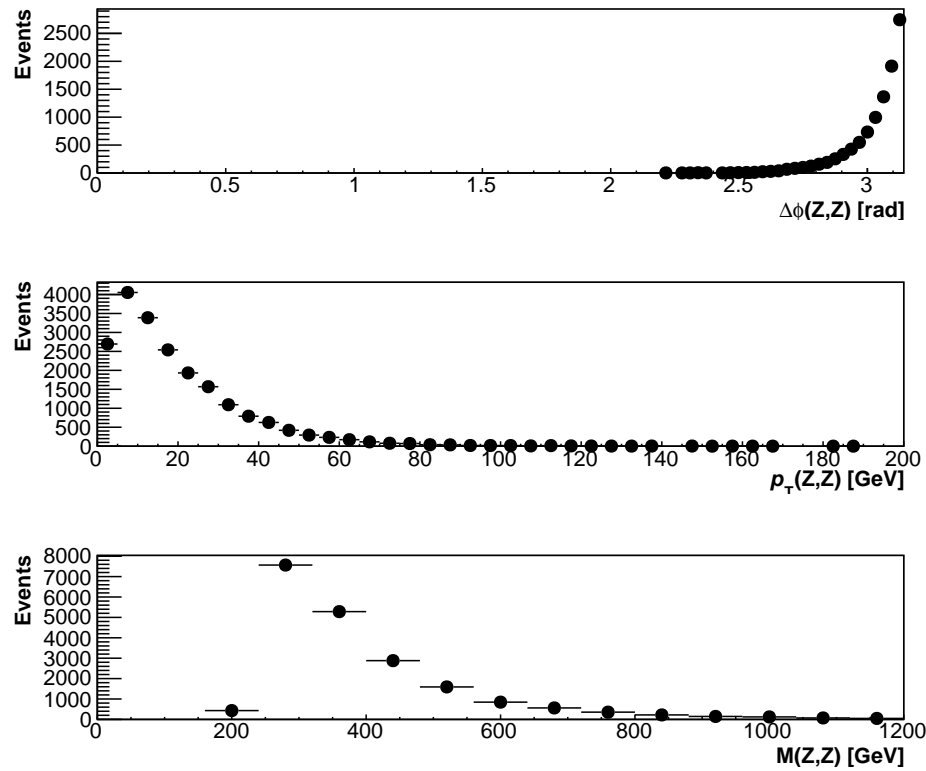


Figure C-2: Distribution of the generator-level kinematic variables of the diboson system in ZZ events after final selection.

Appendix D

Interpolation of Simplified Model dark matter limits

In order to fully populate the m_{med} - m_{DM} plane, more parameter points than reasonably available as FullSim MC samples are necessary. To this end, a reweighting of the available FullSim samples is performed.

Terminology used in this section:

- **FullSim samples:** The samples we get from central production with proper detector simulation. We have 38 (28) of these for the axial (vector) mediators.
- **Target:** a parameter point/sample we want to obtain using our reweighting technique.
- **Reference:** The parameter point/sample we use as a basis to get to the target. The reference is always one of the FullSim samples.

D.1 Calculating the weights

Using the same MADGRAPH model as used for central production, generator-level spectra of the mediator transverse momentum p_T^{med} are obtained. While in the centrally produced samples, MADGRAPH is used to calculate jet multiplicities of both zero and one, the generator samples only contain the zero jet process from MADGRAPH. This is due to the practical limitation that processing time increases dramatically with an added jet, which makes it impossible to generate a larger number of parameter points for reweighting in this configuration. However, it is found that simply using the 0 jet samples alone is sufficient for the reweighting.

To mimic the effects of the analysis selection, a generator-level selection is applied before extracting the p_T^{med} spectra.

- $p_T^{\text{lepton}} > 20 \text{ GeV}.$
- $|\eta^{\text{lepton}}| < 2.5$

- $p_T^{ll} > 60 \text{ GeV}$
- $\Delta\phi(ll, med) > 2.6$
- $|p_T^{ll} - p_T^{\text{med}}| / p_T^{\text{med}} < 0.4$
- $\Delta R(ll) < 1.8$

The p_T^{med} distributions are scaled according to the generated cross-section before applying the additional selection criteria. This ensures that differences in acceptance between target and reference are taken into account.

For a given target and reference, the ratio of the p_T^{med} distributions is then used as a p_T^{med} -dependent weight.

$$w(p_T^{\text{med}}) = \frac{P^{\text{target}}(p_T^{\text{med}})}{P^{\text{reference}}(p_T^{\text{med}})}$$

Where w is the weight and $P(p_T^{\text{med}})$ is the value of the p_T^{med} distribution at a given value of p_T^{med} .

D.2 Choosing a reference

For a given target point, a reference sample is chosen by minimizing the distance between reference and target in the $\log(m_{\text{med}})$ - $\log(m_{\text{DM}})$ plane. In order to improve the performance of the procedure, the optimization is constrained to only allow the reference sample to have relatively larger DM mass than the target $m_{\text{DM}}^{\text{target}}/m_{\text{med}}^{\text{target}} \leq m_{\text{DM}}^{\text{ref}}/m_{\text{med}}^{\text{ref}}$. This requirement aims to take into account that the shape of the E_T^{miss} spectrum becomes increasingly harder as m_{DM} increases.

D.3 Closure testing

In order to test this method, it is possible to reweight FullSim samples to represent parameter points that are also available in FullSim. Thus, one may compare the “real” and reweighted final E_T^{miss} distribution and check their agreement. It has to be noted that this method will generally give a worst-case impression of the performance of the reweighting. Since one reweights FullSim to FullSim, the average distance between target and reference will be much larger than in the real use case, where one always reweights to the nearest FullSim sample.

For each reweighted FullSim sample, the bin-by-bin difference between real and reweighted bin content divided by its statistical uncertainty is recorded (*bin-by-bin pull*). In the absence of systematical shifts induced by the method, the pulls should scatter around zero with a standard deviation of one. The distributions for axial and vector mediators are shown in fig. D-1. Only target points with $100 \text{ GeV} < m_{\text{med}} < 2000 \text{ GeV}$ are considered. In both cases, the width of the distribution is consistent with unity no significant bias in the mean is observed.

The distribution of the pulls is also given per target parameter point (Figs. D-3-D-4) and as a function of E_T^{miss} (fig. D-2). These views allow to see in more detail the behavior of the reweighting and spot possibly pathological features that could be obscured in the overall distributions. No systematic trends are found, indicating that the method works sufficiently well. This assessment has of course to be taken relative to the attainable precision in this test: Due to the limited signal sample statistics, the precision of the closure test method is limited and it is not necessary to obtain a perfect interpolation method, since the limited-statistics argument applies also to the actual analysis case.

A closure test of the expected limits is shown in fig. D-5, showing good agreement in the final median expected limit, which ultimately determines the Z value in the 2D scan. Good agreement is observed.

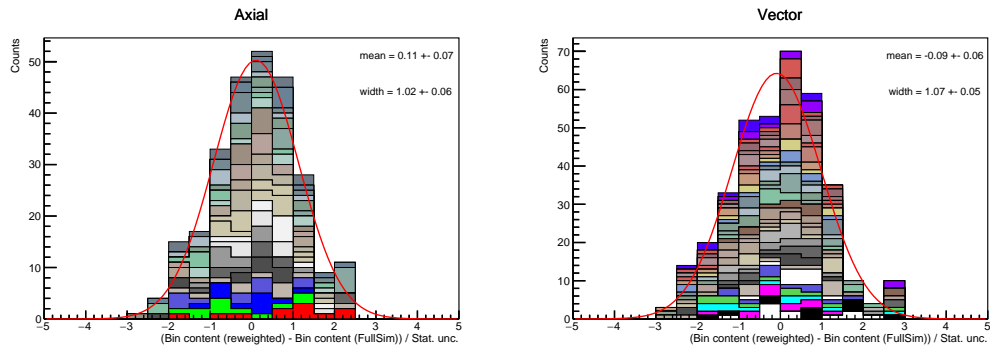


Figure D-1: Bin-by-bin pull distribution in the axial (left) and vector mediator cases (right). For details on how these pulls are calculated, refer to the text. Each color represents one target sample (If the colors are confusing to, you may ignore them altogether, in which case you will see the overall distribution in all points).

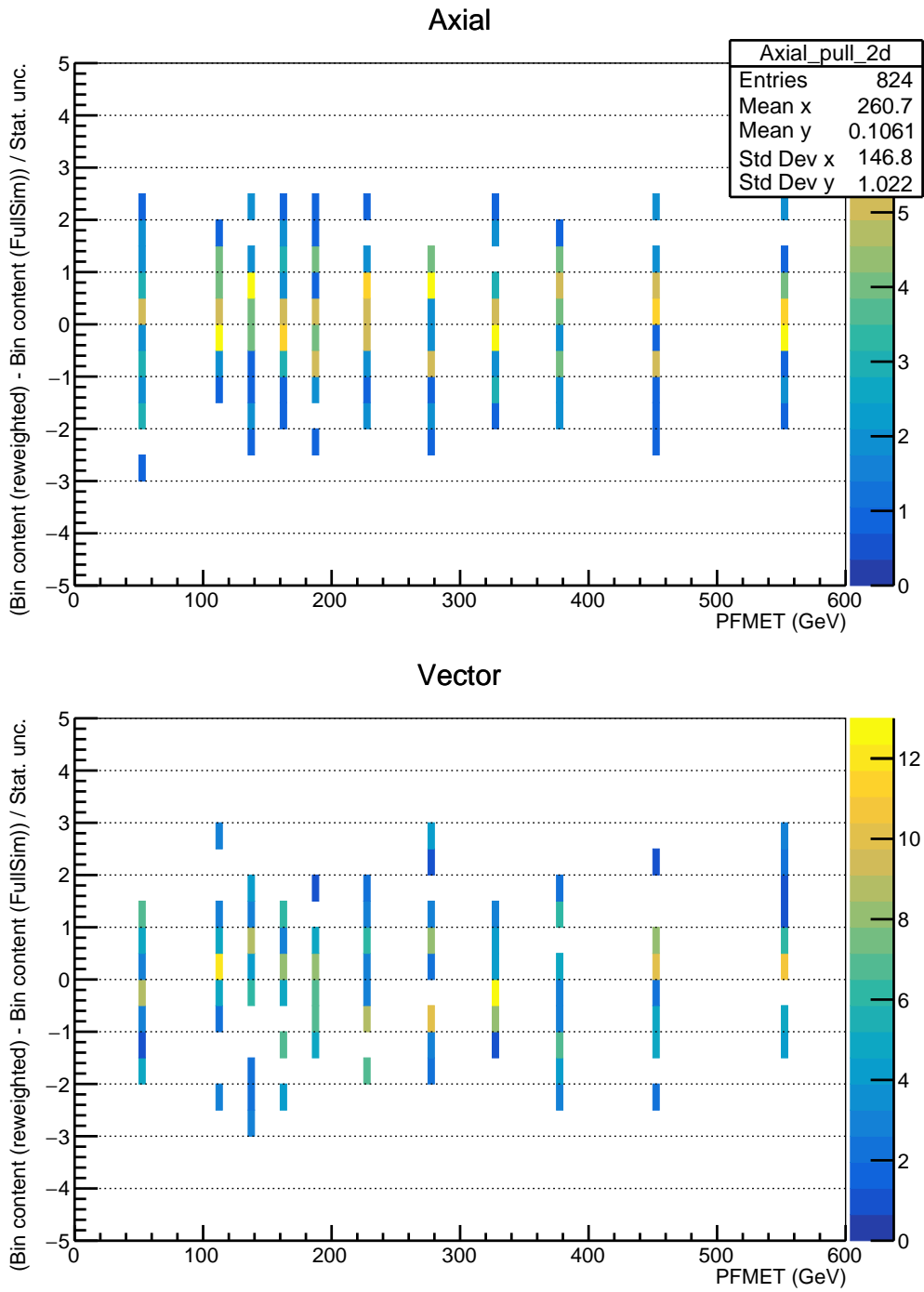


Figure D-2: Same as fig. D-1, but the pull distributions are shown as a function of PF E_T^{miss} .

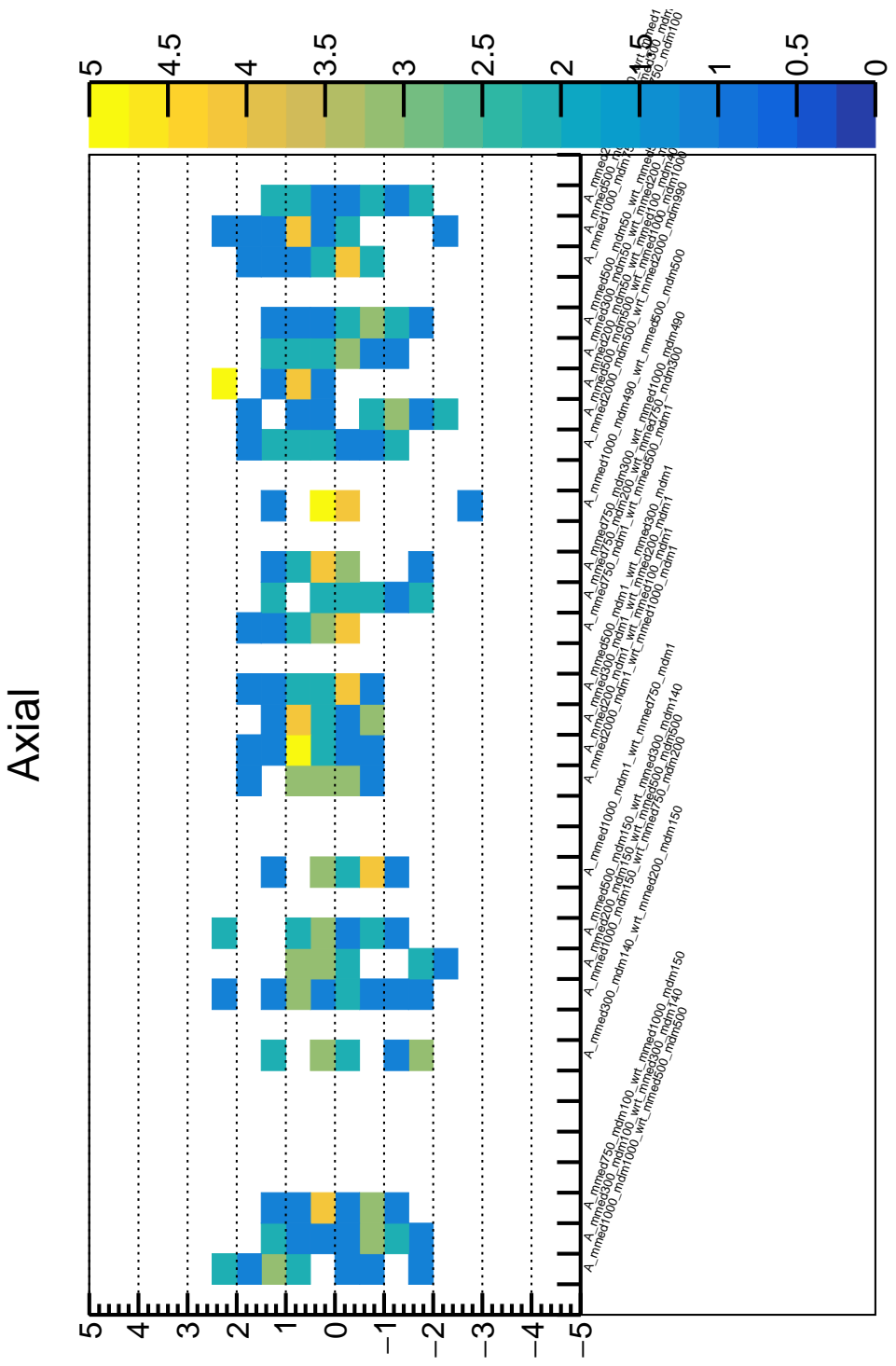


Figure D-3: Same as fig. D-1, but the pull distributions are shown for each individual target point. Each vertical bin in this view corresponds to one color in fig. D-1.

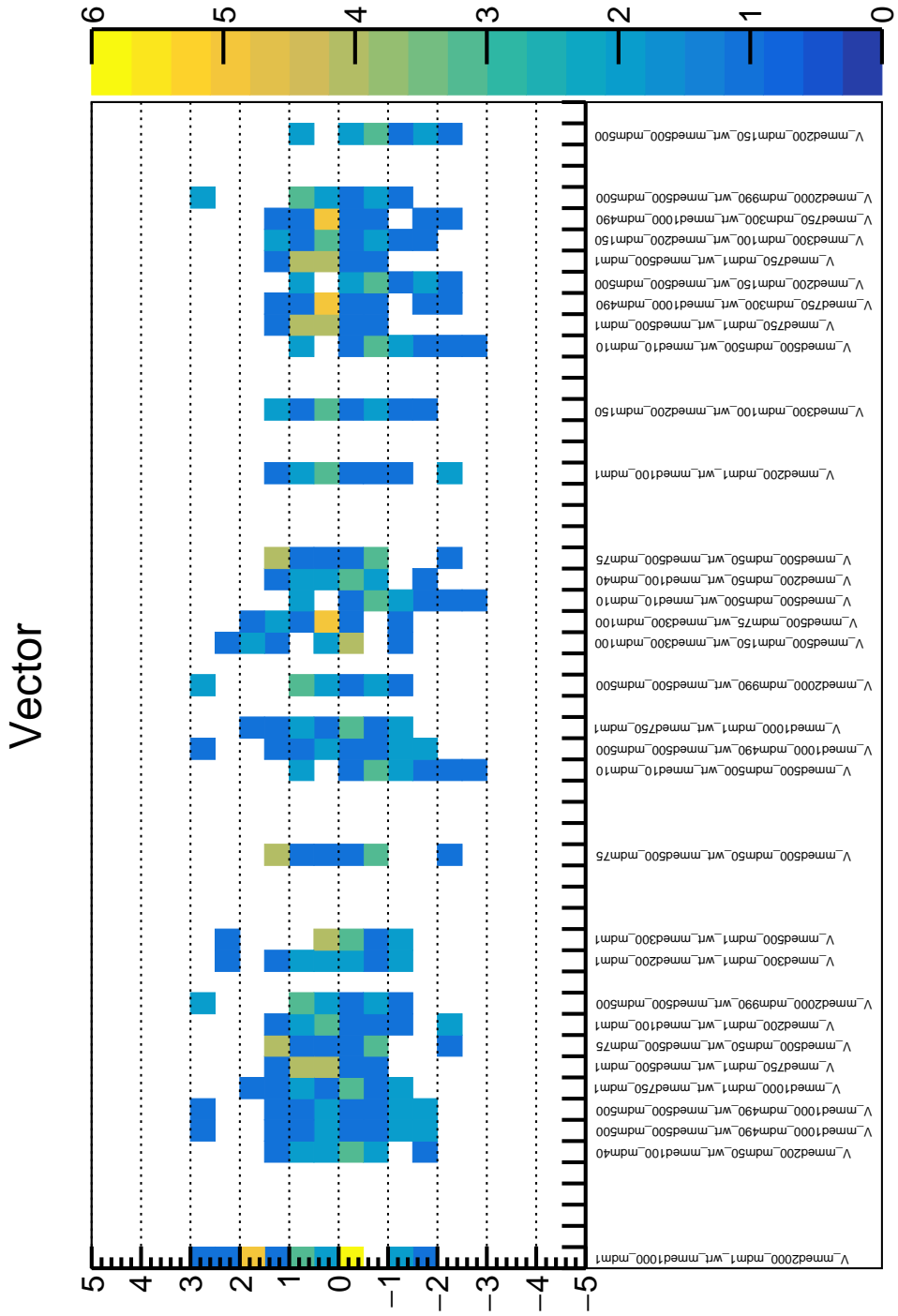


Figure D-4: Same as fig. D-1, but the pull distributions are shown for each individual target point. Each vertical bin in this view corresponds to one color in fig. D-1.

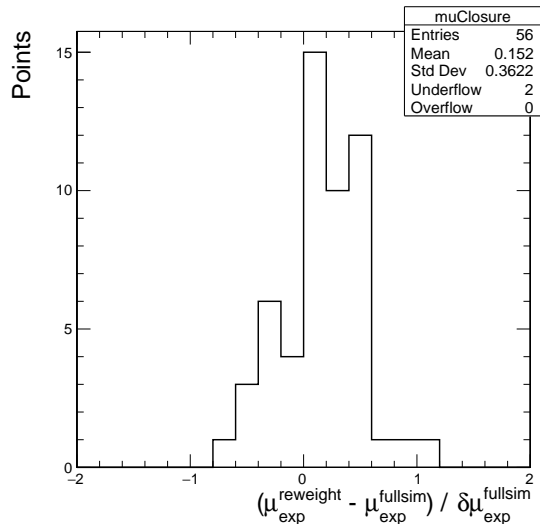


Figure D-5: Closure test of final limits, showing change in the median expected signal strength ($\mu_{\text{exp}} = \sigma_{\text{exp}}/\sigma_{\text{theo}}$) introduced by using the reweighting method for all points that have full simulation available. The two underflow entries are the points $m_A = 10, m_\chi = 1$ and $m_V = 10, m_\chi = 1$.

Appendix E

Cross sections for ADD model

ADD scenario	$\sigma(pp \rightarrow UZ)$ [pb]	ADD scenario	$\sigma(pp \rightarrow UZ)$ [pb]
$M_D = 1.0 \text{ TeV}, n = 2$	8.40e-01	$M_D = 1.5 \text{ TeV}, n = 2$	2.67e-01
$M_D = 1.0 \text{ TeV}, n = 3$	1.04e+00	$M_D = 1.5 \text{ TeV}, n = 3$	2.98e-01
$M_D = 1.0 \text{ TeV}, n = 4$	1.42e+00	$M_D = 1.5 \text{ TeV}, n = 4$	3.65e-01
$M_D = 1.0 \text{ TeV}, n = 5$	2.21e+00	$M_D = 1.5 \text{ TeV}, n = 5$	4.81e-01
$M_D = 1.0 \text{ TeV}, n = 6$	3.96e+00	$M_D = 1.5 \text{ TeV}, n = 6$	6.75e-01
$M_D = 1.0 \text{ TeV}, n = 7$	8.55e+00	$M_D = 1.5 \text{ TeV}, n = 7$	1.05e+00
$M_D = 1.1 \text{ TeV}, n = 2$	6.54e-01	$M_D = 1.6 \text{ TeV}, n = 2$	2.19e-01
$M_D = 1.1 \text{ TeV}, n = 3$	7.95e-01	$M_D = 1.6 \text{ TeV}, n = 3$	2.46e-01
$M_D = 1.1 \text{ TeV}, n = 4$	1.06e+00	$M_D = 1.6 \text{ TeV}, n = 4$	2.93e-01
$M_D = 1.1 \text{ TeV}, n = 5$	1.60e+00	$M_D = 1.6 \text{ TeV}, n = 5$	3.69e-01
$M_D = 1.1 \text{ TeV}, n = 6$	2.67e+00	$M_D = 1.6 \text{ TeV}, n = 6$	5.11e-01
$M_D = 1.1 \text{ TeV}, n = 7$	5.24e+00	$M_D = 1.6 \text{ TeV}, n = 7$	7.49e-01
$M_D = 1.2 \text{ TeV}, n = 2$	5.15e-01	$M_D = 1.7 \text{ TeV}, n = 2$	1.83e-01
$M_D = 1.2 \text{ TeV}, n = 3$	6.06e-01	$M_D = 1.7 \text{ TeV}, n = 3$	1.98e-01
$M_D = 1.2 \text{ TeV}, n = 4$	7.92e-01	$M_D = 1.7 \text{ TeV}, n = 4$	2.32e-01
$M_D = 1.2 \text{ TeV}, n = 5$	1.14e+00	$M_D = 1.7 \text{ TeV}, n = 5$	2.85e-01
$M_D = 1.2 \text{ TeV}, n = 6$	1.81e+00	$M_D = 1.7 \text{ TeV}, n = 6$	3.82e-01
$M_D = 1.2 \text{ TeV}, n = 7$	3.34e+00	$M_D = 1.7 \text{ TeV}, n = 7$	5.49e-01
$M_D = 1.3 \text{ TeV}, n = 2$	4.05e-01	$M_D = 1.8 \text{ TeV}, n = 2$	1.52e-01
$M_D = 1.3 \text{ TeV}, n = 3$	4.74e-01	$M_D = 1.8 \text{ TeV}, n = 3$	1.62e-01
$M_D = 1.3 \text{ TeV}, n = 4$	6.07e-01	$M_D = 1.8 \text{ TeV}, n = 4$	1.89e-01
$M_D = 1.3 \text{ TeV}, n = 5$	8.47e-01	$M_D = 1.8 \text{ TeV}, n = 5$	2.28e-01
$M_D = 1.3 \text{ TeV}, n = 6$	1.29e+00	$M_D = 1.8 \text{ TeV}, n = 6$	2.92e-01
$M_D = 1.3 \text{ TeV}, n = 7$	2.26e+00	$M_D = 1.8 \text{ TeV}, n = 7$	4.04e-01
$M_D = 1.4 \text{ TeV}, n = 2$	3.28e-01	$M_D = 1.9 \text{ TeV}, n = 2$	1.27e-01
$M_D = 1.4 \text{ TeV}, n = 3$	3.79e-01	$M_D = 1.9 \text{ TeV}, n = 3$	1.33e-01
$M_D = 1.4 \text{ TeV}, n = 4$	4.68e-01	$M_D = 1.9 \text{ TeV}, n = 4$	1.52e-01
$M_D = 1.4 \text{ TeV}, n = 5$	6.32e-01	$M_D = 1.9 \text{ TeV}, n = 5$	1.80e-01
$M_D = 1.4 \text{ TeV}, n = 6$	9.20e-01	$M_D = 1.9 \text{ TeV}, n = 6$	2.32e-01
$M_D = 1.4 \text{ TeV}, n = 7$	1.53e+00	$M_D = 1.9 \text{ TeV}, n = 7$	3.01e-01

Table E.1: Cross sections used for limit setting in the ADD scenario. The cross sections correspond to $p_T(\text{Graviton}) > 50 \text{ GeV}$ and truncation is applied.

ADD scenario	$\sigma(pp \rightarrow UZ)$ [pb]	ADD scenario	$\sigma(pp \rightarrow UZ)$ [pb]
$M_D = 2.0 \text{ TeV}, n = 2$	1.07e-01	$M_D = 2.5 \text{ TeV}, n = 5$	5.06e-02
$M_D = 2.0 \text{ TeV}, n = 3$	1.10e-01	$M_D = 2.5 \text{ TeV}, n = 6$	5.62e-02
$M_D = 2.0 \text{ TeV}, n = 4$	1.25e-01	$M_D = 2.5 \text{ TeV}, n = 7$	6.42e-02
$M_D = 2.0 \text{ TeV}, n = 5$	1.43e-01	$M_D = 2.6 \text{ TeV}, n = 2$	4.36e-02
$M_D = 2.0 \text{ TeV}, n = 6$	1.73e-01	$M_D = 2.6 \text{ TeV}, n = 3$	4.06e-02
$M_D = 2.0 \text{ TeV}, n = 7$	2.29e-01	$M_D = 2.6 \text{ TeV}, n = 4$	4.10e-02
$M_D = 2.1 \text{ TeV}, n = 2$	9.09e-02	$M_D = 2.6 \text{ TeV}, n = 5$	4.22e-02
$M_D = 2.1 \text{ TeV}, n = 3$	9.15e-02	$M_D = 2.6 \text{ TeV}, n = 6$	4.48e-02
$M_D = 2.1 \text{ TeV}, n = 4$	9.94e-02	$M_D = 2.6 \text{ TeV}, n = 7$	5.04e-02
$M_D = 2.1 \text{ TeV}, n = 5$	1.16e-01	$M_D = 2.7 \text{ TeV}, n = 2$	3.85e-02
$M_D = 2.1 \text{ TeV}, n = 6$	1.37e-01	$M_D = 2.7 \text{ TeV}, n = 3$	3.39e-02
$M_D = 2.1 \text{ TeV}, n = 7$	1.70e-01	$M_D = 2.7 \text{ TeV}, n = 4$	3.43e-02
$M_D = 2.2 \text{ TeV}, n = 2$	7.77e-02	$M_D = 2.7 \text{ TeV}, n = 5$	3.48e-02
$M_D = 2.2 \text{ TeV}, n = 3$	7.59e-02	$M_D = 2.7 \text{ TeV}, n = 6$	3.70e-02
$M_D = 2.2 \text{ TeV}, n = 4$	8.42e-02	$M_D = 2.7 \text{ TeV}, n = 7$	4.07e-02
$M_D = 2.2 \text{ TeV}, n = 5$	9.24e-02	$M_D = 2.8 \text{ TeV}, n = 2$	3.36e-02
$M_D = 2.2 \text{ TeV}, n = 6$	1.09e-01	$M_D = 2.8 \text{ TeV}, n = 3$	2.99e-02
$M_D = 2.2 \text{ TeV}, n = 7$	1.32e-01	$M_D = 2.8 \text{ TeV}, n = 4$	2.80e-02
$M_D = 2.3 \text{ TeV}, n = 2$	6.56e-02	$M_D = 2.8 \text{ TeV}, n = 5$	2.81e-02
$M_D = 2.3 \text{ TeV}, n = 3$	6.51e-02	$M_D = 2.8 \text{ TeV}, n = 6$	2.97e-02
$M_D = 2.3 \text{ TeV}, n = 4$	6.99e-02	$M_D = 2.8 \text{ TeV}, n = 7$	3.15e-02
$M_D = 2.3 \text{ TeV}, n = 5$	7.56e-02	$M_D = 2.9 \text{ TeV}, n = 2$	2.91e-02
$M_D = 2.3 \text{ TeV}, n = 6$	8.87e-02	$M_D = 2.9 \text{ TeV}, n = 3$	2.52e-02
$M_D = 2.3 \text{ TeV}, n = 7$	1.05e-01	$M_D = 2.9 \text{ TeV}, n = 4$	2.41e-02
$M_D = 2.4 \text{ TeV}, n = 2$	5.72e-02	$M_D = 2.9 \text{ TeV}, n = 5$	2.41e-02
$M_D = 2.4 \text{ TeV}, n = 3$	5.49e-02	$M_D = 2.9 \text{ TeV}, n = 6$	2.49e-02
$M_D = 2.4 \text{ TeV}, n = 4$	5.63e-02	$M_D = 2.9 \text{ TeV}, n = 7$	2.60e-02
$M_D = 2.4 \text{ TeV}, n = 5$	6.04e-02	$M_D = 3.0 \text{ TeV}, n = 2$	2.58e-02
$M_D = 2.4 \text{ TeV}, n = 6$	6.90e-02	$M_D = 3.0 \text{ TeV}, n = 3$	2.13e-02
$M_D = 2.4 \text{ TeV}, n = 7$	8.19e-02	$M_D = 3.0 \text{ TeV}, n = 4$	2.04e-02
$M_D = 2.5 \text{ TeV}, n = 2$	5.04e-02	$M_D = 3.0 \text{ TeV}, n = 5$	2.02e-02
$M_D = 2.5 \text{ TeV}, n = 3$	4.75e-02	$M_D = 3.0 \text{ TeV}, n = 6$	2.05e-02
$M_D = 2.5 \text{ TeV}, n = 4$	4.71e-02	$M_D = 3.0 \text{ TeV}, n = 7$	2.11e-02

Table E.2: Continuation from tab. E.1.

Bibliography

- [1] V. M. Abazov et al. Measurement of the W Boson Mass with the D0 Detector. *Phys. Rev. Lett.*, 108:151804, 2012.
- [2] T. Aaltonen et al. Precise measurement of the W -boson mass with the CDF II detector. *Phys. Rev. Lett.*, 108:151803, 2012.
- [3] M. Aaboud et al. Measurement of the W -boson mass in pp collisions at $\sqrt{s} = 7$ TeV with the ATLAS detector. *Eur. Phys. J.*, C78(2):110, 2018. [Erratum: Eur. Phys. J.C78,no.11,898(2018)].
- [4] K. Melnikov and F. Petriello. Electroweak gauge boson production at hadron colliders through $\mathcal{O}(\alpha_s^2)$. *Phys. Rev.*, D74:114017, 2006.
- [5] S. Catani, L. Cieri, G. Ferrera, D. de Florian, and M. Grazzini. Vector boson production at hadron colliders: a fully exclusive QCD calculation at NNLO. *Phys. Rev. Lett.*, 103:082001, 2009.
- [6] A. Gehrmann-De Ridder, T. Gehrmann, E. W. N. Glover, A. Huss, and T. A. Morgan. Precise QCD predictions for the production of a Z boson in association with a hadronic jet. *Phys. Rev. Lett.*, 117(2):022001, 2016.
- [7] R. Boughezal et al. Z-boson production in association with a jet at next-to-next-to-leading order in perturbative QCD. *Phys. Rev. Lett.*, 116(15):152001, 2016.
- [8] R. Boughezal, C. Focke, X. Liu, and F. Petriello. W -boson production in association with a jet at next-to-next-to-leading order in perturbative QCD. *Phys. Rev. Lett.*, 115(6):062002, 2015.
- [9] S. Dittmaier, A. Huss, and C. Schwinn. Mixed QCD-electroweak $\mathcal{O}(\alpha_s\alpha)$ corrections to Drell-Yan processes in the resonance region: pole approximation and non-factorizable corrections. *Nucl. Phys.*, B885:318–372, 2014.
- [10] J. M. Lindert et al. Precise predictions for $V +$ jets dark matter backgrounds. *Eur. Phys. J.*, C77(12):829, 2017.
- [11] C. Balazs, J. Qiu, and C. P. Yuan. Effects of QCD resummation on distributions of leptons from the decay of electroweak vector bosons. *Phys. Lett.*, B355:548–554, 1995.

- [12] S. Catani, D. de Florian, G. Ferrera, and M. Grazzini. Vector boson production at hadron colliders: transverse-momentum resummation and leptonic decay. *JHEP*, 12:047, 2015.
- [13] S. Frixione and B. R. Webber. Matching NLO QCD computations and parton showers simulations. *JHEP*, 06:029, 2002.
- [14] P. Nason. A new method for combining NLO QCD with shower Monte Carlo algorithms. *JHEP*, 11:040, 2004.
- [15] S. Frixione and B. R. Webber. Matching NLO QCD computations and parton shower simulations. *JHEP*, 06:029, 2002.
- [16] S. Alioli, P. Nason, C. Oleari, and Emanuele Re. A general framework for implementing NLO calculations in shower Monte Carlo programs: the POWHEG BOX. *JHEP*, 06:043, 2010.
- [17] G. Aad et al. Measurement of the transverse momentum distribution of Z/γ^* bosons in proton-proton collisions at $\sqrt{s} = 7 \text{ TeV}$ with the ATLAS detector. *Phys. Lett. B*, 705:415, 2011.
- [18] G. Aad et al. Measurement of the Z/γ^* bosons transverse momentum distribution in pp collisions at $\sqrt{s} = 7 \text{ TeV}$ with the ATLAS detector. *JHEP*, 09:145, 2014.
- [19] G. Aad et al. Measurement of the transverse momentum and ϕ_η^* distributions of Drell-Yan lepton pairs in proton-proton collisions at $\sqrt{s} = 8 \text{ TeV}$ with the ATLAS detector. *Eur. Phys. J.*, C76(5):291, 2016.
- [20] M. Aaboud et al. Precision measurement and interpretation of inclusive W^+ , W^- and Z/γ^* production cross sections with the ATLAS detector. *Eur. Phys. J.*, C77(6):367, 2017.
- [21] A. Sirunyan et al. Measurement of the differential Drell-Yan cross section in proton-proton collisions at $\sqrt{s} = 13 \text{ TeV}$. 2018.
- [22] S. Chatrchyan et al. Measurement of the rapidity and transverse momentum distributions of Z bosons in pp collisions at $\sqrt{s} = 7 \text{ TeV}$. *Phys. Rev. D*, 85:032002, 2012.
- [23] V. Khachatryan et al. Measurement of the Z boson differential cross section in transverse momentum and rapidity in proton-proton collisions at 8 TeV. *Phys. Lett. B*, 749:187, 2015.
- [24] V. Khachatryan et al. Measurements of differential and double-differential Drell-Yan cross sections in proton-proton collisions at $\sqrt{s} = 8 \text{ TeV}$. *Eur. Phys. J. C*, 75:147, 2015.

- [25] V. Khachatryan et al. Measurement of the transverse momentum spectra of weak vector bosons produced in proton-proton collisions at $\sqrt{s} = 8$ TeV. *JHEP*, 02:096, 2017.
- [26] R. Aaij et al. Inclusive W and Z production in the forward region at $\sqrt{s} = 7$ TeV. *JHEP*, 06:058, 2012.
- [27] R. Aaij et al. Measurement of the cross-section for $Z \rightarrow e^+e^-$ production in pp collisions at $\sqrt{s} = 7$ TeV. *JHEP*, 02:106, 2013.
- [28] R. Aaij et al. Measurement of the forward Z boson production cross-section in pp collisions at $\sqrt{s} = 7$ TeV. *JHEP*, 08:039, 2015.
- [29] R. Aaij et al. Measurement of forward W and Z boson production in pp collisions at $\sqrt{s} = 8$ TeV. *JHEP*, 01:155, 2016.
- [30] R. Aaij et al. Measurement of the forward Z boson production cross-section in pp collisions at $\sqrt{s} = 13$ TeV. *JHEP*, 09:136, 2016.
- [31] T. Affolder et al. The transverse momentum and total cross section of e^+e^- pairs in the Z boson region from $p\bar{p}$ collisions at $\sqrt{s} = 1.8$ TeV. *Phys. Rev. Lett.*, 84:845–850, 2000.
- [32] B. Abbott et al. Differential production cross section of Z bosons as a function of transverse momentum at $\sqrt{s} = 1.8$ TeV. *Phys. Rev. Lett.*, 84:2792–2797, 2000.
- [33] V. M. Abazov et al. Measurement of the shape of the boson transverse momentum distribution in $p\bar{p} \rightarrow Z/\gamma^* \rightarrow e^+e^- + X$ events produced at $\sqrt{s}=1.96$ -TeV. *Phys. Rev. Lett.*, 100:102002, 2008.
- [34] V. Abazov et al. Measurement of the normalized $Z/\gamma^* \rightarrow \mu^+\mu^-$ transverse momentum distribution in $p\bar{p}$ collisions at $\sqrt{s} = 1.96$ TeV. *Phys. Lett.*, B693:522–530, 2010.
- [35] V. Abazov et al. Precise study of the Z/γ^* boson transverse momentum distribution in $p\bar{p}$ collisions using a novel technique. *Phys. Rev. Lett.*, 106:122001, 2011.
- [36] G. Hinshaw, D. Larson, E. Komatsu, D. N. Spergel, C. L. Bennett, J. Dunkley, M. R. Nolta, M. Halpern, R. S. Hill, N. Odegard, L. Page, K. M. Smith, J. L. Weiland, B. Gold, N. Jarosik, A. Kogut, M. Limon, S. S. Meyer, G. S. Tucker, E. Wollack, and E. L. Wright. Nine-year Wilkinson Microwave Anisotropy Probe (WMAP) observations: cosmological parameter results. *The Astrophysical Journal Supplement Series*, 208(2):19, sep 2013.
- [37] P. Cushman et al. Working Group Report: WIMP Dark Matter Direct Detection. In *Proceedings, 2013 Community Summer Study on the Future of U.S. Particle Physics: Snowmass on the Mississippi (CSS2013): Minneapolis, MN, USA, July 29-August 6, 2013*, 2013.

- [38] J. Buckley et al. Working Group Report: WIMP Dark Matter Indirect Detection. In *Proceedings, 2013 Community Summer Study on the Future of U.S. Particle Physics: Snowmass on the Mississippi (CSS2013): Minneapolis, MN, USA, July 29-August 6, 2013*, 2013.
- [39] M. Beltran, D. Hooper, E. W. Kolb, Z. A. C. Krusberg, and T. M. P. Tait. Maverick dark matter at colliders. *JHEP*, 09:037, 2010.
- [40] J. Goodman, M. Ibe, A. Rajaraman, W. Shepherd, T. M. P. Tait, and H. B. Yu. Constraints on light Majorana dark matter from colliders. *Phys. Lett. B*, 695:185, 2011.
- [41] Y. Bai, P. J. Fox, and R. Harnik. The Tevatron at the frontier of dark matter direct detection. *JHEP*, 12:048, 2010.
- [42] J. Goodman, M. Ibe, A. Rajaraman, W. Shepherd, T. M. P. Tait, and Hai-Bo Yu. Constraints on Dark Matter from Colliders. *Phys. Rev. D*, 82:116010, 2010.
- [43] P. J. Fox, R. Harnik, J. Kopp, and Y. Tsai. Missing Energy Signatures of Dark Matter at the LHC. *Phys. Rev. D*, 85:056011, 2012.
- [44] A. Rajaraman, W. Shepherd, T. M. P. Tait, and A. M. Wijangco. LHC Bounds on Interactions of Dark Matter. *Phys. Rev. D*, 84:095013, 2011.
- [45] S. Chatrchyan et al. Search for invisible decays of Higgs bosons in the vector boson fusion and associated ZH production modes. *Eur. Phys. J.*, C74:2980, 2014.
- [46] V. Khachatryan et al. Search for dark matter and unparticles produced in association with a Z boson in proton-proton collisions at $\sqrt{s} = 8$ TeV. *Phys. Rev.*, D93(5):052011, 2016. [Erratum: *Phys. Rev.*D97,no.9,099903(2018)].
- [47] G. Aad et al. Search for dark matter in events with a Z boson and missing transverse momentum in pp collisions at $\sqrt{s}=8$ TeV with the ATLAS detector. *Phys. Rev.*, D90(1):012004, 2014.
- [48] G. Aad et al. Search for dark matter in events with a hadronically decaying W or Z boson and missing transverse momentum in pp collisions at $\sqrt{s} = 8$ TeV with the ATLAS detector. *Phys. Rev. Lett.*, 112(4):041802, 2014.
- [49] G. Aad et al. Search for new particles in events with one lepton and missing transverse momentum in pp collisions at $\sqrt{s} = 8$ TeV with the ATLAS detector. *JHEP*, 09:037, 2014.
- [50] V. Khachatryan et al. Search for physics beyond the standard model in final states with a lepton and missing transverse energy in proton-proton collisions at $\text{sqrt}(s) = 8$ TeV. *Phys. Rev.*, D91(9):092005, 2015.

- [51] G. Aad et al. Search for dark matter in events with heavy quarks and missing transverse momentum in pp collisions with the ATLAS detector. *Eur. Phys. J.*, C75(2):92, 2015.
- [52] G. Aad et al. Search for new phenomena in events with a photon and missing transverse momentum in pp collisions at $\sqrt{s} = 8$ TeV with the ATLAS detector. *Phys. Rev.*, D91(1):012008, 2015. [Erratum: *Phys. Rev.* D92,no.5,059903(2015)].
- [53] V. Khachatryan et al. Search for Monotop Signatures in Proton-Proton Collisions at $\sqrt{s} = 8$ TeV. *Phys. Rev. Lett.*, 114(10):101801, 2015.
- [54] G. Aad et al. Search for invisible particles produced in association with single-top-quarks in proton-proton collisions at $\sqrt{s} = 8$ TeV with the ATLAS detector. *Eur. Phys. J.*, C75(2):79, 2015.
- [55] G. Aad et al. Search for Dark Matter in Events with Missing Transverse Momentum and a Higgs Boson Decaying to Two Photons in pp Collisions at $\sqrt{s} = 8$ TeV with the ATLAS Detector. *Phys. Rev. Lett.*, 115(13):131801, 2015.
- [56] V. Khachatryan et al. Search for the production of dark matter in association with top-quark pairs in the single-lepton final state in proton-proton collisions at $\text{sqrt}(s) = 8$ TeV. *JHEP*, 06:121, 2015.
- [57] V. Khachatryan et al. Search for dark matter, extra dimensions, and unparticles in monojet events in proton- $\bar{\Lambda}$ proton collisions at $\sqrt{s} = 8$ TeV. *Eur. Phys. J.*, C75(5):235, 2015.
- [58] G. Aad et al. Search for new phenomena in final states with an energetic jet and large missing transverse momentum in pp collisions at $\sqrt{s} = 8$ TeV with the ATLAS detector. *Eur. Phys. J.*, C75(7):299, 2015. [Erratum: *Eur. Phys. J.* C75,no.9,408(2015)].
- [59] V. Khachatryan et al. Search for new phenomena in monophoton final states in proton-proton collisions at $\sqrt{s} = 8$ TeV. *Phys. Lett.*, B755:102–124, 2016.
- [60] V. Khachatryan et al. Search for dark matter in proton-proton collisions at 8 TeV with missing transverse momentum and vector boson tagged jets. *JHEP*, 12:083, 2016. [Erratum: *JHEP* 08,035(2017)].
- [61] J. J. Thomson. Cathode rays. *Phil. Mag. Ser. 5*, 44:293–316, 1897.
- [62] E. Rutherford. The scattering of alpha and beta particles by matter and the structure of the atom. *Phil. Mag. Ser. 6*, 21:669–688, 1911.
- [63] N. Bohr. I. On the constitution of atoms and molecules. *The London, Edinburgh, and Dublin Philosophical Magazine and Journal of Science*, 26(151):1–25, 1913.
- [64] J. Chadwick. Possible Existence of a Neutron. *Nature*, 129:312, 1932.

- [65] M. Planck. Über das Gesetz der Energieverteilung im Normalspectrum. *Annalen der Physik*, 309(3):553–563, 1901.
- [66] A. Einstein. Über einen die Erzeugung und Verwandlung des Lichtes betreffenden heuristischen Gesichtspunkt. *Annalen der Physik*, 322(6):132–148, 1905.
- [67] A. H. Compton. A Quantum Theory of the Scattering of X-rays by Light Elements. *Phys. Rev.*, 21:483–502, May 1923.
- [68] Hideki Yukawa. On the Interaction of Elementary Particles. I. *Nippon Sugaku-Buturigakkai Kizi Dai 3 Ki*, 17:48–57, 1935.
- [69] J. C. Street and E. C. Stevenson. New Evidence for the Existence of a Particle of Mass Intermediate Between the Proton and Electron. *Phys. Rev.*, 52:1003–1004, Nov 1937.
- [70] S. H. Neddermeyer and C. D. Anderson. Note on the Nature of Cosmic-Ray Particles. *Phys. Rev.*, 51:884–886, May 1937.
- [71] C. M. G. Lattes, H. Muirhead, G. P. S. Occhialini, and C. F. Powell. PROCESSES INVOLVING CHARGED MESONS. *Nature*, 159:694–697, 1947. [,42(1947)].
- [72] E. Fermi. Versuch einer Theorie der β -Strahlen. I. *Zeitschrift für Physik*, 88(3):161–177, Mar 1934.
- [73] C. L. Cowan, F. Reines, F. B. Harrison, H. W. Kruse, and A. D. McGuire. Detection of the Free Neutrino: a Confirmation. *Science*, 124(3212):103–104, 1956.
- [74] G. Danby, J-M. Gaillard, K. Goulianos, L. M. Lederman, N. Mistry, M. Schwartz, and J. Steinberger. Observation of High-Energy Neutrino Reactions and the Existence of Two Kinds of Neutrinos. *Phys. Rev. Lett.*, 9:36–44, Jul 1962.
- [75] M. L. Perl, G. S. Abrams, A. M. Boyarski, M. Breidenbach, D. D. Briggs, F. Bulos, W. Chinowsky, J. T. Dakin, G. J. Feldman, C. E. Friedberg, D. Fryberger, G. Goldhaber, G. Hanson, F. B. Heile, B. Jean-Marie, J. A. Kadyk, R. R. Larsen, A. M. Litke, D. Lüke, B. A. Lulu, V. Lüth, D. Lyon, C. C. Morehouse, J. M. Paterson, F. M. Pierre, T. P. Pun, P. A. Rapidis, B. Richter, B. Sadoulet, R. F. Schwitters, W. Tanenbaum, G. H. Trilling, F. Vannucci, J. S. Whitaker, F. C. Winkelmann, and J. E. Wiss. Evidence for Anomalous Lepton Production in $e^+ - e^-$ Annihilation. *Phys. Rev. Lett.*, 35:1489–1492, Dec 1975.
- [76] K. Kodama, N. Ushida, C. Andreopoulos, N. Saoulidou, G. Tzanakos, P. Yager, B. Baller, D. Boehnlein, W. Freeman, B. Lundberg, J. Morfin, R. Rameika, J.C. Yun, J.S. Song, C.S. Yoon, S.H. Chung, P. Berghaus, M. Kubantsev, N.W. Reay, R. Sidwell, N. Stanton, S. Yoshida, S. Aoki, T. Hara, J.T. Rhee, D. Ciampa,

- C. Erickson, M. Graham, K. Heller, R. Rusack, R. Schwienhorst, J. Sielaff, J. Trammell, J. Wilcox, K. Hoshino, H. Jiko, M. Miyanishi, M. Komatsu, M. Nakamura, T. Nakano, K. Niwa, N. Nonaka, K. Okada, O. Sato, T. Akdogan, V. Paolone, C. Rosenfeld, A. Kulik, T. Kafka, W. Oliver, T. Patzak, and J. Schneps. Observation of tau neutrino interactions. *Physics Letters B*, 504(3):218 – 224, 2001.
- [77] M. Gell-Mann. A Schematic Model of Baryons and Mesons. *Phys. Lett.*, 8:214–215, 1964.
- [78] G. Zweig. An SU₃ model for strong interaction symmetry and its breaking; Version 2. (CERN-TH-412):80 p, Feb 1964. Version 1 is CERN preprint 8182/TH.401, Jan. 17, 1964.
- [79] E. D. Bloom, D. H. Coward, H. DeStaebler, J. Drees, G. Miller, L. W. Mo, R. E. Taylor, M. Breidenbach, J. I. Friedman, G. C. Hartmann, and H. W. Kendall. High-Energy Inelastic $e - p$ Scattering at 6° and 10°. *Phys. Rev. Lett.*, 23:930–934, Oct 1969.
- [80] M. Breidenbach, J. I. Friedman, H. W. Kendall, E. D. Bloom, D. H. Coward, H. DeStaebler, J. Drees, L. W. Mo, and R. E. Taylor. Observed Behavior of Highly Inelastic Electron-Proton Scattering. *Phys. Rev. Lett.*, 23:935–939, Oct 1969.
- [81] J. J. Aubert, U. Becker, P. J. Biggs, J. Burger, M. Chen, G. Everhart, P. Goldhagen, J. Leong, T. McCorriston, T. G. Rhoades, M. Rohde, S. Ting, S. L. Wu, and Y. Y. Lee. Experimental Observation of a Heavy Particle J . *Phys. Rev. Lett.*, 33:1404–1406, Dec 1974.
- [82] J. E. Augustin, A. M. Boyarski, M. Breidenbach, F. Bulos, J. T. Dakin, G. J. Feldman, G. E. Fischer, D. Fryberger, G. Hanson, B. Jean-Marie, R. R. Larsen, V. Lüth, H. L. Lynch, D. Lyon, C. C. Morehouse, J. M. Paterson, M. L. Perl, B. Richter, P. Rapidis, R. F. Schwitters, W. M. Tanenbaum, F. Vannucci, G. S. Abrams, D. Briggs, W. Chinowsky, C. E. Friedberg, G. Goldhaber, R. J. Hollebeek, J. A. Kadyk, B. Lulu, F. Pierre, G. H. Trilling, J. S. Whitaker, J. Wiss, and J. E. Zipse. Discovery of a Narrow Resonance in e^+e^- Annihilation. *Phys. Rev. Lett.*, 33:1406–1408, Dec 1974.
- [83] S. W. Herb, D. C. Hom, L. M. Lederman, J. C. Sens, H. D. Snyder, J. K. Yoh, J. A. Appel, B. C. Brown, C. N. Brown, W. R. Innes, K. Ueno, T. Yamanouchi, A. S. Ito, H. Jöstlein, D. M. Kaplan, and R. D. Kephart. Observation of a Dimuon Resonance at 9.5 GeV in 400-GeV Proton-Nucleus Collisions. *Phys. Rev. Lett.*, 39:252–255, Aug 1977.
- [84] B. R. Stella and H. J. Meyer. Υ (9.46 GeV) and the gluon discovery (a critical recollection of PLUTO results). *The European Physical Journal H*, 36(2):203, Oct 2011.

- [85] F. Abe et al. Observation of Top Quark Production in $\bar{p}p$ Collisions with the Collider Detector at Fermilab. *Phys. Rev. Lett.*, 74:2626–2631, Apr 1995.
- [86] S. Abachi et al. Search for High Mass Top Quark Production in $p\bar{p}$ Collisions at $\sqrt{s} = 1.8$ TeV. *Phys. Rev. Lett.*, 74:2422–2426, Mar 1995.
- [87] G. Arnison et al. Experimental Observation of Lepton Pairs of Invariant Mass Around 95-GeV/c**2 at the CERN SPS Collider. *Phys. Lett.*, B126:398–410, 1983. [,7.55(1983)].
- [88] G. Arnison et al. Experimental Observation of Isolated Large Transverse Energy Electrons with Associated Missing Energy at $s^{**}(1/2) = 540$ -GeV. *Phys. Lett.*, B122:103–116, 1983. [,611(1983)].
- [89] P. Bagnaia et al. Evidence for $Z_0 \rightarrow e^+ e^-$ at the CERN anti-p p Collider. *Phys. Lett.*, B129:130–140, 1983. [,7.69(1983)].
- [90] M. Banner et al. Observation of Single Isolated Electrons of High Transverse Momentum in Events with Missing Transverse Energy at the CERN anti-p p Collider. *Phys. Lett.*, B122:476–485, 1983. [,7.45(1983)].
- [91] S. Chatrchyan et al. Observation of a new boson at a mass of 125 GeV with the CMS experiment at the LHC. *Phys. Lett.*, B716:30–61, 2012.
- [92] G. Aad et al. Observation of a new particle in the search for the Standard Model Higgs boson with the ATLAS detector at the LHC. *Phys. Lett.*, B716:1–29, 2012.
- [93] S. Weinberg. A Model of Leptons. *Phys. Rev. Lett.*, 19:1264–1266, Nov 1967.
- [94] M. Tanabashi et al. Review of Particle Physics. *Phys. Rev. D*, 98:030001, Aug 2018.
- [95] J. C. Collins, D. E. Soper, and George F. Sterman. Factorization of Hard Processes in QCD. *Adv. Ser. Direct. High Energy Phys.*, 5:1–91, 1989.
- [96] R. Placakyte. Parton Distribution Functions. In *Proceedings, 31st International Conference on Physics in collisions (PIC 2011): Vancouver, Canada, August 28-September 1, 2011*, 2011.
- [97] A. J. Baltz. The Physics of Ultraperipheral Collisions at the LHC. *Phys. Rept.*, 458:1–171, 2008.
- [98] Parton distributions for the LHC Run II. *JHEP*, 04:040, 2015.
- [99] D. Abercrombie et al. Dark matter benchmark models for early LHC Run-2 searches: Report of the ATLAS/CMS dark matter forum. 2015.

- [100] ATLAS Collaboration. Observation of a new particle in the search for the Standard Model Higgs boson with the ATLAS detector at the LHC. *Phys.Lett.*, B716:1–29, 2012.
- [101] S. Chatrchyan et al. Observation of a new boson at a mass of 125 GeV with the CMS experiment at the LHC. *Phys.Lett.*, B716:30–61, 2012.
- [102] Ghosh, D. and others. Looking for an Invisible Higgs Signal at the LHC. 2012.
- [103] S. P. Martin and J. D. Wells. Motivation and detectability of an invisibly decaying Higgs boson at the Fermilab Tevatron. *Phys.Rev.*, D60:035006, 1999.
- [104] Y. Bai, P. Draper, and J. Shelton. Measuring the Invisible Higgs Width at the 7 and 8 TeV LHC. *JHEP*, 07:192, 2012.
- [105] G. Belanger, F. Boudjema, A. Cottrant, R.M. Godbole, and A. Semenov. The MSSM invisible Higgs in the light of dark matter and g-2. *Phys.Lett.*, B519:93–102, 2001.
- [106] G. F. Giudice, R. Rattazzi, and J. D. Wells. Graviscalars from higher dimensional metrics and curvature Higgs mixing. *Nucl.Phys.*, B595:250–276, 2001.
- [107] M. Battaglia, D. Dominici, J.F. Gunion, and J.D. Wells. The Invisible Higgs decay width in the add model at the LHC. 2004.
- [108] S. Baek, P. Ko, W. Park, and E. Senaha. Higgs Portal Vector Dark Matter : Revisited. *JHEP*, 05:036, 2013.
- [109] A. Djouadi, O. Lebedev, Y. Mambrini, and J. Quevillon. Implications of LHC searches for Higgs–portal dark matter. *Phys. Lett.*, B709:65–69, 2012.
- [110] A. Djouadi, A. Falkowski, Y. Mambrini, and J. Quevillon. Direct Detection of Higgs-Portal Dark Matter at the LHC. *Eur. Phys. J.*, C73(6):2455, 2013.
- [111] N. Arkani-Hamed, S. Dimopoulos, and G. Dvali. The hierarchy problem and new dimensions at a millimeter. *Phys. Lett. B*, 429:263, 1998.
- [112] N. Arkani-Hamed, S. Dimopoulos, and G. Dvali. Phenomenology, astrophysics and cosmology of theories with sub-millimeter dimensions and TeV scale quantum gravity. *Phys. Rev. D*, 59:086004, 1999.
- [113] T. Han, J. D. Lykken, and R. Zhang. On Kaluza-Klein states from large extra dimensions. *Phys. Rev. D*, 59:105006, 1999.
- [114] Z. Kang. Upgrading Sterile Neutrion Dark Matter to FImP Using Scale Invariance. 2014.
- [115] M. Rinaldi, G. Cognola, L. Vanzo, and S. Zerbini. Inflation in scale-invariant theories of gravity. *Phys. Rev. D*, 91:123527, 2015.

- [116] H. Cheng. The Possible Existence of Weyl’s Vector Meson. *Phys. Rev. Lett.*, 61:2182, 1988.
- [117] T. Banks and A. Zaks. On the phase structure of vector-like gauge theories with massless fermions. *Nucl. Phys. B*, 196:189, 1982.
- [118] Lyndon Evans and Philip Bryant. LHC Machine. *Journal of Instrumentation*, 3(08):S08001–S08001, aug 2008.
- [119] M. Benedikt, P. Collier, V. Mertens, J. Poole, and K. Schindl. LHC Design Report. 3. The LHC injector chain. 2004.
- [120] V. Khachatryan et al. The CMS trigger system. *JINST*, 12:P01020, 2017.
- [121] S. Chatrchyan et al. The CMS Experiment at the CERN LHC. *JINST*, 3:S08004, 2008.
- [122] *Technical proposal*. LHC Tech. Proposal. CERN, Geneva, 1994. Cover title : CMS, the Compact Muon Solenoid : technical proposal.
- [123] E. Gatti, A. Longoni, H. Okuno, and P. Semenza. Optimum geometry for strip cathodes or grids in MWPC for avalanche localization along the anode wires. *Nuclear Instruments and Methods*, 163(1):83 – 92, 1979.
- [124] C. Foudas. The CMS Level-1 Trigger at LHC and Super-LHC. In *Proceedings, 34th International Conference on High Energy Physics (ICHEP 2008): Philadelphia, Pennsylvania, July 30-August 5, 2008*, 2008.
- [125] Khachatryan, V. and others. Performance of electron reconstruction and selection with the CMS detector in proton-proton collisions at $\sqrt{s} = 8$ TeV. *JINST 10 (2015) P06005*, page 6, 2015.
- [126] CMS Collaboration. Commissioning of the Particle-Flow reconstruction in Minimum-Bias and Jet Events from pp Collisions at 7 TeV. *CMS Physics Analysis Summary*, CMS-PAS-PFT-10-002, 2010.
- [127] CMS Collaboration. Performance of muon identification in 2010 data. *CMS Physics Analysis Summary*, CMS-PAS-MUO-10-004, 2010.
- [128] M. Cacciari, G. P. Salam, and G. Soyez. The Anti- k_t jet clustering algorithm. *JHEP*, 04:063, 2008.
- [129] M. Cacciari, G. P. Salam, and G. Soyez. FastJet user manual. *Eur. Phys. J. C*, 72:1896, 2012.
- [130] M. Cacciari and G. P. Salam. Dispelling the N^3 myth for the k_t jet-finder. *Phys. Lett. B*, 641:57, 2006.
- [131] A. M. Sirunyan et al. Identification of heavy-flavour jets with the CMS detector in pp collisions at 13 TeV. *JINST*, 13(05):P05011, 2018.

- [132] V. Khachatryan et al. Performance of photon reconstruction and identification with the CMS detector in proton-proton collisions at $\sqrt{s} = 8$ TeV. *JINST*, 10:P08010, 2015.
- [133] A. Sirunyan et al. Particle-flow reconstruction and global event description with the CMS detector. *JINST*, 12:P10003, 2017.
- [134] Performance of missing energy reconstruction in 13 TeV pp collision data using the CMS detector. Technical Report CMS-PAS-JME-16-004, CERN, Geneva, 2016.
- [135] S. Agostinelli et al. GEANT4: A Simulation toolkit. *Nucl.Instrum.Meth.*, A506:250–303, 2003.
- [136] S. Alioli, P. Nason, C. Oleari, and Emanuele Re. NLO vector-boson production matched with shower in POWHEG. *JHEP*, 07:060, 2008.
- [137] S. Frixione, P. Nason, and C. Oleari. Matching NLO QCD computations with parton shower simulations: the POWHEG method. *JHEP*, 11:070, 2007.
- [138] S. Alioli, P. Nason, C. Oleari, and E. Re. A General Framework for Implementing NLO Calculations in Shower Monte Carlo Programs: the POWHEG BOX. *JHEP*, 06:043, 2010.
- [139] J. M. Campbell and R. K. Ellis. MCFM for the Tevatron and the LHC. *Nucl. Phys. Proc. Suppl.*, 205-206:10–15, 2010.
- [140] J. Alwall, R. Frederix, S. Frixione, V. Hirschi, F. Maltoni, O. Mattelaer, H. S. Shao, T. Stelzer, P. Torrielli, and M. Zaro. The automated computation of tree-level and next-to-leading order differential cross sections, and their matching to parton shower simulations. *JHEP*, 07:079, 2014.
- [141] T. Sjöstrand, S. Mrenna, and P. Skands. PYTHIA 6.4 physics and manual. *JHEP*, 05:026, 2006.
- [142] T. Sjöstrand et al. An Introduction to PYTHIA 8.2. *Comput. Phys. Commun.*, 191:159–177, 2015.
- [143] M. Czakon, P. Fiedler, and A. Mitov. Total Top-Quark Pair-Production Cross Section at Hadron Colliders Through $O(\frac{4}{S})$. *Phys. Rev. Lett.*, 110:252004, 2013.
- [144] T. Sjostrand, S. Mrenna, and P. Z. Skands. A Brief Introduction to PYTHIA 8.1. *Comput.Phys.Commun.*, 178:852–867, 2008.
- [145] V. Khachatryan et al. Event generator tunes obtained from underlying event and multiparton scattering measurements. *Eur. Phys. J. C*, 76:155, 2016.
- [146] P. Skands, S. Carrazza, and J. Rojo. Tuning PYTHIA 8.1: the Monash 2013 Tune. *Eur. Phys. J.*, C74(8):3024, 2014.

- [147] G. Busoni et al. Recommendations on presenting LHC searches for missing transverse energy signals using simplified s -channel models of dark matter. 2016.
- [148] S. Ask. Simulation of Z plus graviton/unparticle production at the LHC. *Eur. Phys. J. C*, 60:509, 2009.
- [149] S. Ask, I. V. Akin, L. Benucci, A. De Roeck, M. Goebel, and J. Haller. Real emission and virtual exchange of gravitons and unparticles in PYTHIA8. *Comput. Phys. Commun.*, 181:1593, 2010.
- [150] The CMS Collaboration. CMS Luminosity Measurements for the 2016 Data Taking Period. Technical Report CMS-PAS-LUM-17-001, 2017.
- [151] V. Khachatryan et al. Measurement of the differential cross section for top quark pair production in pp collisions at $\sqrt{s} = 8$ TeV. *Eur. Phys. J.*, C75(11):542, 2015.
- [152] S. Chatrchyan et al. Energy Calibration and Resolution of the CMS Electromagnetic Calorimeter in pp Collisions at $\sqrt{s} = 7$ TeV. *JINST*, 8:P09009, 2013. [JINST8,9009(2013)].
- [153] A. Bodek, A. van Dyne, J. Y. Han, W. Sakumoto, and A. Strelnikov. Extracting Muon Momentum Scale Corrections for Hadron Collider Experiments. *Eur. Phys. J.*, C72:2194, 2012.
- [154] P. Golonka and Z. Was. PHOTOS Monte Carlo: A Precision tool for QED corrections in Z and W decays. *Eur. Phys. J.*, C45:97–107, 2006.
- [155] A. Banfi, S. Redford, M. Vesterinen, P. Waller, and T. Wyatt. Optimisation of variables for studying dilepton transverse momentum distributions at hadron colliders. *Eur. Phys. J. C*, 71:1600, 2011.
- [156] A. Banfi, M. Dasgupta, S. Marzani, and L. Tomlinson. Predictions for Drell-Yan ϕ^* and Q_T observables at the LHC. *Phys. Lett. B*, 715:152, 2012.
- [157] S. Marzani. Q_T and ϕ^* observables in Drell-Yan processes. *EPJ Web Conf.*, 49:14007, 2013.
- [158] A. M. Sirunyan et al. Measurement of differential cross sections in the kinematic angular variable ϕ^* for inclusive Z boson production in pp collisions at $\sqrt{s} = 8$ TeV. *JHEP*, 03:172, 2018.
- [159] V. Khachatryan et al. Measurements of inclusive W and Z cross sections in pp collisions at $\sqrt{s} = 7$ TeV. *JHEP*, 01:080, 2011.
- [160] M. Botje, J. Butterworth, A. Cooper-Sarkar, A. de Roeck, J. Feltesse, et al. The PDF4LHC Working Group Interim Recommendations. 2011.
- [161] S. Alekhin, S. Alioli, R. D. Ball, V. Bertone, J. Blumlein, et al. The PDF4LHC Working Group Interim Report. 2011.

- [162] H. Lai, M. Guzzi, J. Huston, Z. Li, P. M. Nadolsky, et al. New parton distributions for collider physics. *Phys. Rev.*, D82:074024, 2010.
- [163] A. D. Martin et al. Parton distributions for the LHC. *Eur. Phys. J. C*, 63:189–285, 2009.
- [164] R. D. Ball et al. Impact of heavy quark masses on parton distributions and LHC phenomenology. *Nucl. Phys. B*, 849, 2011.
- [165] J. Butterworth et al. PDF4LHC recommendations for LHC Run II. *J. Phys.*, G43:023001, 2016.
- [166] H. B. Prosper and L. Lyons, editors. *Proceedings, PHYSTAT 2011 Workshop on Statistical Issues Related to Discovery Claims in Search Experiments and Unfolding, CERN, Geneva, Switzerland 17-20 January 2011*, Geneva, 2011. CERN, CERN.
- [167] M. Kuusela and V. M. Panaretos. Statistical unfolding of elementary particle spectra: Empirical Bayes estimation and bias-corrected uncertainty quantification. *Ann. Appl. Stat.*, 9(3):1671–1705, 09 2015.
- [168] K. Melnikov and F. Petriello. The W boson production cross section at the LHC through $O(\alpha_s^2)$. *Phys. Rev. Lett.*, 96:231803, 2006.
- [169] R. Gavin, Y. Li, F. Petriello, and S. Quackenbush. FEWZ 2.0: A code for hadronic Z production at next-to-next-to-leading order. *Comput. Phys. Commun.*, 182:2388–2403, 2011.
- [170] R. Gavin, Ye Li, F. Petriello, and S. Quackenbush. W Physics at the LHC with FEWZ 2.1. *Comput. Phys. Commun.*, 184:208–214, 2013.
- [171] Y. Li and F. Petriello. Combining QCD and electroweak corrections to dilepton production in FEWZ. *Phys. Rev.*, D86:094034, 2012.
- [172] R. D. Ball et al. Parton distributions from high-precision collider data. *Eur. Phys. J.*, C77(10):663, 2017.
- [173] G. A. Ladinsky and C. P. Yuan. The nonperturbative regime in QCD resummation for gauge boson production at hadron colliders. *Phys. Rev. D*, 50:4239, 1994.
- [174] C. Balazs and C. P. Yuan. Soft gluon effects on lepton pairs at hadron colliders. *Phys. Rev. D*, 56:5558, 1997.
- [175] F. Landry, R. Brock, P. M. Nadolsky, and C. P. Yuan. Tevatron Run-1 Z boson data and Collins-Soper-Sterman resummation formalism. *Phys. Rev. D*, 67:073016, 2003.

- [176] S. Alioli, C. W. Bauer, C. Berggren, F. J. Tackmann, and J. R. Walsh. Drell-Yan production at NNLL'+NNLO matched to parton showers. *Phys. Rev.*, D92(9):094020, 2015.
- [177] S. Dulat, T. Hou, J. Gao, M. Guzzi, J. Huston, P. Nadolsky, J. Pumplin, C. Schmidt, D. Stump, and C. P. Yuan. New parton distribution functions from a global analysis of quantum chromodynamics. *Phys. Rev.*, D93(3):033006, 2016.
- [178] A. M. Sirunyan et al. Search for new physics in final states with an energetic jet or a hadronically decaying W or Z boson and transverse momentum imbalance at $\sqrt{s} = 13$ TeV. *Phys. Rev.*, D97(9):092005, 2018.
- [179] A. Bierweiler, T. Kasprzik, and J. H. Kühn. Vector-boson pair production at the LHC to $\mathcal{O}(\alpha^3)$ accuracy. *JHEP*, 12:071, 2013.
- [180] S. Gieseke, T. Kasprzik, and J. H. Kahn. Vector-boson pair production and electroweak corrections in HERWIG++. *Eur. Phys. J.*, C74(8):2988, 2014.
- [181] A. Manohar, P. Nason, G. P. Salam, and G. Zanderighi. How bright is the proton? A precise determination of the photon parton distribution function. *Phys. Rev. Lett.*, 117(24):242002, 2016.
- [182] M. Grazzini, S. Kallweit, and D. Rathlev. ZZ production at the LHC: fiducial cross sections and distributions in NNLO QCD. *Phys. Lett.*, B750:407–410, 2015.
- [183] M. Grazzini, S. Kallweit, D. Rathlev, and M. Wiesemann. $W^\pm Z$ production at hadron colliders in NNLO QCD. *Phys. Lett.*, B761:179–183, 2016.
- [184] J. Baglio, L. D. Ninh, and M. M. Weber. Massive gauge boson pair production at the LHC: a next-to-leading order story. *Phys. Rev.*, D88:113005, 2013.
- [185] S. Frixione, V. Hirschi, D. Pagani, H. S. Shao, and M. Zaro. Weak corrections to Higgs hadroproduction in association with a top-quark pair. *JHEP*, 09:065, 2014.
- [186] S. Frixione, V. Hirschi, D. Pagani, H. S. Shao, and M. Zaro. Electroweak and QCD corrections to top-pair hadroproduction in association with heavy bosons. *JHEP*, 06:184, 2015.
- [187] V. Khachatryan et al. Measurement of the WZ production cross section in pp collisions at $\sqrt(s) = 13$ TeV. *Phys. Lett.*, B766:268–290, 2017.
- [188] The CMS collaboration. Determination of jet energy calibration and transverse momentum resolution in CMS. *Journal of Instrumentation*, 6(11):P11002–P11002, nov 2011.

- [189] J. C. Collins, D. E. Soper, and George F. Sterman. Transverse Momentum Distribution in Drell-Yan Pair and W and Z Boson Production. *Nucl. Phys.*, B250:199–224, 1985.
- [190] A. L. Read. Presentation of search results: the CLs technique. *J. Phys. G: Nucl. Part. Phys.*, 28:2693, 2002.
- [191] T. Junk. Confidence level computation for combining searches with small statistics. *Nucl. Instrum. Meth.*, A434:435, 1999.
- [192] G. Cowan, K. Cranmer, E. Gross, and O. Vitells. Asymptotic formulae for likelihood-based tests of new physics. *Eur. Phys. J. C*, 71:1554, 2011.
- [193] Procedure for the LHC Higgs boson search combination in summer 2011. Technical Report ATL-PHYS-PUB-2011-011, CMS-NOTE-2011-005, 2011.
- [194] D. S. Akerib et al. Improved Limits on Scattering of Weakly Interacting Massive Particles from Reanalysis of 2013 LUX Data. *Phys. Rev. Lett.*, 116:161301, 2016.
- [195] R. Agnese et al. New Results from the Search for Low-Mass Weakly Interacting Massive Particles with the CDMS Low Ionization Threshold Experiment. *Phys. Rev. Lett.*, 116:071301, 2016.
- [196] A. Tan et al. Dark Matter Results from First 98.7 Days of Data from the PandaX-II Experiment. *Phys. Rev. Lett.*, 117(12):121303, 2016.
- [197] G. Angloher et al. Results on light dark matter particles with a low-threshold CRESST-II detector. *Eur. Phys. J.*, C76:25, 2016.
- [198] K. Choi et al. Search for neutrinos from annihilation of captured low-mass dark matter particles in the Sun by Super-Kamiokande. *Phys. Rev. Lett.*, 114:141301, 2015.
- [199] C. Amole et al. Dark Matter Search Results from the PICO-60 C_3F_8 Bubble Chamber. *Phys. Rev. Lett.*, 118(25):251301, 2017.
- [200] M. G. Aartsen et al. Search for annihilating dark matter in the Sun with 3 years of IceCube data. *Eur. Phys. J.*, C77(3):146, 2017.
- [201] M. G. Aartsen et al. Improved limits on dark matter annihilation in the Sun with the 79-string IceCube detector and implications for supersymmetry. *JCAP*, 04:022, 2016.
- [202] M. Neubert, J. Wang, and C. Zhang. Higher-Order QCD Predictions for Dark Matter Production in Mono-Z Searches at the LHC. *JHEP*, 02:082, 2016.
- [203] Backović, M. and Krämer, M. and Maltoni, F. and Martini, A. and Mawatari, K. and Pellen, M. Higher-order QCD predictions for dark matter production at the LHC in simplified models with s-channel mediators. *Eur. Phys. J. C*, 75:482, 2015.

- [204] The CMS Collaboration. Simplified likelihood for the re-interpretation of public CMS results. Technical Report CMS-NOTE-2017-001. CERN-CMS-NOTE-2017-001, CERN, Geneva, Jan 2017.
- [205] A. Sirunyan et al. Search for dark matter and unparticles in events with a Z boson and missing transverse momentum in proton-proton collisions at $\sqrt{s} = 13$ TeV. *JHEP*, 03:061, 2017.
- [206] M. Aaboud et al. Search for an invisibly decaying Higgs boson or dark matter candidates produced in association with a Z boson in pp collisions at $\sqrt{s} = 13$ TeV with the ATLAS detector. *Phys. Lett.*, B776:318–337, 2018.
- [207] A. M. Sirunyan et al. Search for invisible decays of a Higgs boson produced through vector boson fusion in proton-proton collisions at $\sqrt{s} = 13$ TeV. *Phys. Lett.*, B793:520–551, 2019.
- [208] V. Khachatryan et al. Searches for invisible decays of the Higgs boson in pp collisions at $\sqrt{s} = 7$, 8, and 13 TeV. *JHEP*, 02:135, 2017.
- [209] A. Höcker et al. TMVA - Toolkit for Multivariate Data Analysis. Technical Report CERN-OPEN-2007-007, 2007.